POLITECNICO DI MILANO

Facoltà di Ingegneria Industriale

Corso di Laurea in
Ingegneria Energetica

Design and optimization of a setup for SOFC anode characterization

Relatore: Prof. Renzo Marchesi

Co-relatore: P.V. Aravind

A. Casalegno

Tesi di Laurea di:

Francesco GARDUMI Matr. 745887

Alberto LATORRE Matr. 745479

Anno Accademico 2010 - 2011

To my family and to
all those who were near me
in these years
(Francesco)

To my parents, my brother,
my family and friends
who supported me in these years
(Alberto)

We would like to thank all the Fuel Cell group at Process and Energy Department of TU Delft for their help in realizing this study and for kindly giving us the possibility of working with them, in particular P.V. Aravind.

We also thank professor Marchesi and professor Casalegno for their support.

Index

List of acronyms

APU: auxiliary power unit

GT: gas turbine

SOFC: solid oxide fuel cell

FC: fuel cell

YSZ: Yttria stabilized Zirconia

GDC: Gadolinum doped Ceria

EIS: electrochemical impedance spectroscopy

CPE: constant phase element

RQ: parallel circuit of a resistor and a CPE

WS: bounded Warburg element

SEM: scanning electron microscope

XRD: X-ray diffraction

ICP-MS: inductively coupled plasma – mass spectrometry

Index of figures and tables

Introduzione allo studio

Le politiche energetiche attualmente adottate in Europa hanno come obiettivo l'aumento della quota di produzione da fonti rinnovabili e l'aumento dell'efficienza dei sistemi già esistenti per la generazione di energia elettrica e calore. Le celle a combustibile ad alta temperatura rispondono a questi requisiti, in quanto sono adatte alla generazione combinata di energia elettrica e calore, in sistemi centralizzati o non, con rendimenti alti anche su piccola scala. In particolare, sempre maggiore attenzione è rivolta all'uso di biomassa come combustibile, dal momento che può essere disponibile a basso costo ed è neutra dal punto di vista delle emissioni di CO_2. Sono quindi disponibili studi su sistemi integrati Gassificatore-Celle ad ossidi solidi (SOFC)-Turbina a gas, con rendimenti elettrici teorici attorno al 70% e rendimenti attorno al 55% ottenuti su prototipi di piccole dimensioni. Il presente studio è stato condotto presso la University of Technology di Delft, dove la ricerca si sta concentrando sull'alimentazione di celle ad ossidi solidi a biosingas. Il problema principale di tale combustibile, oltre alla necessità di gestire le numerose reazioni che avvengono contemporaneamente in presenza di idrocarburi e di CO, è l'effetto dei contaminanti provenienti dalla biomassa originaria sulle celle. Possono in generale comparire tar, particolato, HCl, H_2S, HCN, KCl, NaCl e composti simili. Il KCl é presente a partire dal K contenuto nella biomassa e anche come derivato dei sistemi di abbattimento di HCl. Nulla si sa sui suoi effetti sulle SOFC e sul grado di abbattimento necessario. Uno studio preliminare dell'ECN (Energy Center Netherlands) ha dato suggerimenti riguardo alle procedure sperimentali e ai possibili impatti, ma alcuni dei risultati trovati contrastano con le predizioni. Lo studio che verrà qui presentato prende le mosse dall'intenzione di investigare più in profondità alla TU di Delft gli effetti del KCl sul funzionamento dell'anodo in una SOFC.

Inizialmente si espone il funzionamento di queste celle ed i principi termodinamici che determinano le perdite di polarizzazione, a cui segue una trattazione sullo stato dell'arte dei materiali utilizzati per anodo, catodo ed elettrolita. Riferimenti sul costo degli stack attuale e in prospettiva servono a supportare l'idea che questa tecnologia si stia sviluppando velocemente e possa diventare competitiva nel futuro molto prossimo. Una certa attenzione è dedicata alla GDC, Ceria dopata con Gadolinio, che è un ossido che sta trovando

applicazione come elettrolita per SOFC a media temperatura e, negli elettrodi, come materiale MIEC ("mixed ionic electronic conductor").

Segue l'introduzione della biomassa come potenziale combustibile per sistemi integrati di gassificazione e generazione elettrica con SOFC e turbine a gas. Si approfondisce particolarmente il significato di sostenibilità di tale fonte, che viene considerata fondamentale negli scenari di soddisfacimento del fabbisogno energetico finché non compete con le colture alimentari. Dopo aver discusso quali tipi di biomassa possono fornire un gas adatto all'alimentazione di SOFC, si espongono i diversi inquinanti possibilmente presenti, i metodi che in letteratura si sono trovati per studiarne gli effetti sugli anodi delle celle e cenni sui sistemi di abbattimento a bassa ed alta temperatura. Una maggiore attenzione è dedicata al KCl, alla sua origine come contaminante nel biosingas alimentato alla cella, alle sue proprietà ed ai pochissimi riferimenti bibliografici che si sono trovati riguardo ai suoi possibili effetti sugli anodi delle SOFC.

Il secondo capitolo presenta la teoria della spettroscopia ad impedenza (EIS). Questa è considerata uno strumento utile nell'investigazione dell'influenza dei contaminanti sul funzionamento delle celle a combustibile: a differenza degli studi di polarizzazione su celle complete (curve I-V), uno studio di impedenza su celle simmetriche anodiche permette di separare i diversi processi che avvengono all'elettrodo a cui viene alimentato il combustibile (la parte più critica) ed analizzare i singoli fenomeni limitanti. La curva I-V invece restituisce una polarizzazione ad una certa densità di corrente, dando informazioni solo sulle prestazioni globali. Una volta che i risultati ottenuti con l'impedenza sono soddisfacenti e che una spiegazione preliminare dei processi di contaminazione è stata trovata, si può pensare ad una modellizzazione elettrochimica e termodinamica da validare in seguito con ulteriori esperimenti.

Segue nel capitolo una revisione di tutti i principali riferimenti letterari riguardo a studi di spettroscopia ad impedenza su anodi di SOFC. Già in tale riassunto emerge quanto sia difficile interpretare i risultati delle misurazioni e soprattutto come sia impossibile confrontare gli studi fra di loro, dal momento che ogni gruppo adotta diverse geometrie dei setup e spesso diverse condizioni. Si perviene quindi ad un insieme di valori da cui emerge che gli archi mostrati dagli spettri di impedenza possono in generale essere attribuiti a famiglie di fenomeni limitanti a seconda dell'intervallo di frequenze, resistenze, capacitanze in cui compaiono e sicuramente a seconda dell'asset utilizzato. Nello studio

condotto all'ECN si sono ottenuti su celle simmetriche con anodi Ni/GDC tre archi, attribuiti a fenomeni di adsorbimento sulla superficie della GDC (alta frequenza), ad una coppia red-ox all'interno della GDC (media frequenza), ad una limitazione nel trasporto di massa dovuta alla geometria utilizzata (bassa frequenza). Tali conclusioni sono supportate da riferimenti alla letteratura, da modelli fisici e da studi del comportamento del sistema al variare di diverse condizioni.

Il terzo capitolo introduce il corpo della sperimentazione della presente ricerca. Per aprire la strada alla ricerca sugli effetti del KCl su anodi Ni/GDC si effettuano misurazioni preliminari con EIS sugli stessi anodi con H_2 umidificato come alimentazione. I risultati devono servire come riferimento per quando si aggiungerà alla corrente il contaminante e devono permettere considerazioni fisiche da cui emerga una modifica dell'asset sperimentale per l'introduzione del KCl ed un set di parametri per i test con KCl.

Si nota da un primo test che i risultati non sono né affidabili né riproducibili. Le misurazioni sono molto sensibili a tutti i fattori esterni e sono presenti anche influenze non meglio definite dell'intero sistema attorno alla cella. Si sottolinea che il laboratorio è nuovo, quindi le sue problematiche ancora parzialmente sconosciute. Inoltre la procedura sperimentale deve essere rifinita: i risultati sperimentali di riferimento sono ottenuti con una simile geometria dell'asset ma comunque in un laboratorio fisicamente diverso. Infine si nota che il metodo di analisi degli spettri di impedenza utilizzato in letteratura soffre molto la discrezionalità dell'operatore ed una piccola variazione dei parametri iniziali nel "fitting" degli archi può causare una grande differenza nel risultato finale. Tutto questo è affrontato tramite nuovi test in cui la procedura sperimentale viene iterativamente affinata ed un metodo di analisi statistica dei risultati viene introdotto in modo da minimizzare gli errori di fitting. Tre tecniche di fitting vengono parallelamente utilizzate ed i risultati appaiono in linea fra di loro, con deviazioni standard accettabili. Si ritiene che la standardizzazione del processo abbia avuto successo. La maggior parte dei problemi riscontrati nell'asset sperimentale viene risolta, cosicché risultati affidabili e riproducibili vengono ottenuti in un certo intervallo di condizioni operative.

Nel corso degli esperimenti si variano alcune condizioni in modo da avere un'analisi di sensibilità riguardo ai parametri più importanti: 1. si studia la possibile variazione degli spettri con la variazione del flusso di idrogeno, tema

non ancora affrontato dal gruppo di ricerca presso cui l'esperimento é condotto. Il flusso idealmente non dovrebbe influenzare gli spettri, ma effetti non previsti potrebbero derivare dal setup. 2. Un altro dei problemi riscontrati nella sperimentazione, di gran peso in quanto contribuisce a rendere i risultati disomogenei e poco interpretabili, è l'influenza di una non giusta umidificazione del flusso (dovuta a problemi tecnici sugli apparati ausiliari, allo scostamento dalle condizioni ideali assunte nei calcoli di equilibrio, oppure a fenomeni di stabilizzazione dei processi all'anodo al variare delle condizioni, per cui i tempi non sono sempre del tutto conosciuti). Essa causa una variabilità dell'arco di bassa frequenza (dovuto al trasporto di massa). Si decide quindi di variare le condizioni di umidificazione delle correnti e registrare gli effetti. Questo può ancora una volta aiutare nella conseguente sperimentazione con KCl perché negli esperimenti preliminari con KCl erano stati riscontrati problemi nell'interpretazione delle variazioni dell'arco di bassa frequenza.

Gli spettri d'impedenza risultano riproducibili ed affidabili nell'intervallo fra 200 e 400 Nml/min, mentre a bassi flussi si è registrato un comportamento instabile: le misurazioni a 100 Nml/min hanno dato risultati discordanti per quanto riguarda soprattutto l'ampiezza dell'arco di bassa frequenza; infatti se nel secondo esperimento si sono manifestati stabilmente valori inferiori, nel terzo i valori sono tornati in linea con quelli degli spettri misurati con flussi più alti, dopo un tempo di stabilizzazione dell'ordine delle tre ore. Al flusso di 80 Nml/min (preso in considerazione per approfondire il comportamento a bassi flussi) i risultati sono stati ancora discordanti. Nel terzo esperimento si sono registrati stabilmente valori dell'arco di bassa frequenza nettamente inferiori rispetto a quelli a 200 Nml/min anche dopo tempi di stabilizzazione molto lunghi (circa 15 ore); questo comportamento si è manifestato a bassi livelli di umidificazione (3 e 4 %) mentre si è registrato un comportamento in linea con quelli a flussi più alti con un livello di umidificazione maggiore (7%). Nell'ultimo esperimento i valori degli spettri registrati a bassi flussi (50 ed 80 Nml/min) sono invece più in linea con quelli a flussi più alti. Un comportamento del genere, in cui si hanno valori molto diversi ed anche oscillanti dell'arco di diffusione, si è pensato che possa essere dovuto a problemi di condensazione in tratti della linea di alimentazione che più sono a contatto con l'ambiente esterno. Una conferma a questa ipotesi è stata che nell'ultimo esperimento, in cui ci sono stati valori più in linea con quelli attesi, la temperatura all'interno del laboratorio fosse sensibilmente più alta, e quindi, forse, con una minore presenza di condensazione. Il fatto che questo comportamento sia presente a flussi più bassi

potrebbe essere invece spiegato dai maggiori tempi di residenza associati alle minori velocità nelle tubazioni o nell'umidificatore stesso. Per i futuri esperimenti con il KCl si può quindi suggerire l'impiego di flussi più alti che hanno mostrato stabilità nel comportamento e riproducibilità nei valori in tutti gli esperimenti. La temperatura considerata per condurre la maggior parte degli esperimenti è di 850 °C, a seguito delle considerazioni sulla temperatura di uscita del biosingas dal sistema di abbattimento di contaminanti proposto in letteratura. A questa temperatura si è verificato un processo di sinterizzazione delle maglie d'oro (che fanno da collettori di corrente) sulla superficie anodica. E' stata così giustificata la riduzione con il tempo del valore registrato della resistenza dell'elettrolita (R_s). Il range di valori trovati è comunque in linea con i valori riscontrati in letteratura. A 750 °C invece si è verificato un aumento con il tempo della resistenza dell'elettrolita, quindi una degradazione delle prestazioni, senza apparente sinterizzazione, data la temperatura più bassa.

A valle di queste valutazioni viene disegnata ed attuata una modifica del setup per la sperimentazione con il contaminante. Secondo quanto proposto nello studio presso l'ECN, viene costruito un elemento in quarzo da inserire nel reattore dove possa essere posto un letto di KCl solido e vengono previste due alimentazioni, una di H_2 secco da far passare attraverso il letto, una di H_2 umidificato da miscelare successivamente. Viene inoltre prevista anche la possibilità di inviare H_2 umidificato direttamente nel letto, previo studio dell'influenza della presenza di acqua.

Nel quarto capitolo sono presentati alcuni strumenti che, parallelamente alla tecnica della spettroscopia ad impedenza, possono aiutare a comprendere e quantificare gli effetti della contaminazione da KCl (SEM, XRD) e altri che verificano la correttezza di alcune assunzioni chimico-fisiche e il corretto funzionamento dell'asset sperimentale (ICP e bubble flowmeter). Infine è presentata anche la modifica del setup apportata per supportare questi ultimi due strumenti.

Nell'ultimo capitolo si procede a modellizzare fisicamente il percorso del gas nell'asset sperimentale dai regolatori di flusso fino all'uscita dal reattore, con l'aiuto di calcoli di equilibrio chimico e termodinamico su software ad hoc. Tali calcoli permettono di avere una predizione dell'umidificazione del flusso nell'ipotesi di saturazione all'interno dell'umidificatore, della sublimazione del KCl nel letto e della possibile presenza di altri composti del potassio,

dell'interazione dei materiali dell'anodo con il flusso alimentato alla cella. Inoltre un approccio teorico permette di discutere e supportare le conclusioni riguardo agli elementi che influenzano i comportamenti difficilmente spiegabili, fra quelli riscontrati negli esperimenti.

Questo lavoro si è proposto, attraverso il suo approccio iterativo, prima di tutto di risolvere alcune problematiche presenti nel nuovo laboratorio sulle SOFC della TU Delft fino ad ottenere spettri riproducibili; innanzitutto si è proceduto a standardizzare le procedure di accensione, riduzione e soprattutto stabilizzazione del funzionamento quando si cambiano singoli parametri. Si è notato che il setup garantisce risultati stabili e riproducibili a tutti i livelli di umidificazione e temperatura considerati solo a flussi alti (dai 200 Nml/min), mentre comportamenti instabili si sono verificati a bassi flussi. I valori delle resistenze dell'elettrolita sono in linea con la letteratura di riferimento.

Un altro problema che causava incertezze nell'interpretazione degli spettri era il fitting, essendo troppo dipendente dai parametri imposti dall'utente. A tal proposito è stato proposto un metodo iterativo e statistico per l'analisi dei risultati che ha ridotto fortemente le incertezze.

Una volta ottenuti risultati riproducibili ed interpretabili si è proceduto ad una modellizzazione del setup considerando tutte le interazioni possibili tra esso, la cella ed il gas alimentato, per permettere in successive ricerche lo studio degli effetti della contaminazione da KCl riducendo il più possibile le incertezze. Sono stati identificati i valori dei flussi (secchi e umidificati) ed i livelli di concentrazione ideali per tali studi. Le modifiche proposte sono state infine attuate ed il set up sarà a breve pronto per futuri studi.

Abstract

High temperature fuel cells are suitable for operation with biosyngas feed, they provide a renewable source for high efficiency combined heat and electricity generation. At Delft Univeristy of Technology Fuel Cell Laboratory influences of contaminants generally present in biosyngas on SOFC anodes are now studied. Preliminary experiments with humidified H_2 and simulated syngas both contaminated by KCl were carried out at ECN (Energy research Center of the

Netherlands). In order to start investigation of KCl effects on a geometrically similar setup at TU Delft, reference Impedance Spectroscopy measurements with humidified H_2 are carried out on Ni/GDC anodic symmetrical cells.

Results are firstly not reliable and reproducible, so an iterative refining of the experimental procedure and setup is done in order to avoid any externality and a set of consistent reference spectra is obtained for further comparison with measurements with KCl. Some unexpected results are found, however, with low flows and detailed investigation of the causes is suggested as a future research topic. In addition, a statistical procedure for analysis of the results is created in order to minimize any error due to discretion of the operator when fitting the obtained spectra.

Based on the results a modification of the setup for measurements with KCl contamination in the feed is designed and built and tools for characterization of experimental conditions are studied and employed. Eventually, a step-by-step study of the gas line in the experimental setup is made, to physically characterize it, find its influences on results of the measurements, understand what the unexpected results may be due to.

Keywords: SOFC, KCl, impedance spectroscopy, Ni-GDC, fitting.

Chapter 1

Solid oxide fuel cells and biosyngas

1.1 Introduction

In a growing demand energy scenario, fuel cells seem to be one of the best alternatives to guarantee the energy supply.

Among fuel cells technologies, Solid Oxide Fuel Cells (SOFCs) are finding increasing attention not only in the academic world but also among small and multinational companies. These cells operate at high temperature (900 to 1300 K). This is the most peculiar characteristic of the SOFCs; in fact many advantages and problems (that will be discussed later) depend on the high operating temperature. The great interest in this technology of these last years is due to the rapid improvements of the research that is approaching SOFCs to be competitive in the market [1][2]. It is interesting to mention and explain the motivations that are leading fuel cells and especially SOFCs to be an attractive solution in energy matters before analyzing their working principle, their thermodynamic, materials and applications.

As in every fuel cell there is no combustion, in fact there is direct conversion of chemical energy into electrical energy so there are no toxic combustion products. This is particularly advantageous in urban areas with big pollution problems where often the heating is still obtained with the combustion of traditional fuels and there are traffic problems (actually PEM fuel cells seem to be more attractive than SOFCs for transportations even if the latter is congenial for auxiliary power applications “APU”) [2][1]. The typical quiet in operations is also an opportunity in urban contests. The absence of moving parts is both a saved cost for the maintenance and an advantage for the efficiency in small scale systems. In fact, unlike internal combustion engines and turbines the efficiency of a fuel cell stack is independent from the dimensions and the economies of scales are reduced [2]. This is interesting for the distributed generation [3], which seems to be the most valuable application for SOFCs; in fact the high efficiency (up to 60% of LHV) [4], makes them advantageous with respect to the small scale turbines (25 to 30% of LHV) or internal engines (25 to 40% of

LHV). There is also the possibility to use the produced heat to generate other electrical power (for example in GT-SOFC systems) or to use it to supply heat demand. Co-generative applications and systems integrated with gas turbines are particularly interesting with SOFC because of the high temperature and, consequently, the high exergetic quality of the wasted heat [3][1]. Another advantage is the capacity of fuel cell stacks to work with high efficiency at partial loads. The electrical net needs the generator to modify the loads in order to follow the demand of the users and to regulate frequency and tension. The traditional plants (turbogas, ICCG, coal and nuclear plants) have lower efficiency with partial loads and renewable plants are sometimes inefficient in modifying them (for example thermo-solar plants).

SOFCs systems are attracting attention also in applications disconnected from the electric net; emergency generators (for example in hospitals) and distributed generation in rural areas [3] are applications in which these systems, with high reliability and high efficiency, seem to be ideal. Another particularly attracting feature is the flexibility in the choice of the fuel. SOFCs fuel cells are definitively the most flexible. Besides Hydrogen, which is the most common fuel for fuel cells, SOFCs can work properly with CO, CH_4, NH_3 and with other hydrocarbons. So biogas, biosyngas, methane and other fuels are suitable for this technology [1][2][3]. This is a great advantage because it makes possible to utilize "dirty" fuel with high efficiency and, as already mentioned before, without pollutants typical of the combustion. It is also possible to use in a proper way the biomass; a great effort in this direction is being made by professor Aravind's research group at the TU Delft.

The high operating temperature raises the kinetic of the processes in SOFCs systems; this way it is possible to avoid the use of noble metals as catalysts [2]. This factor will probably help to keep an advantage in costs with respect to other fuel cell technologies.

SOFCs fuel cells have solid electrolytes; this allows obtain cells with different shapes; tubular and planar cells are the most common. This feature gives this technology other advantages; first of all, a solid electrolyte reduces problems with corrosion that could occur with a liquid electrolyte. This kind of electrolytes is also way more resistant to gas cross over, which is an important loss in cells with liquid electrolytes. In addition flooding in the electrodes and problems due to the movement of a liquid electrolyte are avoided [2].

While especially low temperature fuel cells have a tolerance to impurities close to zero (even CO poisons the catalyst) [2][6], SOFC demonstrate to have a greater tolerance; CO and NH_3 are in fact possible fuels. By the way, tolerance to H_2S is still low (less than one ppm) in YSZ anodes [2] while new GDC anodes like the ones studied in this thesis have a slightly higher tolerance (around 10 ppm) [3].

Even if SOFC is probably the more interesting fuel cell technology (together with PEM), it has still disadvantages and problems that research groups and companies are working on.

Typical problems of fuel cells are the costs. For low temperature fuel cells this is due to the presence of expensive catalyst materials [2]. In SOFCs, on the other hand, the high operation temperature needs particular material and particular fabrication processes that are quite expensive [1][5]. Lowering the operation temperature to 600°C, which is one of the biggest challenges for the research, will reduce the costs and allow SOFCs be competitive in the market. Probably in the coming years, if big companies are able to produce them in a large scale there will be economy scales that will reduce the cost and there will be also investments in infrastructures that, up to now, are insufficient [2][7][1].

Even if, as already mentioned before, SOFCs have better tolerance to impurities with respect to other kinds of fuel cells, the absolute values are still low, so that systems need a clean fuel [3]. This could be obtained by using expensive fuels or by cleaning "dirty fuels" with additional elements of the plant; this is also another aspect that still prevents systems using these cells from being competitive.

Because of the high operating temperatures SOFCs suffer problems not present in low temperature fuel cells. For example, there are quite critical thermo-mechanical stresses due to expansion mismatches among materials. Here is another motivation for the great attention on the choice of the material, fabrication processes and finally their high cost [1][2][5].

The electrolyte of a SOFC shows a higher resistance compared to a MCFC one. The difference is higher if the operating temperature of the SOFC is lower [2]. To avoid excessive thermal stresses the temperature gradients during the operations of heating up and shutting down of the system are quite small. This makes these operations slow. The consequences are that this technology is

suitable for a stationary application and less for more flexible applications like traction in vehicles[1][2].

1.2 Working principles

Even if SOFCs are still considered a great chance in the future for the energy supply, they have a really long story. In fact the first scientist who realized that Zirconia was an ionic conductor and that this feature could be an opportunity, was Nernst in the last decade of the nineteenth century. This idea was then developed since 1930s, but interesting improvements came later. Only in the last decade the investigation began to consider this technology an actual and concrete industrial opportunity in addition to an interesting field of study [1].

Understanding the relative simplicity of the working principle could help also to realize the attention given in the last years. Like every fuel cell, SOFCs are chemical devices that directly convert chemical energy stored in the atomic bonds of the fuel to electric energy and heat. The operation is guaranteed by five components: anode, cathode, electrolyte and two connecting wires.

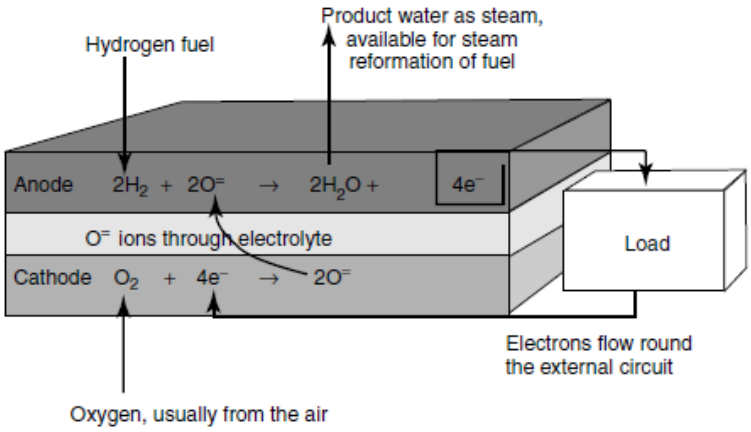

Figure 1.1 Schematic representation of the working principle of a SOFC.

In a SOFC there are two feeds. Fuel, which is fed to the anode, and oxygen (actually air is always used because of the cost of pure oxygen production) fed to the cathode. Anode, cathode and electrolyte are made of porous ceramic

materials that are conductors at high temperatures. In the cathode the oxygen reduction occurs; the electrons coming from the external circuit interact with oxygen molecules through the reaction:

$$O_2 + 4e^- \rightarrow 2O^{2-} \tag{1.1}$$

At high temperature (above 600 °C) these ions can pass through the ceramic matrix of the electrolyte usually made of YSZ (Yttria Stabilized Zirconia). This material however prevents electrons from passing from the anode to the cathode. In the anode side H_2 (hydrogen has been chosen for simplicity, but CO, methane or other fuels can be chosen) is fed and the oxidation reaction occurs:

$$2H_2 + 2O^{2-} \rightarrow 2H_2O + 4e^- \tag{1.2}$$

For released electrons that can't pass through the electrolyte the only way to reach the cathode side is to go to the interconnection wires that constitute the electric external circuit. Thus the overall reaction is:

$$2H_2 + O_2 \rightarrow 2H_2O \tag{1.3}$$

The products of this process are electric energy provided by the electron flow and heat which is due to the losses that will be discussed later on.

1.2 Thermodynamics

FC convert directly chemical energy in to electrical, don't have the thermodynamic limit of cycles with combustion [2]. Winkler [1] suggests that there are two main causes that reduce the efficiency of the transformation: the ohmic resistance and the irreversibility due to the gas mixing, proportional to the quantity of fuel utilized in the cell (the specific process will be analyzed in the next paragraph). An ideal reversible cell could be described before analyzing briefly the thermodynamic behavior with losses. In this model non mixed reactant (with $\sum n_i H_i$ as enthalpy) and product (with $\sum n_j H_j$ as enthalpy) gases are considered. Q_{fcrev} is the heat extracted reversibly from the fuel cell and delivered (reversibly) to the environment and W_{fcrev} is the produced reversible work. It is

also assumed that the cell is in the same thermodynamic state of the environment which is also the reference condition for the next steps.

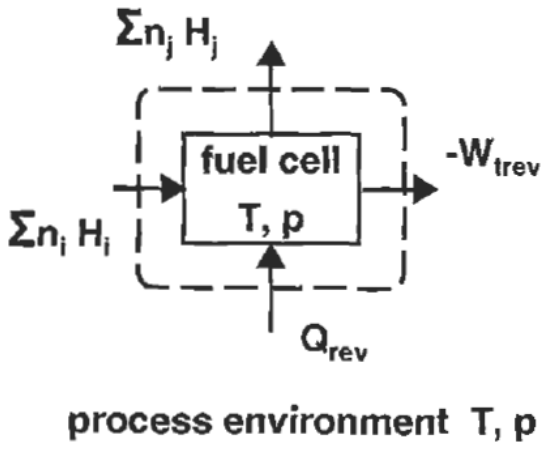

Figure 1.2. First principle balance of a SOFC.

According to the picture, for the first law of thermodynamic:

$$Q_{FCrev} + W_{FCrev} = \Delta H_r \tag{1.4}$$

where ΔH_r is the variation of enthalpy due to the reaction. For the second law of thermodynamics:

$$\oint dS = O \tag{1.5}$$

So the ΔS_r due to the reaction itself must be compensated by the entropy due to the transport of the reversible heat to the environment. The balance can be written as:

$$\Delta S_r - \frac{q_{fcrev}}{T_{FC}} = 0 \tag{1.6}$$

T_{FC} is the operating temperature of the fuel cell. It is now possible to obtain the reversible work by combining the two previous relations:

$$W_{FCrev} = \Delta H_r - T_{FC}\Delta S_r \tag{1.7}$$

Being the reversible work of the reaction equal to the free Gibbs energy of the reaction ΔG_r:

$$W_{FCrev} = \Delta G_r = \Delta H_r - T_{FC}\,\Delta S_r \tag{1.8}$$

The most important thermodynamic quantities are now known, and the reversible efficiency (η_{FCrev}), which is the easiest parameter to evaluate the fuel cell performance, is obtained as the ratio between the free Gibbs energy of the reaction and the reaction enthalpy.

$$\eta_{FCrev} = \frac{\Delta G_r}{\Delta H_r} = \frac{\Delta H_r - T_{FC}\,\Delta S_r}{\Delta H_r} \tag{1.9}$$

Another parameter to evaluate the performances of a fuel cell is the fuel utilization U_f: it represents the fraction of the total fuel input which is electrochemically oxidized by the oxide-ion current [8]. The definition of fuel utilization is:

$$U_f = 1 - \frac{\dot{m}_{FanOut}}{\dot{m}_{FanIn}} \tag{1.10}$$

Where $\dot{m}_{FanOut}$ is the mass flow rate of the fuel at the outlet of the anode, $\dot{m}_{FanIn}$ is the mass flow rate of the fuel at the inlet of the anode. In order to understand the meaning of the fuel utilization it is important to know which reactions take place at the anode and at the cathode, remembering that hydrogen has been chosen as fuel only for simplicity. The fuel fed to the anode is adsorbed, ionized and the electrons are directed to the external electric circuit. At the cathode the oxygen feed is also adsorbed and ionized receiving the electrons from the electric circuit. The oxygen ions passing through the electrolyte bind hydrogen ions and form water. Thus at the anode outlet there are not-spent hydrogen and water. The more is the water at the outlet the lower is the fuel utilization; $\dot{m}_{FanOut}$ decreases because of the increased reacted hydrogen. The mixing of the two flows causes a growth of the irreversibility, thus in a reversible SOFC $U_f \rightarrow 0$. Of course in a real fuel cell U_f has higher values between 0.8 and 0.9.

A match between thermodynamic and electrical quantities could be achieved and this is an advantage in practical purposes because it is easier to control electrical values with respect to thermodynamic values [1].

An easy way to control the rate of the spent fuel is to control the current. According to the anodic reaction:

$$H_2 \rightarrow 2H^+ + 2e^- \tag{1.11}$$

The number of released electrons is twice the number of spent hydrogen molecules, so

$$n_{el} = 2n_{H2} \tag{1.12}$$

The current could be expressed as:

$$I = \dot{n}_{el}(-e)N_A = \dot{n}_{el}F = 2\dot{n}_{H2}F \tag{1.13}$$

Where N_a is the Avogadro number ($6.022 \cdot 10^{23}$ particles per mole), e is the elementary charge ($1.6021773 * 10^{-19}$C), the Faraday's constant is $F = N_a e =$ 96485 C. It is now possible to match thermodynamic and electrical quantities through the reversible power. From a thermodynamic point of view the reversible power can be expressed as the product of reversible work multiplied by the molar flow rate of the fuel. On the other hand, the reversible power could be expressed as the product of reversible voltage and current from an electric point of view.

$$P_{FCrev} = V_{FCrev} I = \dot{n}_{H2} W_{FCrev} = \dot{n}_{H2} \Delta G_r \tag{1.14}$$

Combining (1.13) and (1.14) the reversible voltage can be expressed as:

$$V_{FCrev} = \frac{-\dot{n}_{H2} \Delta G_r}{\dot{n}_{el} F} \tag{1.15}$$

where $\dot{n}_{el}$ indicates how many electrons are released per every spent fuel molecule, n_{el} indicates how many electrons are released per every utilized fuel molecule; the relation between them is:

$$n^{el} = \frac{\dot{n}_{el}}{U_f \ \dot{n}_{FI}} \tag{1.16}$$

Substituting in the reversible potential equation:

$$V_{FCrev} = \frac{-\Delta G_r}{n^{el} F} \tag{1.17}$$

The reversible voltage can't be reached because of the irreversible mixing phenomena that occur in an actual cell during operation. It is possible to quantify these losses in terms of potential (that is called Nernst potential V_n) considering the changes in partial pressure of the components in the system. With the hypothesis of ideal gas:

$$\Delta G_r(T,p) = \Delta H_r(T) - T\ \Delta S_r(T,p) \tag{1.18}$$

With

$$\Delta S_r(T,p) = \Delta S_r(T) - R_m\ ln(K) \tag{1.19}$$

And

$$K = \prod_f \left(\frac{p_j}{p_0}\right)^{vj} \tag{1.20}$$

K is the equilibrium constant and ν_j are molar coefficients of the components, p_j the partial pressure and p_0 the standard pressure (1 bar for example). Substituting:

$$\Delta G_r(T,p) = \Delta G_r(T) + TR_m\ ln(K) \tag{1.21}$$

Putting now this value of the ΔG_r in the reversible potential equation, we obtain the Nernst potential

$$V_N = \frac{-\Delta G_r(T)}{n^{el} F} - \frac{TR_m\ ln(K)}{n^{el} F} \tag{1.21}$$

In a V-T plot it is possible to discuss briefly the effects of operating pressures and temperatures on the Nernst voltage for different fuels (CO, H_2 and CH_4 are taken as example).

$$H_2 + \frac{1}{2}O_2 \rightarrow H_2O \tag{1.22}$$

$$CO + \frac{1}{2}O_2 \rightarrow CO_2 \tag{1.23}$$

$$CH_4 + 2O_2 \rightarrow 2H_2O + CO_2 \tag{1.24}$$

From the reactions it is possible to predict that for hydrogen and carbon monoxide, due to the decreased number of moles, the effect of the increased pressure will be negative for the Nernst potential. On the contrary methane won't give any significant variation of the potential. The effect of the temperature on the Nernst voltage can be seen in the V-T diagram [1]. Since the enthalpies and entropies of reaction are slightly depending on the operating temperature, as a first assumption they could be considered not depending at all. So the cell temperature effect is insignificant for the methane; this is due to the fact that the ln(K) is zero for methane. For hydrogen and carbon monoxide, on the contrary, ln(K) is different from zero so the voltage drop with increasing operation temperature

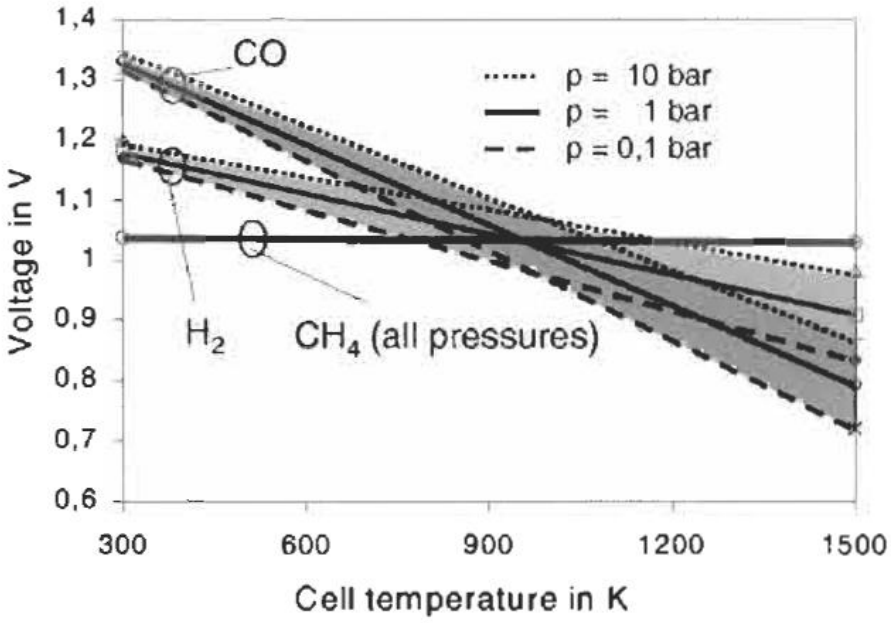

Figure 1.3. V-T plot for different fuel inlets and pressures.

If the losses due to the resistance are considered, there is an additional voltage drop and irreversibility:

$$\Delta V = IR \tag{1.25}$$

The lost power is

$$P_{loss} = \Delta V * I = I^2 R = T_{SOFC} U_f \dot{n}_{FI} \Delta S_{irr} \tag{1.26}$$

And the additional entropy

$$\Delta S_{irr} = \frac{U_f \dot{n}_{FI} R (n^{el} F)^2}{T_{SOEC}} \tag{1.27}$$

Generalizing the equation of the current

$$I = -n^{el} U_f \dot{n}_{FI} F \tag{1.28}$$

It is possible to obtain the fuel utilization as a function of the current:

$$U_f = \frac{I}{\dot{n}_{FI} n^{el} F} \tag{1.29}$$

It is also possible to obtain the Nernst potential in function of the fuel utilization

$$U_f = \frac{y_{FI} \dot{n}_{AnI} - y_{FO} \dot{n}_{AnO}}{y_{FI} \dot{n}_{AnI}} \tag{1.30}$$

y_{FI}, y_{Fo} are the molar concentrations and n_{ain} n_{ao} are the molar flows of the fuel respectively at the inlet and at the outlet.

Not reporting other mathematical passages in which the air excess is introduced, the equilibrium constant is expressed as function of the fuel utilization:

$$K = \frac{U_{fH2} \left(\frac{\lambda}{0{,}21} - U_{fH2} \right)^{1/2}}{\left(1 - U_{fH2}\right) \left[\left(\lambda - U_{fH2}\right) p \right]^{1/2}} \tag{1.30}$$

U_{fH2} is the fuel utilization in case of using H_2, λ is the air excess. The Nernst voltage can be obtained by putting (1.30) into the equation (1.21). It is possible to couple the fuel utilization (proportional to the current) and the voltage in a chart. The higher is the fuel utilization, the lower is the potential, and this is due to the changes in the partial pressures of the reactants. With higher reactant concentrations a higher potential is obtained.

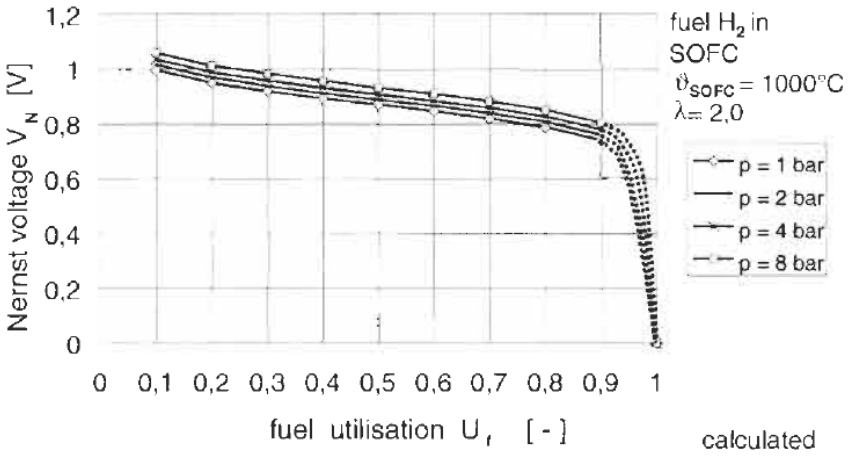

Figure 1.4. Nernst voltage vs fuel utilization plot at different pressures.

For mathematical steps the chosen reference condition is T and P of the environment. It is more common to use standard condition as reference (25 °C and 1 atm). This way the free Gibbs energy is defined as:

$$\Delta G = \Delta G^0 + RT \ln \prod \left(\frac{products}{reactants}\right) \tag{1.31}$$

Remembering that

$$\Delta G = -nFE \tag{1.32}$$

We obtain for a hydrogen fed SOFC:

$$E = -\frac{\Delta G}{2F} = -\frac{\Delta G^0}{2F} - \frac{RT}{2F} ln\left(\frac{p_{H2O}^a}{p_{H2}^a p_{O2}^{c\,\frac{1}{2}}}\right) = E^0 + \frac{RT}{4F} ln\left(\frac{p_{O2}^c {p_{H2}^a}^2}{{p_{H2O}^a}^2}\right) \qquad (1.33)$$

1.3 Polarization

The term polarization indicates a voltage loss or overpotential and appears when a current flows in the system. Even if it is not easy to understand all the phenomena that occur in a fuel cell at different currents, there is a classification of the polarizations: ohmic polarization, concentration polarization and activation polarization [1]. As demonstrated in the previous paragraph the dependence of the Nernst potential from the current is due to the fuel utilization; if an ideal (with $U_f \rightarrow 0$) cell is considered, there are no significant changes in the fuel composition at the outlet of the cell and Nernst potential is not function of the current; in an actual SOFC the fuel utilization is higher, so there are changes in the fuel composition at the outlet of the cell and the Nernst potential is finally function of the current.

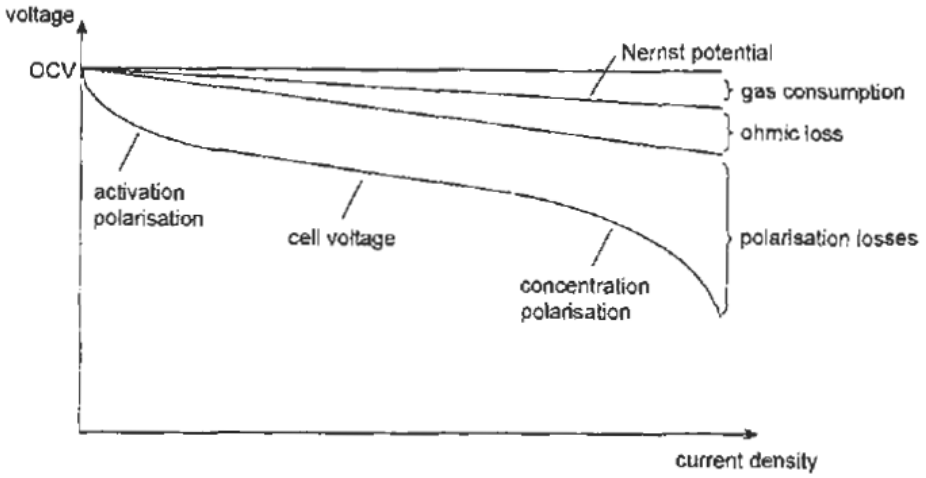

Figure 1.5. I-V curve for a SOFC.

It is possible to represent the losses in an I-V curve which is called "polarization curve". Now it is just possible to notice that, calling E the open circuit voltage,

V the voltage drop due to the load and η the losses, the relation that describes the behavior of a cell in function of the current is [1] :

$$E = V(i) + \eta(i) \tag{1.34}$$

With very high flows at the electrodes (ideal case), while in an actual cell with high fuel utilization:

$$E(i) = V(i) + \eta(i) \tag{1.35}$$

$\mathrm{E} - \mathrm{E(i)}$ is the difference in potential due to the change in the composition.

1.4.1 Ohmic polarization

The ohmic polarization is due to the resistance that a material shows when there is charge transfer [1]. In a SOFC there are both oxygen ions which migrate from the cathode to the anode and electrons which move in the electrodes and in the external circuit. The ohmic polarization is visible in the I-V curve in the mid zone [2][1][6]. It can be noted that the curve has an almost linear behavior (like $\Delta V = RI$). In an equivalent circuit the ohmic polarization is usually described using a simple resistance with zero capacitance; this is due to the fact that the response time is close to zero. The ohmic polarizations depend on the material, in fact every material is characterized by a resistivity; in a fuel cell the overall resistance is composed by the resistance of the anode, of the cathode, of the electrolyte and the contact resistance. So the ohmic losses are expressed with the relation:

$$\eta_{ohm} = (\rho_e l_e + \rho_c l_c + \rho_a l_a + R_{contact})i \tag{1.36}$$

where l_e, l_c, l_a are respectively the thickness of the electrolyte, cathode and anode. The contributions due to the single parts of the cell depend on the structure of the cell. In fact there are anode or cathode supported cells (commonly called "electrode supported cells") characterized by a greater thickness of the anode (or cathode) and by a really thin electrolyte. Usually these kinds of cells are the ones with the lowest ohmic resistance because the electrolyte is the part of the cell with the highest specific resistivity. The electrolyte supported cells, on the other hand, have a higher thickness and then a higher total ohmic resistance.

1.4.2 Concentration polarization

In a solid oxide fuel cell, as already explained, there are diffusion phenomena; the fuel has to pass through the porous anode and to reach the electrode-electrolyte interface where the reactions take place and products must be transported away; the oxidant in the cathode side has to diffuse in the porous cathode and the remaining flow has also to be removed. All these phenomena determine the "concentration polarization" [1] which is the voltage drop due to transport of the species. In an equivalent circuit these losses are usually quantified by a Warburg element, which is an infinite sum of resistors and capacitors. This means that the characteristic time is not zero. Imagining (for simplicity) a hydrogen fed SOFC, the flows could be expressed as proportional to the current as:

$$|j_{H2}| = |j_{H2O}| = 2|j_{O2}| = \frac{iN_A}{2F} \tag{1.37}$$

Where j_{H2}, j_{H2O} and j_{O2} are the flows of the species in the cell, N_A is the Avogadro's Number, F the Faraday's constant and i the current. The binary diffusion is what physically occurs in the transportation of gaseous species. This is mostly function of the binary diffusivity coefficient $D_{H2\text{-}H2O}$ and of the microstructure. The anodic concentration polarization is the voltage loss due to the resistance that the species face when they diffuse in the anodic structure. It is interesting to find out the expression of this loss in order to understand how it is influenced and, eventually, which are the strategies that the researchers are looking for to improve the performance of the cells. This loss could qualitatively be expressed as:

$$\eta_{aconc} = f\left(D_{H_2-H_2O}, Microstructure, Partial\ pressures, Current\ density\right) \tag{1.38}$$

To understand how the current density can influence the concentration losses, it is necessary to introduce the anode-limiting current density. The anode-limiting current density is the current density that flows in the external circuit of the fuel cell when the concentration of the fuel is close to zero, that is, when there is fuel starvation. In this condition the voltage drops to zero [1]. This means that for a correct operation the current density i must be lower than i_{as}. The analytical expression for the anode limiting current is:

$$i_{as} = \frac{2f p_{H2}^{a} D_{a(eff)}}{RT l_a} \tag{1.39}$$

Where $D_{a(eff)}$ is the actual gaseous diffusivity through the anode and it depends on the binary diffusivity coefficients (depending on the species fed to the anode), the volume fraction of porosity $V_{v(a)}$, l_a is the anode thickness and the tortuosity factor τ_a ,which is a value indicating the tortuosity of the structure of the anode (and of the path in which gases have to diffuse). If a very fine microstructure is considered, τ_a also takes into account the effects of Knudsen diffusion, surface diffusion and adsorption/desorption. Thus, the concentration polarization can be expressed as:

$$\eta_{conc}^{a} = -\frac{RT}{2F} ln\left(1 - \frac{i}{i_{as}}\right) + \frac{RT}{2F} \ln\left(1 + \frac{p_{H2}^{a}\, i}{p_{H2O}^{a} i_{as}}\right) \tag{1.40}$$

Now it is possible to understand analytically that if i tends to i_{as} the first term tends to infinity. The partial pressure of hydrogen, of course, has a great influence on the concentration loss; the higher is p_{H2} the lower is the loss. Also the anode thickness and the tortuosity (which influence the D_{eff} in the anode-limiting current equation) are proportional to this voltage drop. On the contrary temperature doesn't have a great influence. A similar approach could be used for the cathode concentration polarization. Defining the cathode limiting current density:

$$i_{cs} = \frac{4F p_{O2}^{c} D_{c(eff)}}{\left(\frac{p - p_{O2}^{c}}{p}\right) RT l_c} \tag{1.41}$$

And the cathodic concentration polarization:

$$\eta_{conc}^{c} = -\frac{RT}{4F} ln\left(1 - \frac{i}{i_{cs}}\right) \tag{1.42}$$

In the cathode there are also transportation processes. In this case there are O_2 and N_2 as gases. The value of the diffusivity is much lower with respect to the anodic one. For two reasons: the binary diffusivity $D_{H2\text{-}H2O}$ is way bigger than $D_{O2\text{-}N2}$ and the partial pressure of the hydrogen in the anode is higher than the partial pressure of the oxygen in the cathode. The consequence is that the cathode limiting current density (i_{cs}) is lower than i_{as} if anode and cathode have

the same thickness. However, the commonly produced SOFC are anode supported, so the anode thickness is higher than the one of the cathode. Thus, the two polarizations are comparable in magnitude.

1.4.3 Activation polarization

In both cathode and anode sides of the cell there are electrochemical reactions that imply charge transfers. These reactions occur in the entire volume of the electrodes if a MIEC (mixed ionic electronic conductor) is considered. Otherwise if only the electrolyte is ionic conductor reactions take place close to the TPB (triple phase boundary). The TPB is the zone of the cell close to the electrode-electrolyte interface where there is the contemporary contact of the gas phase electrode and electrolyte. It is expressed in [m^{-1}].

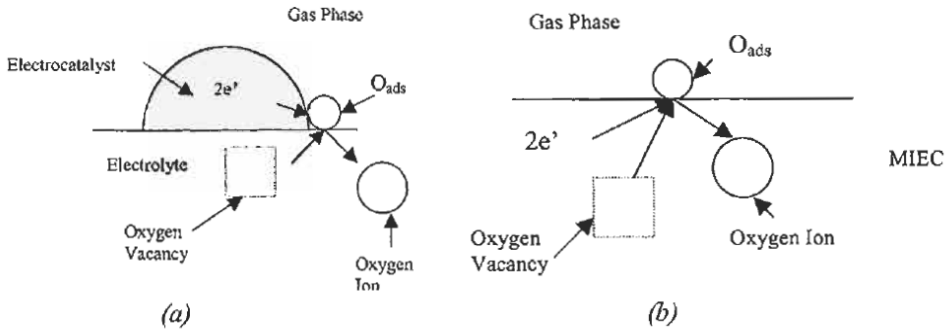

Figure 1.6. Schematic of a possible charge transfer reaction for (a) purely electronically conducting cathode and (b) MIEC cathode material.

Every charge transfer reaction has an energy barrier called "activation energy" that has to be overcome by the reactants to let the reaction occur [1]. These barriers result from the reaction steps of a reaction mechanism. The activation polarization is defined more precisely as the overpotential that has to be spent to overcome the rate-limiting step energy barrier so that the desired reaction-rate is achieved [9]. There are both anodic and cathodic polarizations.

The activation polarizations depend on the reaction rates. Usually there is one (or more) step of the reaction mechanism which is slower. It is the rate

determining step [10][1][9]. For example the models considered by Tiffers and Vikar [1] are shown;

For the cathode

1) Surface adsorption of oxygen molecules on the electronic conductor, which is also the electrocatalyst

$$\frac{1}{2}O_2\ (gas) \rightarrow \frac{1}{2}O_{2ads}\ (electrocatalyst) \tag{1.43}$$

2) Dissociation of adsorbed oxygen molecules into adsorbed atoms

$$\frac{1}{2}O_{2ads}\ (electrocatalyst) \rightarrow\ O_{ads}\ (electrocatalyst) \tag{1.44}$$

3) Surface diffusion of adsorbed oxygen atoms to a three phase boundary (TBP) between the electrocatalyst-electrolyte-gas phase.

$$O_{ads}\ (electrocatalyst) \rightarrow\ O_{ads}\ (electrocatalyst/electrolyte\ TPB) \tag{1.45}$$

4) Formation of oxide ions by electron transfer with incorporation of these ions into the electrolyte:

$$O_{ads}\ (electrocatalyst/electrolyte\ TPB) + 2e'(\ electrocatalyst) + V_{\ddot{O}}(oxygen\ vacancy - electrolyte) \rightarrow\ O_O^X(\ electrolyte) \tag{1.46}$$

For the anode

1) Adsorption of H_2 on the surface of YSZ or Ni from the anode

$$H_2\ (fuel\ gas) \rightarrow\ H_{2ads}\ (YSZ\ or\ Ni) \tag{1.47}$$

2) Surface diffusion of adsorbed H_2 to TPB

$$H_{2ads}\ (YSZ\ or\ Ni) \rightarrow\ H_{2ads}\ (\ TPB) \tag{1.48}$$

3) Anodic electrochemical reaction

$$O_O^X(\ electrolyte) +\ H_{2ads}\ (TPB) \rightarrow\ H_2O\ (\ fuel\ gas) +\ 2e'(\ anode) + V_{\ddot{O}}(electrolyte) \tag{1.49}$$

The reaction rate is proportional to the net current density and associated with it there are the activation polarizations. The activation polarizations are also function of the properties of the material, of the gases and of the temperature (being the reaction thermally activated) [1][9]. Going deeper, an analytic relation between the current density and the activation polarization η_{act} is the Butler-Volmer equation. It is obtained by deducing the forward reaction rate (the first term) from the backward reaction rate [9] equation

$$i = i_0 \left\{ \exp\left(\beta \frac{n_e F \eta_{Act}}{\bar{R}T}\right) - \exp\left[-(1-\beta)\frac{n_e F \eta_{Act}}{\bar{R}T}\right]\right\} \qquad (1.50)$$

Where β is the transfer coefficient, which is the fraction of the interfacial potential at an electrode-electrolyte interface that helps in lowering the free energy barrier for the electrochemical reaction, and its value is usually 0.5 in fuel cell application [9]; i_{0c} is the exchange current density which is a kinetic parameter that depends on the reaction and on the electrode surface where the reactions occur [10][1]. The exchange current density is the current density in an equilibrium condition. It means that the reactions still occur but the backward reaction rates equal the forward reaction rates. The effect is that there is no change in the compositions of the reactants and the products. The exchange current density is also an easy parameter to verify how easily a reaction takes place. A high i_0 indicates that a small overpotential is required to achieve high current flow; on the contrary small values of the exchange current density indicate that a high overpotential has to be spent to achieve low current flows [10].

While β is for complex reactions involving several steps, for an elementary reaction the (1.50) has the same form but there is α (the symmetry factor) which indicates the "proportion of the applied overpotential exerted for the forward reaction"[10].

With β= 0.5 and isolating η,act the equation (1.50) can be expressed as [9]:

$$\eta_{Act} = \frac{2\bar{R}T}{n_e F} \sin h^{-1}\left(\frac{i}{2i_0}\right) \qquad (1.51)$$

To understand the trend of the activation polarization, the Butler-Volmer equation can be analyzed by focusing on the cases of high activation polarization and low activation polarization. The first one, which is typically applied to the cathode activation polarization, is obtained considering that the first term of the B.V. equation is much higer than the second term; the resulting expression is the Tafel equation [9]:

$$\eta_{Act} = -\left(\frac{2\bar{R}T}{\beta n_e F}\right)\ln i_0 + \left(\frac{\bar{R}T}{\beta n_e F}\right)\ln i \tag{1.52}$$

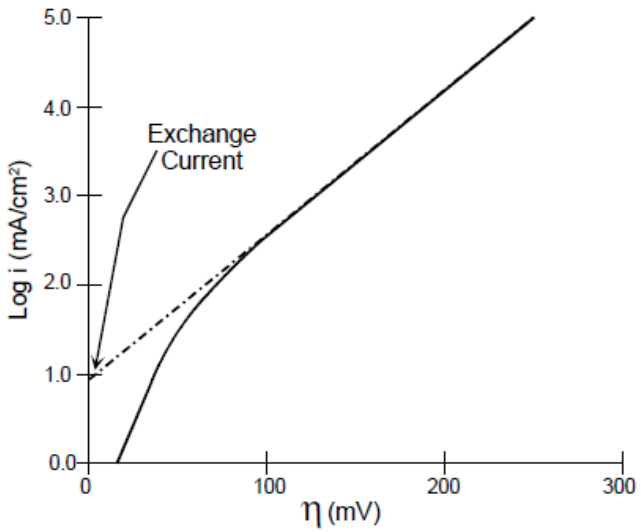

Figure 1.7. Tafel plot.

The Tafel equation shows how the overpotential varies with the current density. The trend has a logarithmic shape. The intercept of the curve with the current density axis gives the exchange current density. The slope of the line is the Tafel slope and it is an indicator of the kinetic behavior: the higher is the value of the slope, the slower is the reaction kinetics [10]. On the other hand the anode is characterized by low activation polarization, due to the lower activation energies of the anode reactions. After some mathematical passages:

$$\eta_{Act} = \frac{\bar{R}T}{n_e F i_0} i \tag{1.53}$$

Being $V = RI$, a charge transfer resistance, R_{ct} can be defined:

$$R_{ct} = \frac{RT}{n_{\alpha} F i_o} \tag{1.54}$$

This value indicates the resistance that the electrons find passing from the electrode surface to the adsorbed species or vice versa.

1.4 Components of the SOFC

After an analysis of the thermodynamics and of the losses, the next step is to present the main components constituting a Solid Oxide Fuel Cell in order to have a better understanding of the physical phenomena, the choices of the materials and the direction that research is taking to improve the performance of such devices.

1.4.1 Electrolyte

As already mentioned the electrolyte is the layer placed between the anode and the cathode. There are no chemical and electrochemical reactions inside, but it has a fundamental role in the charge transfer. In fact the electrolyte allows (at high temperatures) the passage of the oxygen ions to the anode and avoids the electronic conduction. It also must forbid the gases to flow between the electrodes. As anticipated in the ohmic resistance paragraph the electrolyte has a higher resistance with respect to the electrodes one. A challenge of the industry is to make thinner electrolytes in order to reduce the resistance and the losses [1]. Since the electrolyte has to be in contact with both anode and cathode, it must have similar thermal expansion coefficients and be stable in both reducing and oxidizing environments. The stability is also needed to resist (mechanically) to thermal stresses. Finally, its cost should be reduced to contribute to competitiveness of SOFCs in the market [1].

A big challenge for research is to study materials having all these features. Up to now there is quite a large number of studied materials that could have an interesting future in large scale production. The most utilized are the materials with fluorite structure, especially Zirconia based stabilized with other material such as Yttria or Ca; Nernst already discovered the properties of this material in 1890. Also pure Ceria has a fluorite structure and is considered an interesting

option. Talking about non-fluorite structured materials, Perovskites, Brownmillerites and hexagonal structured materials are also considered by researchers [1][5].

This work will focus on Zirconia based fluorite structure stabilized with Yttria because of the structure of the cell used in the experiments. In the fluorite structure there is a face-centered arrangement of cations and the anions occupy all the tetrahedral sites. Thus, there are octahedral interstitial vacancies through which the ion conduction can occur.

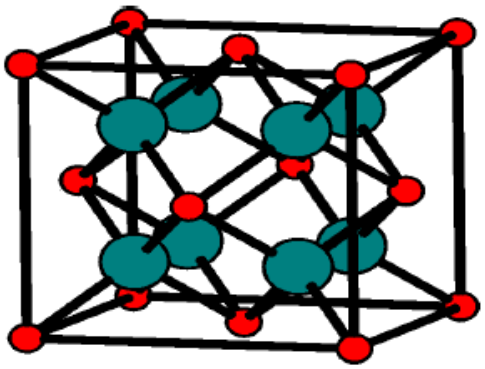

Figure 1.8. Representation of a fluorite structure.

This structure is typical of Zirconia only at temperatures above 2370 °C. At lower temperature pure Zirconia has a lower ionic conductivity. An adequate addition of Yttria has the consequence to reduce this temperature down to environment one. It can be seen in Figure 1.9.

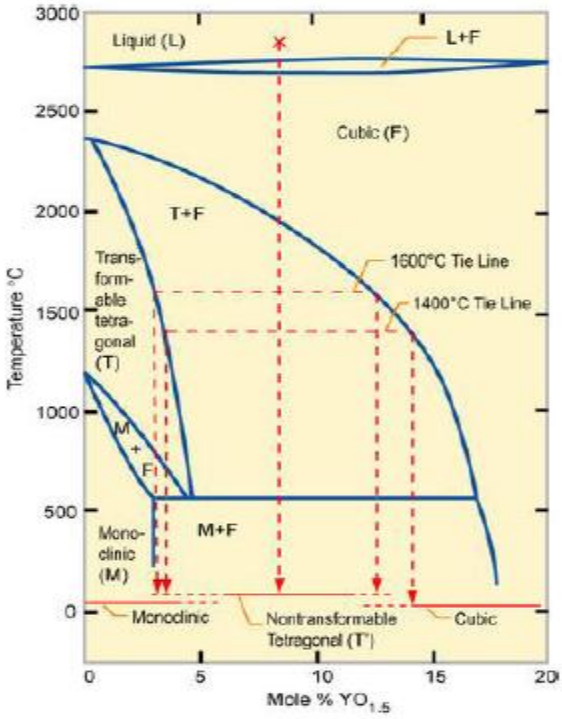

Figure 1.9. YSZ phase diagram.

The working principle is that Y^{3+} ions replace Zr^{4+} so there is a creation of vacancies because three O_2^{--} replace four O_2^{--} ion sites. Analytically:

$$Y_2O_3(ZrO_2) \rightarrow 2Y'_{Zr} + 3O_O^x + V_O \tag{1.55}$$

It can be noticed that every Yttria molecule (or two atoms of Yttrium) a vacancy is given. So the ionic conductivity linearly depends on the concentration of the dopant. Naming σ the ionic conductivity, n the number of vacancies, e and μ respectively their charge and their mobility

$$\sigma = n_e \, \mu \tag{1.56}$$

Analytically the dependence of the ionic conductivity from the vacancy concentration is:

$$\sigma = \frac{A}{T} \; [V_{\ddot{O}}] \; ([V_{\ddot{O}}]^{-1}) \exp\left(-\frac{E_a}{RT}\right) \tag{1.57}$$

Where A is a pre-exponential factor, T the absolute temperature, $[V_o^{\cdot\cdot}]$ the fraction of vacancies and $[V_o^{\cdot\cdot}]^{-1}$ the fraction of unoccupied ion vacancies. It is now clear how an increasing dopant concentration affects the conductivity of the electrolyte.

From Figure (1.10) it can be noted that YSZ is not the material with the highest ion conductivity at the operating temperatures, but it is commonly chosen because of its low electronic conductivity [1][5].

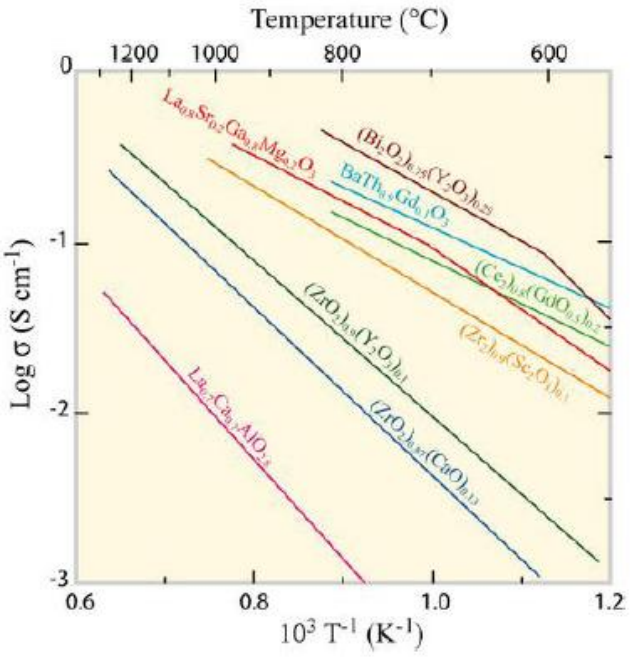

Figure 1.10. Conductivity for different electrolytes.

1.4.2 Anode

In this work there is a particular attention for the anode, since the spectra showing its behavior and its performance are analyzed using anodic symmetrical cells. Talking about the anode structure there is no difference with the complete cell, since during operation it has the same roles. The duties of the anode are multiple; first of all it allows the fuel to diffuse in its structure and to reach the TPB area where the reaction takes place; it also permits the oxide ions brought

by the electrolyte to enter in contact with the fuel molecules and the reaction products to be removed. The anode also lets the electrons released from the reaction flow and reach the external circuit [1]. To make a proper realization of all these duties, a deep material research has been done (and it will be carried on also in the future). It is interesting to summarize the required features that investigated materials have to satisfy. As predictable, they must be both ionic and electronic conductors and they must be electro-catalytically active in order to allow quick electrochemical reactions that minimize resistive and overpotential losses.

Since there are big variations in the composition and thus in the products partial pressures in the anode, the material must be chemically and physically stable with the different product compositions that can appear; for example metal based anodes are not recommendable because of their corrosion problems. Being the anode in contact with the electrolyte and the connections it should be compatible from both a mechanical (having similar expansion coefficient for example) and chemical points of view. Also a redox (due to excursions to high oxygen concentrations) and temperature stability are required especially in start up and shut down transitions. There are also great efforts to increase the anode tolerance to the contaminant poisoning. Talking about the more desirable structure, a 30- 40 % porosity is sufficient to allow the reactants/product diffusion; another important required feature is that the anode structure should allow a triple contact among the gases, metal phase of electrode (for the electronic conduction) and electrolyte: the so-called "Triple Phase Boundary" [1][5]. Finally a desirable anode material should have a low degradation of the performance in the long term and, of course, to contribute to economical viability of the SOFC, also not expensive.

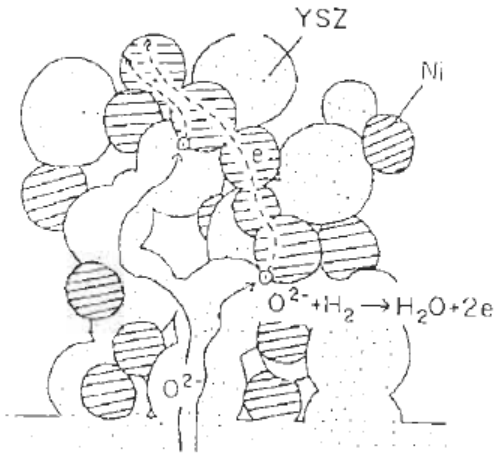

Figure 1.11. TPB for an YSZ anode.

It was not easy to identify materials having all these features; graphite, for example, at high temperature has big problems of oxidation, platinum which has stability at high temperature, showed problems in the long term operation; the same problem occurred with irons. Single phase Nickel as anode material has been discarded due to its thermal expansion mismatch with respect to the Zirconia electrolyte one and because at high temperature a growth of the grain size occurs. This problem also affects the porosity and thus the existence of the TPB itself. Despite its problematic behavior alone, Nickel is widely used combined with ceramic materials, in particular Zirconia. These materials are the so-called "cermets" [1][2][5].

In cermet anode the ceramic phase (Zirconia based) has a support function, avoids the growth of the Nickel grain, guarantees the absence of mismatching with the thermal expansion coefficient of the electrolyte and provides the ionic conduction. The metallic (Nickel, for this work) phase increases the electronic conductivity and has a catalytic function.

Some considerations about the influence of the physical properties on the anode behavior are reported: the electronic conductivity of the anode depends on YSZ particle size (the bigger, the bigger) but a finer structure gives more TPB length and so more space for reactions [11]. The best compromise between these characteristics is ½ ratio fine/coarse YSZ. Moreover, 40% Ni concentration in

the matrix results in the highest electronic conductivity too. It must be more than 30% anyway, because that is the low limit for the behavior of the material to be electronic conducting. The anode is made up of two main layers (this is also the composition of the anodes used for the present study, with addition of a layer of NiO), the bulk anode or substrate, through which mostly diffusion of the gas species occurs, and the functional layer or interlayer, where reactions take place [1][3]. The substrate is the most affected by carbon deposition because oxygen ions hardly diffuse to it to oxidize carbon. Carbon deposition may be avoided in Ni/YSZ electrodes by adding noble metals (which also happens to reduce gas diffusion resistance, apparently). Both these layers are NiO/YSZ but with different particle size mostly, the first is finer for increasing the TPB length and the second is coarser and more porous for enhancing diffusion.

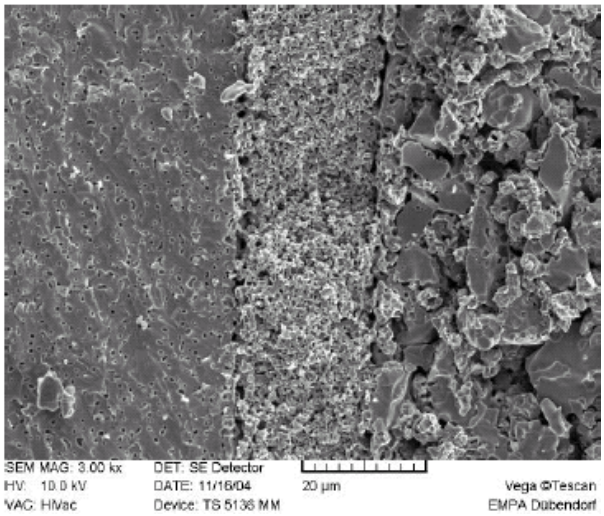

Figure 1.12. SEM image of a electrolyte-electrode boundary.

The reactions seem to take place in a 10 micrometers layer close to the electrolyte material, as claimed by other authors too [12]. In general, reactions take place around the TPB. As already said, it is present only when both electronic and ionic conductors are present. If the electrolyte is extended into the Ni matrix the reaction zone extends too. For this reason mixed conductors can help, because they conduct the oxygen ions and they let the electrons be carried away. A problem of mixed conductors is the low activity towards hydrocarbon conversion. In addition, Primdahl and Mogensen show [13] that the catalytic activity of mixed conductors is low, as addition of a small % of Ni in GDC

anodes for example lowers the polarization resistance of the anode by a considerable amount.

In this thesis the experiments were carried out with Ni/GDC anodes. This material is a cermet in which there is a NiO substrate and a ceramic matrix made by Ceria (CeO_2). Ceria possesses a fluorite structure similar to Zirconia. In this case the chosen dopant is Gadolinium. The substitution of Ce4+ by the trivalent cation Gd3+ enhances the chemical stability, increases the ionic conductivity and suppresses the reducibility of Ceria based materials [14][15]. This chosen material has two other important characteristics: it has higher tolerance to contaminants (particularly to H_2S) [3] and it is the most interesting option for intermediate temperature solid oxide fuel cells, having a higher ionic conductivity at lower temperature with respect to YSZ based anodes.

One of the most interesting features of the SOFCs is that they can work with different fuels. This implies that there are carbon atoms in the feed. This could bring to carbon deposition if the temperature is not sufficiently high and if there is no water enough. If the feed is composed by methane and other fuels, at the anode reforming occurs [1][2][16]. It can be external (before entering in contact with the anode cermet) or internal (occurring inside the anode). Nickel favors the reforming reactions but it could bring to carbon deposition in long term operations. A Cermet doped with copper seems to be quite interesting from this point of view but further studies have to be done because there are still problems of stability.

1.4.3 Cathode

The function of the cathode is to let the fed oxygen molecules be reduced to O^{2-} ions that then will cross the electrolyte and will oxidize the fuel molecules. Oxygen molecules (actually also N_2 molecules since air is commonly used as reagent) diffuse through the porous cathode and reach the reaction zone where the oxygen reduction takes place

$$\frac{1}{2}O_2 + 2e^- \rightarrow 2O^{2-} \tag{1.58}$$

The main required characteristic that it must possess is [1]: a porous structure, high both ionic and electronic conductivity, a chemical and mechanical stability at high temperatures and high catalytic activity for oxygen reduction. Moreover

being the cathode in contact with the electrolyte and the interconnections it mustn't react with them and thermally mismatch them.

The first employed material was Platinum, but it was discarded because of the high costs. The attention was then focused on ceramic materials. The first tested ceramic materials were $LaCo0_3$ but some reactions with the YSZ electrolyte occurred [17]. Then, investigation on cathodes moved to lanthanum manganite ($LaMnO_3$) based materials. In the last years the most used materials for higher temperatures application (above 800°C) are Perovskite materials [2] such as LSM (Lanthanum Strontium Manganite) or LCM (Lanthanum Calcium Manganite). For lower temperatures applications (600 to 800°C) there are still Perovskite structured materials available; for example LSF (Lanthanum Strontium Ferrite) or LSMF (Lanthanum Strontium Manganese Ferrite). There are also investigations on blending cathode and electrolyte materials that show high performance at lower temperatures.

1.4.4 Interconnects

Interconnects (or bipolar plates) are fundamental in SOFC systems operation. In fact they guarantee both electric connection between the cells and gas separation within a cell stack. Also for interconnects the achievement of good performance requires the utilization of technologically advanced (and expensive) materials, that is, some requirements must be satisfied [1]:

- High electronic conductivity and low ionic conductivity at high temperatures;
- Chemical and physical stability in oxidizing and reducing environments;
- Mechanical resistance;
- Thermal expansion coefficients similar to the electrodes ones;
- High thermal conductivity;
- Costs compatibles to make SOFC competitive in the market.

The choice of the material depends on the operating temperatures; for high temperature solid oxide fuel cell (above 850 900 °C) ceramic based material seems to be interesting because of the lack of thermal expansion mismatches

and catalytic poisoning of the cathode due, for example, to Chromium evaporation and deposition on the cathode surfaces typical of metal alloys based interconnects [1][2][5]. Typical ceramic materials are Lanthanum and Yttrium based doped with Magnesium or other alkaline rare elements [5]. For lower temperature applications (below 800 °C) metallic allies based interconnects are considered an option because of their lower costs, more flexibility in the shape and electric conductivity. The most studied alloys are Cr-5Fe-1Y_2O_3 for chromium based alloys but there is also great interest in ferritic steal based interconnects that avoid Chromium deposition problems.

1.5 Design and stacking arrangements

The investigation on SOFCs brought in the decades not only the development of various materials with different operating temperatures and efficiencies but also different designs. Planar and tubular ones are the most studied. In this work a brief overview of the main characteristics, advantages, disadvantages and prospective is presented.

1.5.1 Planar design

In the planar configuration the cells are flat plates and the stacking is obtained connecting the cells in electrical series. In the typical configuration bipolar plates are placed between contiguous cells as shown in figure (1.13)

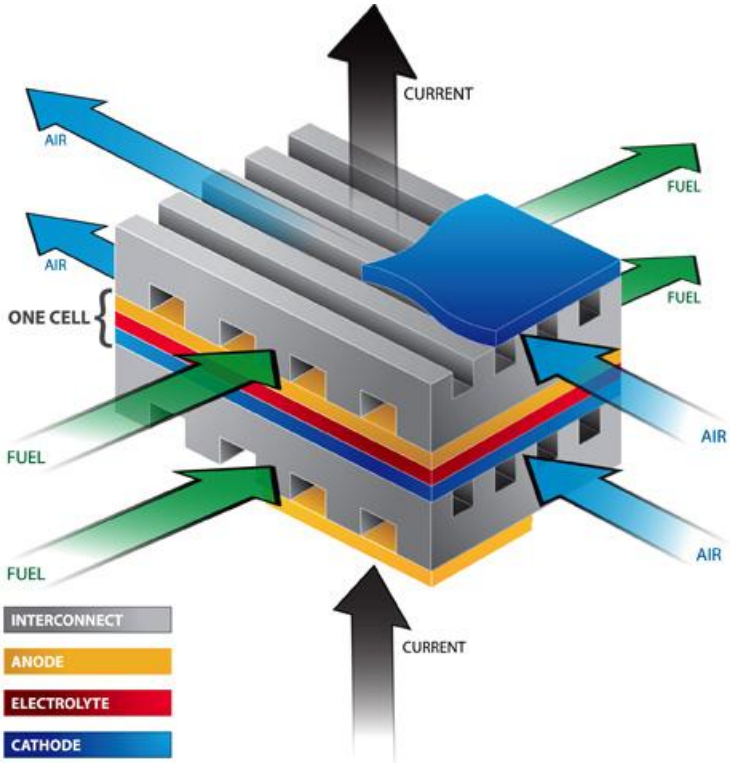

Figure 1.13. Planar design.

Such configuration is very compact; the most important consequence is that higher power densities can be reached and this can be a decisive advantage in small scale applications; electrical connections are short and the consequence is lower ohmic losses (that is an advantage in terms of efficiency) with respect for example to a tubular configuration [5]. Furthermore this geometry can be advantageous economically because of the possibility to develop more economical fabrication methods such as screen printing and tape casting [5][1]. Planar arrangements also have problems with sealing and mechanical degradation because of the thermal stresses at the interfaces between different cells and stack materials.

Some other considerations can be done about the requirements for a correct operation of this devices [1][18]: high electrochemical performance for full open circuit voltages (without any significant leakage or cross-leakage) and also low polarization losses are needed. Due to the high operation temperature, a uniform distribution of temperature and an effective cooling are needed and they could be achieved with an efficient gas flow distribution in both single cell and stack.

Finally, because of the already mentioned mechanical problems that can occur, a reduction of the mechanical stresses is object of investigations.

Talking about the gas flows configurations, effective results in uniform temperature distribution and mass flow transport can be achieved with different geometries such as Z-flows, serpentine flows, radial flows and spiral flows [1]. A brief note can also be done on the gas manifolding which are those parts of the stack that let the feeds flow from a common supply point to the cells and avoid leakages. They could be external or integral depending on whether they are constructed separately or not.

1.5.2 Tubolar design

Starting from the seventies Westinghouse Electric Corporation (now Siemens Westinghouse Corporation) studied this alternative shape of SOFC [1][5]. The first tubular cells were designed with a porous tube that had a structural function and let the oxygen molecule diffuse into the cathode structure. The electrodes and the electrolyte were applied on the tube structure. Modern tubular cells are designed differently; a doped $LaMnO_3$ tube has also the function of the cathode, leading to an increase of the performances [19].

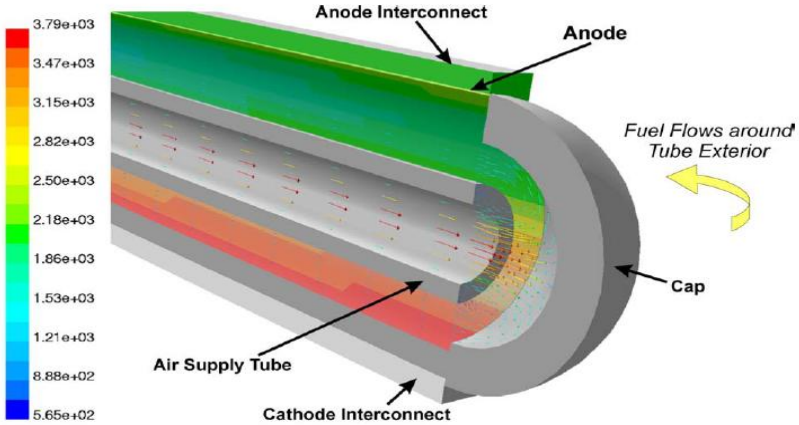

Figure 1.14. Tubolar design

The picture represents a Siemens Westing House tubular fuel cell. One of the ends of the tube is closed and air is introduced close to this point, that is, it can flow to the open side of the tube. Flowing, it enters in contact with the cathode structure and the diffusion and reduction take place. The fuel, on the other hand, flows outside the anode and typical values of utilization are between 50-90%. Anode and electrolyte are usually deposited on the cathode with EVD (electrochemical vapor deposition) techniques. This technique gives good results but it's very expensive [1], and non-EVD techniques (like plasma spraying) are being investigated to reduce costs.

One of the problems of the tubular design is the low power density due to the long path of the electrical power through each cell (modern cells have 10 mm of diameter and 1500 mm of length [1]) and the large voids within the stack structure [5]. The interconnections between the cells are usually made of Nickel; the stacking is obtained arranging tubular cells both in series and parallel dispositions, making sort of cell-bundles.

1.5 Costs

Up to now SOFCs systems are not able to compete with other technologies in the market yet. In fact internal combustion engines and gas turbines capital costs are close to 400-500$/kW while a modern combined cycle is about 1300-1400 $/kW (but it is often used to supply the base load). A SOFC system cost is right now around 10000 $/kW installed. But there is a great interest of big companies and also funding done by national states. For example in 1999 it was founded the most important organization dedicated to develop SOFC technologies: the SECA which means Solid State Conversion Alliance. It is a collaboration between the U.S. Federal Government, private industry, academic institutions and national laboratories [20]. The goals of this organization are first of all to reach 175 $/kW for a stack and 700$/kW for power blocks and to create SOFC systems that can be used in big coal fueled central plants with CO_2 capture [21]. Some companies that are taking part to the project are quickly approaching these goals; Rolls Royce et al. has projected a system with a stack cost estimated as 238 $/kW [22]. The interest of big companies makes this challenge reachable; in a study made by J. Thijssen [7] scenarios of the

manufactured stack and systems with different levels of production (the production volume impact) and the impact of scaling-up of the cells are analyzed and interesting results are gained. There are great economy scales increasing the production; with a hypothetic 10 MW/yr production a cost of 750-800 $/kW (just for the stack) is reachable; with a 1000 MW/yr production volume 175-200 $/kW seems to be an obtainable result. On the contrary, the scaling up influence seems to be less important; a reduction of 20% of the cost could be obtained.

Analyzing the predicted stack costs, the study emphasizes that the main cost will be always the one related to the ceramic cells; also important will be the cost of interconnects and less important will be the balance of stack an assembly and qc costs. A not so different distribution of the costs has been presented by Rolls Royce.

Another study made by Thijssen [23] focused on the cost of the electricity production and a LCOE (levelised cost of electricity) was obtained from 7 to 9,5 $cents/kWh. A great influence of the cost of the fuel (as predictable) was noticed.

There are also studies about the cost structures in a publication of the department of energy [2]: they are analyzed comparing strengths and weaknesses of SOEC and PEFC systems. The results seem to be comparable: SOFC have more expensive materials for electrodes and electrolytes, but they don’t need noble metals as catalysts. Also from the point of view of the balance of plants (that considers all the direct stack support systems, reformers, compressors, pumps, and the recuperating heat exchangers) SOFC and PEFC are comparable; the higher cost of the heat exchanger offsets the absence of the reformer in SOFC systems.

In the picture an estimation of the structure of costs is shown:

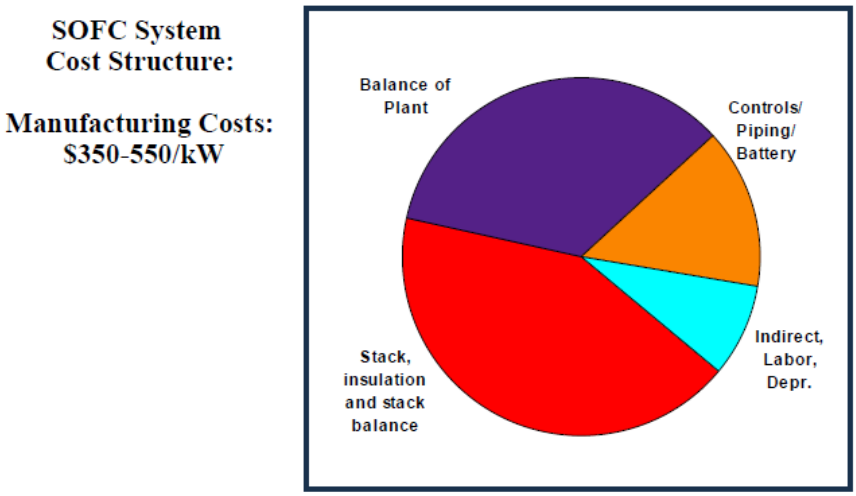

Figure 1.15. Forecast of a cost structure made by a U.S. department of energy research.

It has to be noticed that the different parts of the structure of the costs can have different weights in the final cost depending on the scale of the system. In a small scale system stack insulation and stack balance are key components, while in more complex systems the part of balance of plant has a greater importance.

1.6 Biomass as a fuel for SOFCs

Efforts for limiting dependence of the energy supply on fossil fuels have lately focused on two main strategies: supporting development of renewable energy technologies and increasing efficiency in energy management (be it generation or consumption). High temperature fuel cells were found to match these policies, since they proved to be good devices for highly efficient energy generation, either in large or small scale and centralized or decentralized systems. One of their main advantages consists in their flexibility in operation with different fuels, hydrocarbons included. Even the use of products from gasification of coal or other fossil fuels could be sustainable, since exhaust gases are mostly H_2O and CO_2, which can be easily separated for CO_2 to be sent to a capture and sequestration system. Anyway particular attention was also drawn on the use of biomass for SOFC feeding. Integrated gasifier-SOFC-gas turbine systems are intensively being studied as a solution for efficient and reasonably

costly energy generation. Biomass has the advantage of being CO_2 neutral, as what CO_2 it releases in its combustion it captures when growing. The problem with this source is that it is sustainable as long as its production doesn't compete with food crops and as long as its consumption implies the use of proper devices. Biomass is the main source of energy for many developing countries, where it is used with rather low efficiency mainly for domestic cooking applications. In this case its collection is not controlled and it may cause deforestation, with consequent impoverishment of the soil. Extensive cultivation of energy crop often leads to the same result and it additionally takes land which is then no more available for food crop. Biomass resources include agricultural residues; animal manure; wood wastes from forestry and industry; residues from food and paper industries; municipal green wastes; sewage sludge; dedicated energy crops such as short-rotation (3-15 years) coppice (eucalyptus, poplar, willow), grasses (Miscanthus), sugar crops (sugar cane, beet, sorghum), starch crops (corn, wheat) and oil crops (soy, sunflower, oilseed rape, iatropha, palm oil) [29]. Usually residues, waste and bagasse are used for heat and electricity generation, while sugar, starch and oil crops are used for liquid fuel synthesis. Biomass is usually sent to combustion systems for generation of steam or sent to gasifiers, where it is turned into gases of medium heating value for direct use in gas turbines or engines.

IEA statistics [24] updated to 2009 show a TPES of 12150 Mtoe, of which 10.2% account for biofuels and waste:

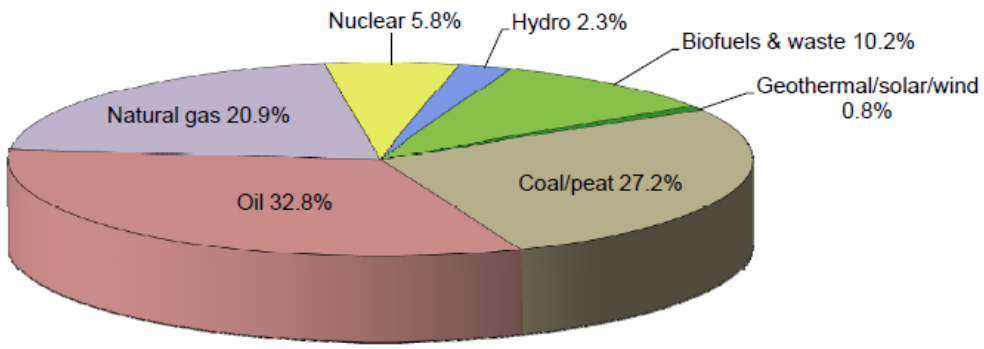

Figure 1.16. TPES in 2009 (source IEA).

As for electricity production IEA reported biomass to contribute by 1.3% in 2005, with a perspective of 3-5% in 2050.

In the last years more and more land has been used for energy crops. When they are grown on land which doesn't fit agricultural use or when they are cyclically interchanged with food crops because they fertilize the soil, they may be considered as sustainable for energy production. Otherwise, agricultural and forest residues or wastes shall be considered more suitable. IPCC (2000) gives a rough estimate of the theoretical global potential of biomass for energy use from different kinds of land [25].

Table 1.1. Global theoretical potential of biomass for energy use (source: IPCC, 2000).

	Area (Gha)	**max dry bioenergy** (EJ)	**max liquid bioenergy** (EJ)
Tropical Forests	1.76	528	211.2
Temperate Forests	1.04	312	124.8
Boreal forests	1.37	411	164.4
Tropical Savannas	2.25		0
Temperate grassland	1.25	375	150
Deserts and Semideserts	4.55		0
Tundra	0.95		0
Wetlands	0.35		0
Croplands	1.6	480	192
Total	15.12	2106	842.4

Indeed, of the global Earth land area of 15.12 Gha, only half is not suitable for cultivation, thus not competing with food crops need in a future scenario where both needs for energy crop and food and wood crop substantially increase with increase in global population. Many factors must be considered which reduce theoretical potential to technical, economical, eventually realizable potential. For example, Smeets and Faaij [26] estimate a global potential of biomass from forestry in 2050 of 112 EJ/year, but they reduce this amount to 71 EJ/year to take into account need for wood other than for energy use and to 15 EJ/year when including economical considerations into the analysis. Frondel and Peters [27] calculated the land needed to meet the goals for biofuels production in Europe in 2010, 11.2 Mha are required, 13.6% of total arable land in EU25.

This is why biomass is believed to be a crucial renewable source for energy production already in the short and medium term as long as its production is strictly regulated as to make it economically, environmentally, socially

sustainable. In a decentralized system, it offers the advantage of making combined production of heat and electricity available and to getting higher independence from the grid. Moreover a thermodynamic effect is also achieved, since when good quality process heat is required it is better to have it close to the consumption point. Connection of a decentralized small scale system could become a good solution when electricity transmission grid is solid and spread enough. In a centralized system, high efficiency sustainable energy production and consumption could be achievable, for example when a SOFC-gas turbine system is connected downstream to a gasifier. A fixed bed gasifier is a still good, cheap solution for such an integrated system. It is discussed whether the cost of the auxiliary systems, required cleaning systems and of the cell itself is still high for considering it economically sustainable with state of the art technologies. But use of a renewable source, very low emission levels, high global efficiency (up to 60% was realized), possible use of low cost fuels already makes it competitive.

Here a general overview of what sources could be used with high temperature fuel cells [28].

Natural gas: the common natural gas which is distributed for civil heating contains mostly CH_4, with minor presence of heavier hydrocarbons and some Sulphur containing gases to make it detectable by odour. In a SOFC system CH_4 can be reformed at the anode chamber and this gives much thermodynamic advantage, since steam reforming is endothermic and it makes it unnecessary to cool the cell. On the other hand, carbon deposition may occur with CH_4 in certain conditions and H_2S concentration must be reduced to avoid poisoning of the anode.

Landfill gas: gases from municipal and industrial waste mainly contain CH_4 and CO_2 and they can represent a highly sustainable source for SOFC systems. However they also have high concentration of contaminants, mainly up to 200 ppm H_2S and Chlorine containing compounds.

Animal wastes could be recovered through anaerobic digestion, thus getting again CH_4 and CO_2, with some content of H_2S.

Gasification synthesis gas can be obtained from coal, coke, biomass and the final composition depends on the gasification process and conditions. The product gases are generally H_2, CO, CO_2, N_2 and at smaller extent CH_4 and

different contaminants. If syngas has to be fed to low temperature cells such as PEMFC or PAFC, it must be almost pure H_2, with very low CO content. Hence it must undergo strong water gas shift, separation from CO_2 and high purification through adsorption processes. Such systems are employed for H_2 production and use in refineries, but they are not economically sustainable for stand-alone low temperature fuel cell systems. SOFCs on the contrary can be integrated with gasification processes, just requiring cleaning of contaminants and being able to work with hydrocarbons. In fact, if gas is fed at high temperatures (provided hot gas cleaning systems are available), no external reformer is necessary, since internal reforming is possible in the anode chamber and it also increases the thermodynamic performance of the cell because it works as a cooling agent itself.

It is beyond the scopes of this work to technically and thermodynamically evaluate any systems for combined heat and electricity production with SOFCs, but it is useful to briefly introduce the topic through an overview of the devices taking part to such systems.

Gasifiers operate a partial combustion of a solid fuel to transfer part of its heating value in the gas coming out. This way fuels like biomass or coal can be used as a source also for internal combustion engines like turbines, provided the composition of the gas which is sent to the turbine is controlled and the right inlet conditions take place. The outlet gas composition and heating value depends on the employed system. Fixed bed reactors are the cheapest and simplest device. They can be fed with air as an oxidant and they process fuels of big particle size. They are the only possible technology for gasification of biomass unless it is dried out and pulverized. In this case gasification takes the longest time (dozens of minutes), hence the mass flow is limited. High content of tars comes out of these beds, but cold gas efficiency (defined as $\frac{\dot{m}_{gas}\, LHV_{gas}}{\dot{m}_{fuel}\, LHV_{fuel}}$) is high. Fluidized beds have higher outlet temperatures, but still lower than the melting point of the ashes, in order not to have them plugging the bed (900-1000 °C). Higher mass flows are allowed, being the characteristic time some minutes. Entrained beds have the shortest conversion time, allowing integration with large scale industrial processes (high mass flow rates). Temperature of the bed is almost uniform and very high (gasification in this case is a poor partial combustion), so that they show the lowest cold gas efficiency. At the same time almost no tars are present in the stream.

It was stated that for operation of SOFC systems with biosyngas another core part is the cleaning section. Cleaning from contaminants can be basically performed in two ways, at high or low temperature. Low temperature cleaning includes the most mature technologies and it is cheaper and easier to realize and maintain. On the other hand, high temperature cleaning suits much more Gasifier-SOFC systems, thermodynamically speaking, as it doesn't require cooling of product gases, then loss of exergy content. However cost of materials and harsher working conditions make it still an expensive solution.

At Process & Energy Department of TU Delft, operation of integrated Gasifier-SOFC/SOFC stack-Gas turbines is being investigated and its chances of becoming commercially available particularly as small scale combined energy production devices. In his work P.V. Aravind [3] demonstrates these systems are likely to become a solution in the next years and builds his considerations on what was already realized and on his own conclusions and his group's. Theoretically it was demonstrated that 70% efficiency can be achieved with integrated systems. Siemens proposed a model for SOFC-GT system and a prototype was installed at university of California, Irvine, which worked for 2900 hours and reached 53% efficiency. Some prototypes of Gasifier-SOFC-GT systems were developed, with hundreds of kW powers, hot or cold gas cleaning processes and global efficiencies between 45 and 60%. Aravind et al. studied a 103 kW system based on a 30 kW gas turbine with 64.5% net efficiency, and 51% total efficiency considering the gasifier (80% conversion efficiency assumed). Many other studies were recently carried out. The global exergy evaluation of such solutions is used as a tool to choose the most efficient configurations and static and dynamic analysis through ad hoc software allows simulating the performance in every possible conditions. Anyway bigger and bigger efforts are now focused on studying the influence of syngas compositions on performance of the cell and it is intended to go deeper in some of the resulting evaluations.

1.7 Biosyngas and its contaminants

Operation of SOFCs with syngas is a well studied topic and there is general agreement about them being able to work with carbon containing fuels. But how different syngas compositions affect the different processes occurring in the cell is still not clear. Moreover, most conclusions on this matter are drawn with

Ni/YSZ anodes, state of the art material, but very few data are available about performance of other anode materials. Of the main components of the gas, hydrogen, carbon monoxide and methane are fuels for SOFC. N_2 is expected to be inert but it may cause diffusion problems. H_2O and CO_2 will contribute to the shift reaction, and CH_4 will get reformed inside the cell to some extent. Fuels containing carbon can cause carbon deposition in certain circumstances. GDC anodes are reported to better perform with carbon deposition compared to Ni/YSZ [3]. In 2005 Aravind et al. [30] published a study of influence of syngas composition on SOFC performance through Electrochemical Impedance Spectroscopy (EIS), which is exactly expected to give separate information about how each process is affected. How EIS works will be later explained, for now it is useful to look into Aravind's conclusions.

Experiments were carried out on GDC and SDC symmetrical (not complete) cells with three different compositions, representative of air gasification, oxygen gasification and pre-reformed gas with steam gasification. Here the simulated syngas compositions as employed in the study:

- 20% H2, 20% CO, 10% CO2, 50% N2 for air gasification;

- 40% H2, 40% CO, 20% CO2 for oxygen gasification;

- 50% H2, 40% CO, 10% CO2 for steam gasification.

It is concluded that dilution with N_2 gives higher diffusion impedance, that is, it affects diffusion phenomena over the anode, CO gives higher diffusion impedance too, while the opposite behaviour is found with CO_2. This is believed to be caused by water formation from gas shift reaction in the presence of CO_2. Afterwards, a preliminary study about effect of H_2S is carried out, to be compared with first available studies on this contaminant. Investigation with 3, 6, 9 ppm (added to the syngas just before it enters the reactor) in the short term reveals no effect of sulphur, while an upper limit of 1 ppm had been found for Ni/YSZ anodes. This could mean that, even if S deposits on Ni surface, doped Ce surface is still available and catalytically active and Ni can still work as a current collector, so that operation is not affected. At higher concentrations however chemical reactions may occur with Ni and this has to be looked into.

In 2007 Aravind [3] better looked into biosyngas contaminants, their effects and tolerance limits for SOFC operation. The concentration of each contaminant

varies upon the kind of biomass, the gasification means and technology, but some reference values can be assumed as an average before gas cleaning section:

Table 1.2. Typical content of contaminants in biosyngas.

Contaminant	Concentration
Tar	5-20 g/Nm^3
Particulates	5-30 g/Nm^3
H_2S	50-200 ppm
Alkali metals	1 ppm –wt
NH_3	4000 ppm
Halides	Few ppm

More detailed discussion of characteristics, possible effects and options for hot and cold gas cleaning of all these contaminants is now needed. For most of them the effects on the anodes have not been studied in detail yet, hence no clear tolerance limits are known, as summed up in Aravind's review [3].

Table 1.3. Biosyngas contaminants and known tolerance limits for SOFC operation.

Contaminant	Typical contaminant presence	Limitations (approximate) in high temperature removal (>873 K)	Limitations (approximate) at lower temperatures (<873 K)	Tolerance limit
Particulate matter	5-30 g/Nm^3	Few mg/ m^3	Few mg/ m^3	No information available
Tar	5-20 g/Nm^3	<100 mg/ m^3	<100 mg/ m^3	No information available
Alkali Metal	1 ppm wt	<1 ppm wt	<1 ppmwt	No information available
HCl	Few ppm to few hundred ppm	Few ppmv	Few ppmv	No information available
Ammonia	4000 ppmv	Few ppmv	Few ppmv	Is a fuel
H_2S	50-200 ppmv	1 ppmv	1 ppmv	1 ppmv

For some time contaminants have been studied mostly from the point of view of their presence in the microstructure of the cell, due to fabrication processes. They were mixed with the cermet anode/electrolyte material powders during fabrication process and their effects during operation with pure feed gas were then observed either at OCV or under polarization [16]. A parallel approach is now to see how they affect the different processes occurring at the cell from outside, so they are fed together with the gas flow.

Particular attention will be given here to alkali metal compounds, like KCl and NaCl, as this study focuses on optimizing an experimental procedure for testing their influence over operation of GDC anodes. A complete knowledge of their chemical and physical features is believed to lead the way for modelling of a setup in which their contamination can be properly simulated.

Tars: they are commonly defined as organic molecules with weights greater than benzene. Being condensable, they may plug pipelines or, at the anode, they could cause carbon deposition with consequent deactivation of the catalysts, if working conditions allow it thermodynamically and kinetically. Their effect has been studied only in the latest years. Their presence can be prevented by

improving gasification conditions. Technologies for low temperature removal are available, like cooling towers, Venturi scrubbers, demisters, low-temperature granular filters, and wet electrostatic precipitators, but in some of these cases, treatment of contaminated water becomes an issue. At high temperature they can just be thermally (above 1273 K) or catalytically cracked. Their presence was experimentally simulated by Aravind by flowing N_2 through a heated solid Naphtalene (C_8H_{10}) bed and then mixing it with humidified hydrogen.

Particulate matter: it includes every organic or inorganic particle in the feed gas, originating from condensed tar (char), from mineral matter present in the original biomass or detached particles from the gasificator. It ranges from sub micron dimension to some micron, which means it can cause high plugging of the porous anodes surfaces. An example for particulate matter can also be condensed alkali compounds. However at common syngas outlet temperatures most particles will be in gas phase and, if they were present at the anode surface as solid particles, it is claimed that they will be mostly carbonaceous compounds, which makes them easily oxidized at high temperature. In order to have a safe operation with SOFC they must be removed at higher extent than what allowed by cyclons; at low temperature bag filters, cartridge filters and packed bed filters may be used, or wet scrubbing (which must work way down 100 °C), while ceramic filters are an option at high temperature.

Halides: they are defined as binary compounds between a halogen atom and another less electronegative element or radical. In biosyngas, mostly HCl and at a minor extent HF and HBr are present. At SOFC operating temperatures they are in the form of acid gases and they are likely to react with Ni and form vapors of the metal. At low temperature they are removed with wet scrubbing (once again the problem of water treating arises), while at high temperature Na or K based sorbent beds can be used to remove them down to sub ppm levels. This way, however, another issue arises, because Na and K could detach from the sorbent and be entrained by the flow, thus causing the concentration of harmful alkali compounds like KCl and NaCl to increase in the product gas to be fed to the fuel cell.

Nitrogen compounds: they will be mostly NH_3 (ammonia) and HCN. Their presence must be limited because they are generally toxic and severe restrictions exist regarding their emission in the atmosphere. As for their effect on the cell, NH_3 is not harmful, since it is known as a possible fuel for SOFC application. Its

presence may cause diffusion impedance of the anode to increase, thus limiting the performance, but it will be basically split into H_2 and N_2 at the anode and then reacted. As for HCN its effects have not been studied in detail so far.

Sulphur compounds: they form during gasification after the presence of solid phase Sulphur in the fuel. In the product gas H_2S is mainly present, since it is the most stable compound at SOFC operating temperatures [31], with some content of SO_x and COS. The concentration depends on the original fuel. In refuse-derived fuels S reaches 1%, which is low enough with respect to the emission requirements. However, it is not enough for safe operation of the cell. Ni/YSZ anodes are reported to be seriously affected even by 1 ppm H_2S, while no information is available about other anode materials. The degrade rate lowers with increasing temperature. Moreover the degradation is recovered after removal of the contaminant from the feed, which indicates that it affects the performance by depositing on the surface of the anode. It is indeed also found to react with Ni to form sulphides, up to a negligible extent as long as the concentration of H_2S is low. Presence of H_2S varies from 20 to 200 ppm in biosyngas. For removal of H_2S at low temperature wet scrubbers or activated carbon can be used, while high removal at high temperature is much more complicated and requires external reactors downstream of gasification units, with metal oxides as sorbents, like Zinc oxide or Ceria. The test conditions employed by Aravind for studying the effects of Sulphur were already discussed.

More literature background is available for H_2S than for other contaminants, all of that with Ni/YSZ as anodes. However the mechanism could be similar for GDC, hence the available results are still a good reference. A later study than Aravind's, in 2008, by Schubert et al. [32], further investigated this field, by means of EIS. Ni/GDC-YSZ-LSM cell stacks are tested with simulated syngas composition and humidified hydrogen at 850 °C with varying H_2S and steam concentration. First measurements with H2S concentrations up to 30% were performed. A cell voltage drop at constant current occurred with 8 ppm H_2S, which didn't increase significantly with higher sulphur contents. This is due to adsorption of the poison on the surface of Ni, which reaches saturation already at low ppm values. The drop was totally recovered when H_2S was removed from the current. The impedance spectra showed a little increase in the low frequency arc. Reaction of H_2S with Ni seems to occur when water partial pressure, then oxygen pressure, is increased. It is also enhanced by lower temperatures.

Study of the effects of all these contaminants is really complicated. It can decline in many different ways: effect of high concentration in the short term, effect of low concentration in the long term, effect on the cell or on more system components, on the anode processes or on the corollary of different reactions, combined effect with other syngas components. In his study [3] Aravind concentrated on the effect of small to medium quantities in a rather short term (24 hours, up to 48, 72 hours in some cases). The longer is the experiment, the harder is to get reliable results, since many processes occur and combine their effects at high temperature. This adds to a still not complete knowledge about the cells themselves (especially when new materials are tested) and the experimental setups for testing (many different assets are employed by different research groups). In the present study, conditions for testing contamination from KCl at medium concentrations in the short term will be created. The effects of this salt are not known yet and interpretation of Aravind's preliminary results was difficult too, so it is suggested to increase the concentration with respect to those he used and keep once again in the short term. Once information about the interaction mechanism between the anode and KCl is available, it is then useful to see the long term effects, because SOFC systems are considered to be advantageous as soon as they reach a long working life.

1.8 Alkali compounds

One of the elements sometimes significantly present in biomass is K. Na appears as well, but usually in lower concentration, so that we can focus on K and extend all the considerations also to Na, since their molecules are very similar. Bakker and Elbersen of WUR [34] show typical values of inorganic matter content in biomass (% on dry basis):

Table 1.4. Typical content of inorganic matter in biomass.

	Occurrence %
SiO_2	0,5-15
K	1-2
Ca	0,1-0,5
S	0,1-0,5
Cl	0,2-2

In young plant shoots even 5% K may be found. Moreover its content in the fuel varies with soil and it can go up to significant concentrations:

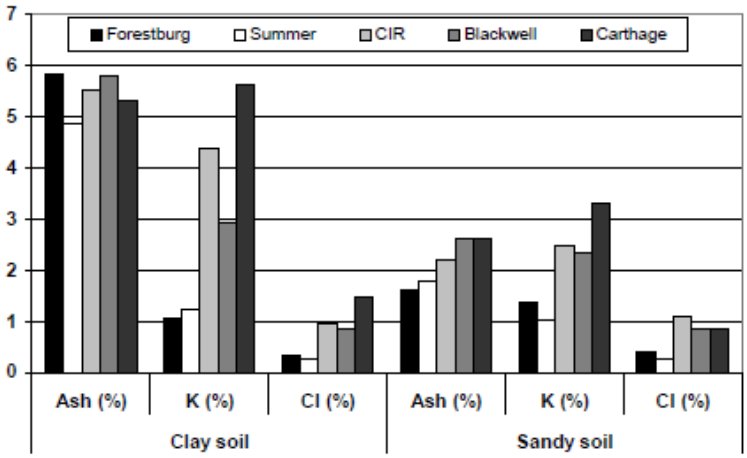

Figure 1.17. Different contents of inorganic matter depending on the soil.

Other authors [35] study the inorganic matter content starting from the composition of the ashes. Comparison between many kinds of biomasses is made:

Table 1.5. Inorganic matter contents in different kinds of biomass.

	Polish coal	Peat	Bark Conifers	Forest residue	Wheat straw	Rice straw	Rice husk	Bagasse	Sunflower stalk
	w-%	w-%	w-%	w-%	w-%	w-%	w-%	w-%	w-%
SiO_2	47,7	32,1	4,8	11,6	59,9	69,9	95,4	73	3,1
Al_2O_3	23,8	17,3	2,8	2	0,8	0,3	0,1	5	0,1
Fe_2O_3	9,5	18,8	1,5	1,8	0,5	0,2	0,1	2,5	0,2
CaO	3,8	15,1	45	40	7,3	3,4	0,4	6,2	6,6
MgO	2,9	2,5	5,2	4,8	1,8	1,6	0,3	2,1	4,3
K_2O	2,4	1,4	8	9,2	16,9	15,3	1,8	3,9	27,5
Na_2O	1,1	0,5	0,9	0,6	0,4	0,4	0	0,3	0
P_2O_5	0,4	3,7	4,2	4,4	2,3	1,5	0,5	1	18,5
Others	8,4	8,6	27,6	25,6	10,1	7,4	1,4	6	39,7

It can be seen that sources like straw and sunflower stalk have the highest average K content. When gasifying, Chlorine present in the biomass usually

combines with K, unless other elements strongly prevail (like Si) and KCl is exclusively volatilized at temperatures above 800 °C (perfectly fitting the temperature range for gasification). Eutectic sodium and potassium salts can vaporize from ash already at 700 °C, while they start to condense on particles in the gas stream from gas phase at 650 °C. For this reason KCl is present as gas phase in the biosyngas which is to be fed to the SOFC system and its effect on it needs to be investigated in order to find the cleaning limit in the flow. Amounts of $(KCl)_2$, KOH, K in gas phase are also recorded to be present after gasification, but they are not taken into account in the present work. Aravind [3], working on integrated gasifier-SOFC-gas turbine systems, highlights that K and Na are required for hot cleaning of halides in the biosyngas before feeding to the SOFC. Thus, former gas cleaning units are an additional source of KCl in the feed gas and they may be the main cause for a significant concentration of the contaminant.

It is now necessary to make an overview of the properties of KCl, as to predict what its behavior could be at high temperatures and at the employed conditions for the experiments. Equilibrium computations will then help mostly in verifying the chance of reaction with other elements. If the gas from biomass gasification is assumed to be fed to the SOFC system as it comes from the reactor, KCl will be in gas phase. The state diagram shows the equilibrium of phases with varying T and P.

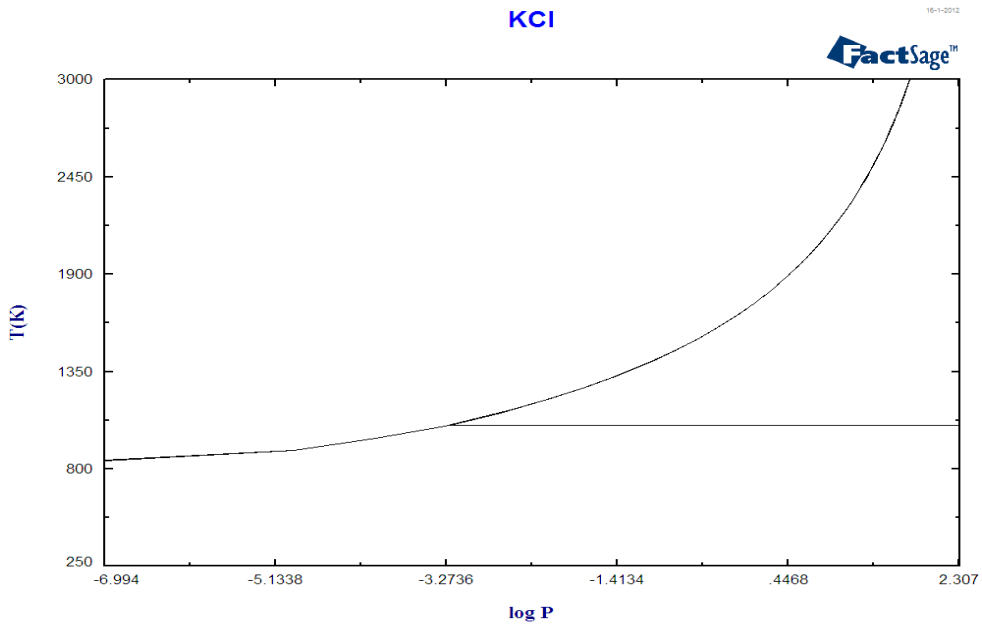

Figure 1.18. State diagram of KCl as calculated with FACTSAGE.

It can be seen that at the employed pressures (ambient pressure) the salt melts at 773 °C and boils at 1420 °C. It must be verified that the temperature of the KCl solid bed doesn't reach the melting point. The solid KCl is driven into gas phase by H_2 through sublimation, since it tends to reach its vapor pressure at the outlet of the bed. Being this a phase equilibrium between gas and solid, the concentration is around ppm values. More care must be taken in the gas sampling procedure, where the probe pipe is placed at the reactor outlet and temperature rapidly drops outside the oven. This means that KCl for sure condenses in it. The following table sums up the most valuable properties of KCl, which will be of use in the calculations for setting up the modified experimental asset (pressure drop calculation through the KCl bed, gas sampling, KCl bed height).

Alkali compounds cause corrosion in gas turbines, heat exchangers etc… Their evaporation and subsequent deposition on walls of biomass gasifiers is a well studied topic. They are lately found to affect reforming catalysts and in all probability they also affect SOFC anodes.

Few references are found about the effects of KCl on the anode material. No reference is found, on the other hand, about experimental setups to study KCl

contamination through the feed gas and procedures to measure the influence. For modeling and building up the setup for impedance measurements with KCl contamination, then, Aravind's experience will be taken as a starting point and developed.

A study from Rostrup-Nielsen and Christiansen in 1995 [16] first led the way to comprehension of the effects of K on the anode material. It focused on a totally different subject than the one of this work, but it is useful to understand the physical processes, to therefore link them to the electrochemical behavior shown in the impedance spectra. Rostrup and Christiansen investigate MCFC cells, the electrolyte of which is most times KCO_3. The alkali contaminant originates in this case from the electrolyte and it is brought to the surface of the anode through cracks or vapor phase transport. Potassium is known as a promoter for the reforming reaction which avoids carbon deposition, but deposition of alkali on Ni or noble metal catalyst's surface results in a decreased reaction rate for reforming. There's adsorption on the surface, which is easier on acidic supports than on basic ones and specifically on less acidic supports, because they have looser bonding than alkali. This means that alkali partial pressure plays a role in the poisoning of Ni. However the limiting process seems to be the adsorption itself: by calculations it is found that addition of alkali on Ni (III) surface in the experiments shows no limitation in the adsorption rate of methane or in Ni reforming catalysis activity. An effect on methane reforming could then come from the fact that reforming is sensitive to the structure of the catalyst. It's speculated that the presence of alkali may enhance the reconstruction of the surface of Ni to Ni (III), which is a less active surface, but this has still to be verified.

Julie Mougin et Al. report in a 2007 study [33] how no evidence is found in literature about effect of alkali compounds on operation of SOFCs. Many studies were indeed carried out on Ni/YSZ performance with H_2S and, in general, it was found to affect the anode operation by depositing on Ni surface and forming Ni sulphides when H_2S was present at some extent. The effects are then partially irreversible and they appear already with low ppm concentrations of H_2S. Anyway the degradation mechanisms are not known in detail yet, since SEM and XRD analyses hardly detect Sulphur at such low concentration. Alternative investigation techniques are lately being used, such as Raman spectroscopy or Impedance spectroscopy, but their results are still difficult to

interpret. On basis of these considerations also study of the effects of KCl may result difficult and this is what Julie Mougin's group investigates.

Tests were carried out for 100 hours on Ni/8YSZ commercial 30 mm diameter pellets, in gas tight chambers where the gas was flown at 800 °C. A simulated syngas composition was fed, with 33% CO, 29% H_2, 29% CO_2, 9% CH_4 on dry basis. Contaminants were added to this feed with concentrations of 100 ppm for both H_2S and KCl. Post-mortem analyses were carried with SEM, XPS and Raman micro-spectroscopy. More experiments were performed with two Ni/8YSZ-YSZ-LSM cells stacks (provided by Julich Research Center), to which 3% humidified H_2 was fed at 800 °C. It was fed alternatively with H_2S (from 3 up to 14 ppm) and without H_2S for 2000 hours, but no KCl was added in this case. In this case I-V curves were recorded at each stage. KCl effect is investigated only in the case of Ni/YSZ pellets and it is highlighted by XPS analysis, which shows peaks corresponding to K^+. This means that KCl is deposited on the anode surface, probably heterogeneously and with different thicknesses. H_2S was detected through SEM, a little by EDX, most of all through Raman spectroscopy. On the contrary XPS didn't detect anything, probably its spot area being too much larger than the small deposits of H_2S on the surface.

From these few references it can be inferred that the effect of KCl on the anode should mostly depend on its concentration. In Mougin's experiments however KCl concentration was high (100 ppm) and so it probably was also for Rostrup and Christiansen. It is then hard to say what could happen at lower concentrations. If KCl really promotes Ni surface faceting this could be sensed also at low concentrations and high and medium frequency responses in impedance spectra could be affected. Many times high frequency shows much noise, especially when high performing anodes are employed and especially at high operation temperatures of SOFC. So as a first step variations in the intermediate frequency arcs may be looked for. If deposition occurs to much an extent (after long time exposure or high concentration exposure), then mass transport phenomena may be influenced too, as it seems to happen in some cases with H_2S contamination [32]. Probably this won't be the case in the experiments which are planned as a prosecution of this study, because in that case diffusion limitation in a stagnant gas layer over the anode is much more important than diffusion into the porous structure. As for alkali metal compounds cleaning systems, cooling down at 550 °C and filtration is suggested as a low temperature

solution. At high temperature there are alkali getters typically working in the range 600-900 °C like activated alumina and bauxite, acidic white clay, kaoline. New solutions are now studied, experimentation is still at the beginning in this field.

References

[1] Subhash C. Singhal, Kevin Kendall, High Temperature Solid Oxide Fuel Cells. Fundamentals, Design and Applications, 2003.

[2] Fuel Cell Handbook (Sixth Edition), EG&G Technical Services, Inc. Science Applications International Corporation, 2002.

[3] P.V.Aravind, Studies on High Efficiency Energy Systems based on Biomass Gasifiers and Solid Oxide Fuel Cells with Ni/GDC Anodes, PhD thesis, November 2007.

[4] A. Boudghene Stambouli, E. Traversa, Solid oxide fuel cells (SOFCs): a review of an environmentally clean and efficient source of energy.

[5] J. Larminie, A. Dicks, Fuel Cells Systems Explained, second edition, 2003.

[6] G. Groppi, Slides of the course "Processi chimici per l'energia e l'ambiente", Politecnico di Milano, 2009.

[7] Jan H.J.S. Thijssen, The impact of Scale-Up and Production Volume on SOFC Manufacturing Cost, 2006.

[8] K. Huang, Fuel utilization and fuel sensitivity of solid oxide fuel cells, 2011.

[9] Chan, Khor, Xia, A complete polarization model of a solid oxide fuel cell and its sensitivity to the change of cell component thickness, 2000.

[10] X . Yuan, C. Song, H.Wang, J. Zhang, Electrochemical Impedance Spectroscopy in PEM fuel cells, Springer-Verlag London, 2010.

[11] M. Verbraeken, Advanced supporting anodes for Solid Oxide Fuel Cells, MSc thesis, EMPA Dübendorf, March, 2005.

[12] Gorte R.J., Vohs, J.M., Novel SOFC anodes for the direct electrochemical oxidation of hydrocarbons, Journal of catalysis, vol. 216, 2003, pp. 477 – 486.

[13] S. Primdahl, M. Mogensen, Mixed conductor anodes: Ni as electrocatalyst for hydrogen conversion, Solid State Ionics 152– 153, 2002, pp. 597-608.

[14] Gadolinium Doped Ceria Nanocrystals Synthesized From Mesoporous Silica, Rossinyol Pellicer Prim Estradè, 2007.

[15] S. Pinol, M. Morales, F. Espiell, Low temperature anode-supported solid oxide fuel cells based on gadolinium doped ceria electrolytes, 2007.

[16] J.R. Rostrup-Nielsen, L.J. Christiansen, Internal steam reforming in fuel cells and alkali poisoning, Applied Catalysis A, 1995, pp. 381-390.

[17] C. S. Tedmon, Jr., H. S. Spacil, S. P. Mitoff, Journal of Electrochemical Society, 116 1170, 1969.

[18] N. Q. Minh, T. Takahashi, Science and Technology of Ceramic FuelCells, Elsevier Science, Amsterdam, Nederlands, 1995.

[19] L. J. H. Kuo, **S.** D. Vora and S. C. Singhal., Am. Ceram. Soc., 1997.

[20] U.s. department of energy, http://www.fossil.energy.gov/programs/powersystems/fuelcells/.

[21] W. Surdoval, The Benefits of SOFC for Coal-Based Power Generation, October 30, 2007.

[22] R. Goettler, Overview of the Rolls-Royce SOFC Technology and SECA Program14th, July 2009.

[23] J.H. Thijssen, J. Thijssen, LLC, Stack Operating Strategies for Central Station SOFC.

[24] IEA energy statistics, 2009.

[25] Biomass Energy and Competition for Land; John Reilly and Sergey Paltsev, MIT, 2007.

[26] Smeets E., A. Faaij, Bioenergy Potentials from Forestry in 2050: An Assessment of the Drivers that Determine the Potentials. *Climatic Change*, forthcoming, 2007.

[27] Frondel M., J. Peters, Biodiesel: A New Oildorado? *Energy Policy*, 35: 1675-1684, 2007.

[28] D.C. Dayton, Fuel Cell Integration. A Study of the Impacts of Gas Quality and Impurities, Milestone Completion Report, June 2001.

[29] Biomass for Power Generation and CHP, IEA, 2007.

[30] P.V. Aravind, J.P. Ouweltjes, E. De Heer, N. Woudstra, G. Rietveld, Impact of biosyngas and its components on SOFC anodes, Electrochemical Society Proceedings volume 2005-7, pp. 1459-1467.

[31] Sasaki et al. Journal of Electrochemical Society, 153 (11) A2023-A2029, 2006.

[32] S. K. Schubert, M. Kusnezoff, C. Wunderlich, Characterisation of Sulphur Poisoning of Anodes in Single-Cell SOFC Stacks Using Impedance Spectroscopy, Fraunhofer Institute for Ceramic Technologies and Systems.

[33] J. Mougin, S. Ravel, E. De Vito, M. Petitjean, Influence of fuel contaminants on SOFC operation: effect on performance and degradation mechanisms, ECS Transactions, 7 (1), 2007, pp. 459-468.

[34] Robert R. Bakker and H.W. Elbersen, Managing ash content and quality in herbaceous biomass: an analysis from plant to product, Wageningen University & Research Centre (WUR), Institute Agrotechnology & Food Innovations-Biobased Products, Nederlands.

[35] Vesna Barišić, Edgardo Coda Zabetta, Combustion of Different Types of Biomass in CFB Boilers, 16th European Biomass Conference, Valencia, Spain, June 2−6, 2008.

Chapter 2

Electrochemical Impedance Spectroscopy (EIS)

EIS has been used in the latest years as a tool for investigating the processes occurring in fuel cells. The principle is simple, it consists in making an AC impulse passing through the cell, with or without bias, calculating the voltage or current response in the frequency domain and obtaining from this an impedance spectrum, where the different impedance elements come mainly from processes and limitations inside the cell. Many authors tried to study the physics of the cell through EIS, deconvoluted the obtained spectra and related the impedances to assumed electrochemical, kinetic, thermodynamic limitations, thus leading to electrical models of the cells (equivalent circuits). Still the interpretation of the data is difficult and makes research in this field slow, for many reasons: the equipments for such studies must be much sophisticated and precise, which means high costs and long time laps when a device breaks; the components are most times very small as well as the measured impedances, so that relative noises may completely invalidate the experiments; every observed process could be due to several causes and often the given explanations are in contrast with one another, making it necessary to repeat the experiments and to carry out new studies over a wider range of boundary conditions.

Anyway, general agreement over many questions and a deeper interconnection between what is observed and what really happens into the cells is being reached, often with the help of other measurement techniques, like SEM (scanning electron microscope, an optical technique) or XRD (X-ray diffraction) already used in the materials science. For this reason we considered the use of EIS fundamental for our study, and we supported it through comparison with the results of other authors, which could either contrast with ours, making it necessary to restart the experiments, or validate our results. In order to get familiarized with impedance spectroscopy it is important to begin with the simplest case studies. In this chapter a description of electrochemical impedance spectroscopy is given, starting from the physical background, to the study of the equivalent circuits which can be obtained and to a brief overview of the equipments and the measurement techniques. A deeper insight of the

conclusions of previous studies of SOFC with EIS is also presented, with different operating conditions and fuel compositions, ranging from H2 to simulated biosyngas, either contaminated or not. This is done in order to highlight on what processes there is agreement and on what, on the contrary, there is discussion. Moreover, results are related to the specific employed setup, as to show the frame of the conclusions of each study.

2.1 Electrical circuits, background

In a DC circuit Ohm's law states that when the voltage and the current response of an element are known, then resistance can be calculated, as:

$$R = \frac{V}{I} \tag{2.1}$$

If AC current flows instead in the circuit, also inductances, capacitances and other frequency-dependent terms have to be taken into account, thus leading to the more general definition of impedance:

$$Z(\omega) = \frac{V(t)}{I(t)} \tag{2.2}$$

The technique which measures the impedance of AC circuit is called AC Impedance Spectroscopy and when it is applied to an electrochemical system it is called Electrochemical Impedance Spectroscopy [1].

As can be seen, voltage and current are time dependent and the impedance Z is frequency dependent. V and I can be seen as phasors, i.e. vectors rotating on a plane at the same frequency, so they can be characterized just by their modulus and phase: $\{V\}e^{i\alpha}$ and $\{I\}e^{i\beta}$. So Z, which is their ratio, can be written as $Z^{ei\theta}$, where θ is the phase between the voltage and the current. Based on Euler law the impedance can thus be expressed as the sum of an imaginary part and a real part, which will be represented as Cartesian coordinates over a Gauss plane ($Z = Z_{re} + Z_{im}$, where Z_{re} and Z_{im} are usually written as Z' and Z'').

When impedance measurements are carried out, a device which generates an alternate impulse is used, as will be described in the following sections. If it is able to work as a potentiostat as well as a galvanostat, either current or voltage can be controlled, in order to obtain a voltage or current response respectively.

The impulse has a given amplitude (of voltage or current) and the response is recorded over a certain frequency range (usually from one tenth of Hz to hundreds of thousands). Every point represents the impedance at one frequency and the results are always displayed as a plot in the whole chosen range. The diagram representing the imaginary part of the impedance over the real part is called Nyquist plot (or Cole-Cole plot or complex impedance plane plot), while the one displaying the modulus and phase of Z over the frequency (often on a logarithmic scale) is the Bode plot. The first gives often a faster overview of the processes, the second is complementary, especially when the Nyquist plot is complicated. The shape of the arcs in the Nyquist plot depends on the kind of processes which are occurring and on the setup.

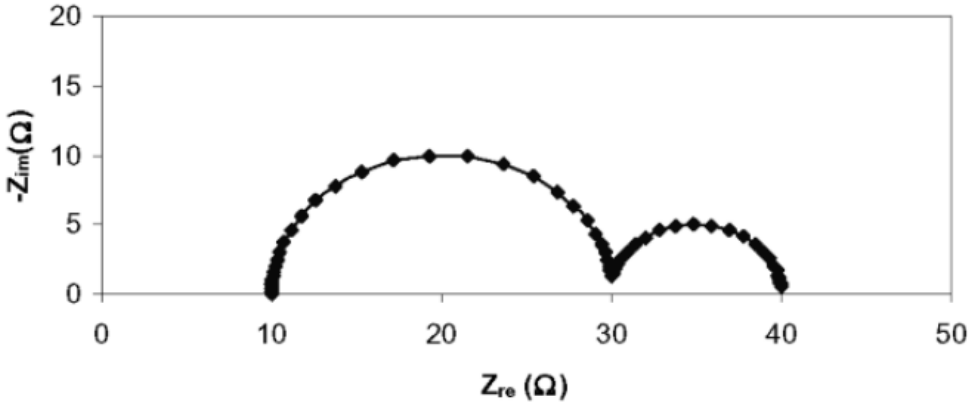

Figure 2.1. Example of Nyquist plot.

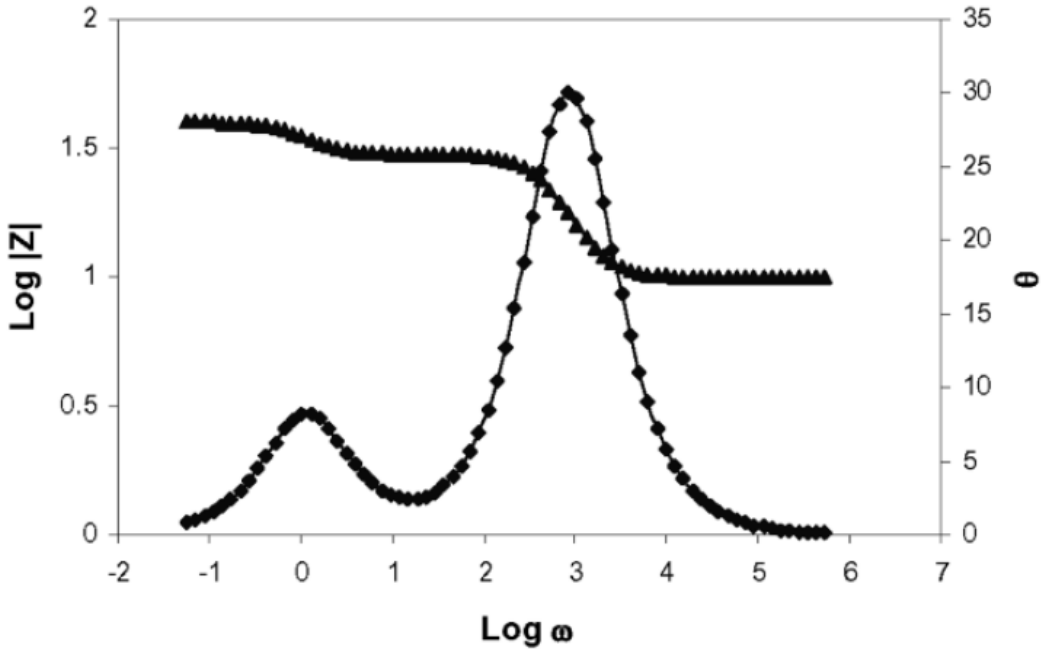

Figure 2.2. Example of Bode plot

2.2 Impedance analysis

From the measured impedance spectrum the equivalent circuit elements must be found. This is one of the most critic points of impedance spectroscopy, the interpretation of the spectra is difficult, because most times the arcs are not clear, they are overlapped and they are distorted by noises. Moreover, an infinite number of circuits can be fitted to the measured spectrum and it is easy to assume elements, hence processes, which don't occur at all in the actual system. A model must be proposed, with initial values of the impedances to be later fitted, but these values must be reasonable and start from physical considerations. The analysis of the distribution of relaxation times (DRT) helps in finding an adequate circuit, so a unique solution. The relaxation time of a process is the characteristic time, the inverse of the summit frequency. It is related to the recovery rate of the steady-state when a perturbation is applied to the system [1]. The summit frequency of a process is the frequency of the peak of the imaginary part of the corresponding arc.

Here it is shown how the DRT of an equivalent electrical element is found. Kramers-Kronig relations are bidirectional relations connecting the real and imaginary part of any complex function which is analytical in the upper half of the complex plane, that is, which is locally given by convergent power series [2]. Every impedance function obeying the Kramers-Kronig relations can be written as the differential sum of infinitesimal R-C parallel circuits in series [3]. Any element has its own relaxation time and the sum to infinity is:

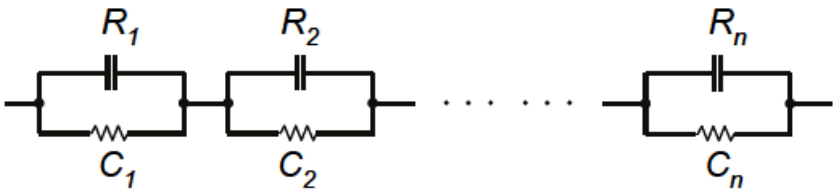

Figure 2.3. Series of R-C circuits.

$$Z_{pol}(\omega) = \sum_{n=1}^{N} \frac{R_{pol,n}}{1 + j\omega\tau_n} = R_{pol} \sum_{n=1}^{N} \frac{\gamma_n}{1 + j\omega\tau_n} \tag{2.3}$$

where the subscript n refers to every R-C element up to N, R_{pol} is the total polarization resistance, j is the imaginary unit, ω is the frequency, τ_n is the relaxation time of the n-th element. γ_n weights the contribution of the n-th polarization process to the overall polarization loss. If the integral sum of the processes is considered, then the total impedance can be written as:

$$Z_{pol}(\omega) = R_{pol} \int_0^{\infty} \frac{\gamma(\tau)}{1 + j\omega\tau} d\tau \tag{2.4}$$

with

$$\int_0^{\infty} \gamma(\tau) d\tau = 1 \tag{2.5}$$

$\gamma(\tau)$ is the distribution function and the term inside the integral in equation (2.4) represents the fraction of the overall polarization resistance with relaxation times between τ and τ + dτ. The problem now is to obtain the function from the equation above. This can be done with the Kramers-Kronig relations as long as the system is linear and time invariant. Every process is found to have its own

DRT with one or more peaks and characteristic features. Thus, from the spectrum it is possible to get the DRT of the total system, deconvolute it into the single contributions with their relaxation times and find what kind of processes is occurring and at what peak frequency. If, for instance, the DRT of a CPE element (which will be later explained) is analytically calculated, through the following formula derived elsewhere [3]:

$$g(x) = -\frac{1}{\pi}\left[z\left(x + j\frac{\pi}{2}\right) + z\left(x - j\frac{\pi}{2}\right)\right] \tag{2.6}$$

where $x = \ln(\tau\omega)$ and z(x) is the analytical form of the imaginary part of the impedance element; this plot is found, with different shapes according to the chosen values for n (a parameter of the CPE), else named CPE-P:

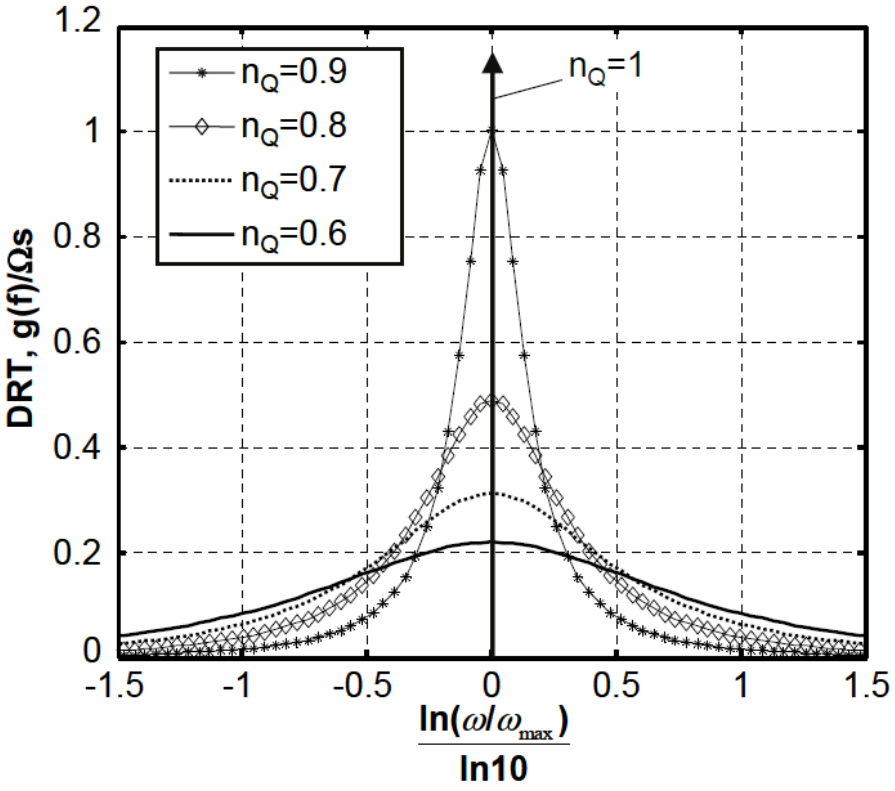

Figure 2.4. Example of analytical DRT.

When the DRT is numerically calculated by software the plots above broaden and they show no ideal peak, due to discretization. When fitting the recorded

spectra to equivalent circuits, this analysis is useful to check the peak frequencies of the processes. But still weaknesses of the fitting techniques are not completely avoided.

Once the processes are identified, the initial values are set through an analysis of the relaxation times and a comparison with literature data. The "instant fit" function in the software ZView helps in this task: it allows fitting the identified arcs individually, as to take the recorded values as starting parameters for the global circuit fitting. Eventually the fitting itself can be performed. The most used method for fitting the impedance spectrum of the proposed equivalent circuit to the actual one is the Non-linear Least Square algorithm. It consists in making an iterative calculation to find the set of parameters (starting from the initial values coming from the analysis described above) which minimizes the sum:

$$Q(P) = \sum_{k=0}^{N-1} \left[w_{k,r} \left(\Phi'(\omega_k, p) - Z'(\omega_k) \right)^2 + w_{k,i} \left(\Phi''(\omega_k, p) - Z''(\omega_k) \right)^2 \right] \qquad (2.7)$$

where $\Phi(\omega_k, p)$ is the model fit function, $p = (R_1, Q_1, \ldots, R_n, Q_n)$ is the parameters vector, Z_1 and Z_2 are the real and imaginary parts of the measured impedance. $w_{k,r}$ and $w_{k,I}$ are the weighting factors of the k-th point and they are all set to 1 if there is no mentionable change in the absolute error over the frequency range of the measurement. A measurement of the goodness of the fit is often given by Chi-Squared test. Chi-squared, which is similar to the sum of square quantities, is defined as [4]:

$$\chi^2 \equiv \sum_{i=1}^{2N} \left\{ \frac{1}{\sigma^2} [y_i - y(x_i)]^2 \right\} \qquad (2.8)$$

where σ^2 is the variance (calculated between the values from the fitting and the actual measurements), y_i for $0<i<N$ is the real part of the measurements, $y(x_i)$ is the real part of the fitted circuit, y_i for $N<i<2N$ is the imaginary part of the measurements and $y(x_i)$ for $N<i<2N$ is the imaginary part of the fitted circuit. In general, the less is this sum, the better is the fitting.

The software which is used in this study to fit circuits, ZView from Scribner Associates, implements the Non-linear least squares method as a fitting algorithm and this test as a check and considers a value of χ^2 of E-3 already acceptable [5]. However, by experience in this study it is found that with small resistances χ^2 values of E-4, E-5 are required for a good fitting.

2.3 Correspondence between impedance spectra and polarization curves

EIS is a powerful tool since it makes it possible to distinguish the contributions of different processes on the polarization of the cell, even when they are overlapped. But performing EIS measurements is complicated and interpreting the results is even more challenging. Moreover, they represent the situation just for a single operation point at time, being it at OCV or at a chosen polarization. A steady indication of the characteristics with respect to the current is given. For all these reasons most time the fastest and easiest way to characterize the cell is getting the I-V curve. It is indeed believed that the best way to study the cell's performance is to perform both the measurements. Impedance spectra and polarization curves are linked to one another, since polarization resistance at one current value is the tangent to the polarization curve at that current value. In fact, the polarization resistance is the AC impedance recorded with EIS when frequency approaches to zero, that is, where only ohmic components are sensed [1]. It is the low frequency limit of the spectrum, including the electrolyte (also called "series") resistance and the polarization (activation plus concentration) resistance of the cell. On the impedance spectrum the contributions are clearly divided, on the I-V curve they are only displayed as one potential drop from the reversible potential.

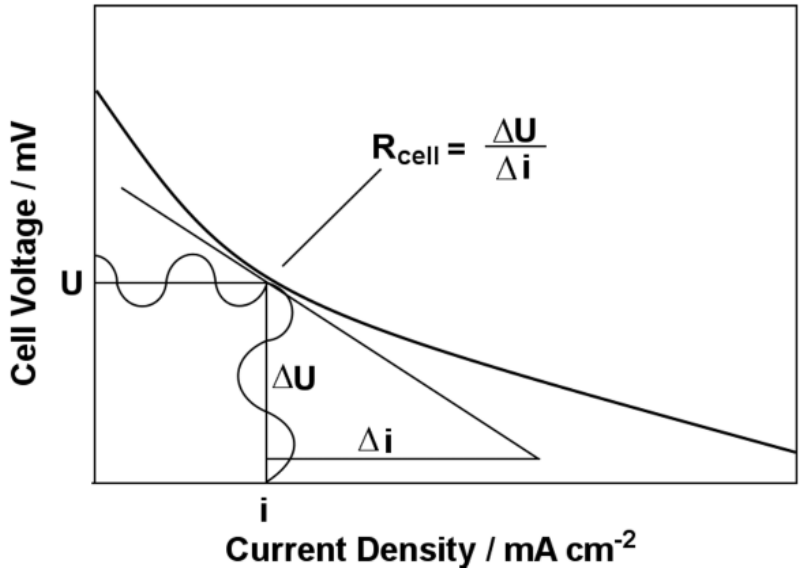

Figure 2.5. Relation between the I-V curve and and the polarization resistance.

Hence, it can be said that EIS measurements at OCV provide a first indication of what the processes and their relative weights are at certain boundary conditions, but they don't correspond to any working condition of the cell. Real operation will have to be investigated adding a bias to the signal of the frequency analyzer once processes are qualitatively known with measurements at OCV.

In the following sections a description of the main components of a typical impedance spectrum of a SOFC anode and the corresponding physical processes is given.

2.4 Series resistance

It appears as the high frequency intercept of the Nyquist plot on the real axis. It takes into account the internal resistance of the electrolyte, of the conducting wires and the contact resistance of the current collectors. In SOFCs the electrolyte resistance dominates over these other phenomena [24], especially over the electrode internal resistance. It has high dependence on the temperature, being smaller at higher temperatures. For this reason when the electrolyte is a solid oxide it needs to work at high temperatures to conduct properly (600 to 1000 °C).

This resistance is so called because it is in series with all the other processes and if the total anodic polarization is to be evaluated the value of the series resistance just needs to be subtracted to the real part of the impedance.

2.5 Kinetic control

Kinetics is fast in a SOFC electrode, being the operating temperatures high, so it becomes a limitation only under a high frequency impulse, where high means up above thousands of Hz. The first element which accounts for kinetic limitations is the charge transfer resistance R_{ct}, which represents the resistance to the transfer of electrons from the electrode surface to the adsorbed species on the electrolyte or from the adsorbed species to the electrode. The value of this resistance falls down under polarization, which means that it is related to the overpotential [1]. In fact, from thermodynamic considerations the expression of the current is derived, as a function of the exchange current density and the overpotential (as was shown in the first chapter):

$$i = i_0 \frac{n_\alpha F \eta}{RT} \tag{2.9}$$

where i_0 is the exchange current density, F the Faraday constant, η the overpotential, R the gas constant, T the temperature, n_α the number of electrons exchanged in the reaction.

From Ohm's law potential is related to the current through resistance, so the charge transfer resistance is defined as:

$$R_{ct} = \frac{RT}{n_\alpha F i_0} \tag{2.10}$$

The bigger is the overpotential, the smaller is the resistance, at a constant current.

As explained, this resistance arises whenever two materials through which current is passing are in contact, like the electrode and the electrolyte [6]. This is not the only process occurring. The first model for the electric double layer forming at the interface between the electrode and the electrolyte is due to Helmoltz in the 19th century [7]. The interactions between the ions in solution and the electrode are electrostatic and, as the electrode holds a charge on its

surface, redistribution of the ions in the electrolyte close to the interface occurs. This way the interface stays electrically neutral. A sort of electrical double layer forms in that region and it is well represented by a capacitance C. In an ideally polarizable electrode the resistance and the capacitance are in series and at the DC limit of the impulse no current can pass. However real electrodes are reactive systems, where the two processes happen to be in parallel and current passes anyway [6]. The simplest circuit representing a cell can now be introduced, only accounting for the ohmic part and the kinetics, the Randles cell. Here the equivalent circuit and the Nyquist plot follow, together with the mathematical model of the circuit.

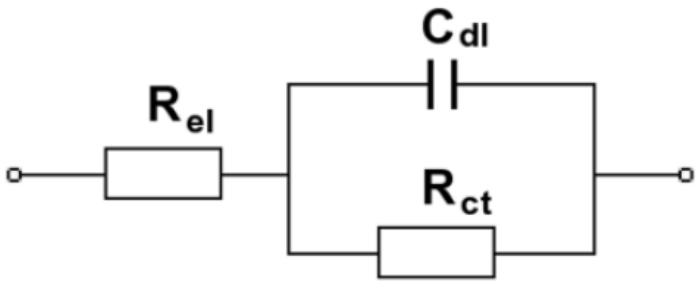

Figure 2.6. Randles cell circuit.

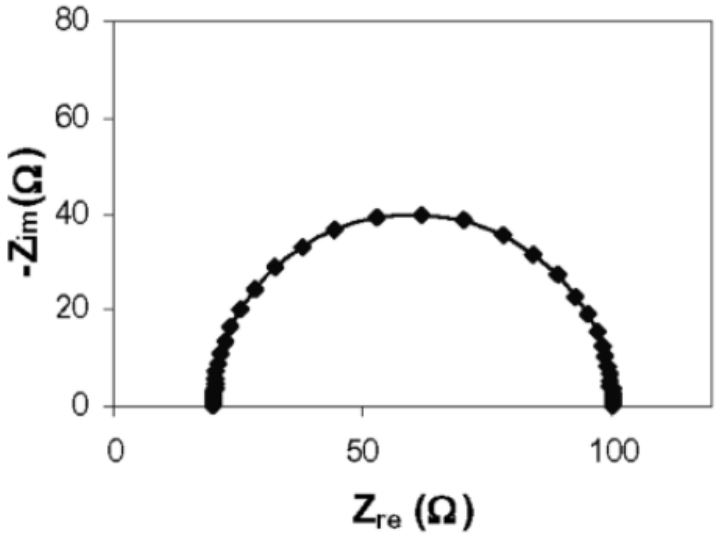

Figure 2.7. Nyquist plot of a Randles cell circuit.

From this circuit it can be clearly seen that there are a high frequency intercept (left), which represents the series resistance R_s and a low frequency intercept. At low frequency the capacitance becomes infinite, hence all the current passes through R_s and R_{ct}. Thus the low frequency intercept represents the sum of these two. From a DC point of view, it is the slope of the I-V curve at the chosen potential, as was anticipated.

With the following calculations it is intended to show how such a circuit can show up as a semicircle on the complex plane. If R_s is not taken into account (it only shifts the semicircle to the right, being entirely real), the impedance of the parallel of R_{ct} and C_{dl} is:

$$Z(\omega) = \frac{1}{R^{-1} + i\omega C} = \frac{R}{1 + i\omega RC} = \frac{R(1 - i\omega\tau)}{(1 + i\omega\tau)(1 - i\omega\tau)} \tag{2.11}$$

$$Z(\omega) = \frac{R}{1 + \omega^2\tau^2} - i\frac{\omega R\tau}{1 + \omega^2\tau^2} \tag{2.12}$$

Where this time R is the charge transfer resistance, ω is the angular velocity, τ = R*C is the time constant. The imaginary part is maximum at the summit frequency ω_{max}. To sum up, the parallel between the resistance and the capacitance represents one single process with its own time constant and it is displayed on the Nyquist plot as one single arc. In the Nyquist plot ideally as many arcs show up on the impedance spectrum as the number of processes actually occurring. Elimination of ω in the equations above leads to another form, where it is clear that the plot of Z_{im} over Z_{re} gives a semicircle with the origin as the high frequency intercept:

$$\left(Z_{re} - R_s - \frac{R_{ct}}{2}\right)^2 + Z_{im}^2 = \left(\frac{R_{ct}}{2}\right)^2 \tag{2.13}$$

$\frac{R_{ct}}{2}$ is the radius of the semicircle and $\frac{1}{R_{ct}C_{dl}}$ is the summit frequency of the process.

The rough surface of the interface between the electrode and the electrolyte and the not entirely homogeneous properties of the employed materials often may end in an uneven charge distribution, mostly of the electric double layer. This was found to be the cause for the semicircle to be depressed. The depression

analytically results from a semicircle rotation in the complex plane [1]. It can be modeled by an additional frequency dependent resistance in the parallel circuit:

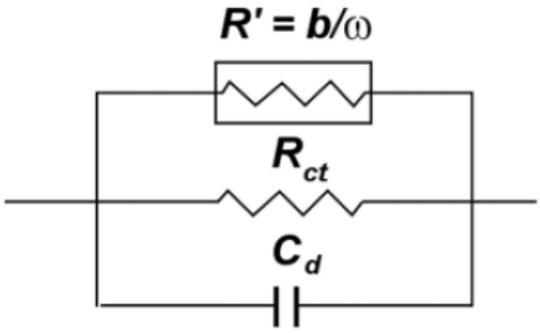

Figure 2.8. Equivalent circuit of a depressed semicircle.

The resolution of the circuit leads to a new expression for the semicircle on the complex plane, where a phase arises compared to the former semicircle and the radius increases, so that the low frequency intercept is the same:

$$\left(Z_{re} - \frac{R_{ct}}{2}\right)^2 + \left(Z_{im} + \frac{R_{ct}}{2bC_d}\right)^2 = \left[\frac{R_{ct}}{2}\sqrt{1 + \left(\frac{1}{bC_d}\right)^2}\right]^2 \qquad (2.14)$$

One way to simplify this result is to introduce a so called constant phase element, CPE, which in the former parallel circuit takes the place of C_{dl}. Its impedance is given by

$$Z_{CPE}(\omega) = q^{-1}(i\omega)^{-n} \qquad (2.15)$$

where q is a proportional factor (which takes the place of C), while n (in the figure "P") gives the depression of the arc. With lowering n the arc is more and more depressed.

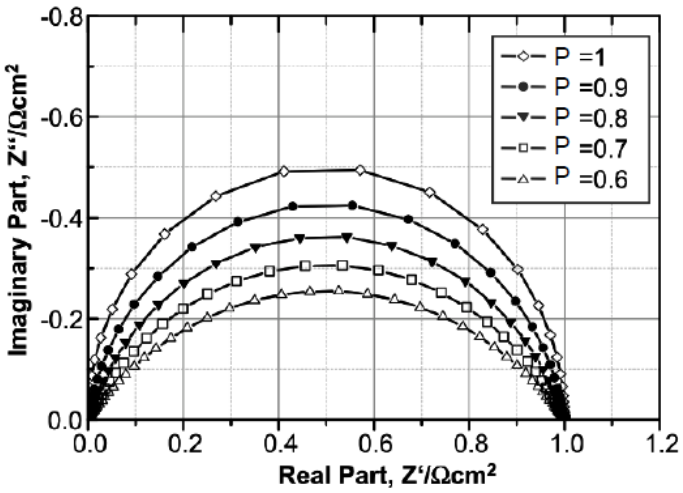

Figure 2.9. Semicircle depression as a function of n.

n = 1, 0, -1 respectively corresponds to a perfect capacitance, resistance, inductance. For 0<n<1 the same semicircle lowers. n = 0.5 gives a Warburg element, which will be explained in the following section.

2.6 Mixed kinetic and diffusion control

Reactions are believed to take place within 10 μm from the electrolyte [25], within the functional layer, and in the vicinity of the triple-phase boundary region (TPB), where gas in the pores, electrode material and electrolyte material meet. The TPB region can be more or less extended depending on the anode to be mixed conducting or not. Either case, diffusion of gas, ions, charged species into the anode plays a key role in the hydrogen oxidation process, being it more important when the cells are anode supported, because the diffusion path into the porous structure is longer. The electrodes employed in this study are porous. Normally porous electrodes are made up of two main layers [10], a substrate, with a coarser structure to enhance gas diffusion to the reaction sites, and a functional layer, with a finer structure, to increase the TPB length and thus enhance the reaction kinetics.

Also diffusion above the anode surface must be considered, whatever the experimental setup employed. If the flow is perpendicular to the surface and ceramic gas diffusers are placed on both sides of the cell, it is demonstrated that

a stagnant gas layer forms over the anode, which is controlled by diffusion only [8]. If the flow is parallel to the surface, in order to avoid the stagnant gas layer as much as possible [9], a diffusion limitation will be present at any case, but this time the thickness of the layer is also controlled by convection.

At the operating temperatures of SOFCs, the anodes are kinetically highly performing, so that there's a minor relative weight of the kinetic part of the process than in the low temperature cells.

From all these considerations it is concluded that the Randles cell model, which is useful to easily understand the theory of equivalent circuits, is not enough to properly describe the physics of the cell. Some element which describes the different possible forms of diffusion over or into the anode must be added. In the circuit an element accounting for diffusion must be added, resulting in the following:

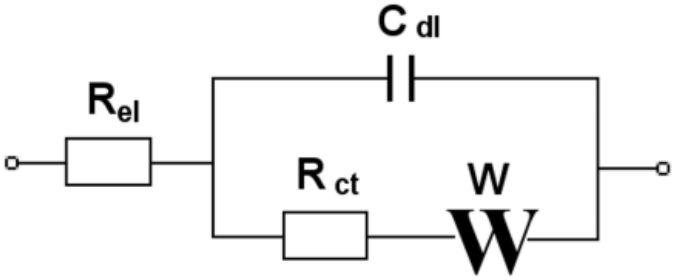

Figure 2.10. Equivalent circuit for mixed kinetic and diffusion control.

"W" is the Warburg element (it will be explained next), which accounts for diffusion. It consists in a real and an imaginary part, it is an impedance. The ensemble of R_{ct} and W is called Faradaic impedance and it is frequency dependent, being not a simple resistance.

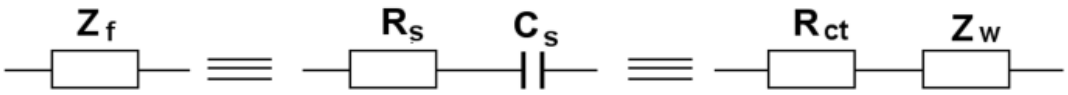

Here a mathematical model of a cell with mixed diffusion and kinetic control is presented as studied elsewhere [1], starting from practical considerations.

If the Faradaic impedance of a planar electrode is expressed as the series between a real part R_s and a pure capacitance C_s and a sinusoidal current

$$I = I_m \sin(\omega t) \tag{2.16}$$

is applied to the cell, a voltage drop will occur, being the expression

$$V_f = IR_s + \frac{q}{C_s} \tag{2.17}$$

By differentiation of the potential, the equation becomes

$$\frac{dV_f}{dt} = (R_s I_m \omega)\cos(\omega t) + \frac{I_m}{C_s}\sin(\omega t) \tag{2.18}$$

In the electrode a charge transfer reaction takes place, as explained, so that an equilibrium potential is present, to which a potential due to the sinusoidal perturbation adds.

$$\varphi = \varphi_e + V_f \tag{2.20}$$

Hence the total potential is a function of the applied current and of the concentrations of the oxidant and reductant over the electrode surface.

$$\frac{d\varphi}{dt} = \left(\frac{\partial\varphi}{\partial I}\right)\frac{dI}{dt} + \left[\frac{\partial\varphi}{\partial C_0(0,t)}\right]\frac{dC_0(0,t)}{dt} + \left[\frac{\partial\varphi}{\partial C(0,t)}\right]\frac{dC_R(0,t)}{dt} \tag{2.21}$$

where C_O and C_R are the concentrations of the oxidant and the reductant in the anode. Being the equilibrium potential constant over time, the differential can be written as

$$\frac{dV_f}{dt} = R_{ct}\frac{dI}{dt} + \beta_o\frac{dC_o(0,t)}{dt} + \beta_R\frac{dC_R(0,t)}{dt} \tag{2.22}$$

where

$$R_{ct} = \left[\frac{\partial V_f}{\partial I}\right]_{C_o(0,t)C_R(0,t)} \tag{2.23}$$

$$\beta_o = \left[\frac{\partial V_f}{\partial C_o(0,t)}\right]_{I,C_R(0,t)} \tag{2.24}$$

$$\beta_R = \left[\frac{\partial V_f}{\partial C_R(0,t)}\right]_{I,C_o(0,t)} \tag{2.25}$$

In order to obtain the differential of the sinusoidal potential, these three values and the three derivatives above must be found. For the derivatives of the concentration one only needs to take into account the diffusion coefficients and some initial conditions, then they are related with some passages to known parameters. At the same time R_{ct} is easily related to the kinetics of the cell, as already shown, and β_0 and β_r to the surface concentrations of the species.

$$R_{ct} = \frac{RT}{nF\,i_0} \qquad \beta_0 = \frac{RT}{nF\,C_0^*} \qquad \beta_R = \frac{RT}{nF\,C_R^*}$$

This way a final expression for the voltage is found:

$$\frac{dV_f}{dt} = \left(R_{ct} + \frac{\sigma}{\sqrt{\omega}}\right) I_m \omega \cos(\omega t) + I_m \sigma \sqrt{\omega} \sin(\omega t) \tag{2.26}$$

Where

$$\sigma = \frac{1}{nFA\sqrt{2}}\left(\frac{\beta_o}{\sqrt{D_o}} - \frac{\beta_R}{\sqrt{D_R}}\right) \tag{2.27}$$

In equation (2.26) the real and imaginary part are clearly divided, so that R_s results as the sum of R_{ct} and $\frac{\sigma}{\sqrt{\omega}}$ while C_s is $\frac{1}{\sigma\sqrt{\omega}}$. The total faradaic impedance is:

$$Z_f = R_{ct} + \frac{\sigma}{\sqrt{\omega}} - j\frac{\sigma}{\sqrt{\omega}} \tag{2.28}$$

where the sum of the last two terms, one real and one imaginary, gives the Warburg impedance. It can be noted that R_{ct} depends on i_0, so on the kinetics of the cell, while the Warburg impedance depends on the kind of reaction, on the surface concentrations of the species, on the diffusion coefficients and on the frequency. From the expression of the Warburg impedance it is now clear why a CPE with n = 0.5 represents a Warburg element. It can be inferred that an

equivalent element fitted by a CPE with an exponent close to 0.5 will be most probably related to diffusion.

Now it is useful to investigate a little more in depth what the behavior of a Warburg element is on the Nyquist plot.

When an equivalent circuit as the one displayed above is considered, the total impedance is written as:

$$Z = R_{el} + \frac{1}{\left(\frac{1}{Z_f}\right) + j\omega C_d} \tag{2.29}$$

With some algebraic passages the real and imaginary parts of the impedance are expressed as functions of the parameters of the circuit:

$$Z_{re} = R_{el} + \frac{R_{ct} + \sigma/\sqrt{\omega}}{(C_d\sigma\sqrt{\omega} + 1)^2 + \omega^2 C_d^2 (R_{ct} + \frac{\sigma}{\sqrt{\omega}})^2} \tag{2.39}$$

$$Z_{im} = \frac{\omega C_d (R_{ct} + \frac{\sigma}{\sqrt{\omega}})^2 + \sigma/\sqrt{\omega}(\sqrt{\omega} C_d \sigma + 1)}{(C_d\sigma\sqrt{\omega} + 1)^2 + \omega^2 C_d^2 (R_{ct} + \frac{\sigma}{\sqrt{\omega}})^2} \tag{2.40}$$

The high frequency limit of these equations ($\omega \to \infty$) leads to the expression of the semicircle presented above. In fact in this circuit the high frequency part of the spectrum is still a semicircle. However at very low frequencies ($\omega \to 0$) the behavior is different. The real and imaginary impedance are simplified as:

$$Z_{re} = R_{el} + R_{ct} + \frac{\sigma}{\sqrt{\omega}} \tag{2.41}$$

$$Z_{im} = \frac{\sigma}{\sqrt{\omega}} + 2C_d\sigma^2 \tag{2.42}$$

With elimination of the frequency the imaginary part as a function of the real part (Nyquist representation) is found:

$$Z_{im} = Z_{re} - R_{el} - R_{ct} + 2C_d\sigma^2 \tag{2.43}$$

The dependency is linear, with a unitary slope. Its intersect is given by the three last terms of the equation. Both Z_{im} and Z_{re} depend on the square root of the frequency, so the Nyquist plot of this impedance with varying frequency is a straight line with 45° slope. The overall plot is ideally the following:

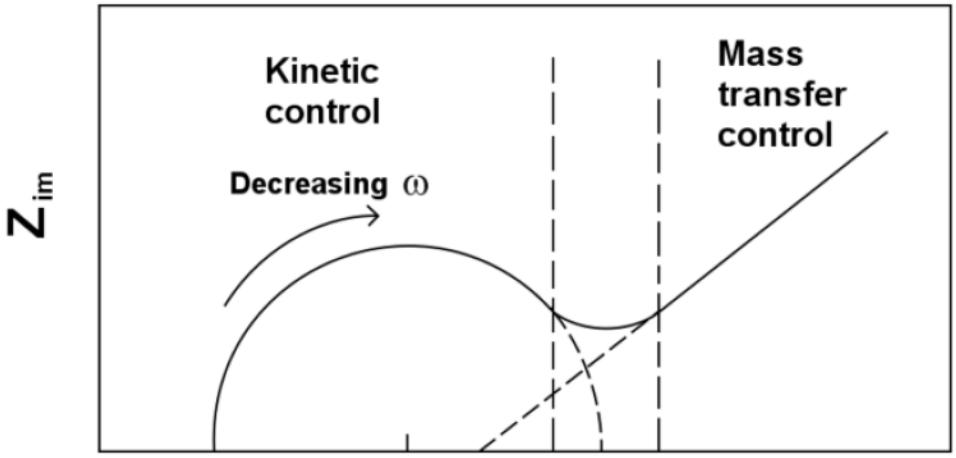

Figure 2.11. Ideal Nyquist plot for mixed kinetic and diffusion control.

Besides the mathematical representation of the model, an intuitive explanation of what happens and how kinetic and mass transfer controls are important in different frequency ranges is also useful. Kinetics is fast in SOFCs, so at low frequencies it is not sensed as a limitation. On the contrary, when impedance measurements are performed, at high frequencies the drawn current varies rapidly and, since it is the driving force for the reactions to take place, they must follow at the same rate. As a consequence a charge transfer resistance arises, while mass transfer limitations are not identified because the concentrations of the species in space keep constant (they don't have time to vary). At low frequency kinetics is much faster than the imposed variation, so it is not a limitation. On the other hand concentration has more time to vary, under varying driving force and it is sensed as impedance. Moreover, the behavior of the low frequency part is different depending on the thickness of the diffusion layer. If it is thick, it behaves as semi-infinite means, as the concentration wave (due to the sinusoidal current) doesn't penetrate it all. The low frequency process is in this

case pure diffusion and it shows up as a straight, 45° inclined line. The feature appearing on the Nyquist plot is the so called infinite length Warburg element. It is represented, as already anticipated, by a CPE with n = 0.5 and $q = \frac{{l_d}^2}{D_{eff}}$, where l_d is the actual diffusion length and D_{eff} is the effective diffusion coefficient of the gas. If on the contrary the layer is thin, the concentration wave has time to penetrate the whole means and every limitation at the far end of the layer is sensed. In this case a finite length Warburg element will be featured. Since this element is most times present in the equivalent circuit of a cell it is useful to describe how its impedance is modeled:

$$Z_{G-FLW}(\omega) = R_d \left\{ \frac{\tanh(\sqrt[P]{i\omega T})}{\sqrt[P]{i\omega T}} \right\} \tag{2.44}$$

The diffusion resistance Rd is the ω→0 limit of the Warburg impedance [6]. When a finite resistance is present at the far end, like in the interface between a metal and an oxide, current passes and a transmissive boundary condition occurs. The diffusion line then bounds towards the real axis and ends with a pure resistance. This happens especially at low inflow rates, because the variations of hydrogen partial pressure strongly increase in their amplitude and penetration into the gas chamber. The expression of the impedance can be simplified as:

$$Z_{wtr} = R_d \left\{ \frac{\tanh(\sqrt{iT})}{\sqrt{iT}} \right\} \tag{2.45}$$

When the diffusion wave encounters a big impedance instead ($Z \to \infty$), a reflective boundary condition takes place and the diffusion line on the Nyquist plot bounds up to big imaginary values, as if an ideal capacitor blocking DC current was present. This feature often appears with conducting polymers and porous electrodes.

$$Z_{wr} = \left(\frac{1}{\omega T C_d}\right) \left\{ \frac{Cotnh(\sqrt{iT})}{\sqrt{iT}} \right\} \tag{2.46}$$

In both cases the higher frequency shoulder of the diffusion line is present and it is present both at high and low inflow rates.

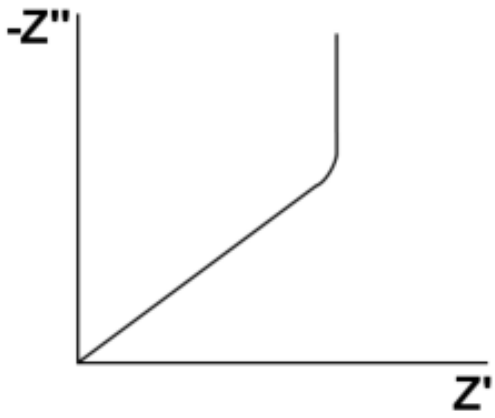

Figure 2.12. Reflective boundary condition.

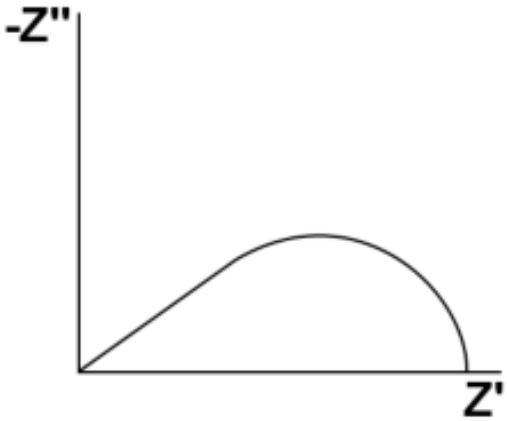

Figure 2.13. Transmissive boundary condition.

In conclusion of this section, a brief discussion of the relationship between the modelling of diffusion in the EIS theory and in thermodynamics (polarization curves) is useful to make a complete overview of the phenomena. A more in depth analysis will be given in the following sections when describing the results of the most important studies of SOFCs with impedance spectroscopy.

Basically diffusion in a cell follows two different mechanisms, the first being diffusion of ions or molecules inside the structure of the anode, the second diffusion over the anode surface and into the gas chamber from the feed channel [9]. Both these processes are identified in experiments [9, 11], but each can be relevant or not depending on the employed setup. The so called concentration

polarization [11], is made up of two contributions, gas conversion and gas diffusion. The first takes into account the apparent resistance which arises from the fuel partial pressure in the gas flow channel over the anode not being constant due to the finite flow rate (this happens because the fuel reacts along the channel; if the flow rate was infinite, concentration would be constant). However it has been demonstrated that it won't be present in setups with symmetrical cells in a single gas atmosphere [11]. The second comes from the gradient of concentration due to diffusion in the stagnant gas layer over the anode and/or in the porous material to the electrode/electrolyte interface [20]. Whenever they are sizeable, the arcs coming from these processes can be modelled with different equivalent circuits, not only with the Warburg element, showing how the common practice is more complicated than the theory. Primadhl et al. [11] and Aravind [12] found that, using an experimental asset similar to the one which was employed in this study, one of the arcs in the impedance spectrum is due to diffusion over the anode. A stagnant gas layer forms, in which movement of the molecules towards the surface is driven almost only by a concentration gradient. As equivalent circuit elements Primdahl used an R-CPE circuit, while Aravind used a Warburg element and this confirms what above. But in order to study the dependency of the resistances on the gas pressures they derived a model from thermodynamics and this was the same in both cases. It comes from different considerations than the ones which led to the expression of the Warburg element (showed above), but the conclusions are exactly the same, the physics behind the phenomena is the same. Both the Warburg element and the R-CPE circuit for diffusion modelling have theory of molecular diffusion as a basis. It gives an expression for the diffusion overpotential, which is directly related to the resistance of the impedance spectroscopy:

$$R_D = \frac{\eta_D}{i} = \left(\frac{RT}{2F}\right)^2 \frac{l}{PD_{eff}} \left(\frac{1}{X_{H_2,B}} + \frac{1}{X_{H_2O,B}}\right) \tag{2.47}$$

where η_D is the diffusion overpotential, $X_{j,B}$ the molar fractions of the j species in the bulk gas, D_{eff} the effective binary diffusion coefficient for H_2-H_2O mixtures. This model holds well for binary gas mixtures [8], though results vary according to the equation which is chosen for calculation of D_{eff} (Primdahl used Fuller correlation). Aravind suggests a more accurate model [12], accounting for multi-component gas mixtures, so new diffusion coefficients are taken from Stephan-Maxwell approach for multi-component gas diffusion. This way more

than one diffusion coefficient is accounted for in the equation and diffusion of every component into the mixture becomes dependent on the concentration of the other ones. Showing how the result comes out from the initial thermodynamic considerations is out of the scope of the present section and we refer to Aravind's work for this [8]. Anyway the outcome is alike the former one but more refined and more suitable for the present case study:

$$\eta_D = 2\left(\frac{RT}{2F}\right)^2 \frac{l}{P}\left(\frac{1}{D_{H_2O-Mix} X_{H_2O,B}} + \frac{1}{D_{H_2-Mix} X_{H_2,B}}\right) I \qquad (2.48)$$

These formulas were both derived for the stagnant gas layer but, as Primdahl shows, they can also be used for diffusion into the porous anode, with corrections for the diffusion coefficients: Knudsen diffusion takes place in the substrate. What conclusions these considerations lead to will be discussed in the following sections.

2.7 Other circuit elements

It was already stated that the basic equivalent element is the RC or RQ circuit, of which an intuitive explanation was given for the charge transfer process. However many other elements in the real system can affect the impedance spectrum and many times a capacitance or inductance in series with the whole circuit can appear. The impedance of a capacitor is expressed by

$$Z = \frac{1}{i\omega C} \qquad (2.49)$$

It only consists of imaginary part and this varies with frequency. If the capacitor is in series with a resistor its Nyquist plot behaves like a blocking circuit.

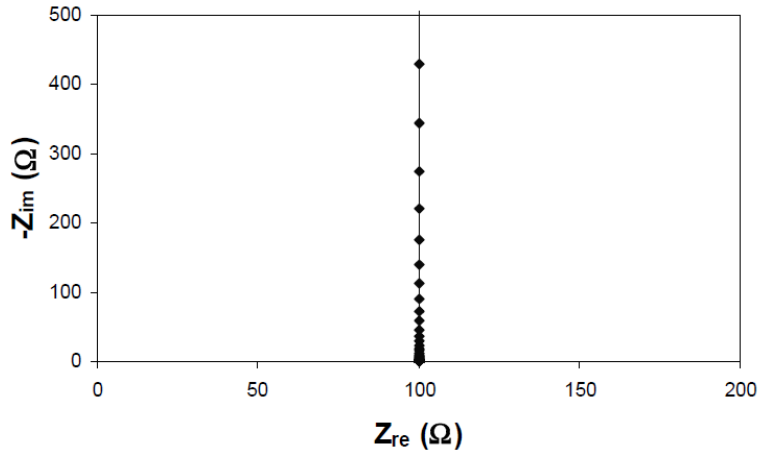

Figure 2.14. Nyquist plot of a capacitor in series with a resistance.

The feature is the same for a series of a resistor and an inductor, but with the vertical line reversed in the positive imaginary half-plane.

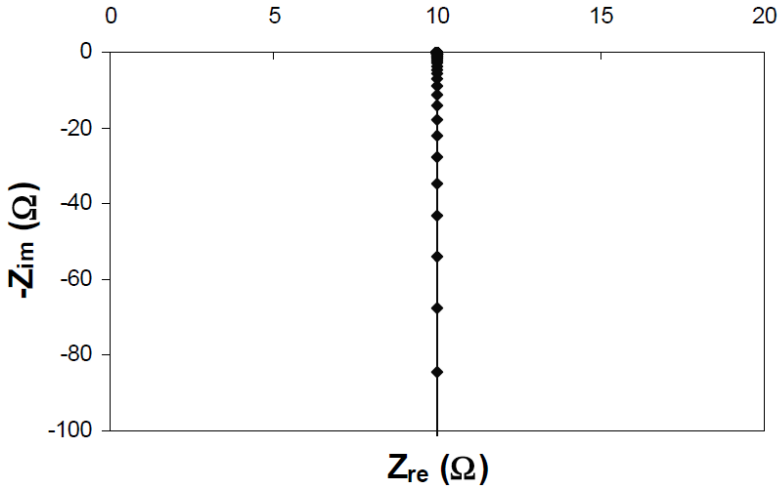

Figure 2.15. Nyquist plot of an inductor in series with a resistance.

Features like these often appear in series with other circuit elements mostly due to the characteristics of the circuits. The wires from the cell to the impedance station can typically cause an inductive line at very high frequency, which rapidly goes to zero with lowering frequency and lets the arcs of the electrode impedance show up. A capacitor associated with high frequencies instead of an

inductor is not expected and it could mean that there's a loosened contact in some part of the circuit.

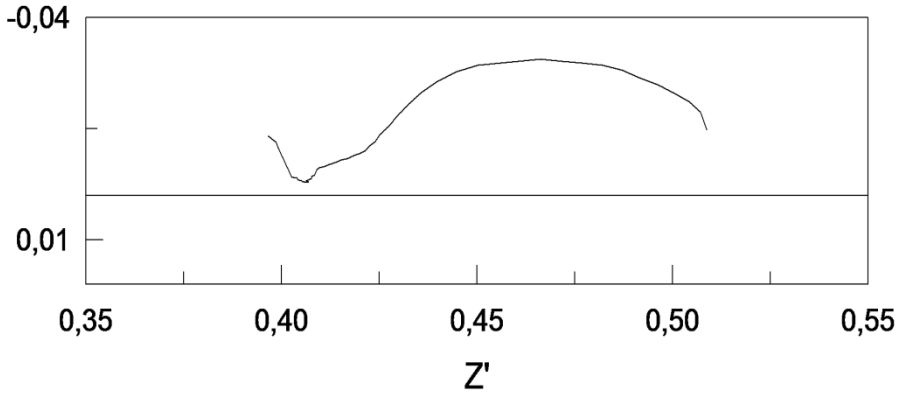

Figure 2.16. Nyquist plot from the experiments, with influence at high frequency.

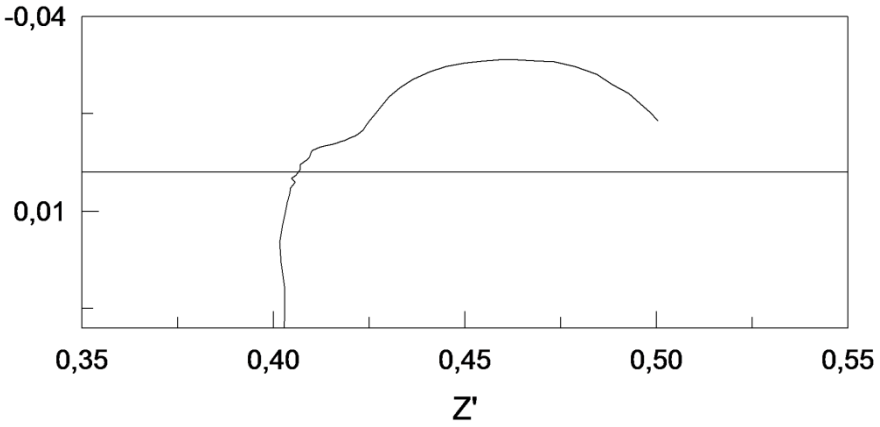

Figure 2.17. Nyquist plot from the experiments, with expected high frequency.

Many more structures can appear in the spectra depending on the equipments and the tested cells. Also at low frequencies inductance may have effects, showing inductive loops. Eventually, it is intended to present one more structure, which is usually employed in cathode circuits fitting, but it may also appear in anode analysis since it is similar to the Warburg element. Several studies are available about cathode performance and it is generally agreed that its impedance in SOFCs is dominated by surface exchange of O_2 and oxygen

ions solid state diffusion. The commonly used fitting element is the Gerischer impedance [3].

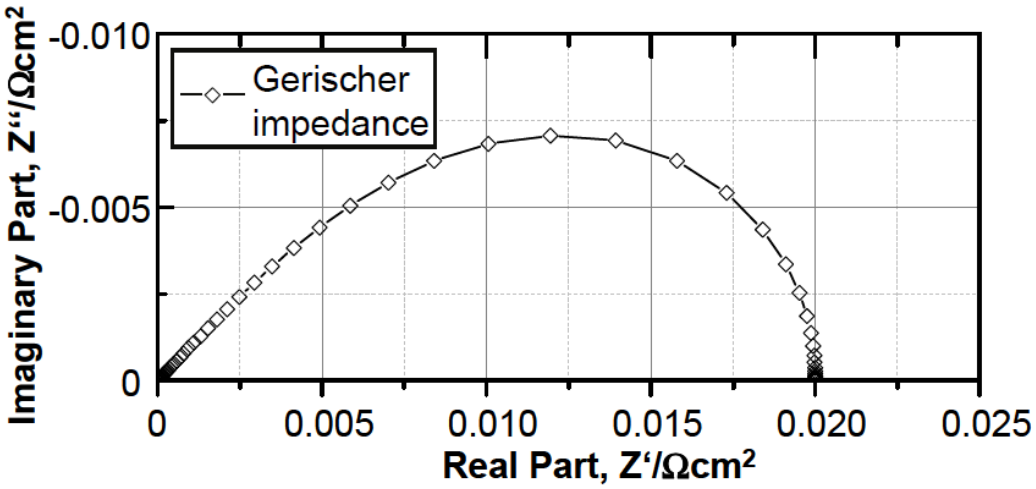

Figure 2.18. Nyquist plot of a Gerischer element.

2.8 Interpretation of the spectrum

The spectrum of a symmetric fuel cell, like the ones which will be used in this study, is made up of different contributions, then of different arcs. The spectrum of a complete cell can show even five processes [3]. Hence, for fitting such impedance spectra, equivalent circuits with many processes in series are required. Voigt's structure is usually employed as a model for SOFCs [1]. It consists in a series of R-C circuits, which should look like following.

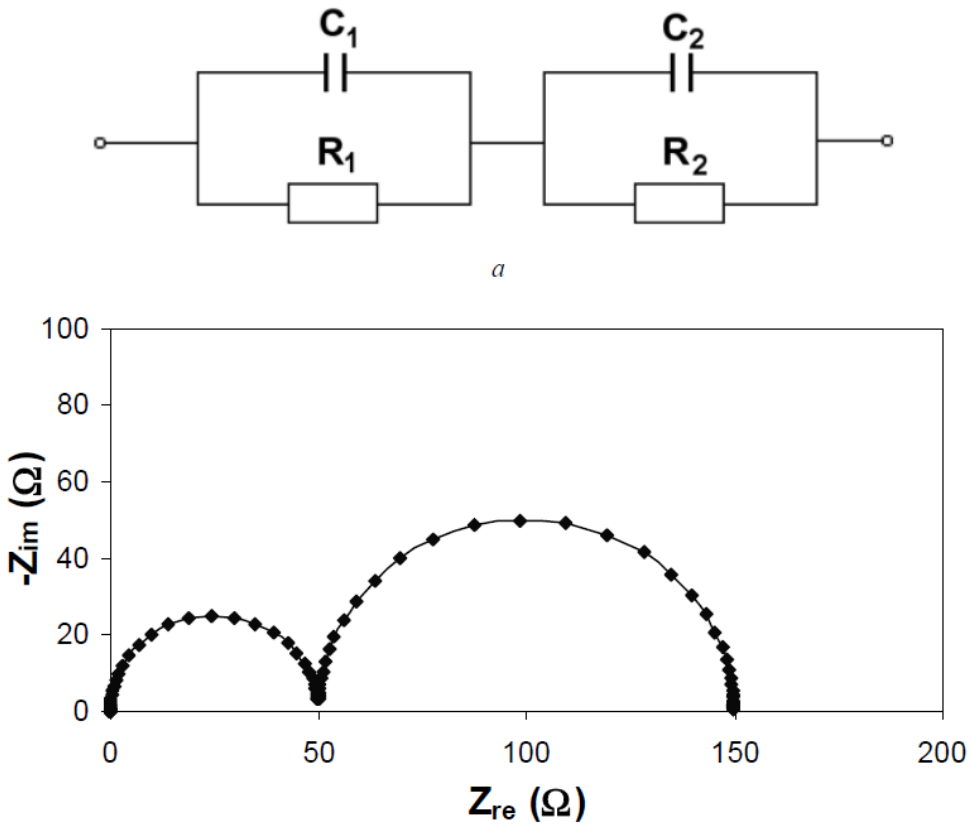

Figure 2.19. Equivalent circuit and Nyquist plot of two processes in series.

In this case, it is characterized by two time constants. The arcs usually don't look so defined, this depending on the ratio between the capacitors. For this reason in many cases it is difficult to properly identify all the processes.

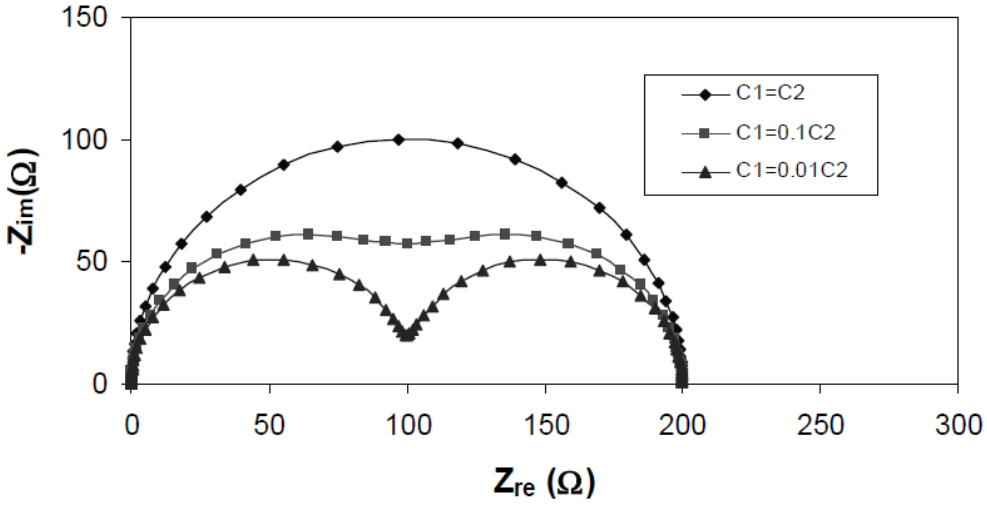

Figure 2.20. Change in shape with change of the ratio between capacitances.

2.9 Experimental background of SOFC impedance spectroscopy

As explained in the introduction of this chapter, the spectra obtained with impedance spectroscopy are extremely sensitive to the setup and its imperfections. Research in the field is not uniform yet, so that the experiments aren't carried under standardized conditions. Thus, it is still difficult to compare the results from different studies, even as for the shape of the spectra. In the setup used for the present study the gas diffusers are below and above the cell, so the flow doesn't hit directly the cell, but it has to go through the channel. This is done only through diffusion, because on one hand there is not convection but on the other hand there can't be void in the anode chamber. It is then expected that the low frequency region will be dominated by diffusion in this setup, while the high frequency by kinetics as always, being the arc small since the electrodes are highly performing. It is commonly expected that with such a setup three arcs appear in the spectrum for anode symmetric cells. However, depending on the arrangements, only two main arcs could also be found.

Here an overview and discussion of the most valuable results in the investigation of the SOFCs physics through impedance spectroscopy follows. Sometimes also considerations under polarization are presented. They just serve as a reference for this study, as it will focus on OCV impedance.

De Boer [13] studies in depth the hydrogen oxidation process at the anode, to get a reaction mechanism for it and consequently its rate limiting steps. This can lead to a structured explanation of the high and mid frequency part of the spectrum. His reference is Norby's results [15], which show two impedance arcs for completely metallic Ni porous anodes. Study on these anodes is useful since their composition is much simpler than the one of mixed conducting anodes and they represent a first step in the investigation of impedance spectra. One of the arcs is due to charge transfer while the low frequency arc seems to be related to adsorption and its diameter decreases with increasing p_{H2O} and increases with increasing p_{H2}. Aaberg [16] proposes a mechanism in which adsorption of H_2 on Ni and its diffusion to YSZ are fast; so protons may accumulate on YSZ surface and formation of water becomes the rate determining step.

Based on these studies De Boer finds a first reaction mechanism for Ni electrodes, which is then verified with experiments. He calculates the reaction constants assuming Langmuir adsorption and he writes the equilibrium current (exchange current density) as a function of these constants, then of the surface coverage θ by different atoms. An exponential dependence of the reaction rate and the exchange current density on p_{H2} and p_{H2O} comes from this all. The proposed mechanism is the following:

$$H_2 + 2s_{electrode} \rightarrow 2H_{ads} \tag{2.50}$$

$$H_{ads} + O_o^x \rightarrow OH_o^* + e + s_{electrode}$$

$$OH_o^* + s_{electrode} \rightarrow OH_{ads}^- + V_o^{**}$$

$$H_{ads} + OH_{ads}^- \rightarrow H_2O_{ads} + e + s_{electrode}$$

$$H_2O_{ads} \rightarrow H_2O_{gas} + s_{electrode}$$

The experimental investigation is made on Ni electrodes placed on Yttria-stabilized Zirconia electrolytes. The employed setup is similar to the one of the present study (see chapter three for details), with two electrodes, a single gas atmosphere and the gas flowing perpendicular to the cell. Cells are studied under both OCV and polarization. The electrochemical characterization is made with 100 ml/min H_2 flow, He as an inert gas, 10 mV signal of the potentiostat in the f range 1 MHz to 0.1 Hz, 850 to 600 °C temperature sweep.

A big single arc is found, overlapping with a smaller one.

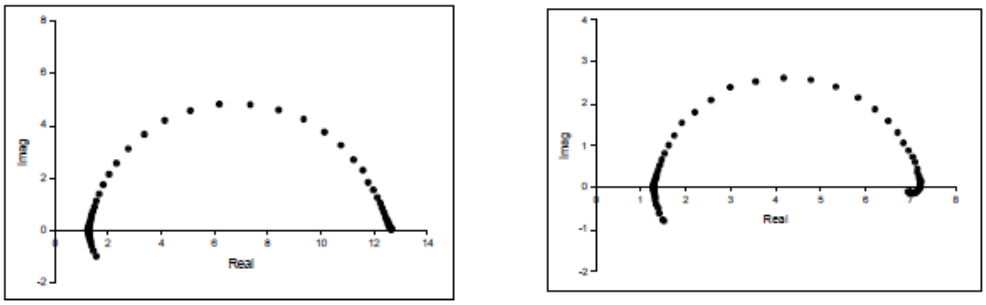

$\eta = 0$ mV $\eta = 83$ mV

Figure 2.21. Nyquist plots from De Boer's study with different polarization.

The fitting circuit accounts for those two arcs (LR-(RQ)1-(RQ)2).

The dominant arc decreases with increasing anodic polarization and this behavior is generally achieved. De Boer claims that this polarization is somehow related to TPB length. Diffusion limitations are in this experience negligible with respect to other processes. Impedance measurements as functions of p_{H2} and p_{H2O} are taken to validate the proposed model. As for the first arc no dependence is found with H_2, a little with H_2O; as for the second arc the resistance increases with increasing p_{H2}, decreases with increasing p_{H2O}.

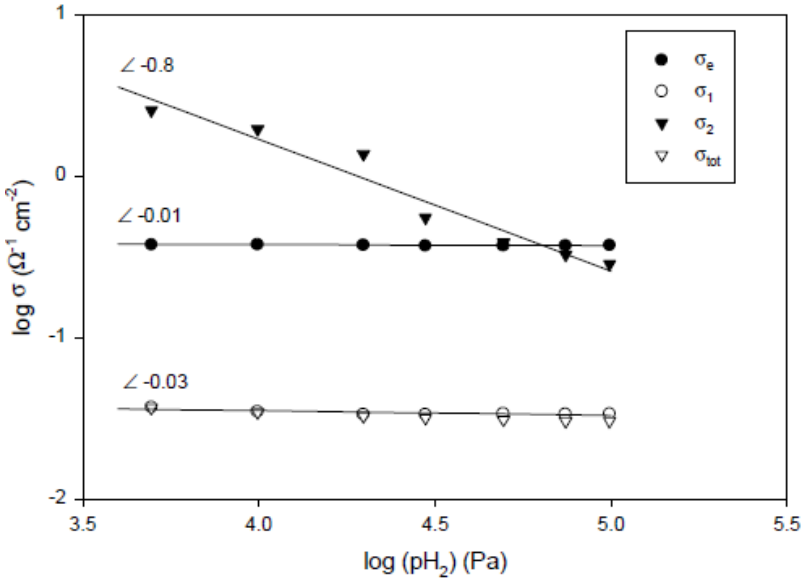

Figure 2.22. Dependency of the conductivities on p_{H2}.

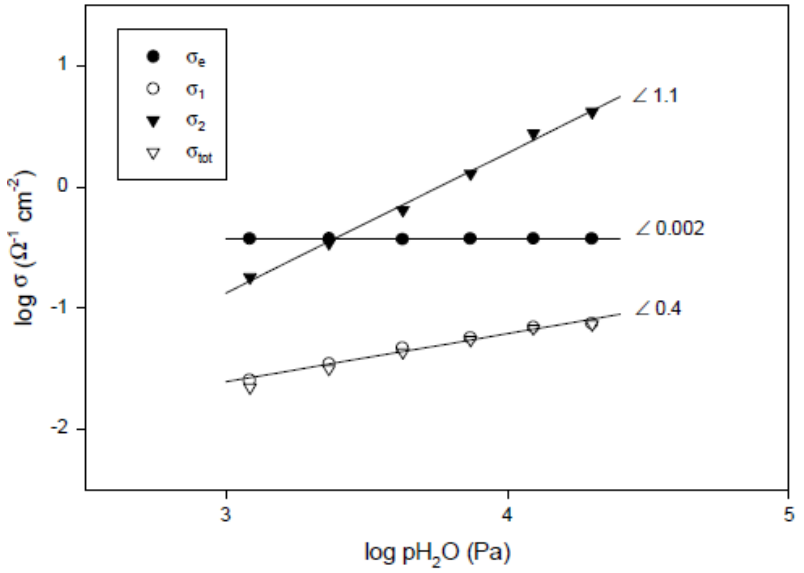

Figure 2.23. Dependency of the conductivities on p_{H2O}.

Here σ_i are the conductivities and they are calculated as $\sigma_i = \frac{1}{AR_i}$, where A is the surface of the working electrode and R_i is the resistance of the process as

coming from the fitting. Subscripts e, 1, 2 refer to the electrolyte, the first process, the second process respectively.

A comparison with the results from Norby et al. is made: they found two arcs as well, of which the first one has really similar dependencies on p_{H2O} and TPB length and it is ascribed to charge transfer reaction associated with double layer capacitance. As for the low frequency one Norby relates it to a reaction resistance and associated surface coverage of adsorbed species. Adsorption/desorption/diffusion of water at the anode could be a limiting step in that frequency region. If the conductivities of the first arc are compared to the postulated ones for the different limiting reaction mechanisms it is found that the limiting step could involve OH^- in the Zirconia matrix or at Zirconia surface: the limiting step is thus found to be adsorption of hydroxile ions at the Zirconia surface. From image analysis it is found that the total electrode conductivity decreases with time, that is, with decreasing Ni perimeter (which is somehow related to TPB length). The biggest degrade occurs in the first 30 hours of operation, then the conductivity stabilizes. This will be confirmed elsewhere [10]: pure Ni electrodes and some cermet electrodes show degrade during operation, while for example Ni/GDC electrodes have a pretty more stabile behavior with time.

Hendriksen in 2006 [17] uses both complete cells and anodic symmetric Ni/YSZ cells, in a temperature range which is slightly higher than De Boer's (700-850 °C), Au or Ni meshes as current collectors (instead of Pt, as for De Boer's experiments).

One or two non-diffusion related arcs are found with anodes, of which the main is due to charge transfer processes and is dependent on the microstructure. They appear in the frequency range between 1000 and 10000 Hz. With a full, anode supported, cell one or two arcs are found in the region below 100 Hz, related to gas concentration processes at the anode. Altogether, five processes are identified in a complete cell. Also in this case a drastic degrade of the performance occurs in the long term operation test and the biggest change is shown in the frequency range 1 to 20 kHz (high frequency, microstructure related processes). It is expected, on the basis of what observed by De Boer.

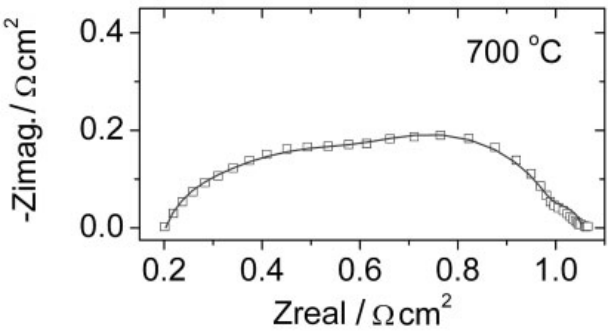

Figure 2.24. Nyquist plot from Hendriksen's study.

In 1999 Primdahl [11] at Risø National Laboratory distinguishes between two main phenomena visible in impedance spectra of high temperature fuel cells.

Two particular setups are employed in Primdahl's experiments: one consists in a three electrodes system with pellet electrolyte, built to make the placement of the reference electrode easier and more precise. The anode and cathode feeds are separated and the pressure is 2 atm. The second consists in two pellets with facing electrodes. For the first setup he found at least three arcs with Ni/YSZ anodes over Pt counter and reference electrodes. The first arc appears at kHz frequency and is sensitive to the anode microstructure, in line with experiments from other authors. It is related to charge transfer processes. The small capacitance of around 10 $\mu F/cm_2$ is ascribed to the electrical double layer between anode and electrolyte material. Its small capacitance makes also the time constant of the process small, so that it appears at high frequency. The third one has a peak at 1 Hz and is ascribed to gas conversion processes. It is not present in the spectrum of the two-pellets setup, so it is concluded that it shouldn't show up in experiments with small samples at 1 atm. Gas conversion processes are associated with variations in the Nernst potential due to passage of current at a finite fuel flow rate, as already explained.

The intermediate frequency arc, between 10 and 100 Hz, is the hardest to interpret: through comparison with more experiments in which an additional Ni felt current collector is placed over the electrode it is concluded that the arc is due to formation of a stagnant gas layer of finite dimension (mm-cm scale) over the anode. This diffusion limitation is well described by the diffusion equation already presented above.

$$R_D = \frac{\eta_D}{i} = \left(\frac{RT}{2F}\right)^2 \frac{l}{PD_{eff}} \left(\frac{1}{X_{H_2,B}} + \frac{1}{X_{H_2O,B}}\right) \quad (2.51)$$

Diffusion into the porous structure of the anode causes in this case a really small resistance (which is calculated with the same equation as above, but using Knudsen diffusion coefficients), in fact it is negligible when the cell is not anode supported (the anodes are thin). Moreover, the time constant places the process around 45 kHz, so that it is concealed by the high frequency arc of the charge transfer process.

In a further study in 2002, Primdahl and Mogensen [14] investigate the impedance dependency on the anode composition, by employing different ceramic and mixed conducting anodes. This time symmetrical cells are tested, in order to focus on the behavior of the anodes, and the setup is studied to minimize gas diffusion and gas conversion limitations.

How the anodes are affected by addition of a small amount of Ni or by feeding with isotopes of Hydrogen is investigated. It is reported that an increase in concentration of Ni in the anode material by few % points lowers much the resistances for fully ceramic anodes (as expected) but also for Ni/GDC anodes, which already contain 40% Ni. This may be ascribed either to an increase of the TPB or more probably to the unsintered contacts between Ni and GDC being free from contaminants or reaction products. Thus, the effect in this latter case must be looked into.

The spectra show two main arcs. The first is due to kinetic limitations but it is not investigated. The low frequency region shows an isotope effect and its magnitude indicates that it could be due to adsorption of H_2 on the mixed ionic and electronic conductor surface and/or to dissociation of H_2 molecules into ions. This may also go along with a surface diffusion limitation of Hydrogen species, but only if adsorption and dissociation of H_2 are limiting as well.

Verbraeken [10] compares the reaction mechanism proposed by De Boer for hydrogen oxidation and the results from Primdahl and Mogensen. According to Langmuir adsorption model:

$$r = k_1(1 - \theta_H)^2 pH_2 - k_{-1}\theta_H^2 \quad (2.52)$$

where θ represents the number of occupied sites of H_2 on the electrode. Its limit at low temperature or high p_{H2} is 1, while at high T or low p_{H2} it is 0. This should result in a clear trend, as resistance R of the process is proportional to 1/r. But Mogensen and Skaarup [23] showed that the assumption of θ close to zero at certain conditions is almost never valid. Even at high temperature, if p_{H2} is high, the surface coverage approaches 1. Moreover, hydrogen adsorption on Ni is a thermally activated process, it should occur more easily at high temperature. Primdahl and Mogensen find almost no dependence of the resistance from p_{H2} and they claim that the rate limiting step is always adsorption/dissociation of H2, as its coverage is close to 1.

The experimental investigation of Verbraeken stems from these considerations and it focuses on the relationship between the microstructure of the anode and the impedance behavior. As an experimental asset, symmetrical cells with thin electrolyte (40 μm) are employed in this study, since it concentrates on the performance of anodes with varying composition and microstructure. OCV measurements are carried out. Both Ni/YSZ and Ni/GDC electrodes are tested, to compare their performance and verify the assumptions made on material science basis. The experiments are carried out in a similar setup to the one of this study, in single atmosphere gas and the spectra are taken as functions of p_{H2}, p_{H2O}, temperature. They are fitted, for the Ni/YSZ anodes, with the following circuit:

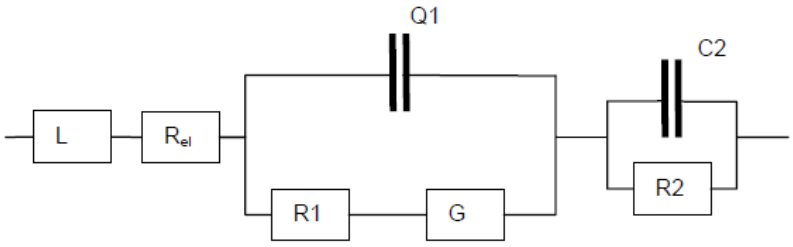

Figure 2.25. Equivalent circuit used by Verbraeken.

A SEM analysis performed after medium term operation (150 hours) shows no difference in the microstructure. However, all the Ni/YSZ anodes show in the spectra a great degradation, bigger with higher amounts of fine YSZ.

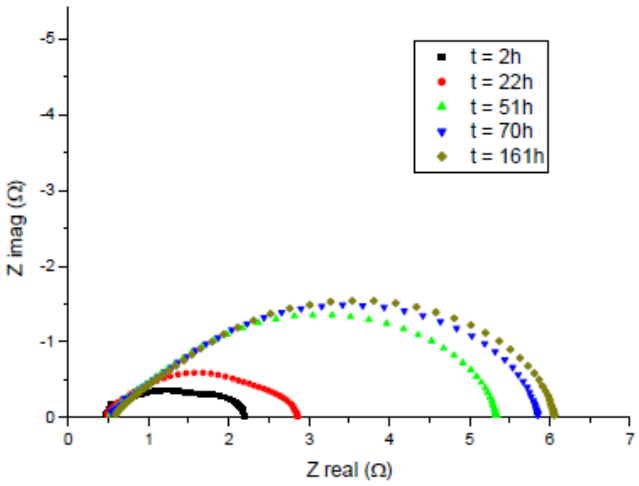

Figure 2.26. Impedance plots over time.

According to Verbraeken, this happens because coarse YSZ better adheres to Ni and stops agglomeration. Ni/GDC showed no degrade, which means that it is the functional layer which is affected, not the substrate. The phenomena is ascribed to the presence of impurities in the powder. In the impedance spectra the agglomeration results in higher impedance at high frequency, mostly in the first 50 hours. It is confirmed that the high frequency arc is always dependent on the microstructure. When polarizing the cell, the impedance falls down, as expected. Higher fine YSZ content results in lower impedance, due to increased TPB length and probably an increased number of adsorption sites. As De Boer claims, when the YSZ matrix is finer, also the dispersed Ni particles are.

The p_{H2}, p_{H2O}, temperature dependency are the most valuable data for understanding the limiting reaction steps, as already found in other studies.

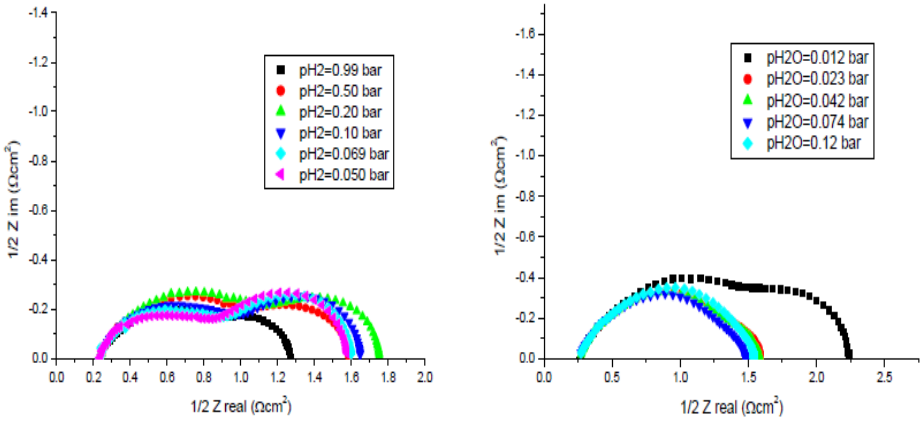

Figure 2.27. Nyquist plots with variation of p_{H2} and p_{H2O} on Ni/YSZ anodes.

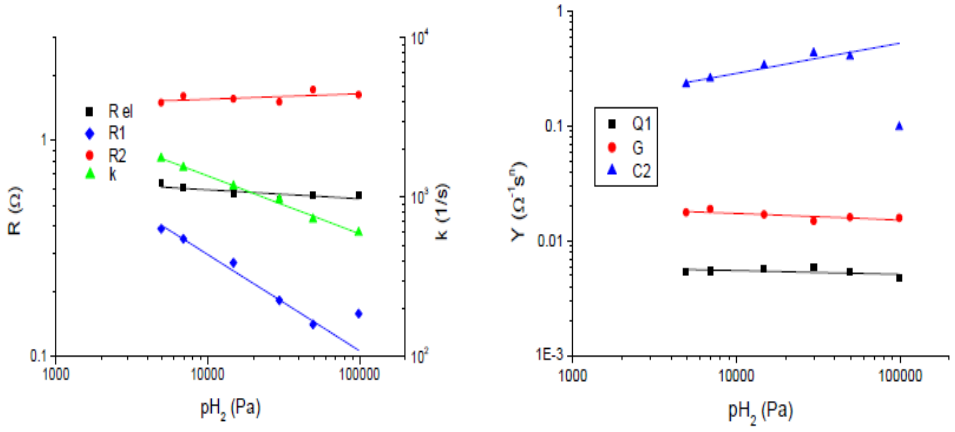

Figure 2.28. Dependency of the resistances and the capacitances on p_{H2}.

Figures show two dominant arcs at 100 and 1 Hz. The lower frequency arc decreases with increasing water pressure while its behavior with p_{H2} is not as expected. The overall electrode resistance decreases when lowering hydrogen partial pressure. The other arc is less dependent from the partial pressures. The series resistance is 0.4-0.7 Ohm, slightly more than literature values for 30-40 μm electrolytes. This is probably due to the fact that the electrolyte is thin. In fact, he reports what Wanzenberg et al. found [18]: there might be non ideal contacting between the electrolyte and the anodes, which becomes more significant for thin electrolytes. R_1 is independent from water and H_2 partial

pressures, while Q_1 depends on water, which suggests it could be somehow related to diffusion processes (CPE-P=0.6, close to the 0.5 of the Warburg element). K (the reaction rate constant of the side reaction) is higher for higher water pressure and fine YSZ content; this indicates that this side reaction could be a step of H_2 oxidation.

As for the temperature dependency of the processes, the activation energy of the electrolyte (series) impedance is in line with literature values for oxygen ions conductivity in YSZ, with a value of 70-99 ± 9 kJ/mol. The reaction rate constant is in line too, but the activation energy increases with higher fine YSZ amount. This is not understood since the reaction should benefit from an increased number of reaction sites. The main electrode impedance has high activation energy, 125 to 140 kJ/mol. This value is out of the range for adsorption of H_2 or gas diffusion/conversion processes. It may indicate that oxygen ions release from the electrolyte is the rate limiting step this time. The inverse reaction of this one, happening at the cathode, is well understood:

$$O_o^x + ad \leftrightarrow O_{ad} + V_o^{**} + 2e$$

Its activation energy is 125-135 kJ/mol. A bad adherence of the YSZ into the functional layer to the electrolyte could be the cause for oxygen ions not to be easily released, since TPB length is reduced. Another explanation may be a charge transfer limitation which controls the hydrogen oxidation at low temperatures, as suggested by Holtappels et al. [19].

It is interesting to spend a few words on the behavior of Ni/GDC electrodes, which are then analyzed in Verbraeken's study. The approach to the interpretation of the spectra is the same as for the Ni/YSZ electrodes and the basic physics is the same, so that the former evaluations are of use all the same. However, some differences are recorded from the previous case. Here obtained spectra and the equivalent circuit which was used for the fitting are presented.

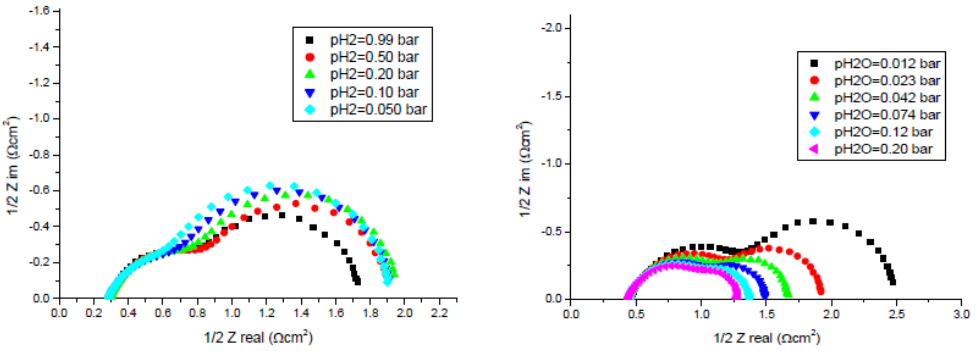

Figure 2.29. Nyquist plots with variation of p_{H2} and p_{H2O} on Ni/GDC anodes.

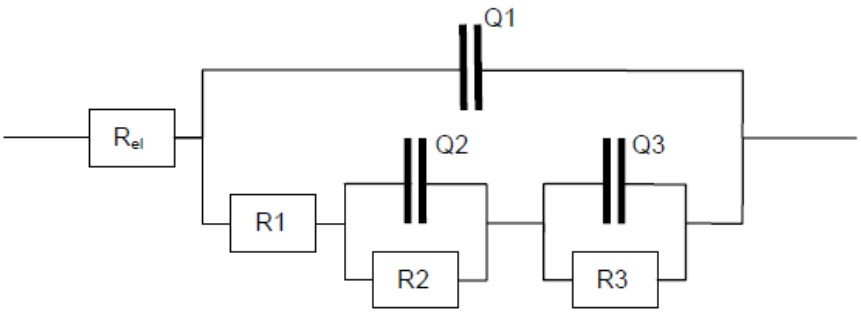

Figure 2.30. Fitting circuit used by Verbraeken for Ni/GDC anodes.

In the impedance spectrum three arcs appear, at around 100-1-0.05 Hz, and no degradation occurs, in contrast with the other anodes. The cause has already been anticipated. As for the dependency from the partial pressures, R_1 shows no dependency on p_{H2}, while it is slight for R_2 and R_3 and bigger for Q_2 and Q_3. The first arc is independent on p_{H2O}. All the capacitances are independent too, while R_2 and R_3 have strong dependence (mostly R_3). It is expected that some of the impedances are a function of p_{O2}, as CGO's electronic conductivity is highly dependent on it. On the contrary only a slight dependence of the sole mid frequency arc is recorded. It's not clear why. The trends with varying temperature are well reported through the activation energies:

Table 2.1. Activation energies for Ni/GDC anodes.

Circuit element		Activation energy (kJ/kmol)
Rel		99
R1		124
R2	<650 °C	134
	>650 °C	92
R3		47
Q1		15
Q2		-4,3
Q3		29

Calculation of the activation energy comes from the assumption of Arrhenius type dependency of a thermal activated process. The process dependency on temperature can be written with the following equation:

$$z = Aexp\left(-\frac{E_a}{RT}\right) \tag{2.53}$$

where z is the process in general, A is a pre-exponential factor, E_a the activation energy, R the gas constant, T the temperature. A clearer form is:

$$lnz = \left(-\frac{E_a}{R}\right)\left(\frac{1}{T}\right) + lnA \tag{2.54}$$

from which it is found that the activation energy of a process is represented by the slope of the straight line representing the natural logarithm of the same process over 1/T.

The total anodic polarization obtained in these experiments is higher than what reported in the references. The capacitance of the first arc is higher than usual values for the double layer capacitance (0,1-10 μm), being around 20-60 mF. This may be due to the fact that the material is finely distributed, with consequent larger surface, then capacitance. The mid frequency arc is the most discussed. Its resistance has an activation energy of 92 kJ/mol and the capacitance is 100-300 mF. Primdahl ascribed an arc with similar capacitances to gas conversion processes. They are due to current flowing in the cell and

causing local atmosphere changes, which make the Nernst potential vary. However gas conversion processes are fairly independent from the temperature and they are not expected to occur with symmetrical cells. Verbraeken suggests the presence of a red-ox couple in Ceria as the most probable cause, also on basis of the slight dependence of the capacitance on p_{O2}. Eventually, the third arc is ascribed to water adsorption limitation, not to hydrogen adsorption as suggested by Primdahl. However the explanation of this conclusion is not clear: the independence of the resistance on p_{H2} found by Primdahl indicates that the coverage is close to one, as reported above, and this gives rise to an adsorption limitation; moreover, it is claimed that addition of a small percentage of Ni wouldn't change the arc, because 40% Ni is already present. In Primdahl's and Mogensen's experiments not only ceramic electrodes were used, but also mixed: the Ni/CG1 [14] with 40/60 ratio of Ni/GDC was highly affected by small addition of Ni.

Bessler in 2006 approached the study of the gas concentration impedance of SOFCs [9]. A complete knowledge of what could happen in the low frequency region when taking the spectra helps understanding the whole result and concentrating on the region of interest, whatever it is. Bessler's new approach consists in creating a model which takes into account the coupling between diffusion in the flow channel and diffusion into the porous electrode, thus more detailed than the former Fickian approaches. He runs simulations with the transport equations and validates them with available experiments results. Two arcs are found when considering the whole model, among which the charge-transfer processes do not appear. The arc at low frequency (5 Hz) is due to the channel flow (in this model it is parallel to the surface of the anode, contrary to all the experimental setups shown so far), the one at mid frequency (100 Hz) is related to diffusion into the porous structure. These results are in qualitative agreement with Hendriksen's.

2.10 Investigation of Ni/GDC anodes by means of Impedance spectroscopy

All the case studies above refer to experiments with EIS, but investigating mostly Ni/YSZ anodes or complete cells, since they still are the state of the art technology for SOFCs. Some of the setups are similar to the one which is used in this study [11], some are almost the same geometry [13]. However the direct

references for experiments in this work are Aravind's study on high efficiency energy systems based on biomass gasifiers and SOFC with Ni/GDC anodes [8] and Sarda's research which was carried out in the same laboratory as the present one at TU Delft [6]. In both cases GDC anodes are used for EIS at OCV, for investigating the anode performance with particular gas feed compositions. For experiments the same setup geometry as in this study is used in both cases and same symmetrical anodic cells (from the same producer).

These two studies give the reference measurements and corresponding values of the resistances for standard operation with humidified H_2. Results are obtained after a deep study and refining of the experimental conditions, in order to get reliable and reproducible measurements for further comparison when conditions are changed. Anyway standardization of the measurement technique and procedure is not a scope in these works. Neither is found any detailed reference about post-processing of EIS responses in literature. In this study it is intended to look into the procedure for obtaining reliable results and the iterative experimentation to find and solve the problems of the setup. This will lead to validate the reference measurements, to plan a modification of the setup for studies with KCl contamination and to build a preliminary model for predicting and analyzing results in the continuation of the research. The employed setup is not described, as it and issues relating to its geometry will be discussed in detail in the next chapter.

Aravind performed measurements at four different temperatures, 1023, 1073, 1123, 1173 K. These temperatures are close to those at the outlet of gasifiers and of high temperature cleaning systems. Here an image of the obtained spectra with 100 Nml/min flow of 4.2% humidified H_2.

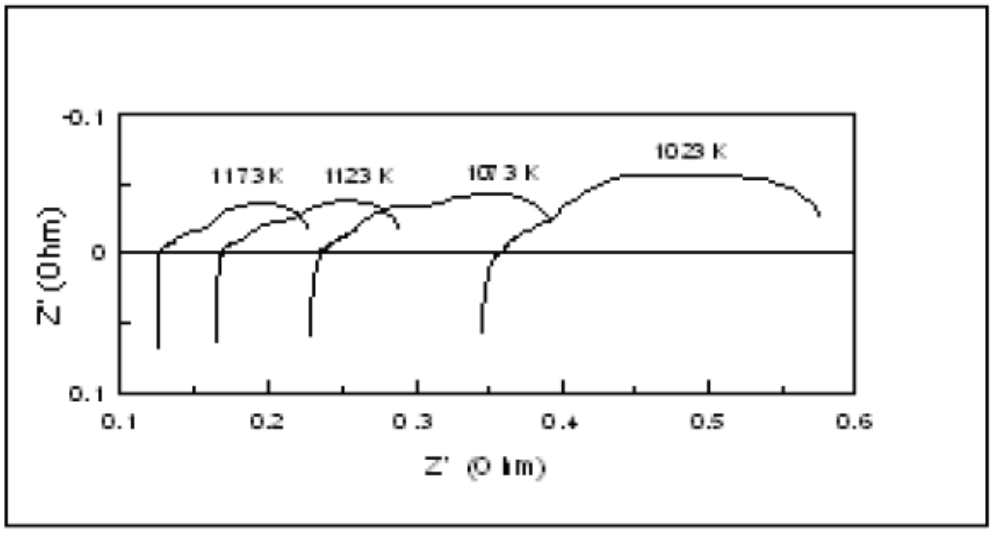

Figure 2.31. Nyquist plots from Aravind's study at different temperatures.

Data from the frequency response analyzer are elaborated with ZView as a software. On the axes, imaginary and real parts of the impedance are represented in [Ohm*cm^2] as referring to 1 cm^2 surface of the sample. Since samples are bigger, all the values have to be multiplied by its real surface in cm^2. Sarda's results are much alike Aravind's.

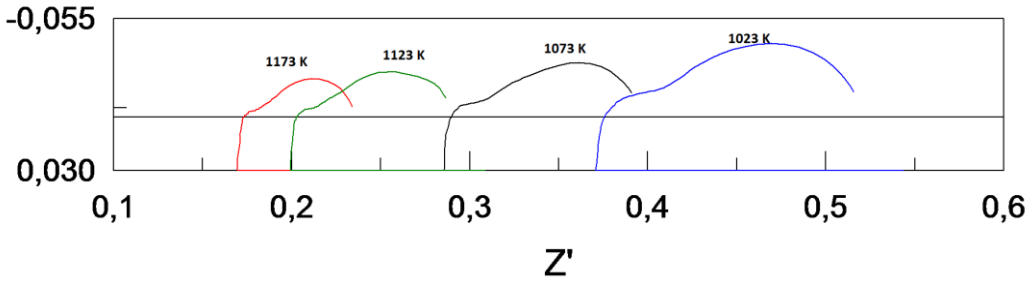

Figure 2.32. Nyquist plots from Sarda's study at different temperatures.

Based on qualitative analysis of the shapes and on literature, three arcs are identified in these spectra and they are fitted to the following equivalent circuit:

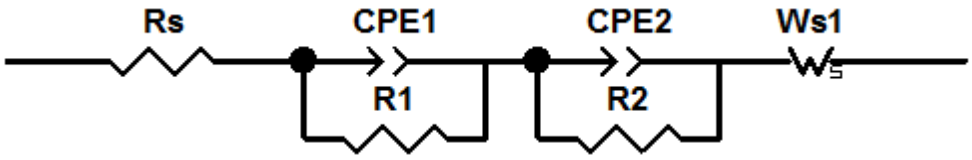

Figure 2.33. Fitting circuit used by Sarda.

Aravind uses an R-C element for the second process, but the outcome is the same as long as CPE-P2 is let free to stabilize to a value close to 1. Here the values from the fitting at 850 °C and the activation energies obtained from the temperature sweeps in Aravind's work.

	Peak f (Hz)	fitted circuit	R (Ohm)	p	Act. Energy (kJ/mol)
ARC 1	500	RQ	0,042	0,44	99
ARC 2	8	RC	0,013	1	142
ARC 3	0,5	WS	0,06		4

Table 2.2. Characteristics of the arcs from Aravind's study.

Aravind further analyzes the nature of the arcs by performing experiments with varying moisture and N_2 content. High activation energies of the first two arcs indicate that they originate at the anode, while low activation energy of the third arc indicates that it is due to diffusion related processes. The capacitance of the first arc is a few hundreds of mF/cm^2, which allows claim that it may be due to accumulation of mono-charged species on Ceria surface, hence adsorption phenomena. This is in line with phenomena in the same frequency range recorded in the formerly presented studies [11]. It seems not to be in the range for charge-transfer phenomena, which were found to show up at higher frequencies [11, 14]. The resistance of the arc at intermediate frequency increases with higher humidification and has high activation energy. It is then ascribed to a red-ox couple in the bulk of Ceria, which is affected by the electronic conductivity of Ceria, which decreases with higher p_{O2} (conductivity of Ceria is enhanced by reducing environment) and increases with higher temperature. This confirms what suggested by Verbraeken [10]. As for the low frequency arc it is ascribed to diffusion in a stagnant gas layer around the diffusers over the anode. The conclusion is validated with the same model as Primdahl used [11], as the same stagnant layer forms also in his similar geometry. This appears to be a peculiarity of employing a setup with gas flow

perpendicular to the cell holder. Calculated values match with the experimental ones when a diffusion length of around 2 cm is assumed, comparable to the radius of the reactor, which supports the conclusion of radial diffusion through gas diffusers without convection. A preliminary CFD model with simplified geometry seems to confirm this option. Primdahl's model is modified for taking into account diffusion coefficients in multi-component gas mixtures. Calculations from the model confirm the observed trend for different humidification and N_2 concentrations: with higher water ratio diffusion resistance diminishes, because both x_{H2} and x_{H2O} are at the denominator (from the formula); with higher concentration of N_2 diffusion coefficients of H_2 and H_2O decrease, because $D_{i\text{-}mix}$ for multi-component mixtures depends on the concentrations of other components. Only the frequency range given by Aravind for the low frequency process is different from Primdahl's.

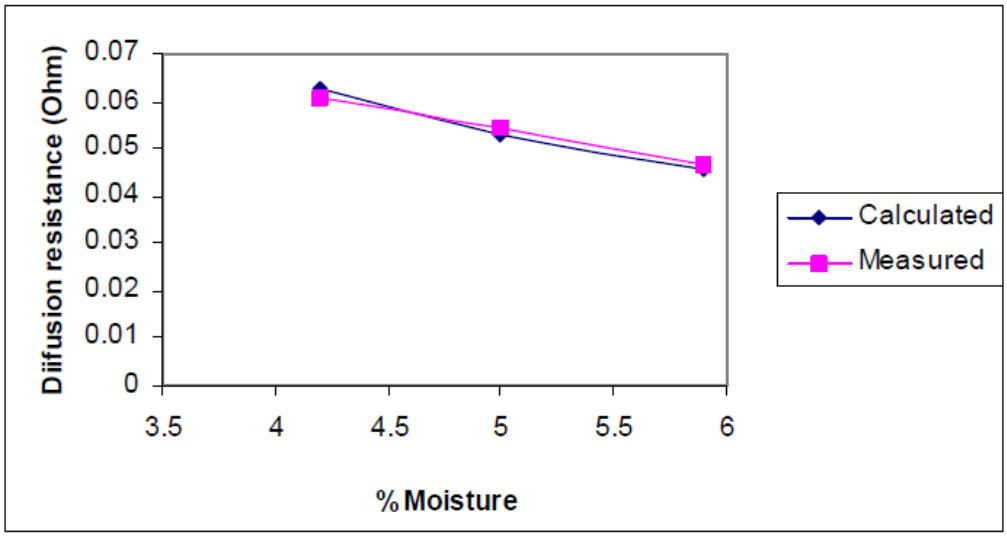

Figure 2.34. Diffusion resistance over water content from Aravind's study.

Sarda doesn't perform such accurate analysis, since his scope is to set a reference point for further measurements with NH_3 feed (it is proved to be suitable as a fuel for SOFCs). However he presents a useful review of some conclusions in literature about the typical frequency ranges and capacitances recorded for different processes and it is reported as a reference also for this work.

Charge transfer phenomena are usually found in the range 1-50 kHz and show capacitances in the order of tens of $\mu F/cm^2$. Based on Bessler's conclusions [20], Aravind [8] states that charge transfer may not cause an arc at typical working temperatures for SOFC. This seems to happen in his experiment like in Bessler's. Also Primdahl only finds arcs at a considerably lower frequency than the one of charge transfer processes with symmetrical Ni/CGO anodes [14]. Medium frequency arc and low frequency arc usually appear in the range of 10 Hz to 1 kHz and 0.1 to 10 Hz respectively. The first range is considered suitable for gas diffusion in the current collector and in a stagnation layer over the anode [11]. However, it may also relate to steps of the Hydrogen oxidation reaction [14]. A capacitance of few hundreds mF/cm^2 as associated with this range could be explained with adsorption of mono-charged species on Ceria surface [8] or on the surface of the anode [6, 21]. The low frequency arc is considered to be in the range for gas conversion or adsorption limitations, depending on the setup [11, 14]. When the capacitance is in the order of a few F/cm2 (0.2-2.5), however, it could relate to absorbed charged species rather than surface adsorption [22]. Aravind suggests that in this frequency range the arc could also be ascribed to a red-ox couple on Ceria surface when Ni/GDC anodes are employed [8], based on the observed dependence on water content. As already shown, the same result was obtained by Verbraken [10].

Formation of a stagnant gas layer in some particular setups has already been highlighted [11]. It leads to appearance of an arc around hundreds of Hz. However Aravind found it to show up at considerably lower frequencies, around 0.5 Hz [8]. As for diffusion in the porous anode, it is reported to be significant at very different frequencies depending on the setup [11, 20]. However, it is not expected to be relevant for anodes like the ones employed in the present study due to their little thickness, based on what concluded Primdahl [11]. The capacitance associated with the arc when a stagnant layer is present is found to be around 0.1-1 F/cm^2. Sarda's study confirms both the expected frequency and capacitance for diffusion in the gas channels [6].

As can be seen, there's not common agreement about the impedance features of various processes, neither about their frequency ranges. Moreover, all these data are hardly comparable since most times they were obtained with different experimental setups and no standardized measurement procedures. It comes once again out how it is very important to develop a solid procedure for carrying experiments and analyzing results.

Results and values from Sarda's fittings of the arcs at 750 and 850 °C are presented, as a reference for experiments at 750 and 850 °C in this study.

Table 2.3. Results from Sarda's study.

	Resistance (Ohm*cm^2)	Capacitance (F/cm^2)	RQ-P value	Peak f (Hz)
750 °C				
Rs	1,844			
ARC 1	0,057	0,00989	0,72	128,89
ARC 2	0,098	0,482	0,81	1,61
ARC 3	0,117	1,045	0,49	0,55
850 °C				
Rs	0,999			
ARC 1	0,011	0,0176	0,97	422,52
ARC 2	0,028	0,497	0,66	4,94
ARC3	0,121	1,113	0,48	0,5

2.11 EIS analysis of KCl contamination over Ni/GDC anodes

Aravind creates a setup for testing KCl contamination on Ni/GDC anodes and carries the first experiments. The setup is described in detail in the next chapter, however here the experiments are briefly described. A humidified H_2 flow is fed to the symmetrical Ni/GDC cell and another dry flow is led through a quartz evaporator tube inside the reactor, where a KCl bed is placed. By setting different heights for the bed, four concentrations of the contaminant are obtained: 14.5, 16.3, 32, 36.3 ppm. Measurements are performed at 850 °C. Only for 36.3 ppm a significant change in the arcs is recorded over time.

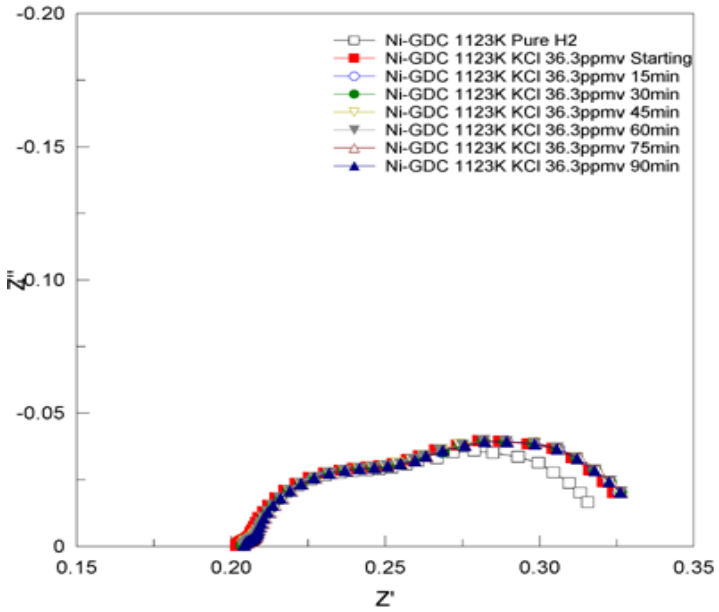

Figure 2.35. Results from experiments with KCl contamination.

Variations in R_s and in the low frequency arc were recorded but they weren't expected. Widening of the low frequency arc is ascribed to non-perfect mixing between the humidified and the dry flow, which meet right before the ceramic gas diffusers in the reactor. For obtaining a higher concentration of KCl the dry flow through the bed is increased, while the humidified one is decreased. Though the total humidification is kept constant, it is possible that the dry flow influences more the diffusion process in the stagnant layer before the anode.

References

[1] X. Yuan, C. Song, H. Wang, J. Zhang, Electrochemical Impedance Spectroscopy in PEM fuel cells, Springer-Verlag London, 2010.

[2] Wikipedia.

[3] A. Leonide, SOFC modeling and parameter identifications by means of Impedance Spectroscopy, Scientific Publishing, 2010.

[4] R.A. Latham, Algorithm Development for Electrochemical Impedance Spectroscopy Diagnostics in PEM Fuel Cells, Lake Superior State University, 2001.

[5] Universidad de la Habana, Breve tutorial de ZView.

[6] V.Sarda, Ammonia as a fuel for Solid Oxide Fuel Cells, MSc thesis, TU Delft, August 2011.

[7] Helmholtz, H. Pogg.Ann. LXXXIX, 1853.

[8] P.V.Aravind, Studies on High Efficiency Energy Systems based on Biomass Gasifiers and Solid Oxide Fuel Cells with Ni/GDC Anodes, PhD thesis, November 2007.

[9] Wolfgang G. Bessler, Gas Concentration Impedance of SOFC Anodes, 7th European SOFC Forum, Lucerne, Switzerland, July 3-7, paper P0707, 2006.

[10] M. Verbraeken, Advanced supporting anodes for Solid Oxide Fuel Cells, MSc thesis, EMPA Dübendorf, March 2005.

[11] S. Primdahl and M. Mogensen, Gas Diffusion Impedance in Characterization of Solid Oxide Fuel Cell Anodes, Journal of The electrochemical Society, 146 (8) 2827-2833, 1999.

[12] P. V. Aravind, J. P. Ouweltjes, J. Schoonman, Diffusion Impedance on Nickel/Gadolinia-Doped Ceria Anodes for Solid Oxide Fuel Cells, Journal of The Electrochemical Society, 156 _12_ B1417-B1422, 2009.

[13] Baukje de Boer, SOFC Anode: Hydrogen oxidation at porous nickel and nickel/yttriastabilised zirconia cermet electrodes, The Netherlands, 1998.

[14] S. Primdahl, M. Mogensen, Mixed conductor anodes: Ni as electrocatalyst for hydrogen conversion, Solid State Ionics 152– 153 (2002), 2002, pp. 597– 608.

[15] T. Norby, O.J. Velle, H. Leth-Olsen and R. Tunold, Reaction resistance in relation to three phase boundary length of Ni/YSZ electrodes, Proc. Of the 3rd International Symposium On Solid Oxide Fuel Cells, Honolulu, Hawaii, 1993, pp.473-78.

[16] R.J Aaberg, R. Tunold, S. Tjelle, R. Ødegård, A Possible Reaction Mechanism for the Oxidation of H2 on Ni/YSZ cermet Electrodes, The Electrochemical Society, Aachen, 1997, pp 557- 64.

[17] R. Barfod, A. Hagen, S. Ramousse, P. V. Hendriksen, M. Mogensen, Break Down of Losses in Thin Electrolyte SOFCs, Materials Research Department, Risø National Laboratory, Denmark, 2006.

[18] Wanzenberg E., et al., Influence of electrode contacts on conductivity measurements of thin YSZ electrolyte films and the impact on solid oxide fuel cells, Solid state ionics, vol. 164, 2003, pp. 121 – 129.

[19] Holtappels P., et al., Reaction of hydrogen/water mixtures on nickel-zirconia cermet electrodes, Journal of the electrochemical society, vol. 146, 1999, pp. 2976 – 2982.

[20] W.G. Bessler, Gas concentration impedance of solid oxide fuel cell anodes. I. Stagnation point flow geometry, Journal of the Electrochemical Society, 2006.

[21] S. Primdahl, Y.L. Liu, Ni Catalyst for Hydrogen Conservation in Gadolinia-Doped Ceria Anodes for Solid Oxide Fuel Cells, Journal of The Electrochemical Society, 2002. 149(11), pp. A1466-A1472.

[22] S. Primdahl, M. Mogensen, Oxidation of Hydrogen on Ni/YSZ-Cermet Anodes, Journal of Electrochemical Sociecty, 144 3409-3419, 1997.

[23] M. Mogensen, S. Skaarup, Kinetic and geometric aspects of solid oxide fuel cell electrodes, Solid state ionics, vol. 86 – 88, 1996, p. 1151 – 1160.

[24] Subhash C Singhal, Kevin Kendall, High temperature solid oxide fuel cells: Fundamentals, Design and Application, Elsevier, 2003.

[25] Gorte, R.J., Vohs, J.M., Novel SOFC anodes for the direct electrochemical oxidation of hydrocarbons, Journal of catalysis, vol. 216, 2003, pp. 477 – 486.

Chapter 3

Experimental analysis with Hydrogen

On the basis of the previous dissertation we choose to adopt impedance spectroscopy for investigating the cell behaviour at OCV. It is suggested that investigation under polarization is carried out only once processes are identified at OCV, where resistances are higher. In fact, it allows distinguish the effects of the various processes occurring during operation, unlike polarization measurements, which give a global overview of the performance of the cell. EIS over anode symmetrical cells results in a further insight into these processes, since it focuses on the anode response alone, separately from the cathode. It's been more and more used lately, to look into the effects of various fuel feeds (with or without contaminants) on operation, just by studying the physical processes at OCV.

Two main techniques are commonly used in studies with EIS: three electrodes configurations and anode symmetrical cells. The first method is commonly used when a polarization study is required. It consists in using a working electrode which is where the reactions take place, a counter electrode which guarantees the current circulates through the cell and prevents it from passing through the reference electrode and eventually a reference electrode which has a stable potential and which acts as reference voltage value in the measurements [3]. The placement of the reference electrode is critical. The electrolyte is generally used as reference electrode because it is quite stable and not polarized. Sometimes, especially in thin electrolyte this assumption is not true. Another disadvantage of this technique is that the placement can affect the measurements which have a great sensitivity. It can happen that even a good alignment leads to distorted spectra. If a polarization study is not required, the way to avoid these problems is to use anode symmetrical cells. In this case the reference electrode is unnecessary [4]. This is due to the fact that it is not necessary to distinguish the behavior of the two electrodes. So there are just the working electrode reactions taking place and the counter electrode which gives a reference to measure the voltage difference. The working principle of anode symmetrical fuel cells is different with respect to standard SOFC cells. In the latter, there are two sealed electrode chambers with different feeds and the difference in concentration of oxygen between them is the driving force. In anode symmetrical fuel cells the

driving force is the AC signal which polarizes the electrodes [2]. Depending on the direction of the current (which is sinusoidal) one electrode will behave as the anode and the other as the cathode. In the cathode side the water present in the feed is electrolyzed into hydrogen and oxygen. This one reacts with the electrons and turns into oxygen ions that migrate through the electrolyte to the anode where they react with hydrogen to form water again. The resulting polarization impedance is the sum of the two electrodes and the electrolyte impedances.

In this work it is intended to support Aravind's preliminary analysis about the effects on the impedance spectra of KCl contamination in the fuel feed [1]. As already said, KCl originates from gasification of biomass and it is present up to some extent in biosyngas to be fed to the SOFC. The former study was carried out in another laboratory and, moreover, some of the results were unexpected, based on theoretical background. In order to repeat the experience and go deeper into this field it is then necessary to create a new setup for KCl testing in the SOFC laboratory at TU Delft. Results with the existing setup must be obtained before making any modification, to set a reference point for future measurements and to make sure no unknown externalities are affecting the measurements. It is known that the experimental configuration, as well as the physical devices themselves, influences the results, since they are extremely sensitive to many conditions. Moreover the experimental station for impedance at TU Delft is new and only one study was carried out on it. The setup still needs investigation. The reference experiments for this work are Aravind's [1] and Sarda's [2], the latter having performed impedance analysis on the same setup as the present one. They both recorded spectra at four temperatures, in steps of 50 K from 1023 K to 1173 K. Ni/GDC anodes can work also at lower temperatures, but first of all this is a good operational range for research purpose, especially with particular fuels or contaminants, secondly they should come to a conclusion about the possibility of feeding biosyngas to a cell/stack system, being it available at temperatures around 900 °C.

In the following sections a study of anode performances under different conditions with humidified H_2 as a feed will be presented. In his experience with KCl Aravind showed how the specific used setup can give results which probably are not a response of the cell but of the system built around it. Starting from this consideration and from the conclusion that the observed widening of the impedance arcs in his experiments was probably due to non perfect mixing

of the dry and humidified flows in the reactor it was chosen to further investigate the original setup for reference measurements with H_2 and H_2O. This is also supported by the analysis of preliminary results, which showed variations and unexpected behaviors. Additionally, it was found that not extensive information about optimized and standardized procedures for impedance measuring and arcs fitting is available in literature. A detailed study of a reference case and detailed presentation of the employed procedure and the solved and unsolved problems was decided to be the most important step for starting research with KCl contamination. The aim is to obtain reliable and reproducible results for further comparison when the setup is changed. Additionally, conditions in the experiments are changed as to specifically study what consequences will have similar changes when KCl is added. The mass flow rate is varied in order to see if the behavior of the cell and the setup is stable when it changes and what the best parameters for next experiments are. Humidification is varied to see whether condensation takes place in the harshest conditions planned for experiments with KCl and what limitations arise from humidification problems in the setup. From this whole experience an optimized procedure for testing, with information about fitting, stabilization times, parameters variations, unexpected behaviors of the setup is to be found and hopefully used in the prosecution of the research. It will be noticed that big part of the discussion on the spectra lies on the low frequency part of the arcs: it is not expected to change with addition of KCl but it is the most susceptible to external conditions. For this very reason an attempt is made to find all the main causes for its possible variations and to make it as stabile as possible.

3.1 Experimental

The gases are stored in tanks outside the laboratory. The pressure is reduced and they are taken inside through pipelines. A main on-off valve controls the feed before the mass flowmeters and pressure at that point is 2.1 bar. On the contrary, after the controllers (at the reactor) pressure is around 1.05 bar. This is enough to guarantee the flow as long as no valuable leakages are present and as long as, in the case of KCl bed, it doesn't cause too much a pressure drop. The anodic gas N_2 flow controller has a full scale indication of 100 Nml/min with a least value of 2.5% of the full scale. Heating up can be performed with cathodic gas controller, which has got a higher full scale. The H_2 controller goes up to 500 Nml/min, so the least readable value is 12.5 Nml/min. After mixing, the gas is

bubbled through a pot filled with water, the humidifier, temperature of which is controlled to set the desired level of humidification at the outlet. Another thermocouple is placed on the top of the pot to better control temperature. The humidifier can be by-passed with an on-off valve. The pipeline after the humidifier is traced not to have condensation of moisture. Also the quartz holder which gas goes into is traced, through a ceramic part covered with electrical resistance. Ceramic is thermally insulating, so, at equilibrium, it serves as an element for heating homogeneously the gas inside. The presence of a hot spot on the quartz could cause the flow to be non homogeneous, with consequent effects on the performance of the cell. The only critical element is the connection between the traced piping and the quartz holder, so that it will be necessary to always check if it carries condensation. The ceramic sample holder is built into the quartz element, which is threaded into the quartz reactor. This way the cell ends being as high as the hot spot of the electrical oven. At the reactor's outlet a metal pipe is connected as soon as the temperature allows it and gas is bubbled through one water column which gives a check that the gas is correctly flowing. A temperature controller is used to regulate the temperatures of the oven, of the humidifier through which the inlet gas passes, of the traced flexible tube that connects the humidifier to the sample holder, and the inlet of the sample holder. The controller has programs to set the ramp-ups and the ramp-downs of the system. The temperature measurements are ensured by thermocouples set close to the interest points and connected to the controller. In the control panel there is also a gas flow regulator which allows modifying H_2, O_2, N_2, CO, CO_2 flows. Here follows a sketch of the experimental setup, while later on another sketch displaying modifications will be presented.

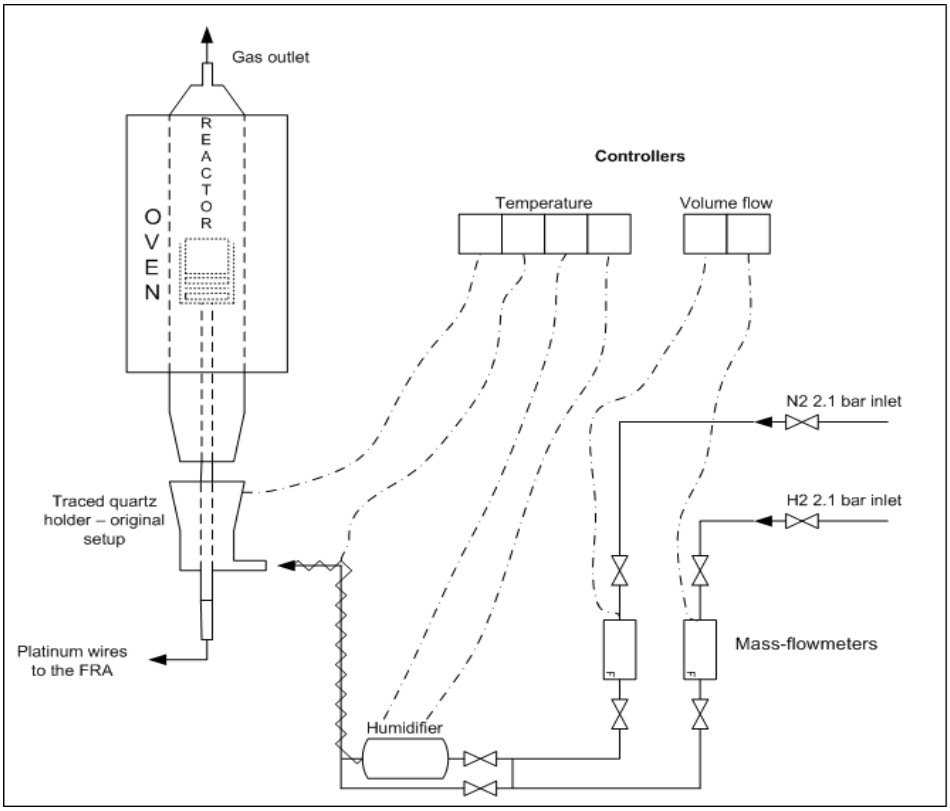

Figure 3.1. Sketch of the setup at TU Delft with planned modifications.

The experiments are carried out with electrolyte supported ESC2 Anode symmetrical cells. This fuel cell is made of: two anodes with 22 mm of diameter and with a thickness of 35 μm and an electrolyte between them with 25 mm of diameter and 94 μm of thickness (it is way thicker than the electrodes, they are electrolyte supported cells). The anodes are composed of Nickel which is both a good electronic conductor and a good catalyst for oxidizing Hydrogen and of a matrix made of GDC (Gadolinium doped Ceria) which is ionic conductor and has a better tolerance to contaminants (for example H_2S) with respect to YSZ anodes. Every anode has a three layers lay-out: there is an adherence layer (next to the electrolyte) of $Gd_{0,4}Ce_{0,6}O_{1,8}$ + 2 mol% CoO, a functional layer of $NiO/Gd_{0,1}Ce_{0,9}O_{1,95}$ and a contact layer of NiO. The electrolyte is made of 3 mol% Yttria-stabilised tetragonal Zirconia (TZ3Y). The cell is placed on the ceramic holder. In order to let the electrons flow between the two anodes (the direction depends on the polarization in each instant) there are golden wires spot welded with golden meshes glued to the anode external surfaces.

There are two (one per side) ceramic supports contacting the anodes and the golden meshes. They also have the function of gas diffusion layers. They are made of several parallel channels 1 mm width and 2.5 mm depth. A weight is put over the cell-diffusers system in order to ensure a better contact among the parts. The sample holder is placed into another quartz tube inside the oven, which acts as a reactor. At the base of the quartz holder for the cell, there is one inlet for the ceramic support, so that it can be threaded from the top when preparing the set up. Platinum wires are spot-welded to the golden wires of the collector meshes and pass inside the support to go to an electric box. There are four of them, which serve respectively as Working Electrode, Counter Electrode, Reference Electrode 1, Reference Electrode 2 (We, Ce, Re_1, Re_2). In a symmetrical cell the working and counter electrodes are continuously switched one into the other, so that they are completely interchangeable, as long as they are not short-circuited. The reference electrodes are not necessary in such a setup, so here they only serve as an auxiliary circuit. Every connection can show a resistor or a capacitor in the spectrum, making it impossible to have a clean response. The electric box connects them to the FRA (frequency response analyzer), through four more wires. The proper working of these last is checked with a “dummy resistor”, an artificial impedance which is connected to the FRA through the wires, allowing to see whether they influence the frequency response or not. They work fine.

The impedance station is equipped with a potentiostat which through an alternate voltage input gives the cell the AC current used for the measurement of the performance. There are a working electrode (We) plug, a counter electrode (Ce) and two reference electrode (Re_1, Re_2) plugs. As already explained in anode symmetric fuel cells reference electrodes aren't functional.

The set up is equipped with a frequency response analyzer. The potentiostat provides a sinusoidal voltage input (so that it gives an AC signal to the cell through its impedance). The response of the anodes goes to the FRA that measures the gain and the phase between two points in the system. These instruments are connected to a workstation which uses ZPlot and ZView as software. The plots reported in this work are fitted using ZView, which processes the data recorded by ZPlot.

In the following sections three tests are presented. Since it is intended to gradually understand the processes which could affect the measurements in an

experimental asset for impedance measurements, an iterative approach is used, where results of each experiment are discussed and the procedure is refined after conclusions from each experience. As an outcome, reliable, reproducible results, along with explanations of the experimentally recorded problems are expected, to make a starting point for testing of the anodes with KCl.

3.2 First test

This test didn't give any reliable results, but it is briefly presented to show the detailed procedure for building and heating up and to show the starting point of the study.

Procedure for building up the cell:

- Golden meshes are cut into two circles for the electrodes. Golden wires are spot welded to them, two per side, in more than one point to make a better contact. The settings for the welder are taken from Sarda's thesis [2]: hold time 70 ms, squeeze time 140 ms, energy 22 Ws, current from 0.8 to 1.4 kA. These parameters are assumed to be safe for not cutting the wires while welding.
- The meshes are stuck with paraffin glue to the cell. The wires from the meshes are connected and welded to the platinum wires of the cell and the four of them are kept separate through ceramic separators. It is noted that the ceramic weight over the cells shows cracks from a previous preliminary experiment. This may be due to too big a cool-down or ramp-up rate of the system (240 °C/hour).
- Sealing paraffin grease is put on the connection between the quartz element and the reactor and the sample holder is threaded inside.

Procedure for starting and heating up:

- The ramping up program is set to 150 °C/hour (safe for cracking of ceramics, the producer suggests to keep below 5 °C/min as a ramping rate), up to 700 °C. Once it reaches the desired temperature it automatically stabilizes.
- For heating up 100 Nml/min dry N_2 are used.

Procedure for reducing:

- Dry Hydrogen is used, gradually switching from 100 ml/min N2 to 200 ml/min H_2 in half an hour (reduction procedure is described for every experiment, since it varies).
- H_2 is then humidified and let stabilize before taking the first measurement. Needed stabilization times will be discussed, they may vary depending on employed conditions.
- The FRA is checked with a dummy resistor directly connected to the wires. The measurement of the spectrum is carried out and it gives the expected 2 arcs as a response.

Procedure for cooling and shutting down:

- The flow is set again to dry N_2, 100 ml/min, the H_2 valve is closed. The cooling program uses the same ramp as the heating one: 150 °C/hour. All the tracings and the humidifier temperature are set to ambient temperature.

Impedance spectra are recorded all along the experiments, with a frequency range from 0.1 to 60000 Hz (which with a logarithmic scale means 59 points in around 4 minutes each spectrum). It is decided not to go further at high frequency because only more inductance from the wires would be recorded and no significant result from the cell. The spectra are in the first quadrant only as soon as the wires connected to the FRA are switched.

The first spectra are taken at 700 °C but no significant result is found, as the indication of over current keeps showing up. This must be due to the employed configuration short-circuiting the cell. When the right configuration is found, it is kept as the right and reference one and spectra are taken. Much noise is recorded, especially at high frequency, which is partly due to the wires, partly to more time for stabilization being needed. The temperature switch is more or less 2 °C/min, safe for cracking, so the ramp up to 750 °C is done in 30 minutes, followed by a stabilization period of 15 minutes, from references. This is concluded not to be enough, since spectra keep refining with time. One night elapses between the first experiments at 800 °C and the last ones and they are different in shape. No problem is encountered when recording spectra at higher temperature. The cell doesn't show any degradation during the whole test, which lasts 26-27 hours from the first to the last measurement, excluding the times for ramping up and cooling down.

Though not always the second arc is well defined, it is decided to fit the spectra with three arcs. This accounts for what is physically predicted and what was said to be generally agreed in the theoretical study of EIS [1, 2, 6] for this kind of setup. Taking a look to the Bode plot of one of the arcs supports this decision, since in some cases three peaks are well defined in the phase plot (θ over Log(f)).

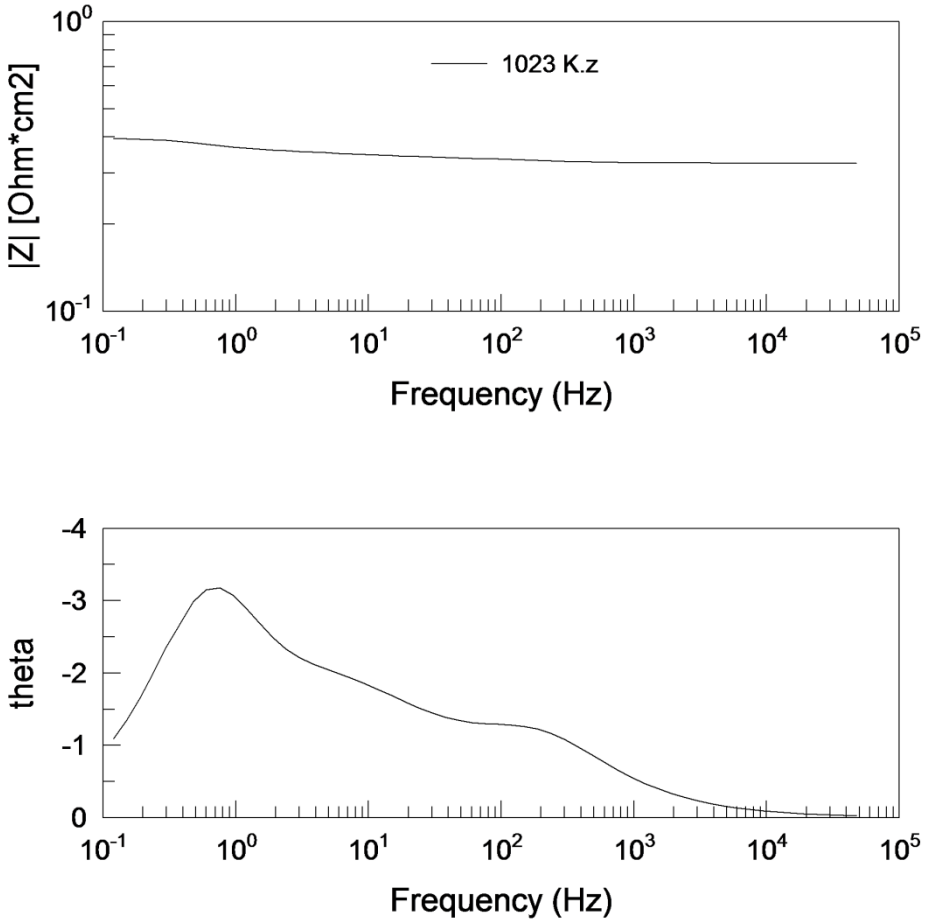

Figure 3.2. Bode plot of the impedance spectrum at 1023 K.

The chosen equivalent circuit is shown below. It was used for fitting spectra for all the experiments, since the equivalent processes are expected not to change with varying conditions.

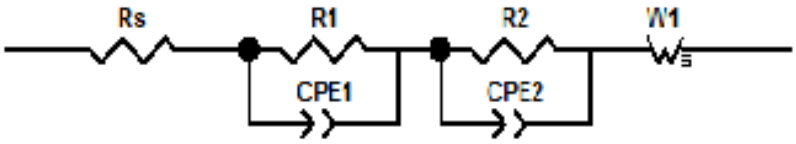

Figure 3.3. Chosen circuit for fitting.

Here R_s is the series resistance, calculated as the intercept of the impedance spectrum with the real axis at high frequency. This is simply found with the "Instant fit" function and it is used as a fixed degree of freedom when fitting (it is a start point, not a value which distance from the real one needs to be minimized). The arcs are respectively fitted with RQ_1, RQ_2, W_s elements (R-CPE, R-CPE, finite Warburg), as the first one is initially assumed to represent some limiting adsorption phenomena, the second one a limiting reaction, the last one mass transfer processes due to the geometry of the setup (which could be avoided with different configurations) [1]. An RQ element is the parallel between a resistance and a CPE (as already described). In ZPlot the impedance of a CPE is represented as $Z = \frac{1}{T(i\omega)^P}$, where T and P are the degrees of freedom in the fitting. The maximum value of P is 1, which corresponds to an RC element, so it is fixed to 1 when after the fitting it exceeds that value.

It is important to give reasonable initial values for the iterative fitting in the program, because a single shape can be fitted in many ways. The function "instant fit" in ZView allows fitting a range of points which is considered to represent mostly one arc to a single element. The obtained values for the parameters of that arc are used as initial values for fitting the overall circuit.

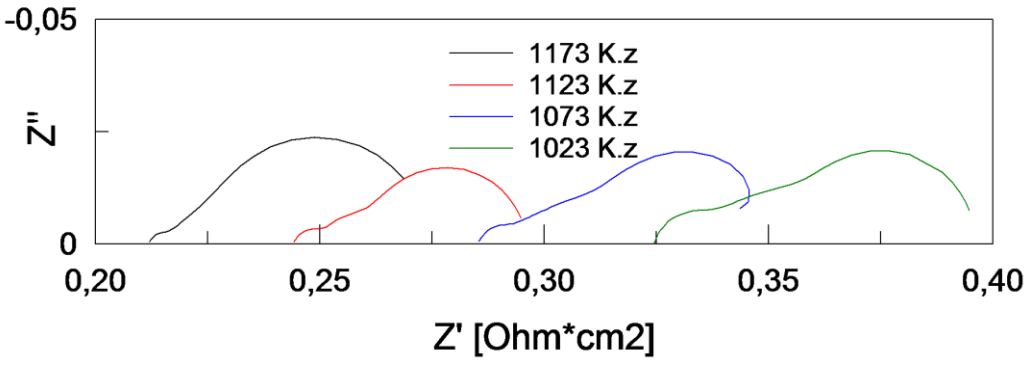

Figure 3.4. Fitted spectra from the first experiment at four employed temperatures.

The most representative arcs at the four employed temperatures are presented above. The spectra are not in the expected range of R_s, being this generally lower than expected for this kind of cells. Also the difference of resistance between each spectrum at different temperatures is doubtful. The shape is also different than the one of Aravind's experiments. In addition a great variability mostly in the width of the low frequency arc is noticed at constant nominal conditions.

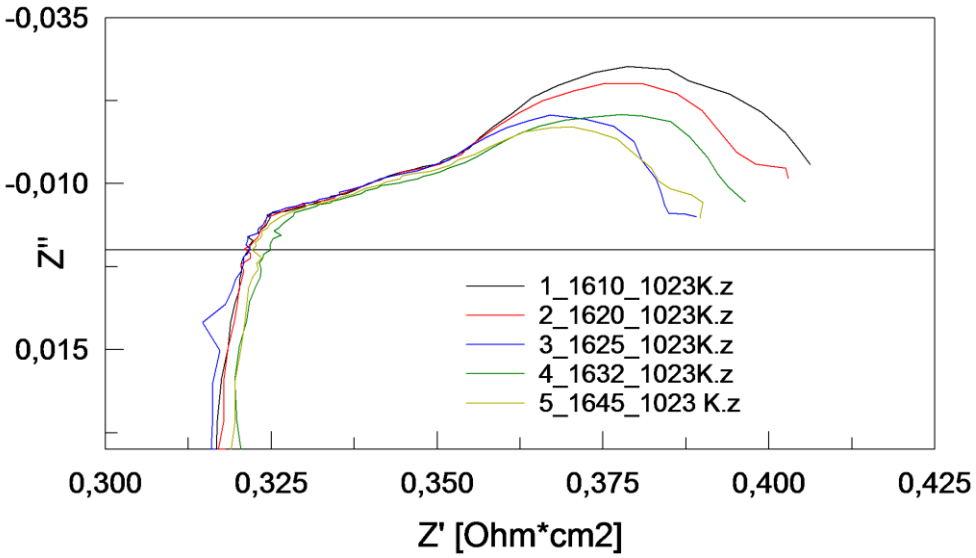

Figure 3.5. Spectra recorded at different times at 1023 K and same flow conditions.

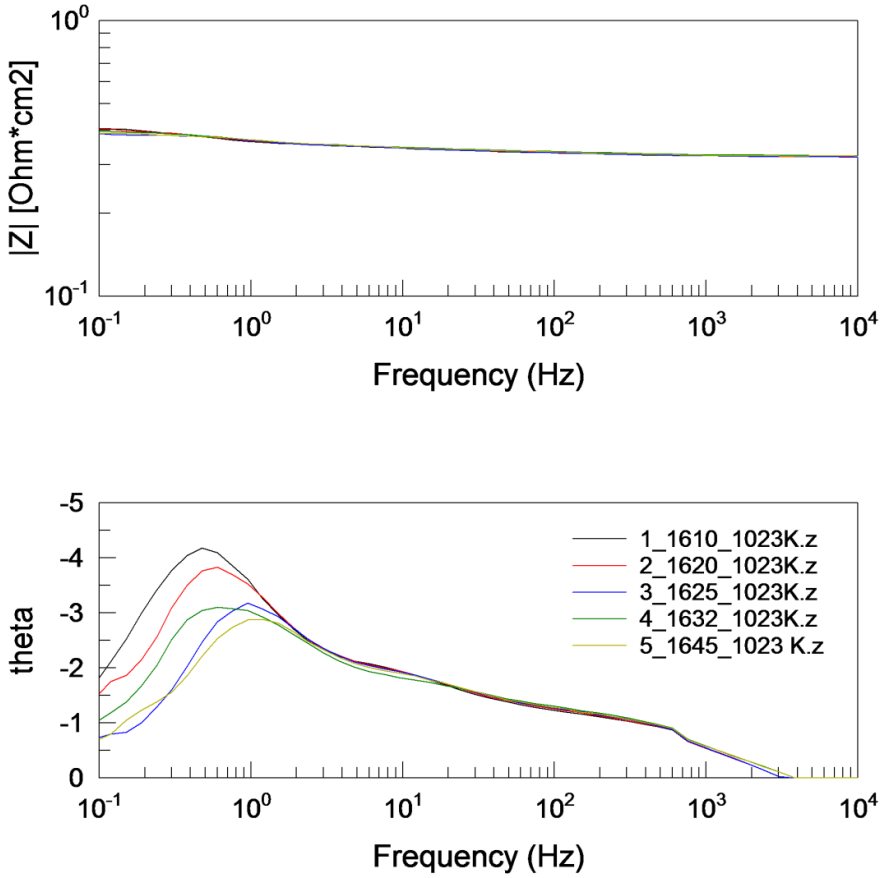

Figure 3.6. Spectra recorded at different times at 1023 K with same conditions, bode plots.

However, it is tried to use spectra closest to the average behaviour at each temperature to compare them and obtain a trend of R_s, R_1, R_2, WR with temperature. The result confirms what physically expected from lowering temperature. Only WR at 900 °C is out of range and this is ascribed to some temporary oscillation of humidity.

Table 3.1. Resistances of the three arcs and Rs from the first experiment at different T.

T (°C)	900	850	800	750
Resistances (Ohm*cm2)				
R_s	0,804740949	0,927523815	1,054754233	1,233340581
R_1	0,004407639	0,010788166	0,01111508	0,021236114
R_2	0,001993796	0,007697687	0,022807963	0,031338141
WR	0,112371031	0,08043228	0,084032137	0,083644402

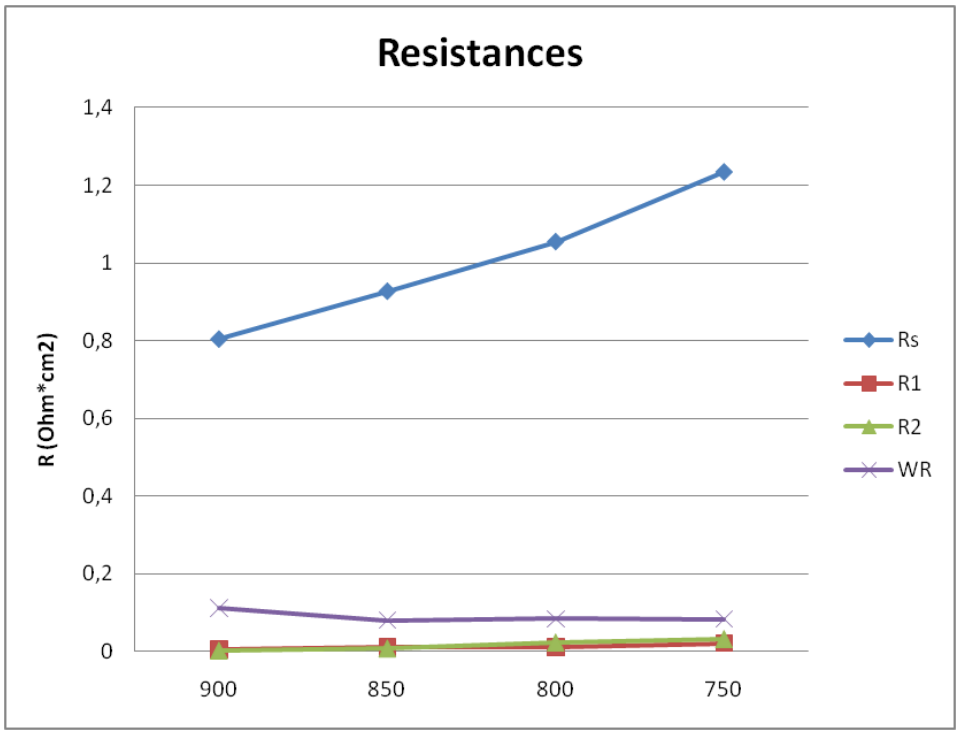

Figure 3.7. Trend of the resistances from the first experiment with T.

R_1 and R_2 slightly increase with lowering temperature, while WR is almost constant, except for the outlier value of WR at 900°C. R_s increases linearly.

Refining of the experimental procedure and better understanding of what is distorting spectra from the expected behaviour is needed before carrying out the following experiments. The laboratory is new and it needs solid characterizing to obtain reliable and reproducible results.

3.3 Second test

The need for a second test comes from the problems encountered during the first one: they had to be fixed to get a reliable reference measurement for the new setup. During some preliminary experiments water condensation had occurred in the connection pipe between the feed and the quartz element (which cannot be properly isolated and becomes the most critical part, as will be showed) and this was taken care of, since water plays a key role in the outcome of the

measurements of high performing anodes. The tracing of the quartz holder was replaced by a new one and no more condensation apparently took place. Moreover, temperature of all the tracing elements was raised. The problems with the first measurements and the noises were partly ascribed to the electrical wiring. So the connections of the platinum wires to the cables of the FRA were fixed, the electric box checked and the FRA wires taken care of before tests. Moreover, a suitable position for the wires of the FRA was looked for, since it seemed to affect the measurements significantly. It was however kept into account that problems were also due to stabilization of the cell itself and of its working conditions when changed. Then during the experiments longer stabilization periods were used and recorded.

SEM and XRD analysis were carried out on the sample of the first experiment to show if its structure had been affected, modified, damaged during operation. They didn't show anything unusual; the porous structure in the SEM image appears to be regular, with no extended cracks, just showing the presence of some residuals over the surface. They may be due to sintering of the golden mesh on the anode at high temperature. Some regions with crystals grown inside the structure are also caught. They are just imperfections in the structure. Results follow. Images with X1500 and X5000 enlargements are presented.

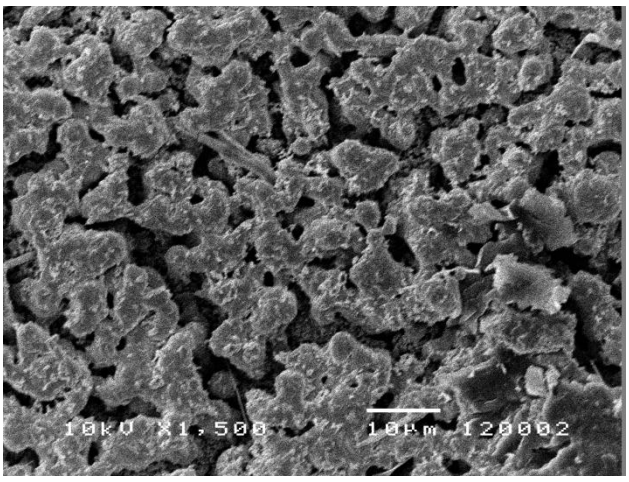

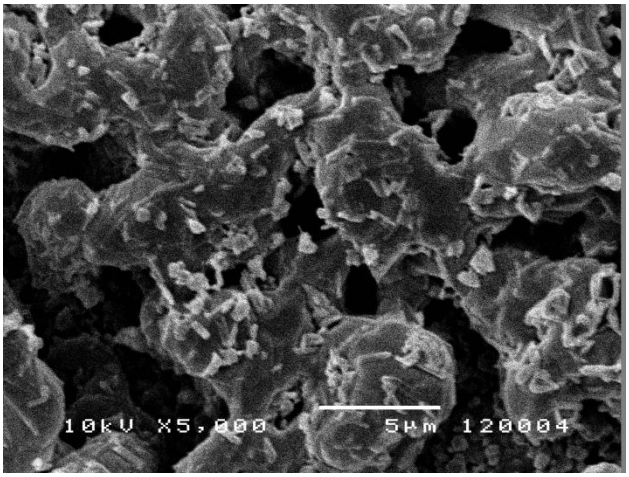

Figure 3.8. SEM images of the sample of the first experiment with x1500 and x5000 enlargement respectively.

Here a table with the most important elements found with XRD is presented:

	Compound	Conc.	Absolute
	Name	wt(%)	Error (%)
1	Al	0.056	0.007
2	As	0.012	0.003
3	Au	3.4	0.08
4	Ca	0.058	0.01
5	Ce	9.9	0.2
6	Co	0.053	0.01
7	F	0.61	0.05
8	Fe	0.025	0.008
9	Gd	1.9	0.1
10	Hf	0.19	0.03
11	Ni	51	0.4
12	O	7.2	0.7
13	P	0.003	0.002
14	Rb	0.13	0.01
15	Si	0.4	0.02
16	Y	1.3	0.03
17	Zr	24	0.1

Figure 3.9. Results from XRD analysis on the sample from the first experiment.

It must be kept present that SEM is a surface analysis, not showing anything of the inside structure, and XRD penetrates to some extent into the material, but it gives no information about differences in composition at different depths of the sample. A global, mean composition of the whole penetration length is given. As expected, some percentage of Au is found, probably due to what stuck on the surface of the sample from the golden meshes. The global analysis regularly reveals predominant Ni, then Ce oxide and some Zr oxide (concentration of which is lower in the outer layers, so it is less detected by X-ray).

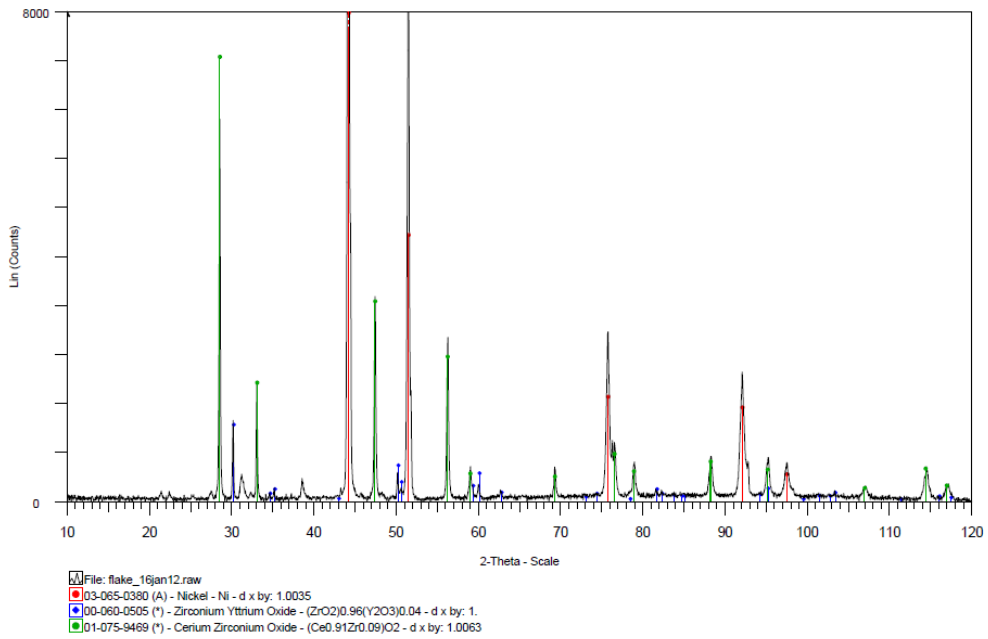

Figure 3.10. Peaks from XRD analysis on the first sample.

The analyses show the expected results, for which reason they are taken as a reference for the future experiments with KCl contamination, where the superficial structure is expected to be affected. It is not possible to have analyses on a same sample before and after contamination, firstly because SEM is destructive, secondly because after cooling down the same anode can't be used for new experiments.

From observation of the sample holder it is noticed that it is dirtier than before use, which means that carbon deposited from former experiments (former than this study) was not completely removed. Since carbon deposition had to be removed from the sample holder, cell, diffusers, reactor, the set up was fed with 80% N_2 and 20% O_2 at 900 °C for a weekend to oxidize the deposits. The result was good but the sealing grease oxidized because of the higher operation temperature. It was cleaned with Acetone. It is then reported that that kind of grease is good as a sealing when the cell temperature is not higher than 850 °C.

A new cell is used. Also new gold meshes are cut. The golden wires are spot welded to the mesh with the same operation values of the welder of the last experiment. One purpose of these experiments is also to check qualitatively whether there are important leakages, so an H_2 detector is used. No leakage is found, however a modification to the setup for inserting a bubble flowmeter is

projected and planned for next experiments, in order to have a rough quantitative check.

As a heating rate, 60 °C/hour is chosen, much safer than for former experiment. A 100 Nml/min dry N_2 flow is used. After one night, reduction is performed at 750 °C: gradual switch to H_2 starting from 25/85 Nml/min of H_2/N_2 is done. Steps of 5 Nml/min until 40 are employed, then steps of 20 Nml/min until 100, then steps of 50 Nml/min, while N_2 is set to zero. Eventually 200 Nml/min H_2 are flowing. The whole reduction takes about 35 minutes. Afterwards, H_2 is humidified at 30 °C (4.2% humidification). One hour is chosen as a stabilization period (more than for the former experiment, by experience), after which the first spectra are recorded. At the end of the whole experiment (around four days) apparently the cell is not broken or cracked due to thermal fatigue, but it looks damaged by the gold wires. Some darker spots also show up on the anode surface and the holder seems to be dirtier than before the experiment. Maybe some carbon is still hanging around in the pipes and it detaches at high temperatures and long time exposure. The temperatures of the controllers are: 35 °C top of the humidifier, 30 °C the humidifier (to have 4.2% saturation at equilibrium), 106 °C the traced pipe, 153 °C ceramic holder.

First spectra are recorded before the weekend. Condensation starts once more at connection of the inlet pipe. Then while running the setup the tracing of the inlet pipe is enlarged, by adding a layer of isolating tape over the Aluminium foil covering the resistor. In addition the temperature of the quartz holder is raised to 155 °C. After these modifications condensation apparently stops. Experimental conditions are made harsher by a great drop of ambient temperature too. Spectra after the condensation problems still look variable both in the high and the low frequency part. Catch up of formerly condensed water is believed to be cause for some of them to show a lower mass transport arc. Some spectra show a capacitor at high frequency instead of inductance and much noise in the high frequency part. It is found that behaviour becomes much better if the wires are drifted apart. It is suggested that mutual magnetic interaction between the four wires be the cause for such behaviour. However more stabilization time may also be needed.

The setup is then kept running in temperature for the whole weekend (about 65 hours). After this period the H_2 flow is again set to 200 Nml/min. It appears that less time is needed for stabilization, since the sample is already reduced. After

about 30 minutes the first spectra are taken. Noises are much reduced and the arcs well defined. The f range is 0.1-100000 Hz this time. Some points are added at high frequency to check if the inductive behaviour of the wires is now as expected. But the inductance at high frequency is still almost zero, which means some capacitive elements could be still overlapping to the inductance of the wires. This will not influence much the behaviour and effects are recorded only in the very high frequency region. However the wires are checked again during the experiment and the problem is solved. The flow is then switched to 400 Nml/min and let stabilize for one more hour. It seems that actually it needs more, but noises could be ascribed once again to the interactions with the wires. Eventually 100 Nml/min is set as a flow and let stabilize for at least one hour. Spectra are recorded. After 15 more hours the flow is set to 200 Nml/min humidified H_2 again and the cell temperature is raised up to 850 °C with steps of 2-3 °C/min, with 30 minutes for stabilizing at the end of the sweep. A blackout occurs, which causes the temperature to drop to 750 °C. When all the conditions are restored, two spectra are taken. However, one hour is let in between and more spectra are recorded to check if the blackout had any effect on the cell. No good spectrum is obtained anymore, so that the system is cooled down.

The same circuit as for the former case is chosen for fitting. Here Nyquist and Bode plots are presented as a starting point for qualitative evaluation.

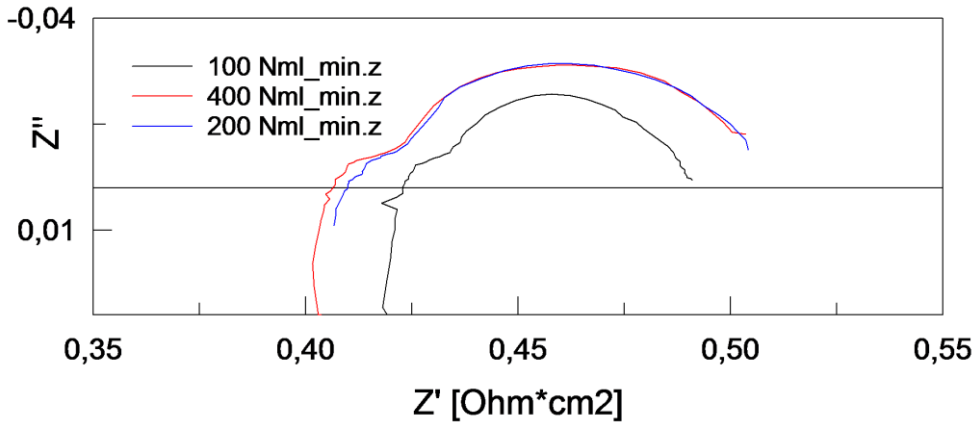

Figure 3.11. Nyquist plots of the spectra recorded at 100, 200, 400 Nml/min volume flows and 750 °C in the second test on the same day.

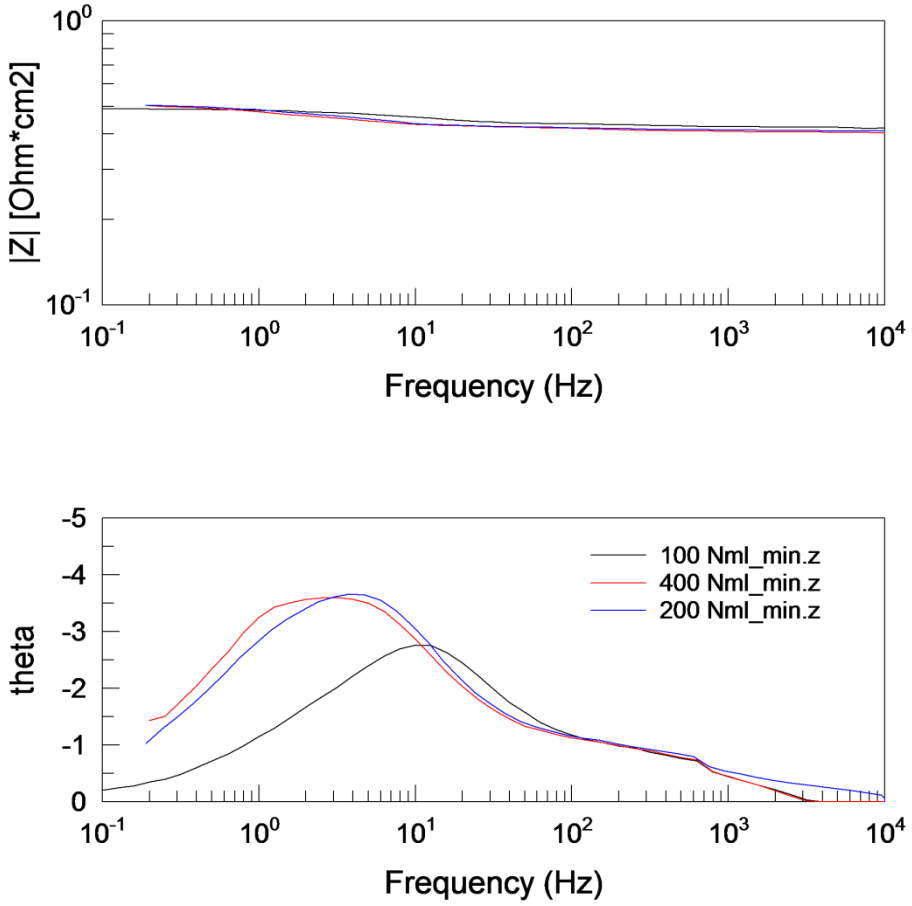

Figure 3.12. Bode plots of the spectra recorded at 100, 200, 400 Nml/min volume flows and 750 °C in the second test on the same day.

These spectra are taken during the same day, at 750 °C, with variation of flows. At a first sight, these spectra seem to agree with Aravind's and Sarda's in shape and range of resistances. Most of the problems from the former experiments are fixed. There is good agreement between spectra with 200 and 400 Nml/min H_2 flow, while the spectrum at 100 Nml/min behaves differently. In particular it is noted in the Nyquist plot that the low frequency region is significantly smaller, while in the Bode plot that the peak frequencies of the medium and high frequency arcs shift to higher frequency. Moreover, a sudden shift to the right when flow is switched to 100 Nml/min is recorded. A qualitative comparison of the results for 750 and 850 °C with Sarda's and Aravind's spectra is also useful.

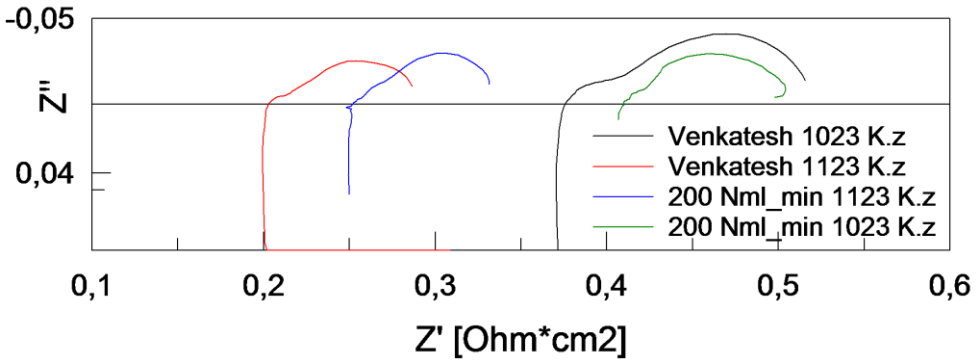

Figure 3.13. Comparison of representative spectra at 750 and 850 °C with Sarda's.

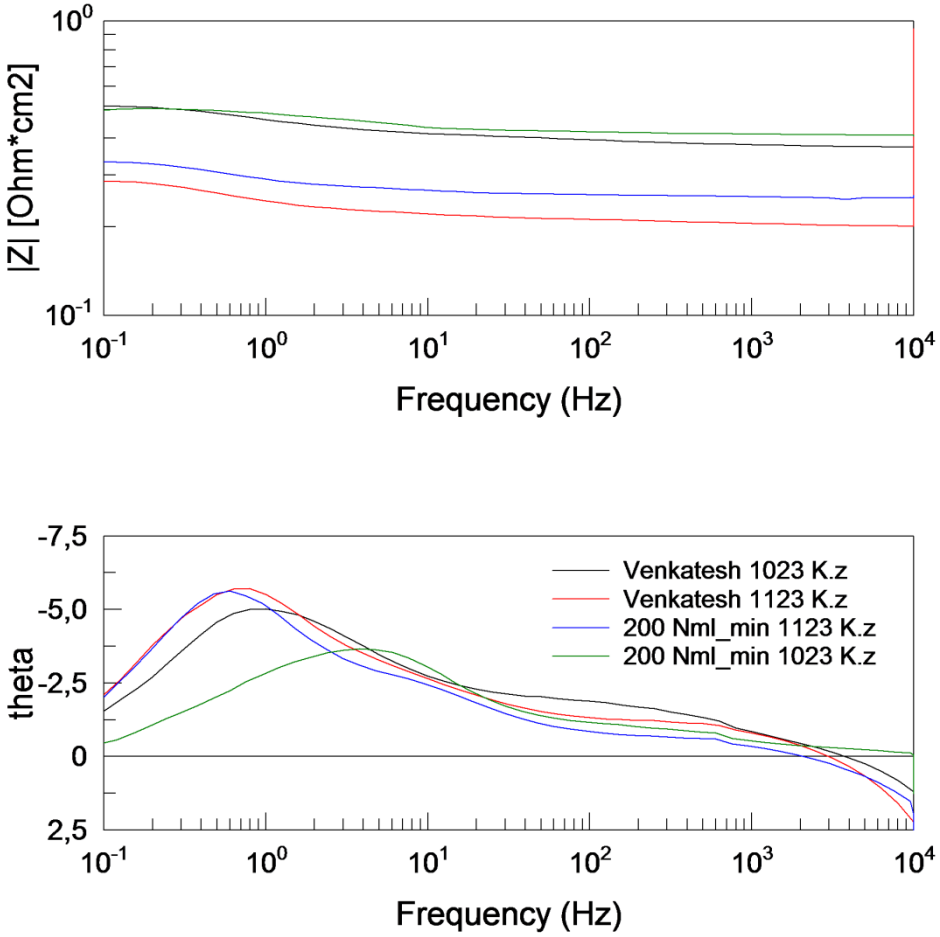

Figure 3.14. Bode plots of the spectra compared with Sarda's.

Sarda's spectra at 750 °C are found to be bigger, mostly in the high and intermediate frequency region. This can't be explained because the exact experimental conditions which were employed in that study are not known. Along the duration of the experiment (around 110 hours) great degradation is recorded, revealed by continuous increase of the series resistance. So difference in series resistance between the present results (black and green in the figure) and Sarda's is ascribed to degradation. In fact, these spectra were recorded after three days of operation. The ones of the first day had the same series resistance as Sarda's. Also Aravind's results are shown, for 750, 800, 850, 900 °C.

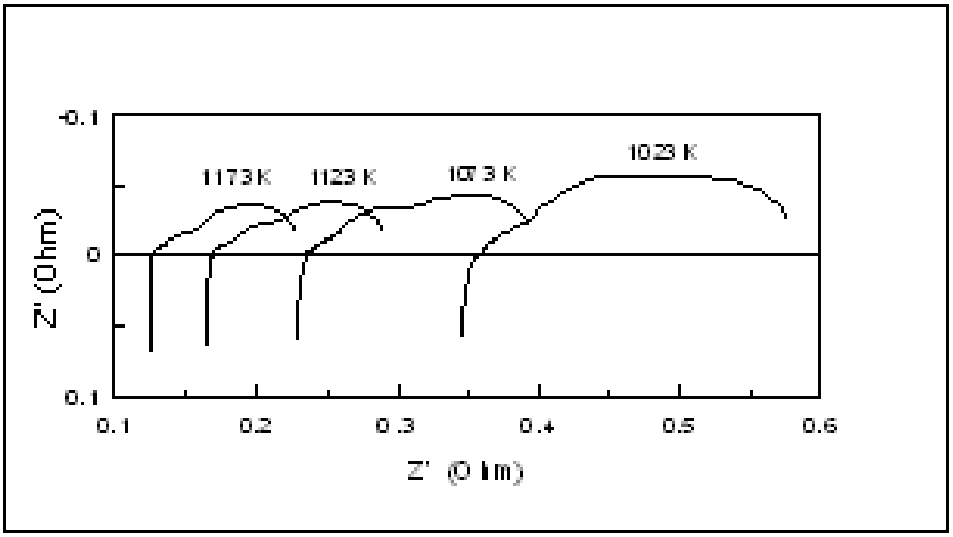

Figure 3.15. Spectra from Aravind's study at the different employed temperatures.

For causes of all these differences and effects of the experimental conditions to be determined, fitting of all the arcs and detailed analysis of the spectra is carried out. Reliable results are available in literature with pure humidified H_2 and there's some agreement about some of the processes. But little literature is available about experimental issues and effects of the components of the global system on the spectra. It is intended to reach more a solid understanding of how the system works. It is confirmed and it will be further explained that the fitting result highly depends on how the fitting is performed. The instant fit function on ZView for single arc fitting can give significantly different results depending on which point is decided to be the limit of the arc. Actually, this is a weakness of the method and KK transform function doesn't avoid it completely. If even slightly different values from instant fit are used as starting parameters for the equivalent circuit, totally different results may be obtained. Chi-squared

distribution, which is an output of the program, could not show this problem. This is why, keeping the same equivalent circuit, many fittings are performed for each arc and the results are compared to find what the average trend is. When a spectrum is found to be out of range, fitting is repeated, with the only change in the initial parameters. Corrected results are shown. Resistances from the results are divided by two (because the output includes contribution from both the anodes) and multiplied by the surface of the cell, since the output is given by the program in [Ohm*cm^2] assuming a surface of 1 cm^2 [2]. The actual surface is 3.8013 cm2.

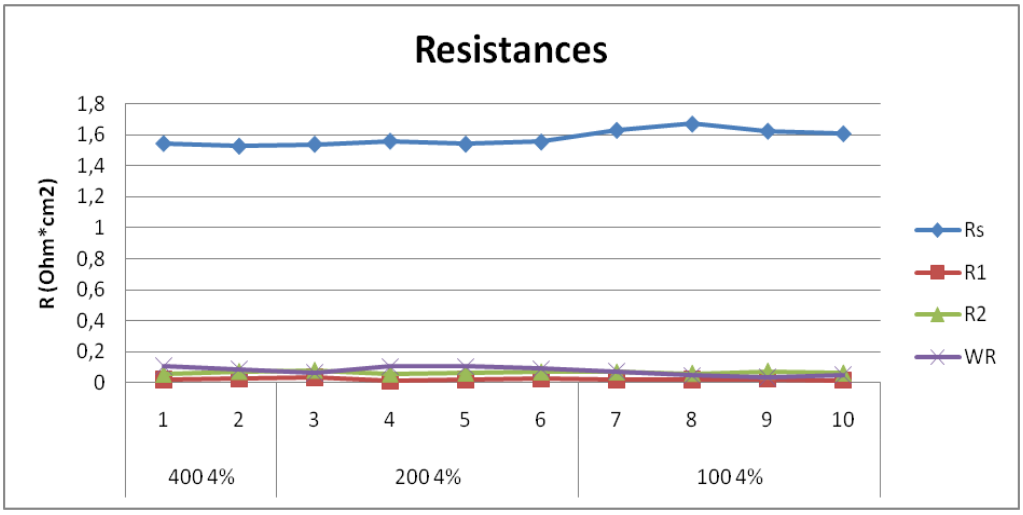

Figure 3.16. General trend for resistances.

The first global overview shows that in general values throughout the experiments are more or less constant, as it should be. Variation of the flow rate is not expected to result in variation of any of the arcs from the spectra (as long as the range is limited) and R_s is not expected to change either, since humidified H_2 is safe for operation of the cell. Anyway a more in-depth view reveals interesting details:

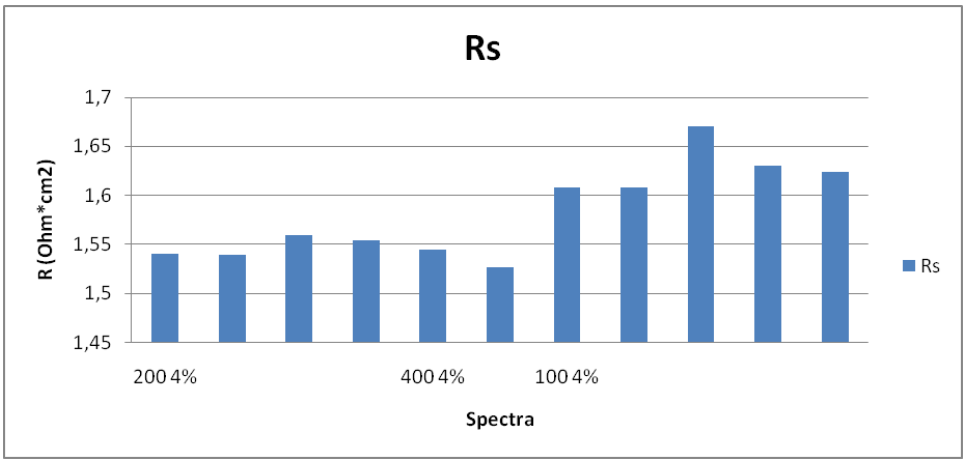

Figure 3.17. R_s oscillation during the same day of experiments (not due to degradation).

Here the series resistances of some spectra as recorded on the same day are shown in a temporal order from left to right. As it was already clear from the Nyquist plots, R_s of spectra at 100 Nml/min is in average higher than R_s of the others. There is no clear explanation for this, since it contrasts with every evaluation about the other resistances, as it is discussed here below. On the contrary, if resistances from spectra of different days are presented, general trend becomes clear, which shows high degradation rate (strong increase in R_s). It comes out that this degradation rate is faster in the first day, when the biggest condensation problems occur, while it stabilizes more after the weekend, when working with 200 and 400 Nml/min. The last big increase is the one shown by 100 Nml/min.

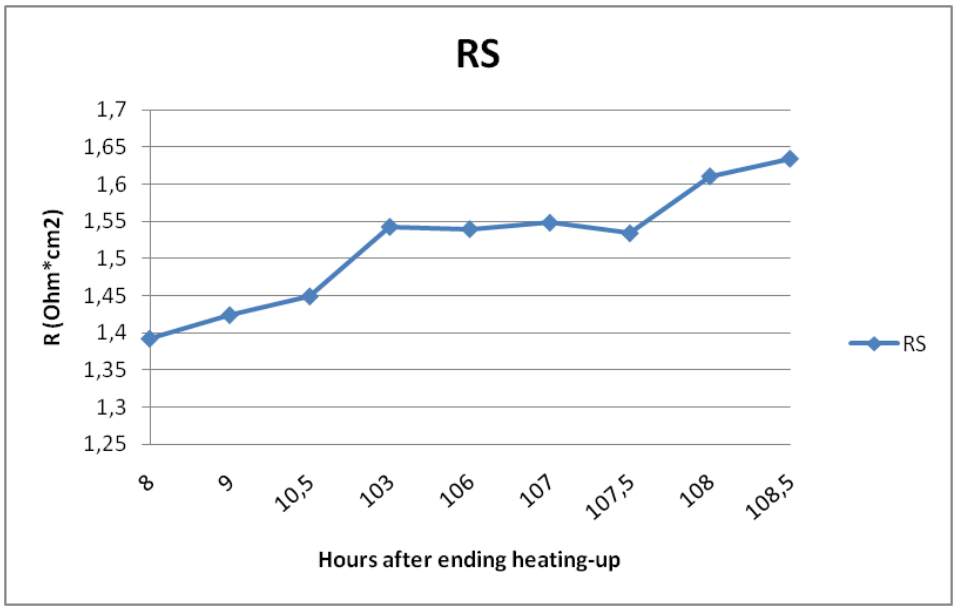

Figure 3.18. Rs change with time during the hole experiment.

R_s is made of the contribution from the electrolyte and from the contact with the current collectors. Then high degradation rate could derive either from a progressive worsening of the contact between the anode surface and the gold mesh or of the spot weldings, either from damage in the structure of the cell. As for the worsening of the contacts, this causes R_s to increase, but it is suggested the degradation rate slows when humidification is improved, because water is electrically conductive. Otherwise, continuous change in Rs could be ascribed to humidification problems, since a variation also shows up when the flow is switched to 100 Nml/min, that is, when sudden change in the low frequency arc is recorded too. An explanation is looked for into literature. P.Kim et al. [5] studied the effects of water starvation on the anode, using Ni-CGO/YSZ/Ni-CGO symmetrical cells. They investigate the behavior of the spectra when varying moisture fraction in the gas feed and temperature: temperature is varied from 873 to 833 K, while the feed is switched from 97% H_2 – 3% H_2O to 97% H_2 – 3% N_2 (moist to dry hydrogen). They record two main arcs. When decreasing the operating temperature the high frequency arc increases significantly while the low frequency one remains constant, when humidified hydrogen is fed. On the contrary, when dry hydrogen is fed, the variation of the high frequency region is the same as with humidification (so the arc is ascribed

to charge transfer processes), while the low frequency feature varies with temperature when it is not supposed to. Moreover, the time constant of the low frequency arc increases by a large amount, indicating that the controlling process is probably no more mass transfer. The change in the low frequency arc is then ascribed either to slow surface diffusion and dissociative adsorption of H_2 (due to lack of oxide species, which is also a consequence of water starvation) or to degrade shown by the anodes during the time range of the experiment (appearance of cracks was revealed by SEM analysis of the anodes). What the precise cause is for cracks to form is not clear. Also the electrolyte resistance keeps increasing during experiments, both with dry and humidified hydrogen. Moisture seems not to influence the degradation rate and this confirms that change in electrolyte resistance over time even with humidified H_2 may occur, as happened during the second test in the present study. Probably continuous variation in R_s along the experiment has not to be ascribed to humidification problems. Kim shows an increasing rate for R_s of 0.08 $\Omega cm^2 h^{-1}$ in 60 hours. The one recorded in the present experiment is however significantly lower.

Now the trend of the other resistances is discussed.

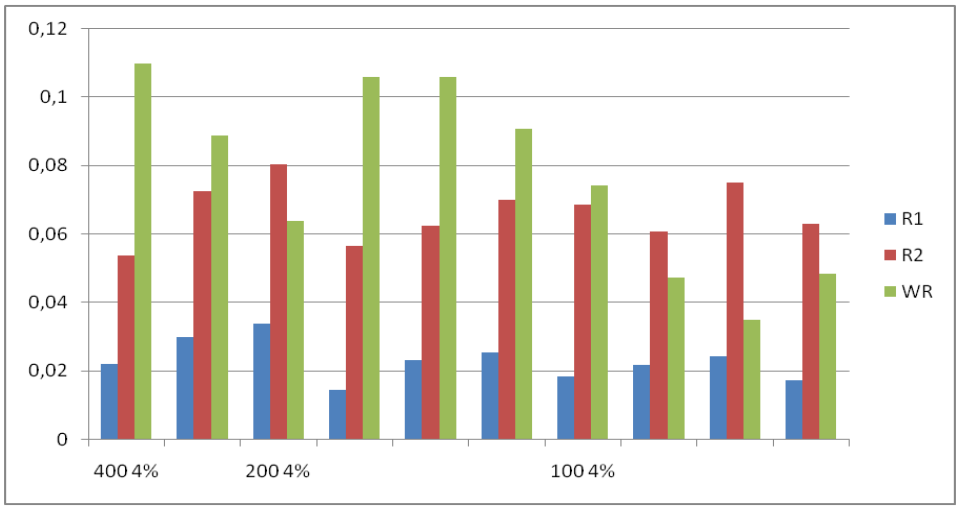

Figure 3.19. Comparison of the resistances of the three arcs.

Contrary to what was said about the degradation rate, this table supports conclusion that the large difference in R_s for spectra at 100 Nml/min H_2 may be related to humidification, though it is not understood why it is higher. It could also come from problems in the wiring and this needs to be further looked into.

Average decrease of WR when the flow rate is switched from 400 to 100 Nml/min is recorded. From Aravind's model and experimental validation [1], mass transport is enhanced by water addition, so WR is expected to decrease. Hence, it seems that sharply lowering flow causes it to be more humidified somewhere in the system. This also may be due to catch up of water which unexpectedly condensed and it has to be investigated deeper. In fact, it come out that for KCl experiments keeping the flow between 200 and 400 Nml/min will be safer, but what problems occur at lower flows helps understand the limitations of the setup.

Eventually a table with mean, variance, standard deviation of the parameters from the fittings is presented. The values are calculated over a few cases, but here it is only intended to show the range for each one and its variability. A more detailed analysis will be carried out in the next section.

Table 3.2. Preliminary statistical analysis of data recorded in the second experiment.

	400 4%			200 4%			100 4%		
Peak f (Hz)	mean	Var	St. D.	mean	Var	St. D.	mean	Var	St. D.
ARC1	185,33	642,98	25,36	219,73	590,05	24,2909	266,46	2277,43	47,72
ARC2	4,64763	0,3486	0,59	5,5909	1,7624	1,32755	11,32	5,21194	2,283
ARC3	0,84359	0,0153	0,124	1,0501	0,0449	0,21198	1,8527	0,20088	0,448
C (F/cm^2)	mean	Var	St. D.	mean	Var	St. D.	mean	Var	St. D.
ARC1	0,07117	0,0004	0,02	0,0592	0,001	0,03209	0,0592	6,1E-05	0,008
ARC2	1,04023	0,0012	0,035	0,8601	0,0652	0,25537	0,4064	0,00969	0,098
ARC3	0,5968	0,0332	0,182	0,4474	0,0224	0,14971	0,3201	0,02767	0,166
R ($Ohm*cm^2$)	mean	Var	St. D.	mean	Var	St. D.	mean	Var	St. D.
Rs	0,76787	4E-05	0,006	0,7741	3E-05	0,00508	0,8167	0,00018	0,013
R1	0,02585	3E-05	0,006	0,0241	6E-05	0,00801	0,0204	1,1E-05	0,003
R2	0,06316	0,0002	0,013	0,0673	0,0001	0,01024	0,0667	4,2E-05	0,006
WR	0,09926	0,0002	0,015	0,0915	0,0004	0,01981	0,0512	0,00027	0,017
Pol.	0,18827	2E-05	0,004	0,1829	5E-05	0,00689	0,1383	0,00024	0,015

It is then concluded that more problems have to be figured out and some of the recorded behaviours need to be further investigated to check whether they have

physical meaning. This can lead to final conclusions about the influences of the reference setup over results of the measurements and to get reliable and reproducible results. Moreover, further analysis at 850 °C is needed. This will bring multiple advantages: some phenomena which occurred at 750 °C and which are thought not to be influenced by temperature will be checked at a different temperature; reference arcs at the temperature for KCl experiments employed by Aravind (850 °C) will be recorded; by changing one condition with respect to the former experiment and reproducing the others, more information can be obtained about behaviours which have not been explained yet. Eventually it was concluded that a procedure for fitting the arcs must be formalized and standardized, with help from a statistical analysis of the results. This way the presented errors coming from the "Instant fit" and the operator himself can be minimized and a more reliable post-processing procedure and more reliable results can be found.

3.4 Third test

Experiments with 400, 200, 100, 80 Nml/min will be carried out, in order to further investigate the influence of the variation of the flow which was noted in the former test. A range in which results are stabile and reproducible must be found, to set the flow for KCl experiments within that range. In fact, whenever problems are encountered, they mostly appear in the low frequency region of the spectra and this must be avoided, since Aravind [1] recorded an unexpected behaviour with KCl in that very region. Once again it must be kept present that the low frequency region is the most suitable for detailed analysis with this kind of cells and setup, because it is the dominating part of the spectrum. Finding a trend in the high frequency part is difficult, since values of the resistances are much smaller and relative noises are significantly higher: the employed anodes are high performing anodes; if TPB processes are to be studied, ad hoc SOFC anodes must be built, which widen the high frequency response, and a setup which avoids diffusion limitations must be used. The safe operation volume flow range seems up to now to be between 200 and 400 Nml/min according to former experiences, but this must be confirmed with more reliable measurements. Moreover, behaviour at low flows hadn't showed any unexpected result in Aravind's experiments with a similar setup. Humidification for each flow is varied from 3 to 4 to 7%, in order to compare the lowering of the low frequency arc with flow to its lowering with higher water content. One

first hypothesis from former results is that low flows get totally saturated in the single-pot humidifier, while non-ideal conditions are reached for higher flows. This must be verified either. Varying humidification is also considered to be useful for verifying if and where condensation still occurs after improving the isolation and for setting the conditions for the flows in the experiment with KCl (this will be explained in the modelling chapter).

Building-up and heating-up procedures are the same as in former experiments. Platinum wires from the sample to the FRA are checked and better fixed with respect to last measurements. From observation of formerly used samples carbon deposition seems to have occurred again. This may then be due to use of paraffin as sealing grease. It is replaced with Si based grease. Isolation of the traced feed pipe and of the quartz holder is further improved and their temperatures are set to higher values. Reduction is different due to the different scale of the new mass flowmeter for H_2: it has a full scale value of 1500 Nml/min, hence the least controllable flow is 37.5 Nml/min (2.5%). At 700 °C the flow is switched first from sole N_2 to 80/100 Nml H_2/N_2 for 20 minutes, then to 150/70 Nml for the same time, to 200 Nml/min H_2 for 15 minutes and eventually to 400 Nml/min. Temperature is raised to 850 °C and let stabilize for 2 hours after finishing the ramping. A check of the temperature at the outlet of the reactor, after the oven, is made with a laser thermometer, to verify whether it is low enough to seal the connection for the ICP setup with normal sealing grease (below 250 °C). It is found to be around 150 °C, completely safe.

First spectra seem stabile, but they soon begin to be unreadable. Only after more than 3 hours the results are stabilized, appearing to be in line with those of the former experiment at 850 °C. After switching the flow again to 200 Nml/min one night elapses before new experiments. Results once again are in line with the former ones and perfectly fitting those at 400 Nml/min. Eventually flow is switched to 100 Nml/min to confirm the variation observed in the former experiment. Unstable behaviour is observed for two hours, with generally small spectra. Then the shape stabilizes, fitting the arcs at 200 and 400 Nml/min. It appears then that two different behaviours can be recorded at 100 Nml/min, as if some condition changed with such a low flow. To verify this, flow is decreased to 80 Nml/min. Stabilization is reached within two hours, to very small spectra (mainly due to much a smaller Warburg resistance) and no change is recorded for 20 hours. It seems confirmed that at low flows two shapes can alternatively arise, one perfectly fitting spectra at 200 and 400 Nml/min (which is expected),

one much smaller (due to something occurring in the setup). This will be investigated. After every night, a switch of the arcs to the left, to slightly smaller series resistances, is recorded. This switch is more intense and continuous when performing experiments at 80 Nml/min. Measurements at 200 Nml/min and at 80 Nml/min at 7% humidity follow. This is obtained by raising temperature of the humidifier to 39 °C. This moisture concentration is close to the one which is planned for the highest needed humidification in KCl experiments (it will be shown in the modelling chapter). No condensation is apparently detected, but temperature of the tracing of the quartz is increased to make sure. No significant Ni oxidation is expected through equilibrium calculations with this amount of water (see chapter fivre for details). Spectra are all the same, stabilizing fast and not oscillating. Spectra at 80 Nml/min fit those at 200 Nml/min, thus being bigger than those at 4% with the same flow rate. With switch to 3% of moisture the behaviour is once again different. Both at 80 Nml/min and 200 Nml/min continuous oscillation of the low frequency arc is observed. This seems to be due again to difficulty in stabilizing the water concentration after switching from 7% to 3%. It will be further investigated. As a general trend, arcs at 200 Nml/min are consistently bigger than those at 4% humidity, arcs at 80 Nml/min are in line with those at 4%, thus following the smaller of the two recorded behaviours. One final check at 80 Nml/min with 7% humidification is made in order to confirm that measurements have not been affected by externalities. Same exact behaviour as for former measurements at 80 Nml/min and 7% is recorded. When conditions are changed it is always verified that the temperature of the cell keeps constant. Maximum variations are around 1 °C (0.12%), hence they can't result in any noticeable change in the spectrum. When flow is decreased, an increasing in temperature by 0.5-1 °C is noted as well. A larger flow provides a larger heat exchange rate and with a constant temperature of the oven the temperature of the cells lowers a little.

To make sure that not big leakages are occurring, a rough but fast and effective method for checking the flows is used, with a bubble flowmeter (the working of which is explained in chapter 4). A leakage detector helps in finding if there is effectively a leakage and in detecting its position. A bubble flowmeter gives a rough quantitative esteem of its intensity. Three measurements are taken:

Nominal 100 Nml/min N_2: at indication of 100 Nml time is 53.88 s.

Nominal 100 Nml/min N_2: at indication of 50 Nml time is 28.51 s.

Nominal 100 Nml/min H_2: at indication of 35 Nml time is 20 s.

In all three cases flow is found to be around 100 Nml/min as indicated by the mass flowmeter, but it must be kept present that this is a hand-made measurement and error may be bigger than the possible leakage.

Here again a detailed presentation, analysis and comparison of the most significant and representative spectra is made, in order to explain mostly the phenomena which were observed and not expected. It is intended to draw conclusions about the behaviour of the employed experimental setup, as to make following experiments with KCl reliable and reproducible. An explanation for the unexpected behaviour at low frequency will also be reached. Particular attention will be given to elapsing times between recorded phenomena and to the time trend of the fitted parameters. If changes are to be ascribed to particular processes, they must be located in the timeline. Moreover, from former experience, it is decided to post-process results with a statistical analysis over the dozens of recorded spectra. This way results are made more solid with respect to mistakes of the operator in fitting and a formalization of the fitting procedure is reached.

3.5 Detailed discussion of results of the third test

As a first indication, the Nyquist and Bode plots of the representative results for each flow at 4.2% humidification are shown.

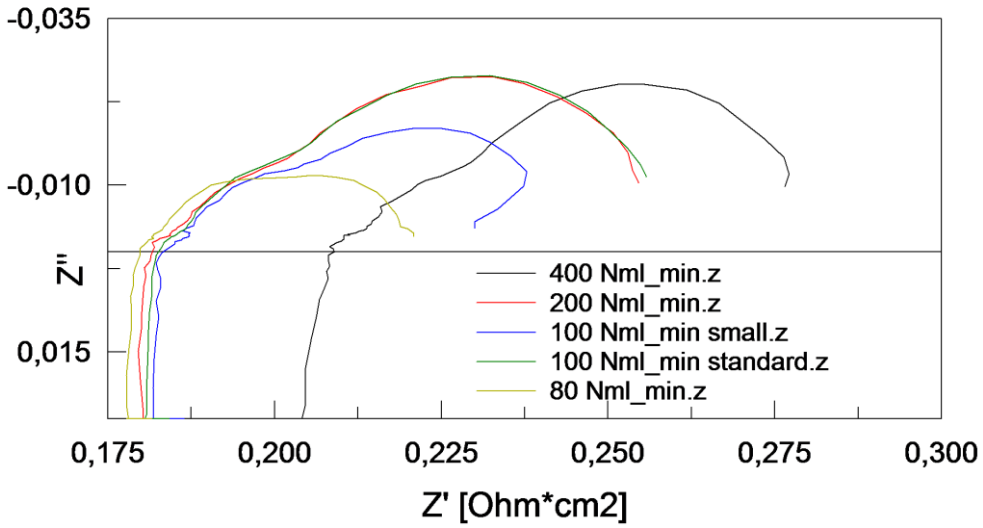

Figure 3.20. Comparison between spectra recoded at different flows (not necessarily on the same day) at 4.2% humidification.

At 200 and 400 Nml/min there is again agreement in shapes and dimensions. This supports conclusion that working between those flows gives the most reproducible results. Noises in the high frequency part are due to the already mentioned problems of stabilization on the first day of the measurements. At 100 Nml/min at first the low frequency part seems to be lower, then it stabilizes exactly on the shape of the arc at 200 Nml/min. With low flow, then, results seem to alternate between a small feature and a standard feature, which is what theoretically predicted (the shape of the arcs should not change with flow, unless starvation occurs). The mass flow rate is then lowered and at 80 Nml/min it fast stabilizes to a small low frequency arc, which doesn't change for more or less 15 hours. Observed stabilization times can be summed up: it took almost 24 hours after starting the heating-up to have the first reliable spectrum; results at 200 Nml/min are perfectly stabilized since they are taken after one night; with 100 Nml/min the first stabilized spectrum is obtained after 3.5 hours. It is then possible that in the former experiment when 100 Nml/min flow was fed more time was needed for stabilization. At 80 Nml/min no significant change is recorded already after 2 hours and 15 minutes, until the day after. It is assumed to be completely stabilized to a small feature.

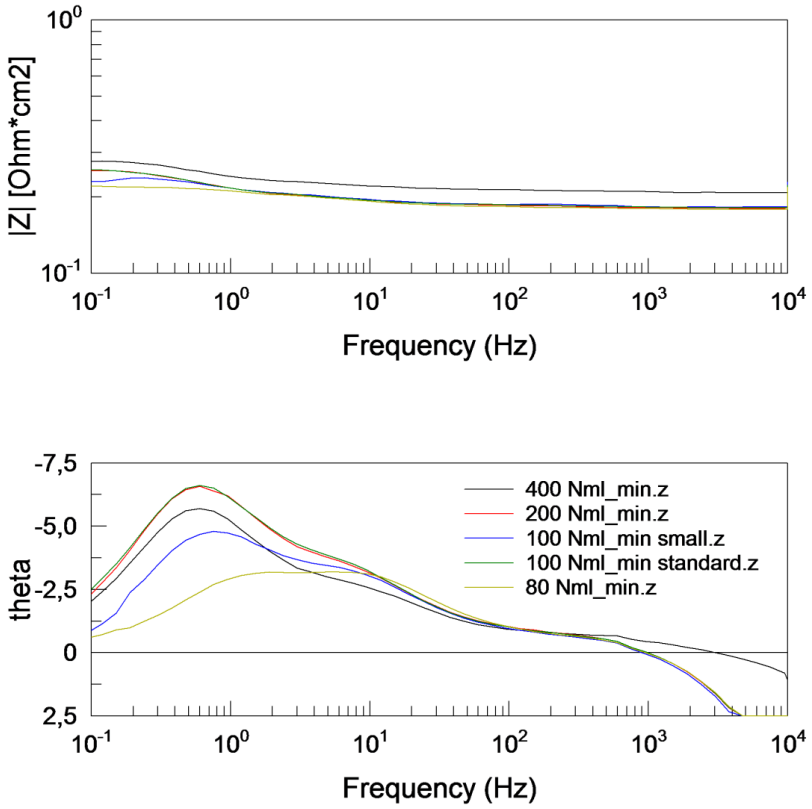

Figure 3.21. Bode plots of the results from different flows at 4.2% humidification.

Variation in the peak frequency and phase amplitude is also observed. This plot can be compared to the one recording variations with humidification, to get information about what the experimental issue is with flow variation. A comparison with results of the former experiment gives a qualitative indication of the change in the shape from 750 °C to 850 °C and of the general agreement with results at 850 °C:

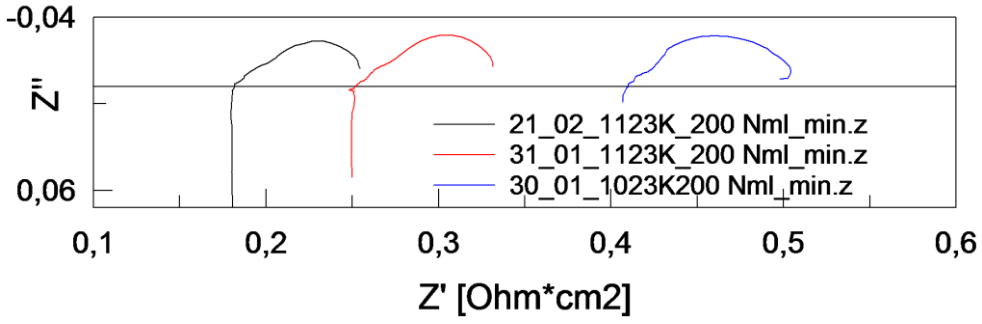

Figure 3.22. Comparison with results from the former experiment.

The shapes at 850 °C are concluded to be reproducible. The difference in Rs is due to the strong degradation recorded in the second experiment. The spectrum at 750 °C shows a higher electrolyte resistance, higher R_1 and R_2 and an almost constant low frequency arc, which is all expected. Individual values will be discussed, but a qualitative analysis already gives information about what is expected by a numerical analysis and about the orders of magnitude.

Since differences between 400 and 200 Nml/min were never recorded, for the other two humidity levels only 200 Nml/min and 80 Nml/min are kept as a reference. Here some of the spectra.

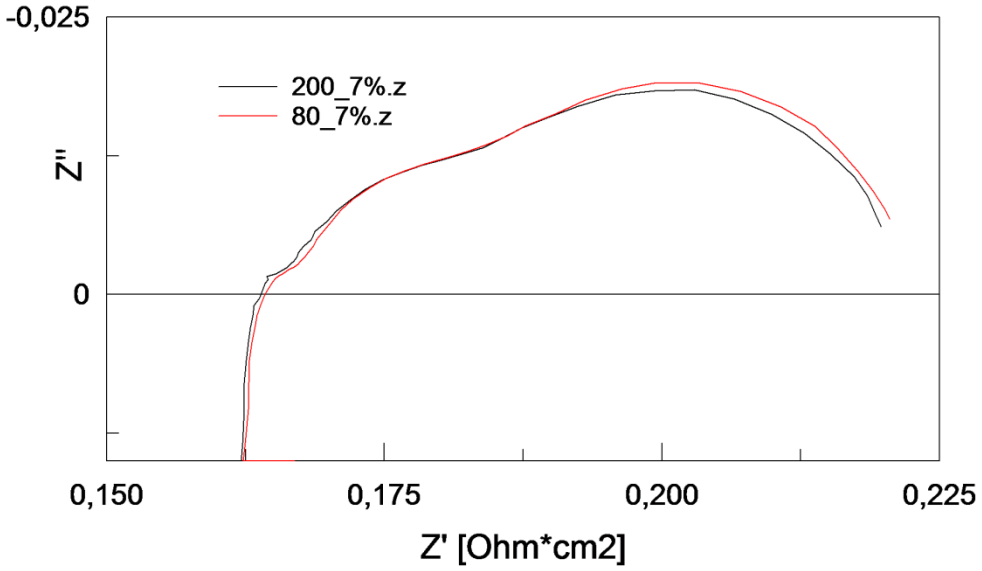

Figure 3.23. Results with different flows at 7% humidification.

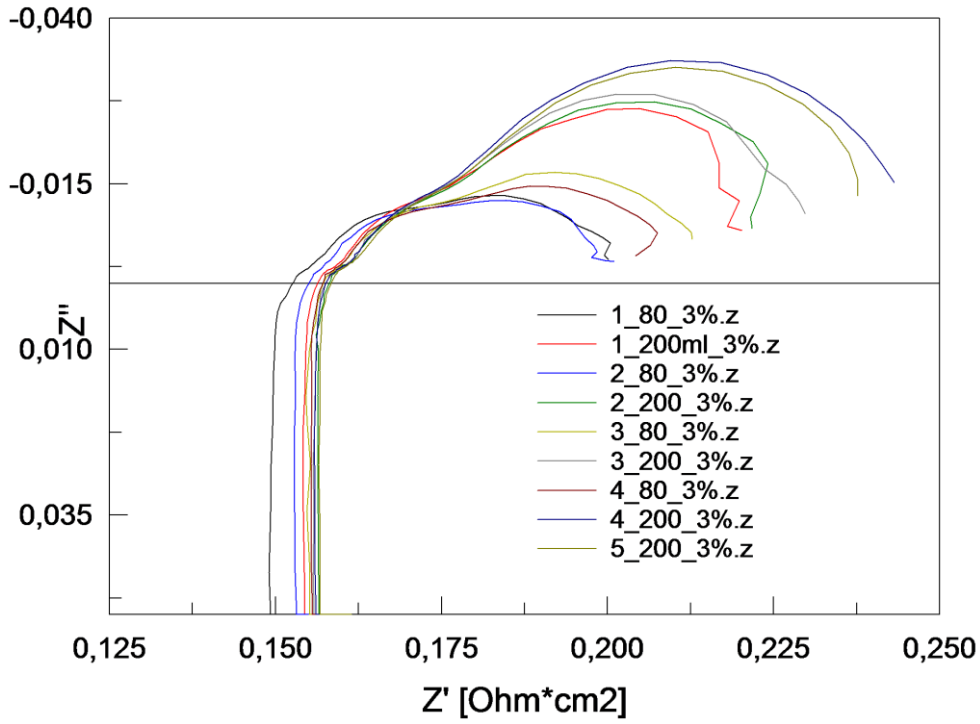

Figure 3.24. Results with different flows at 3% humidification.

Behaviours for low flow at 7% and 3% are found to be contrasting. When, for 200 Nml/min, humidification is switched to 7% it only takes 1.5 hours to stabilize. Afterwards, flow is decreased to 80 Nml/min and it keeps the same shape all along 3.5 hours. It is then considered to be stabilized and it behaves like 200 Nml/min. The behaviour with small low frequency arc doesn't show up, unlikely what observed at 4%. On the contrary, when humidification is decreased to 3% (25 °C of the humidifier from equilibrium calculations for ideal gases) the low frequency arc seems once again to be smaller than theoretically expected, in line with case at 4%. It is one more time observed that no gradual change happens at low flows, but only two behaviours separated by a step appear. As is clear from the picture, both low frequency features at 80 and 200 Nml/min oscillate. This is believed not to be due to stabilization, since all the spectra are recorded one night after changing humidification. On the other way, it is likely that water causes this behaviour: it might be possible that water cumulated somewhere in the pipes or over the anodes, causing the response not to be unique along time. Probably such phenomena take much more time to disappear. Obtaining conclusions about what happens at low flows may also give information about this issue.

A comparison with the stabilization times at 750 °C is hardly reliable, since in the former experiment too many externalities affected the spectra (condensation in the pipes, wiring effects...) and made them variable. The only valuable observation is that all along the first day of the second experiment the arcs were not well defined, which means that also in that case at least 24 hours were needed from the time the setup was switched on to stabilize the cell.

The last observed behaviour from visual analysis of the spectra is the continuous decrease in R_s during the experiment, which totally contrasts with the strong increase of the former experiment. One suggested cause for this is the progressive sintering of the gold meshes on the anode surfaces: in fact, after cooling down, the meshes are found to stick over the anodes and hardly separated. Be it kept present that in the former experiment the temperature was 100 °C lower. No other unexpected and sudden variation of R_s is recorded, contrary to the former experiment and this seems to confirm that sudden variations recorded were not due to change of flows and possibly related humidification issues, but only to electrical contacting problems. Here a graph is presented with the trend of R_s along the total duration of the experiment (82-83 hours after the 12 hours needed for ramping up):

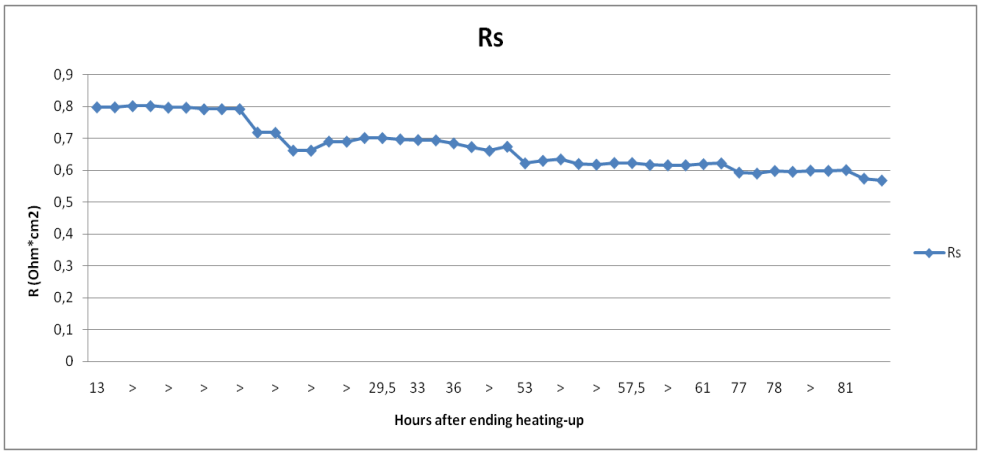

Figure 3.25. Trend of Rs during the whole experiment.

Now a quantitative analysis of the results is presented. As already demonstrated, the result of the fitting is highly sensitive on the employed procedure. Firstly, a careful choice of the fitting circuit must be done based on literature references. It is however better to try different solutions and compare the results. Secondly, it must be kept present that a tool like the “Instant fit” function of ZView gives

variable results and if they are used as initial values for the equivalent circuit fitting, very different output may result. Sometimes it is noted that values for the first and the second arc come out inverted in the fitting, though their sum is equal. KK transform is found to be a good check for the number of assumed processes and their peak frequencies, but it is not enough to guarantee a reliable fitting alone. The same is said for Chi-squared distribution: the fitting is good only if the sum of Chi-squared is small, but not necessarily if Chi-squared is low the best fitting has been found.

Based on these considerations a procedure for fitting is iteratively refined during post-processing of the different results and eventually it is definitely employed for analyzing the spectra from the present test. Consequent steps are listed:

1. More spectra for each condition are recorded and fitted. Each one is fitted more times. From observation of the spectra it is inferred that results must be similar to each other, since they are this time stabilized, alike one another, very well defined. When a spectrum is found to be out of range, fitting is repeated giving as initial values those which were found to best represent the general trend from one of the formerly fitted spectra. Eventually mean and standard deviation of resistances of the spectra for each condition are calculated.
2. The ZView function “Merge/Combine data files” is used, to put the points from different spectra at given conditions altogether and find a circuit which best fits all the points at the same time (Chi-squared is minimized over more points for each frequency).
3. The same function is used to find a circuit which best fits all the individual fittings at a given condition.
4. Comparison between these three techniques is made.
5. A check on the mean values and relative errors of peak frequencies and capacitances of every one of the three arcs is made at all conditions, to find whether they lie in the expected range from literature (which was discussed in chapter two). Peak frequencies and capacitances are calculated from the parameters obtained by the fitting, which have no physical meaning but they are only numerical representations. Hence, they must be taken as a tool to confirm, but not as an absolute reference.

Results are shown, of the resistances of the $R_s(R_1Q_1)(R_2Q_2)(W_S)$ circuit and of the peak frequencies.

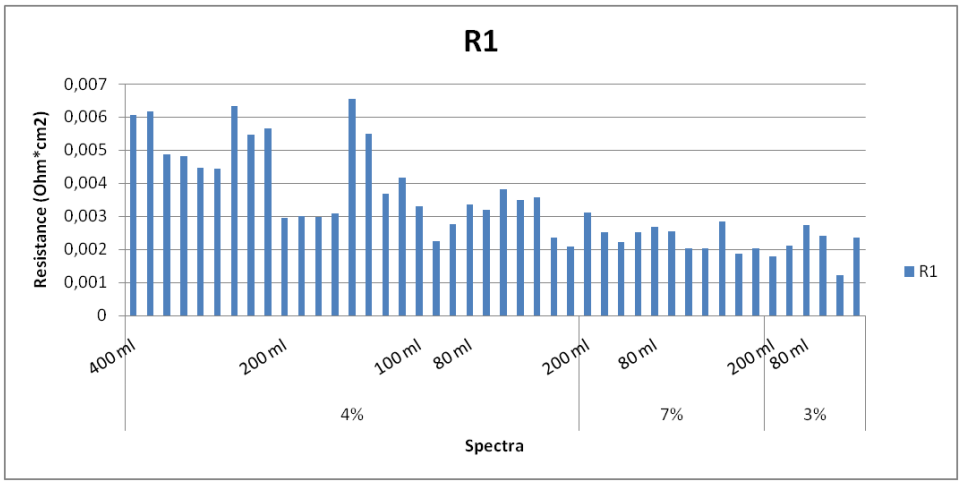
R1
Resistance (Ohm*cm2)
0,007
0,006
0,005
0,004
0,003
0,002
0,001
0
400 ml
200 ml
100 ml
80 ml
200 ml
80 ml
200 ml
80 ml
4%
7%
3%
Spectra
R1

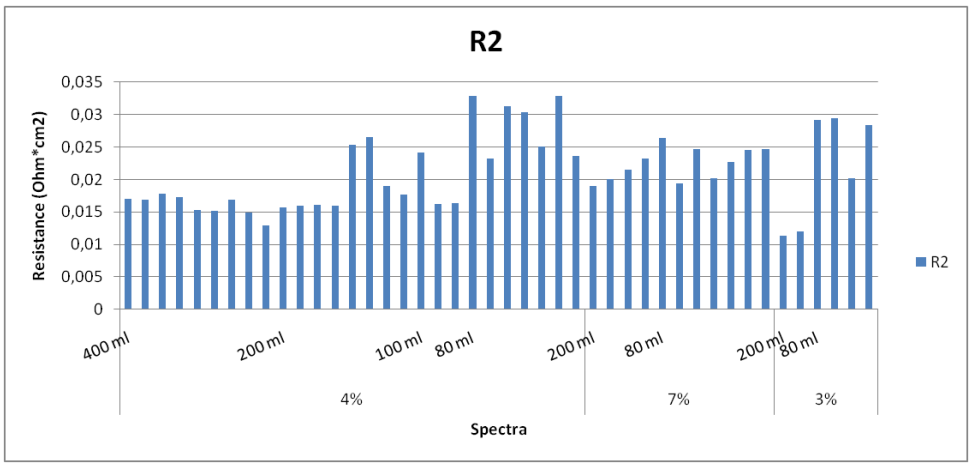
R2
Resistance (Ohm*cm2)
0,035
0,03
0,025
0,02
0,015
0,01
0,005
0
400 ml
200 ml
100 ml
80 ml
200 ml
80 ml
200 ml
80 ml
4%
7%
3%
Spectra
R2

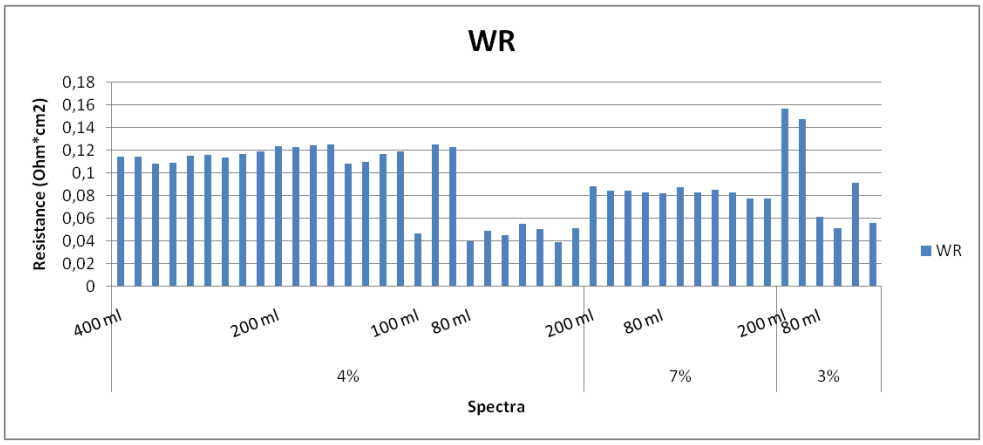

Figure 3.26. Values of the resistances for all the most significant spectra at the different conditions employed in the experiment.

The peak frequency for an RQ element is calculated as [2]:

$$fp = \frac{1}{2\pi \sqrt[P]{RT}} \tag{3.1}$$

where P and T are respectively the parameters from the fitting CPE-P and CPE-T (n and Q in theory) and R is the resistance of the arc. The peak frequency for the WS element is calculated as:

$$fp = \frac{2{,}53}{2\pi T} \tag{3.2}$$

where T is the WT element from the fitting of the Bounded Warburg.

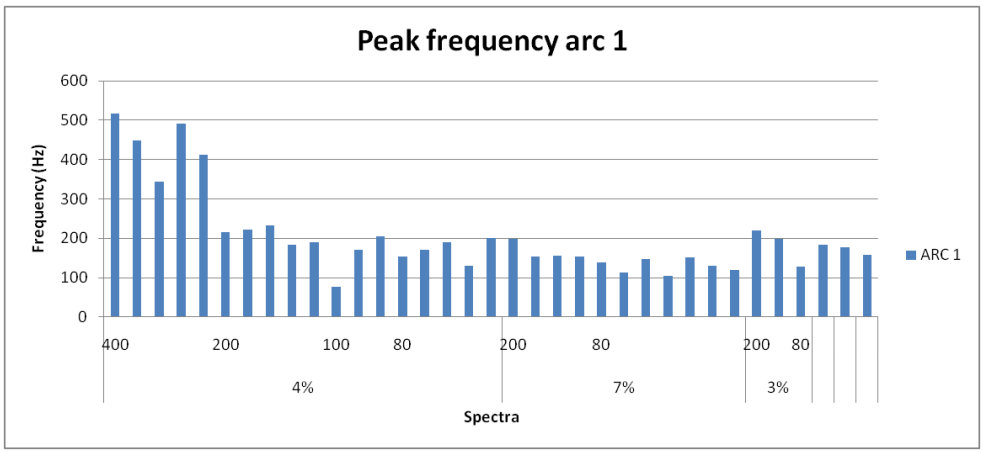

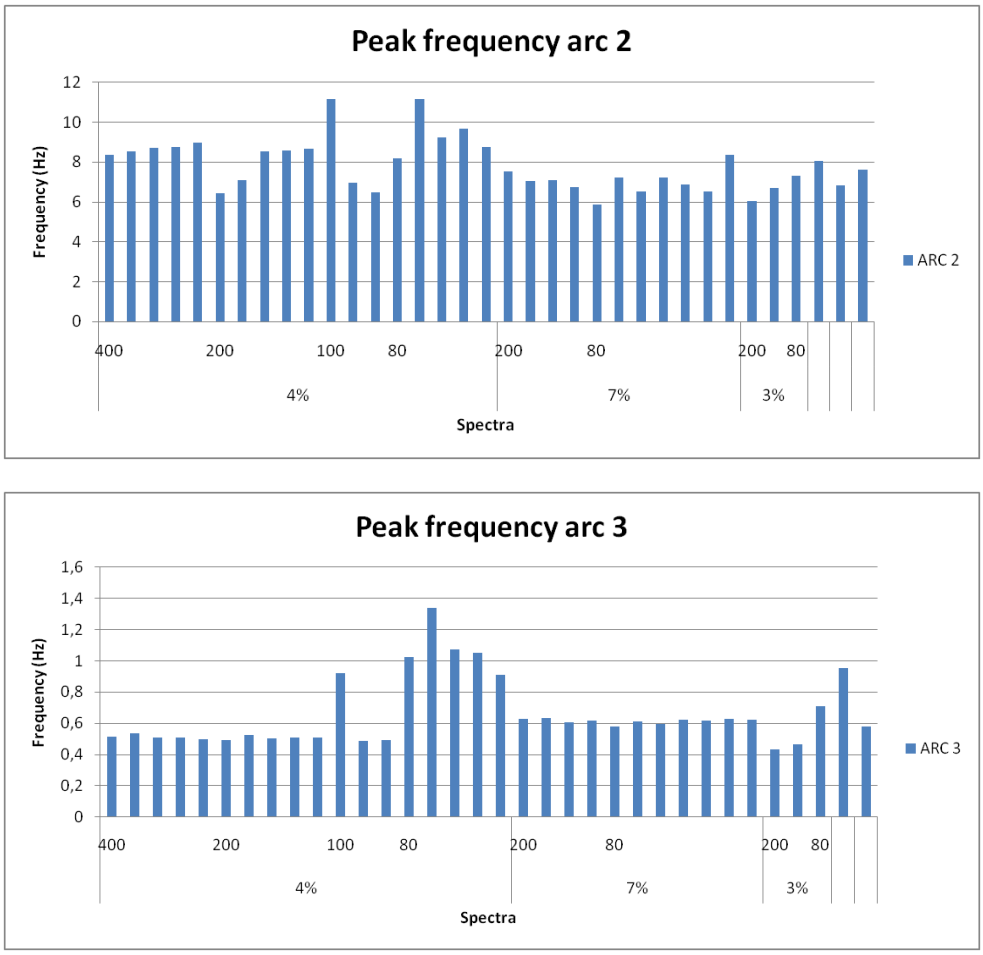

Figure 3.27. Peak frequencies for arcs 1, 2, 3, for all the most significant spectra at every condition.

R_1 seems not to have a clear trend, a part from 400 Nml/min, which appears to have higher R_1 in average. However it is hard to draw a conclusion about this: as already mentioned, the employed anodes are high performing and they are not suitable for detailed analysis of the kinetics. The same result appeared in the former experiment, though with more noise. Two more peaks are recorded for 200 Nml/min but both the presented values are from the same spectrum. It is likely that it had not a well defined high frequency part, in fact the other fittings are in line with each others. R_2 is higher in average with higher humidification and for 100 and 80 Nml/min at 3 and 4%. That is, either when humidification is effectively increased either when low flows appear to have a much smaller low frequency part, R_2 is higher. This supports conclusion that the medium frequency arc could arise due to a Red-ox couple in Ceria, as Aravind suggested

[1]. Higher water content, then higher pO_2, makes the environment less reducing and a red-ox couple in Ceria arises. The low frequency arc shows the clearest trends: they confirm what already observed by qualitative analysis of the arcs. The flow at 200 Nml/min follows the expected trend with humidification; 100 Nml/min starts with a small arc and then stabilizes on the behaviour of 200 Nml/min; 80 Nml/min shows a much smaller arc at 3% and 4% humidification, while it stabilizes as theoretically expected at 7%. The change in dimension for low flow at 3% and 4% is much bigger than the change due to controlled variation of the humidification up to 7%. This means that the hypothesis of better saturation when the flow is lower is disproved. The difference between conditions of ideal and non-ideal saturation would be much less. As for the peak frequency its variations are consistent with variations observed in the resistances: for R_1 the frequency lies between 100 and 200 Hz in all the cases except for 400 Nml/min, where it is higher, but of the same order of magnitude; for R_2 it shows smaller a variation than the resistance; for Warburg it is clearly observed that when the arc lowers, it shifts to the right in the Bode plot, to higher frequencies. This effect may be only due to its bigger overlapping with the intermediate frequency arc when their dimensions become more comparable. The same suggested Aravind [1] to explain variations in the peak frequencies when N_2 was added to the flow.

As an indication of how results change when the outlier spectra are fitted again, a comparison between standard deviations for resistances and frequencies is presented. Lowering of the values for standard deviations is taken as a measure of the improved reproducibility of the spectra:

Table 3.3. Standard deviations of the values of the resistances with the original fittings and with correction of the wrong fittings.

Standard dev. (Ohm*cm2)	400 4%	200 4%	100 4%	80 4%	200 7%	80 7%	80 3%	200 3%
With outliers								
Rs	0,0038	0,022	0,0017	0,0066	0,0024	0,0201	0,0044	0,0014
R1	0,0007	0,0014	0,0181	0,0103	0,0077	0,0004	0,0007	0,0002
R2	0,0016	0,0044	0,0086	0,0106	0,0086	0,0029	0,0044	0,0005
WR	0,0033	0,0066	0,049	0,0059	0,0022	0,0039	0,018	0,0055
Tot. Pol.	0,0025	0,0016	0,0395	0,0056	0,0012	0,0028	0,0131	0,0048
Correction								

Rs	0,0038	0,022	0,0016	0,025	0,0025	0,0231	0,0038	0,0017
R1	0,0007	0,0014	0,0005	0,0006	0,0004	0,0004	0,0006	0,0002
R2	0,0016	0,0044	0,0046	0,0043	0,0019	0,0026	0,0044	0,0005
WR	0,0033	0,0066	0,0446	0,0062	0,0023	0,0038	0,018	0,0066
Tot. Pol.	0,0025	0,0016	0,0395	0,0052	0,0015	0,0028	0,0121	0,0059

With correction of the outlier spectra no significant change results in the standard deviation of the total polarization resistance, but in many cases a drop of an order of magnitude in R_1 and R_2 is recorded, which means that those resistances are more in line with each other and variations due to physical phenomena are more likely to be found.

Verifying that the peak frequency and the capacitance are in the expected range is considered to be a strong check for the fitting, as long as all the other tools are jointly employed. Once the right spectra are selected, mean values and standard deviations between them are calculated. Also the capacitance for each equivalent element is calculated from parameters of the fitting. Capacitance is a frequency dependent term as already mentioned, then as a representative value it is calculated for the peak frequency. As for a CPE it is calculated as [2]:

$$C = T(2\pi fp)^{P-1} \sin\left(\frac{P\pi}{2}\right) \tag{3.3}$$

where T and P are the CPE-T and CPE-P parameters from ZView respectively. The capacitance for a bounded Warburg element is calculated as:

$$C = \frac{l^2}{3D_{i,eff}R} \tag{3.4}$$

where l is the diffusion length, $D_{i,eff}$ is the diffusion coefficient and R is the Warburg resistance. Since

$$T = \frac{l^2\omega}{D_{i,eff}} \tag{3.5}$$

Then the capacitance can be calculated from the fitting parameters at the peak frequency as:

$$C = \frac{T}{3R(2\pi fp)} \tag{3.6}$$

Here mean values for R_s, R_1, R_2, WR, total resistance, f_p, C are presented, for each condition.

Table 3.4. Mean values from the fittings at all the employed conditions.

	400 4%	200 4%	100 4%	80 4%	200 7%	80 7%	200 3%	80 3%
R_s (Ohm*cm2)	0,797	0,693	0,696	0,654	0,621	0,604	0,6	0,595
R_1	0,005	0,004	0,003	0,003	0,003	0,002	0,002	0,0021
R_2	0,016	0,019	0,019	0,028	0,021	0,023	0,012	0,0257
WR	0,114	0,119	0,098	0,047	0,085	0,082	0,152	0,0679
Tot. Pol.	0,135	0,142	0,12	0,079	0,109	0,108	0,166	0,0958
f_p 1 (Hz)	442,7	209	150,8	169,5	165,3	129,4	209,8	160,58
f_p 2	8,672	7,86	8,198	9,407	7,096	6,938	6,379	7,3201
f_p 3	0,513	0,507	0,634	1,078	0,622	0,611	0,448	0,7267
C 1 (F/cm^2)	0,133	0,419	0,835	0,617	0,734	1,069	0,743	0,9619
C 2	2,131	2,176	2,215	1,199	2,039	1,95	4,087	1,6624
C 3	1,357	1,316	1,248	0,792	1,236	1,329	1,331	1,2091

Both R_1 and R_2 appear to be lower than what Aravind [1] and Sarda [2] obtained at same conditions (850 °C and 4.2% humidification). Anyway the frequency range and capacitance for process 1 are of the same order of magnitude as Aravind's, thus supporting his conclusion about the nature of the high frequency process. It is suggested that it consists in adsorption phenomena on Ceria surface. As for process 2, its trend with variation of humidity and of the flows has already been highlighted and is confirmed in this brief statistical analysis. Comparison with results from the other fitting techniques (merged fitting) will make this conclusion more solid. The capacitance is around 1-2 F/cm^2. As for the low frequency region, some more detailed discussion is made.

The total diffusion resistances as calculated with the simplified model for a stagnant gas layer proposed by Primdahl [6] for the employed conditions of the experiment are:

Table 3.5. Expected resistances of the low frequency arc from Primdahl's diffusion model.

T (K)	% water	R (Ohm*cm2)	WR Tot (Ohm*cm2)
1023	0,04	0,029257	0,111215
1123	0,03	0,046524	0,176852
1123	0,04	0,035256	0,134021
1123	0,07	0,020796	0,079054

Here Fuller's equation was used to calculate the binary diffusion coefficient for H_2-H_2O mixture:

$$D_{H_2-H_2O} = \frac{10^{-7}T^{1.75}\sqrt{\frac{1}{M_{H_2}}+\frac{1}{M_{H_2O}}}}{P\left(\sqrt[3]{\nu_{H_2}}+\sqrt[3]{\nu_{H_2O}}\right)^2} \quad (3.7)$$

where T is 1123 K, M_i is the molar mass of the gas, P is the pressure in Pa and ν_i is the diffusion volume of the component, 7.07 and 12.7 for H_2 and H_2O respectively [7]. The obtained diffusion coefficient is D_{eff} = 8.67E-4.

As expected, there is a small thermal deactivation of diffusion and with higher water content the resistance decreases. This is in general the observed trend in the experiment when 200 and 400 Nml/min flows are fed. A diffusion length of 2 cm, which corresponds to the radius of the reactor as to assume that the limiting process is radial diffusion (like Aravind claimed [1]), is used. At 850 °C errors of the model by 16.2% for 3% humidification (which is the least reliable case, due to oscillation of the spectra), 12.3% for 4% humidification and -7% for 7% humidification are reported for 200 Nml/min flow. These values are here considered to be acceptable: the diffusion length of 2 cm has been assumed as best representing the diffusion limitation, but a little difference in the actual value could make part of the recorded error between the model and the measurements. The employed seteup is geometrically identical to Aravind's but it is physically different. Hence, it is confirmed that the arc arises from a diffusion limitation in a stagnant gas layer over the anode, while porous diffusion in the thin anode gives a negligible contribution in this case, since it was found to be negligible for <100 μm anodes with around 50% porosity [6]. The CFD model which Aravind presented [1], though simplified, seems to catch

the process. The 80 Nml/min flow is clearly off these values, which leads to conclude that either some hypothesis of the diffusion model is not valid in this particular setup at low flows (which is not likely, since Aravind's setup was quite similar and he worked with 100 Nml/min), either something occurs in the setup with humidity, which is not understood yet. If the experimentally obtained mean values for WR are used in the equation to inversely obtain the water content that theoretically corresponds to the width of the low frequency arc (with all the already made assumptions), these results are obtained:

Table 3.6. Back calculation of the real moisture fraction from the experimentally obtained resistances.

Case	% water	WR
400 4%	0,047	0,1141
200 4%	0,044	0,1189
100 4%	0,054	0,0984
80 4%	0,122	0,047
200 7%	0,064	0,085
80 7%	0,070	0,0821
200 3%	0,035	0,1522
80 3%	0,085	0,065

If lowering of the arc with 80 Nml/min 3% or 4% humidified is ascribed to condensed H_2O capture in some part of the system, then it appears that the real humidification of this flow at the anode is 12.2% instead of 4.2% and 8.5% instead of 3.5%. More experiments must be carried out to verify that this behaviour is consistently present and humidification measurements are suggested in parts of the setup, such as the traced feed pipe after the humidifier.

Eventually, the mean of the individually fitted spectra is validated through comparison with fittings from ZView function "Merge/Combine Data files", as anticipated in the outline of the fitting procedure. Here results are reported on a logarithmic scale, where the lowest resistances actually appear higher on the axis:

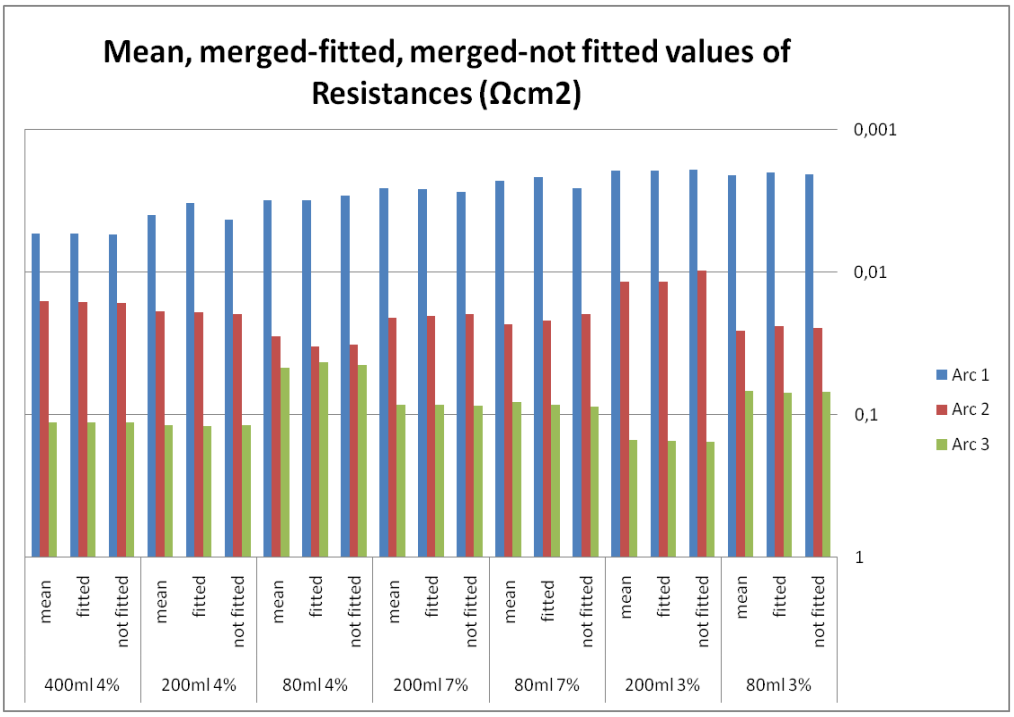

Figure 3.28. Comparison between the results of the techniques for fitting.

The values for each arc and each condition are in very good agreement and the trends are confirmed and clearly visible. Results from this study are summed up in the following table. The confidence interval was calculated by adding ±2σ to every mean value, where σ is the standard deviation. This means that, assuming a Gauss distribution of the data, 95% of the sample group lies within the interval.

Table 3.7. Results of the statistical analysis for all the experimental conditions.

	400 4%	200 4%	100 4%	80 4%
process 1	adsorption mono-charged species Ceria	adsorption mono-charged species Ceria	adsorption mono-charged species Ceria	adsorption mono-charged species Ceria
process 2	red-ox couple Ceria	red-ox couple Ceria	red-ox couple Ceria	red-ox couple Ceria
process 3	stagnant layer diffusion	stagnant layer diffusion	stagnant layer diffusion + uptake condensed water	stagnant layer diffusion + uptake condensed water

Rs (Ohm*cm^2)	0,7968±0,0077	0,69307±0,04397	0,69563±0,00314	0,65421±0,05
R1	0,00537±0,00148	0,00399±0,00272	0,0028±0,00108	0,00312±0,00129
R2	0,01601±0,00313	0,01902±0,00883	0,0189±0,00912	0,02849±0,00867
WR	0,1141±0,00664	0,1189±0,01315	0,0984±0,0891	0,047±0,01237
TOT	0,1355±0,005	0,1419±0,00317	0,1201±0,07904	0,0786±0,01044
f_p 1 (Hz)	442,74±135,97	208,97±42,35	150,78±131,63	169,49±55,88
f_p 2	8,67±0,48	7,86±2,08	8,2±5,13	9,41±2,24
f_p 3	0,51±0,03	0,51±0,02	0,63±0,5	1,08±0,31
C 1 (F/cm^2)	0,1331±0,0827	0,4189±0,2531	0,8353±0,6486	0,6165±0,5674
C 2	2,1307±0,2287	2,176±0,7791	2,215±1,9082	1,1991±0,2179
C 3	1,3569±0,0722	1,3164±0,1266	1,2476±0,3981	0,7923±0,4937
Stab. Time (h)	>5	all night	3,5	3,5

	200 7%	**80 7%**	**200 3%**	**80 3%**
process 1	adsorption mono-charged species Ceria	adsorption mono-charged species Ceria	adsorption mono-charged species Ceria	adsorption mono-charged species Ceria
process 2	red-ox couple Ceria	red-ox couple Ceria	red-ox couple Ceria	red-ox couple Ceria
process 3	stagnant layer diffusion	stagnant layer diffusion	stagnant layer diffusion	stagnant layer diffusion + uptake condensed water
Rs (Ohm*cm^2)	0,621±0,005	0,60443±0,04624	0,59951±0,0076	0,59497±0,00333
R1	0,00259±0,00077	0,00229±0,00077	0,00195±0,0012	0,00211±0,00044
R2	0,02097±0,00371	0,02323±0,00517	0,01166±0,0089	0,02575±0,00097
WR	0,085±0,00462	0,0821±0,00752	0,1522±0,036	0,068±0,01315
TOT	0,1085±0,00297	0,1076±0,00562	0,1658±0,02422	0,0958±0,01174
f_p 1 (Hz)	165,27±43,12	129,37±35,22	209,78±28,8	160,58±43,69
f_p 2	7,1±0,67	6,94±1,57	6,38±0,91	7,32±1,09
f_p 3	0,62±0,02	0,61±0,04	0,45±0,05	0,73±0,29

C 1 (F/cm^2)	0,7336±0,3367	1,0694±0,5069	0,74316±0,5426	0,9619±0,0656
C 2	2,0387±0,2104	1,9505±0,2417	4,0865±0,8659	1,6624±0,9206
C 3	1,2363±0,1261	1,3292±0,1767	1,3313±0,3829	1,2091±0,1651
Stab.Time, h	3	2	unknown	unknown

3.6 Transient conditions

It was explained how the low frequency arc is due to diffusion in a stagnant gas layer over the anode. It is then clear that mostly the first and second arc will give an indication about reaching the stabilization after reduction is terminated, since they are related to processes occurring into the anode. Noises in the first 24 hours after heating-up are mostly ascribed to this.

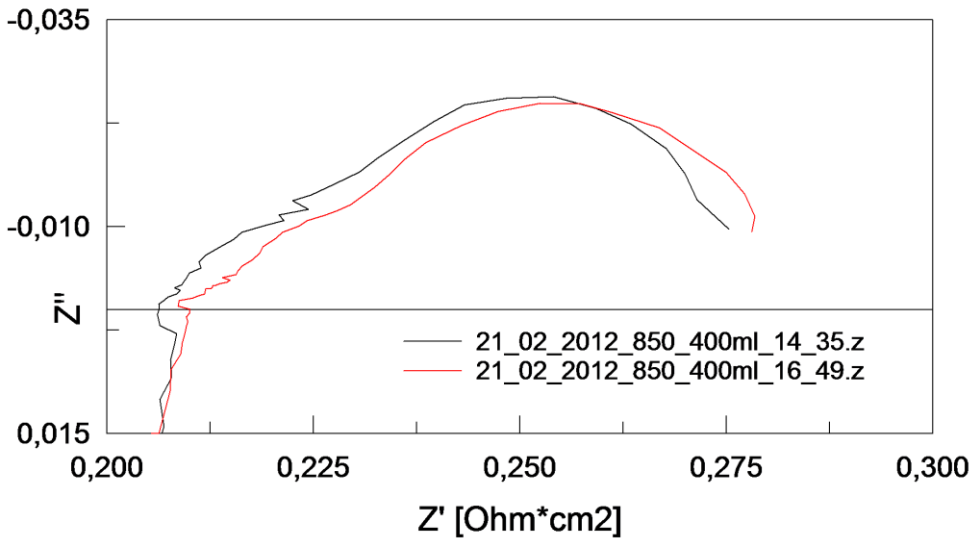

Figure 3.29. Different behaviours in the high frequency region during stabilization.

The wiring may also affect the measurements in the beginning, since it is very sensitive to every external condition and an incorrect positioning may result in big noises. These will also appear mostly in the high frequency region and the very high frequency region, where the first arc hasn't appeared yet. If no inductance or a very small one is visible in the plot, then a capacitance may be overlapping.

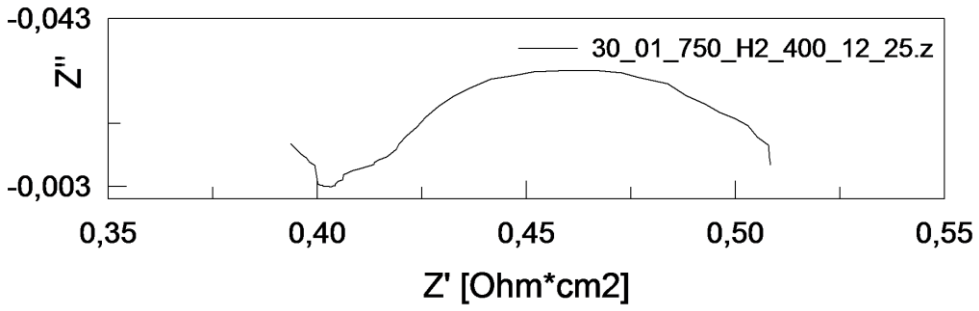

Figure 3.30. Appearance of a capacitor at high frequency instead of an inductor.

Once the cell and the anode are stabilized, variations in conditions result in much more physical behaviours of the spectra and the trend is clear already after some time, though stabilization may take much more time.

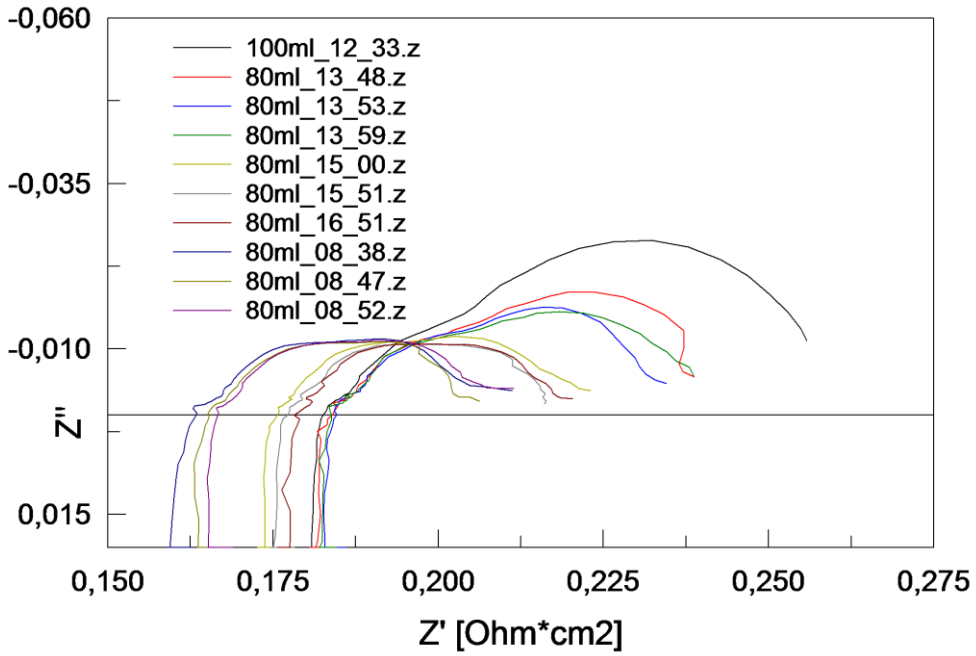

Figure 3.31. Transient condition switching from 100 to 80 Nml/min.

Here the transient condition when the flow is switched from 100 Nml/min to 80 Nml/min is shown. The variation of flow actually seems to cause a variation in humidification, since with time the low frequency arc regularly decreases and the intermediate frequency arc slightly increases, as if humidification was increased. The opposite behaviour is shown when humidification is lowered.

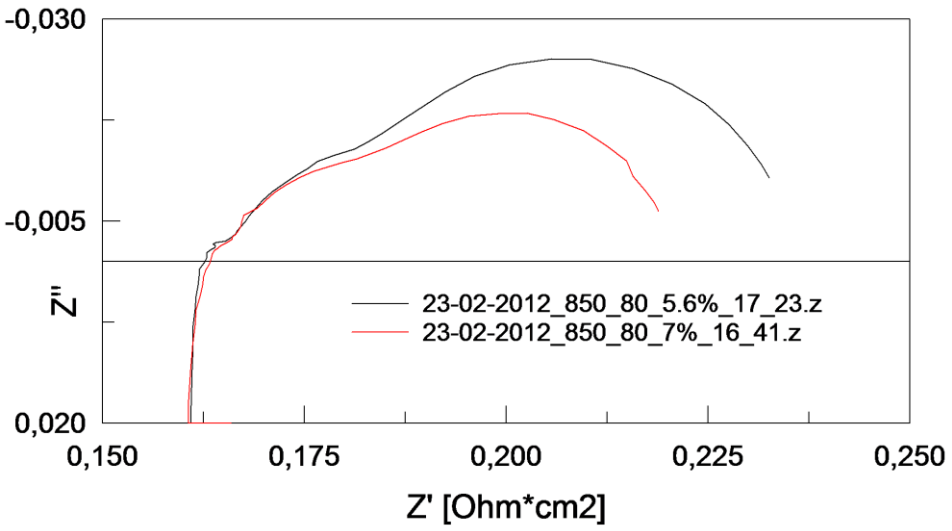

Figure 3.32. Transient condition when switching from 7% to 4% humidification at 80 Nml/min.

Of course in most cases it takes time before the bulk anode senses the change in conditions, which results in a clear variation of the spectrum only after one or two hours.

3.7 Conclusions

Two first conclusions can be made from the experiments. The results are in all cases reliable and reproducible in the flow range between 200 and 400 Nml/min and with lower flows at high water contents (7%). From this the suggestion comes for experiments with KCl to work with a total flow around 200-300 Nml/min. The humidified flow in those experiments is expected to behave better at higher water contents as results from the experiments show, probably because a more saturated flow is less influenced by water stagnation in some points of the setup. The operation of the humidifier has been proved to be reliable with 7% humidification. At low flows and low humidification unexpected behaviours in the low frequency region appear.

One more test at 3%, 4% and 7% with flows from 200 Nml/min down to 50 Nml/min and a new massflowmeter with a full scale value of 500 Nml/min is carried out. All results are in line with what theoretically expected and none of the formerly recorded behaviours shows up. The spectra are much noisy in the

high frequency and reasons are no further investigated. However the low frequency is well defined and the trend is clear.

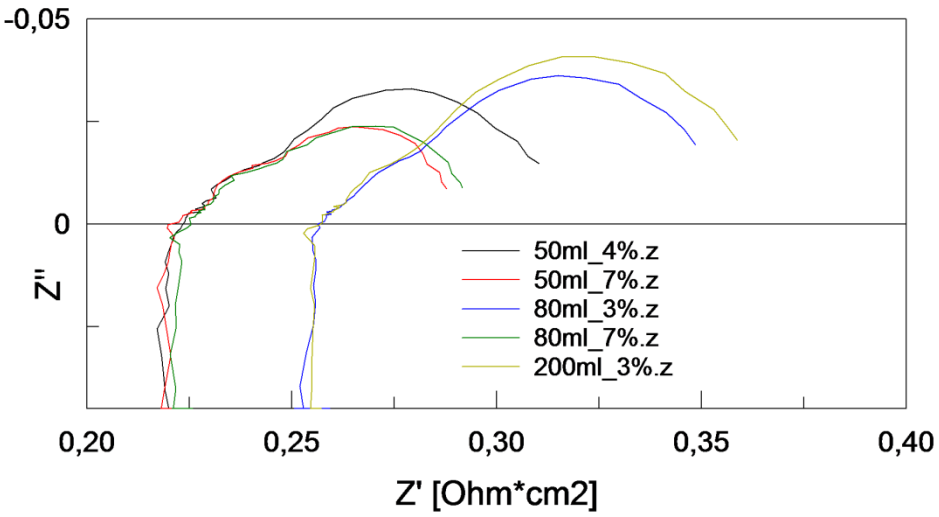

Figure 3.33. Comparison of results from the fourth experiment, with use of lower flows.

Table 3.8. Results from the most representative spectra of the last experiment.

	80 3%	80 3% 2	200 3%	200 3% 2	50 4%	50 7%	50 7% 2	80 7%
R1	0,0037	0,0038	0,0023	0,0025	0,0022	0,0057	0,0036	0,0023
R2	0,0132	0,0149	0,0117	0,0126	0,0176	0,021	0,0226	0,0192
WR	0,1688	0,1642	0,1877	0,1882	0,1509	0,103	0,1127	0,1096

They are then concluded to be completely reliable, but still not fully reproducible until the cause for the variations in the former experiments is found. Ideal/non-ideal saturation in the humidifier was already confuted as a hypothesis. The higher full scale value of the mass flowmeter in the third experiment may have resulted in lower precision at low flows (80 Nml/min). With a readable value of 2.5% of the full scale, the actual flow may have been around 50 Nml/min in the worst case. Being the flow very low the gradient in the gas stagnant layer may have changed, making diffusion faster. However this is avoided, since measurement with the new mass flowmeter and 50 Nml/min didn't show this behaviour. If the mass flowmeter had some effect on the measurements, which is possible, it must have been some unknown effect, to be

better investigated. One last explanation lies once again on the chance of massive condensation in some part of the setup and in particular conditions. In fact, what changes between this fourth experience and the former ones is the external temperature, then the room temperature (being the ambient not well heated). In the first cases temperature is around 15 °C, in the latter it is around 25 °C. There was a difference of 11% in the Warburg resistance between 80 Nml/min and 200 Nml/min at 3% moisture content in the last test. The difference in the third one was 134%, which could confirm that condensation still occurs, but this time it is almost negligible. When condensation takes place, low flows may get much more saturated in some parts of the setup, being much slower then high flows (1/8 between 400 and 50 Nml/min). This must happen where the temperature is high enough to allow high vapour pressure in the flow: at 80 Nml/min the actual humidification (assuming that the low frequency lowering is effectively due to humidification) was found to be around 12%. Sarda's experiments didn't show this behaviour, but they were carried out during summer. Since the small low frequency features didn't appear anymore it wasn't possible to verify whether and where condensation took place. The most critical parts are the head of the humidifier, the traced pipe and the connection with the quartz holder. This will be further highlighted in chapter 5. When such behaviour re-appears it is suggested to perform humidity measurements and psychrometric analysis in these parts.

With all these elements from experience, in the next session a modelling of the modifications for experiments with KCl is studied and realized in the TU Delft setup. In the next chapters a study of the tools for characterization in the experiments and a thermodynamic modelling of the whole setup will be given. Results from the experience and from practical considerations made in this chapter are used to decide what to model and how. The most critical points will be thermodynamically analyzed, to have a more complete integration between experience and theory.

3.8 Modifications to the setup

The original setup has to be modified to allow measurements with KCl in the flow. The only reference for the new asset is Aravind's PhD work, in which he analyzed the influence of various contaminants present in biosyngas on the performance of Ni/GDC symmetrical cells. He started the first experiments to

open discussion about alkali poisoning. Actually, projecting the modifications on another asset than the one he used may lead to new problems. The simplest possible modification has to be designed, to make any study technically and economically feasible. Then, solid KCl is likely to be used. It needs to be put as close as possible to the sample: it can't be put in the humidifier, since it dissolves in the water but it won't evaporate; moreover, the further it is from the reactor, the bigger is the chance of it depositing in the piping and maybe corroding it. Here comes the solution Aravind used: an evaporator tube at the inlet of the reactor, in which a solid KCl bed is put. With a low H_2 mass flow through the bed at high temperature solid-gas phase equilibrium for KCl is (reasonably) reached and some KCl evaporates. A temperature gradient arises along the evaporator as it is put into the reactor. By setting the height of the bed to the level at which the temperature is the equilibrium one for the desired concentration in the gas flow, that desired concentration is ideally obtained. This asset of course contrasts with the necessity of formerly heating up and reducing the cell in pure N_2 and H_2 flows. For this reason two gas inlets must be present, one of which by-passes the KCl bed. Here the evaporator Aravind designed and had built.

Figure 3.34. Picture of the modified quartz holder for experiments with KCl.

A third pipe is connected to one of the inlets through a valve. A small pipe is built along the big one for the KCl bed, to carry the thermocouple that measures the temperature along the pipe to set the height of the KCl bed. This all device must be in quartz to make it easily cleaned and resistant at the high working temperatures (until at least 900 °C). Moreover, having it transparent is helpful for observing what happens inside. Aravind's modified holder didn't perfectly fit the reactor of TU Delft SOFC laboratory, so it had to be re-designed and re-built. In fact, when built on the existing setup it gave rise to big leakages from many parts (a 200 Nml/min flow couldn't reach the top of the setup). It was suggested that the valve with the third inlet would be deleted from the design, to make the element simpler and to avoid leakages. Here the sketch is presented, made with mechanical design software.

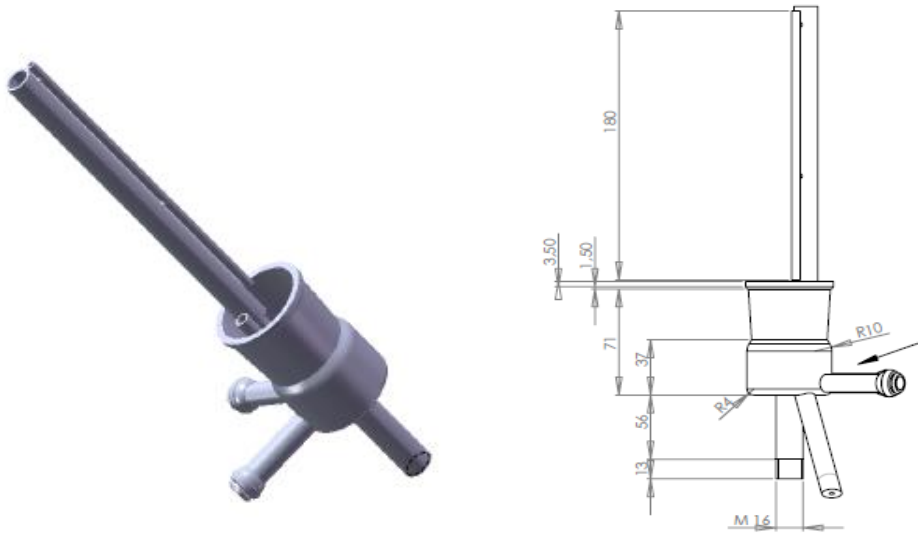

Figure 3.35. Solid works project of the modified quartz holder for experiments with KCl.

Since, as already discussed, Aravind ascribed the widening of the low frequency arcs to possible non perfect mixing between the humidified and the non humidified current, it is suggested that, as a first attempt, all the humidified H_2 passes through the bed. This way, when heating up with N_2 and when reducing with pure humidified H_2 the flow is led to the outer part through a valve and bypasses the bed; after reduction the valve switches the feed to the second inlet and humidified H_2 passes through the bed itself. This would avoid mixing problems but new problems could arise from adsorption of vapour on solid KCl, thus packing the bed. Other species may also form during flow of the gas in the bed, from reaction of K and Cl with water (mostly KOH and HCl), hence this

matter has to be investigated with equilibrium computation (see chapter five). Moreover, during experiments it wouldn't be possible to change the concentration of KCl in the flow, unless the system is cooled down and the height of the bed is modified. If the modification is made, it allows to verify Aravind's conclusion, but with fixed operational conditions for each experiment. For this reason one more modification is designed: a pipe is drawn from the station of the complete cell, using a three-way valve, so that when the station is not working one more H_2 feed is available for impedance experiments. The flowmeter is calibrated for a maximum flow of 1000 Nml/min, this meaning that the minimum is 5% of the full scale, 50 Nml/min. It's not possible to pass the pipe through the humidifier, so that it will carry dry H_2, which can go directly to the evaporator tube, as to exactly reproduce Aravind's asset. This way the problem of possible condensation in the KCl bed is avoided. Non perfect mixing is going to be an issue once again and an experiment with pure H_2 in the same modified setup may be needed to get a term of comparison and to be able to separate the effects of KCl when it is present. Moreover this configuration makes it much more important to get solid conclusions about low frequency behaviour and influence of flow and humidification variations in the experiments with sole humidified H_2. Another problem could derive from the dry flow not to be traced from the complete cell to the impedance station. If in the quartz holder it doesn't reach fast a high temperature, it could cool the humidified flow and cause condensation. Using higher flows could help enhancing the mixing, by having a higher Re number in the overall flow, as far as in all the experiments that level of flow is kept constant. With this configuration it is possible to vary concentration of KCl by mixing differently the two flows, the humidified one by-passing the evaporator and the dry contaminated one. As it is not well known how KCl interacts with the anode and by what this interaction is influenced, every other condition has to be kept as much constant as possible: the total flow rate and the moisture level in the total flow (4.2%) are fixed, which means that with increasing KCl (that is, dry flow), the other inlet needs to be humidified every time more. It is important to reach a compromise between the need for mixing and humidifying, in order not to have increased condensation in the pipeline of the humidified flow.

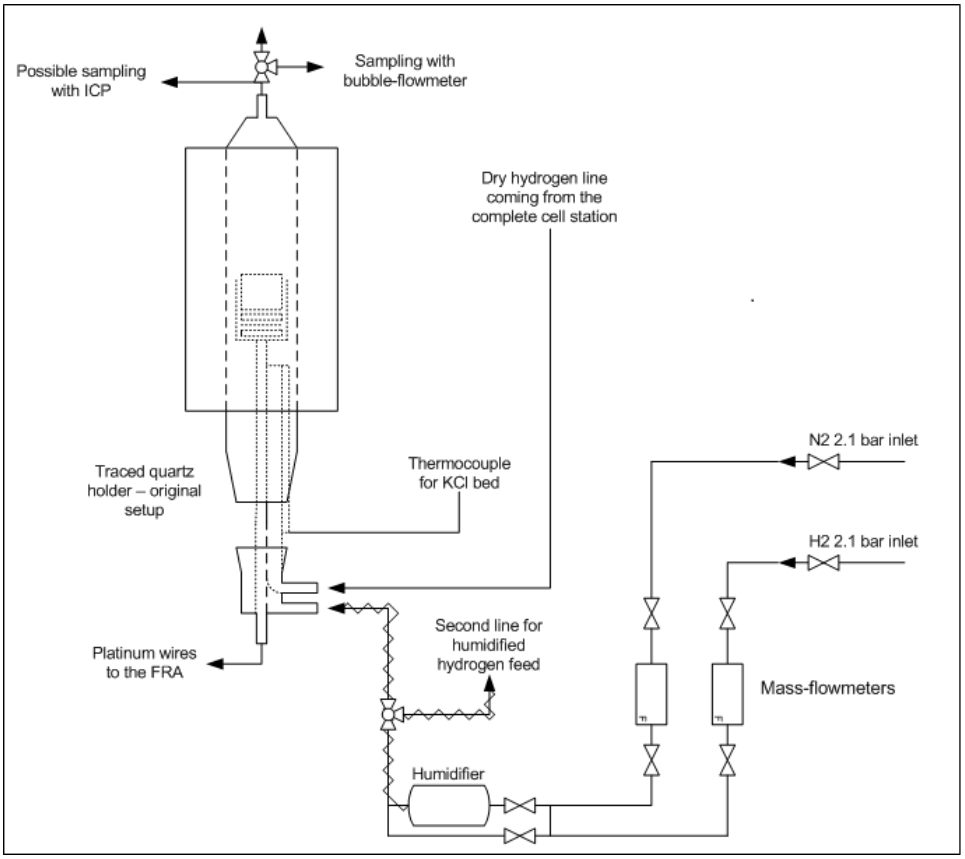

Figure 3.36. Sketch of the modified setup for experiments with KCl.

The figure above shows the main elements of the modified asset. It should also be noted that the pressure drop along the KCl bed needs to be predicted, because it could make the flow more difficult with the employed conditions, impossible in the worst case (pressure in the system is 1.05 bar and mass flow controllers are not built to adapt to the counter pressure, they shut down the flow in case it is too high). In that case KCl with a higher grain size should be used for the bed. Preliminary calculations are performed with Ergun's model for fixed beds elsewhere in this work (see chapter five).

The figure also shows a further modification on the top of the reactor. On the metallic pipe which takes the gases to the outlet a three-way valve is placed, to allow deviate the flow to a bubble flowmeter when measuring leakages is needed. Particularly for analysis of the feed with contaminant it will be necessary to know the value of the volume flow as best as possible. Aravind showed how KCl concentration in the flow is not exactly how predicted by

equilibrium calculations. In particular, it happens to be higher, probably due to entrainment of some particles from the bed. So gas sampling is needed to know the exact value of KCl concentration and it is carried out through ICP-MS technique. All these devices for detailed analysis of experimental conditions and their working principles are presented in the next chapter.

References

[1] P.V. Aravind, Studies on High Efficiency Energy Systems based on Biomass Gasifiers and Solid Oxide Fuel Cells with Ni/GDC Anodes, PhD thesis, November 2007.

[2] V.Sarda, Ammonia as a fuel for Solid Oxide Fuel Cells, August 2011, MSc thesis, TU Delft, 2011.

[3] X. Yuan, C. Song, H.Wang, J. Zhang, Electrochemical Impedance Spectroscopy in PEM fuel cells, Springer-Verlag London, 2010.

[4] M. Verbraeken, Advanced supporting anodes for Solid Oxide Fuel Cells, MSc thesis, EMPA Dübendorf, March 2005.

[5] P. Kim, D.J.L. Brett, N.P. Brandon, The effect of water content on the electrochemical impedance response and microstructure of Ni/CGO anodes for solid oxide fuel cells, Journal of Power Sources 189, 2009.

[6] S. Primdahl, M. Mogensen, Gas Diffusion Impedance in Characterization of Solid Oxide Fuel Cell Anodes, Journal of The electrochemical Society, 146 (8) 2827-2833, 1999.

[7] E.N. Fuller, P.D. Schettler, J.C Giddings, Ind. Eng. Chem., 58(5), 19, 1966.

Chapter 4

Advanced tools for characterization of the setup

The study of the effects of KCl contamination on Ni/GDC anodes is still in a preliminary phase. Since the effects of such contaminations are probably quite limited from a quantitative point of view, other advanced investigation tools can be used in parallel with EIS studies in order to understand the physical phenomena occurring during the measurements and to verify the goodness of the assumptions done in the modeling of the new setup. SEM, XRD and ICP are considered suitable for a complete analysis. In fact, they helped analysis of the results in the previous sections and it is useful to understand how they work and what their limits are.

In the next sessions detailed presentation of the working principles will be given.

4.1 SEM

In order to understand what happens when KCl particles in the feed flow interact with the anode materials, the option to use the SEM (Scanning Electron Microscope) has been considered. This kind of study has been done to verify the existence of phenomena not detected in the chemical equilibrium calculation. For example, [1] Rostrup-Nielsen and Christiansen suggested that when the potassium interacts with anode material, it slows down the reforming reactions because of a modification of the faceting of the Nickel to Ni(III).

SEM stands for Scanning Electron Microscope; this technique doesn't use the light but an electron beam as radiation source [2]. There is a thermionic "electron gun" used to shot electrons on the sample. This beam passes through condenser lens and deflection coils before interacting with the sample [3].

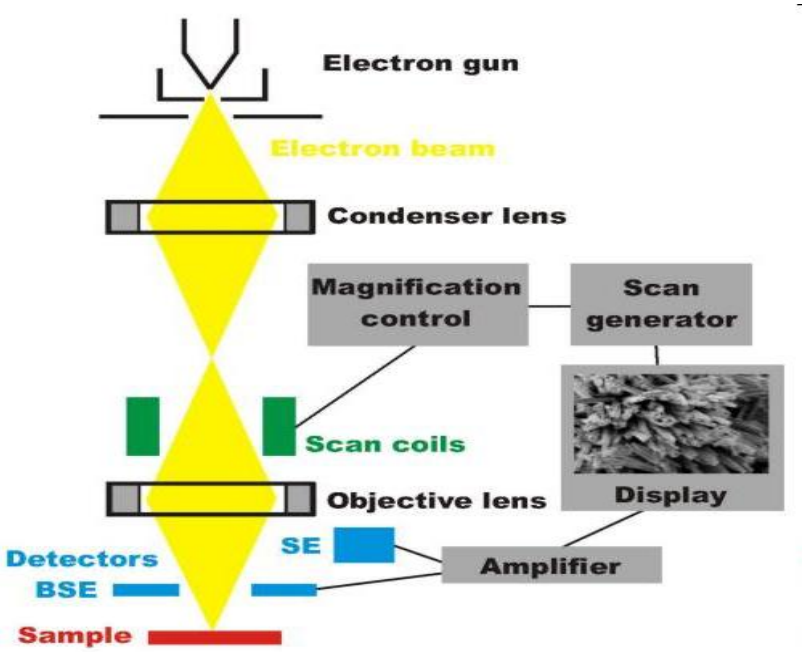

Figure 4.1. SEM diagram of operation.

Once they interact there are secondary electrons, backscattered electrons, X-rays and Cathode-luminescences leaving the surface [3]. Obviously, these products have to be detected to give results.

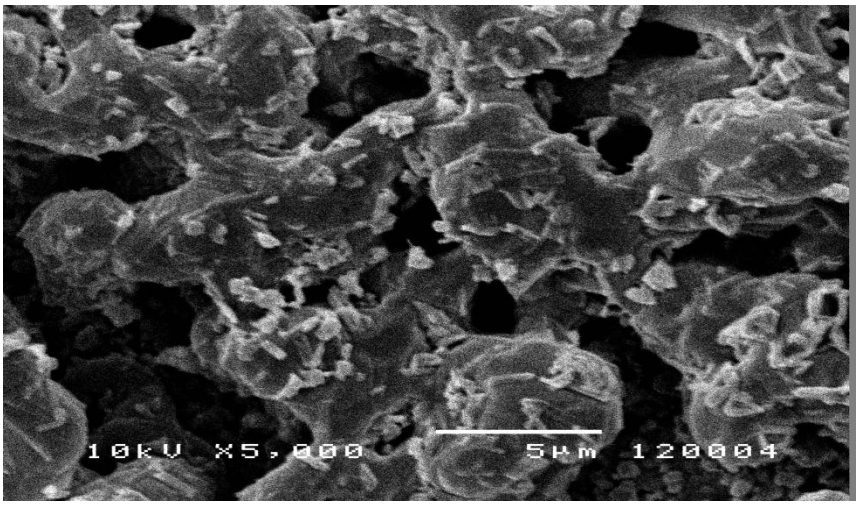

Figure 4.2. SEM of the anode used in the first test (December 2011).

Secondary electrons are generated from the collision between the electrons of the beam and the outer electrons of the atoms of the sample. They have a lower energy with respect to the incoming electrons hence the sample must be in a vacuum environment [2][3]. Secondary electrons detectors are common in almost all SEMs. They produce SEI (secondary electron imaging) which provides high resolution images with an excellent three-dimensional appearance. They are able to reveal detail with less than 1 nm in size. The magnification starts from about 10 times up to 500000 times [2]. The back-scattered electrons (BSE) are electrons of the beam that are reflected by the sample atoms through an elastic scattering. BSE detectors are used along XRD analysis to study the composition of the sample since the intensity of the signal is strongly related to the atomic number [3].

There are also X-rays emitted by the analyzed material they can be used to study its composition; the most commonly used technique is EDS (energy dispersive spectrometer).

4.2 XRD

X-ray diffraction is a versatile, non-destructive method that is commonly used to reveal information about the analyzed materials, especially crystal structure, chemical compositions and physical properties.

This technique is based on the constructive interference of monochromatic x-rays and crystalline sample. This constructive interference is possible only when Bragg's law condition is satisfied: $n\lambda = 2dsin\theta$ where n is an integer, λ is the wavelength of the incident wave, d is the spacing between the planes in the atomic lattice, θ is the angle between the incident ray and the scattering planes [4]. XRD analysis needs a particular instrumentation: first of all an x-rays source, a collimator, a monochromator (in order to obtain monochromatic x-rays) and detectors [5]. When the analyzed crystal is illuminated by the x-rays beam, many "spots" are revealed by the detector. Size and shape of the unit cell determine the position of the spots. The intensities of the spots, on the contrary, are affected by the arrangement of the atoms. By determining the intensities of the spots it is possible to determine the structure and the composition of the crystal [6].

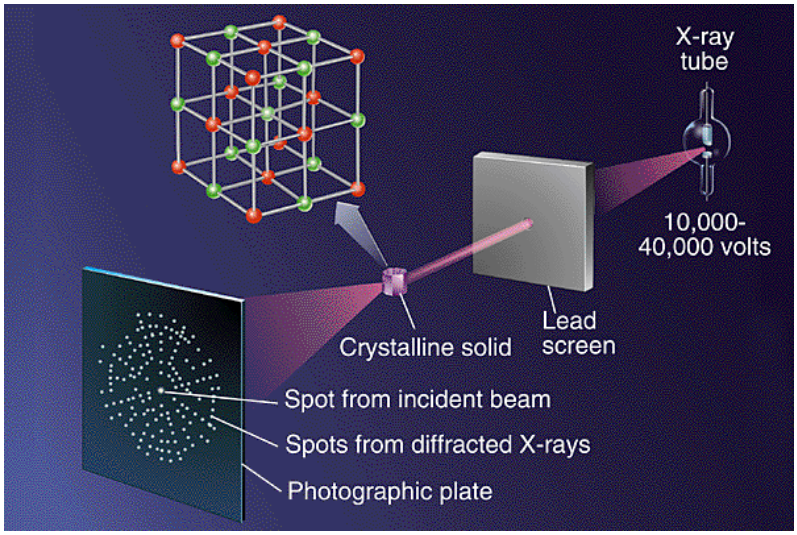

Figure 4.3. XRD diagram of operation.

The results of an XRD analysis are reported in an intensity vs. angle plot. The plot shows different peaks. While the position of them is due to the size and shape of the unit cell, their intensity is due to the arrangement of the atoms [6]. It is possible in this way to identify also the components of the analyzed sample. An XRD intensity vs. angle plot was presented in the third chapter showing the peaks in the symmetric cell after its utilization. Quantitative analysis such as the Rietveld method [6] permits to identify the weight percentage of the components in the sample.

4.3 ICP

ICP-SM stands for Inductively coupled plasma mass spectrometry [8]. This technique has been developed during 1980's and now it is a useful tool to detect particles up to few ppts [9]. It consists of a combination of the ICP which guarantees a simple introduction of the sample and a quick analysis, and a mass spectrometer which is very accurate. The ICP-MS technology actually can be thought to be made of four main processes [9]: sample introduction and aerosol generation, ionization done by an argon plasma source, mass discrimination and detector and finally data analysis.

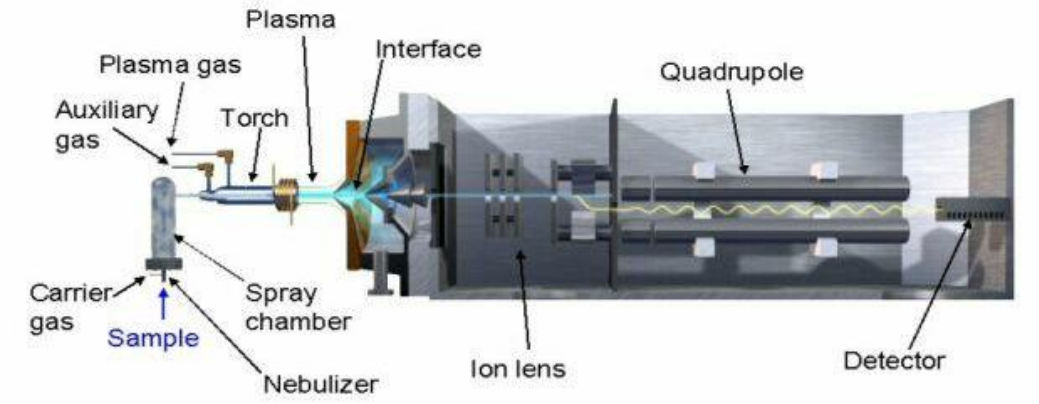

Figure 4.4. ICP-MS Diagram of operation.

4.3.1 Sample Introduction

A liquid or a semi-solid (like a slurry) solution is introduced into a nebulizer. Once it entered the device it is aspirated along with an argon gas flow. It forms a fine mist that exits the nebulizer like an aerosol and passes through a spray chamber in which the largest droplets are removed (for example in a cyclonic spray chamber) in order to obtain fine droplets that can be easily vaporized in the ICP torch. This is not the only method used to introduce the sample: there are also the laser ablation, electro thermal vaporization (ETV) torch vaporization (ITV) but they are not as common as the nebulization method.

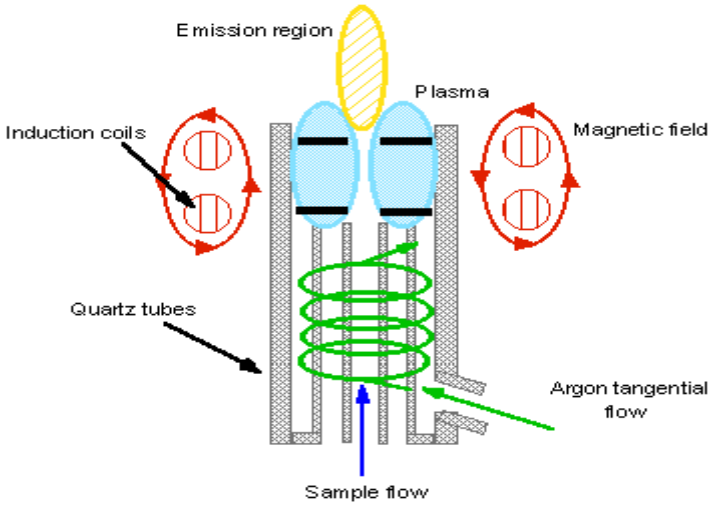

Figure 4.5. Sampple introduction.

4.3.2.Ionization

The nebulized sample is then introduced into a plasma torch where it is going to be ionized. The atomization and the ionization of the sample occur in a torch that consists of three concentric quartz tubes. The top of the torch is placed inside an induction coil supplied with a radio frequency electric current [8][9]. A flow is introduced between the two outermost tubes. Then an electric spark supplies electrons to the flows. These electrons then will interact with the radio-frequency magnetic field done by the induction coil. They are accelerated and they interact with the Ar flow producing Ar^{+} and e^{-} until a dynamic equilibrium is reached. The ionized flow reaches very high temperature becoming plasma and making the "typical" flame of the upper part of the torch. The sample enters from the bottom and goes to the upper part of the torch. There, it finds the argon plasma. The extremely high temperatures of the argon plasma at first atomize and then ionize the sample. The ionization is fundamental because it is the only way for the particles of the stream to be detected by the mass spectrometer.

4.3.3 Mass Spectrometer

Before the ionized stream goes to the mass spectrometer, it has to pass an interface between the ICP and the MS in which a vacuum atmosphere is provided. The vacuum is necessary to prevent the particles from interacting with air molecules and it is obtained through a series of pumps that finally reach a pressure around 133 Pa [9][10].

Then the sample enters the mass spectrometer like an ion beam at high speed. This beam has to pass through quadrupole analyzers that are able to distinguish and select different ions because of their specific mass-to-charge ratio. Different ratios can be obtained varying DC and AC voltages applied to the quadrupoles [9].

4.3.4 Detector

The ions of the species that is going to be detected are sent to a horn-shaped detector which is an electron multiplier. It has a charge opposite with respect of the one of the ions. When the ionic beam strikes the surface secondary electrons are emitted. These electrons let other secondary electrons be released. Finally there are 10^8 electrons per ion that enter the detection zone. This electron flow is used to analyze the results [9].

4.3.5 Data analysis

The detected inputs are then analyzed through data elaborators that finally give the users the results of the measurements.

4.4 Practical application of the ICP and modification of the setup

As already anticipated in the third chapter, the height of the KCl bed in the evaporator is set to the temperature at which a certain concentration of the contaminant in the flow is obtained. The assumption is that the equilibrium is the dominant condition to determine the concentration, thus, the dragging of KCl particles is neglected [7].

It is necessary to verify whether this assumption is correct. The idea is to measure the concentration of KCl particles over the anodes and close to the outlet of the vessel. The assumption to neglect the particles adsorbed by the

anode material is made. This is due to the fact that the variation of the concentration due to this phenomenon is orders of magnitude smaller with respect to the employed concentrations in the flows.

The measurement could be carried out using ICP-SM [7]. To obtain an ICP – MS measurement with the setup described in the previous chapter a high temperature gas sampling is needed. This is due to the fact that KCl condensation begins at temperatures around 973 K and this should affect the measured values. The only way to avoid it is to sample the gas as close as possible to the cell. The idea is to put a thin 9 mm diameter quartz tube into the vessel from its top. The tube has to quit the vessel; it is L-shaped (see figure (4.6)) and its length is about 5+15 cm. The length has been chosen to be sure that the gas temperature decreases below 573-673 K as to be tolerated by the Teflon flexible tube that is connected to the quartz tube.

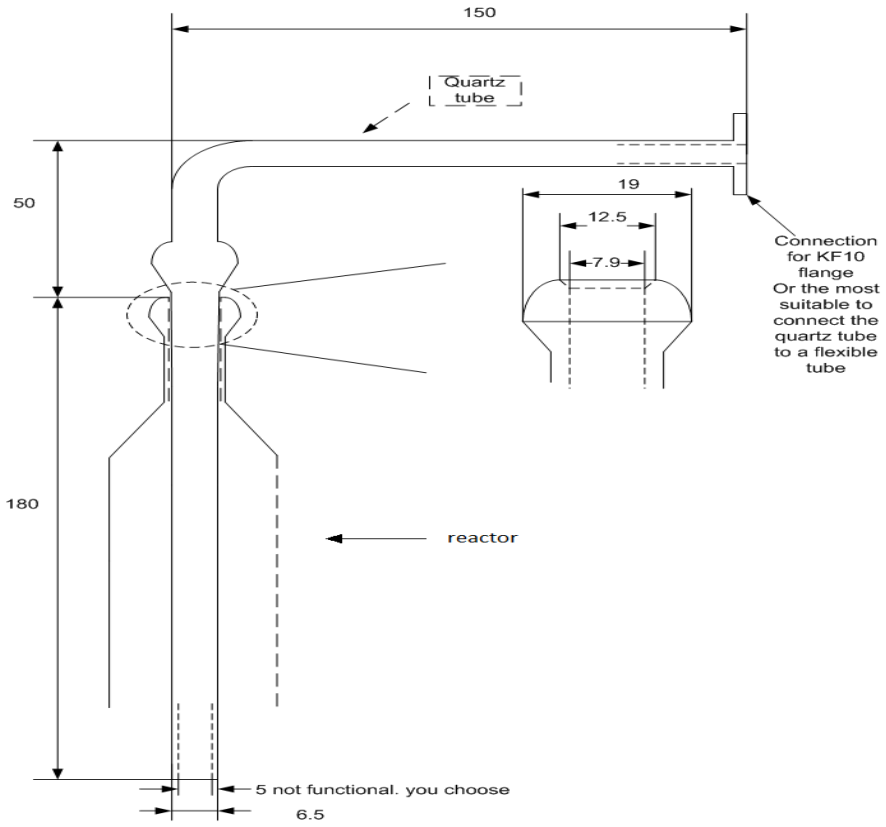

Figure 4.6. Sketch of the quartz tube for ICP probing.

The end of this Teflon tube is then immersed in a 3-4 liters water tank through which the gas has to flow and the absorption process occurs. In fact the KCl particles are absorbed in the water during the bubbling. In order to make the ICP-MS measurements, the gas flow must be allowed through the water tank for a chosen time calculated to let the water tank reach a desired theoretical concentration. If only the concentration absorbed with the bubbling is considered, the results aren't correct. In fact the condensed KCl particles along the tube have to be considered too. This is done by letting a known (150 ml for example) water quantity flow into the tube (dragging the residual KCl particles) and adding it to the one in the water tank. This way the ICP-MS measurements are able to give the effective concentration flowing in the system. These measurements take into account the actual concentration in the flow; thus, this is a check for the initial assumption of considering only the values due to the chemical equilibrium because the dragging phenomena in the KCl evaporator are considered.

4.4 Bubble flowmeter

The bubble flowmeter is an instrument that allows rather accurate calculations of the gas flows by measuring the passage time of a soap film between two marks of a known volume. The instrument is composed by a glass tube with the volumetric marks, a gas inlet (set at the bottom part) and a small rubber bulb attached at the base of the glass tube. In the setup considered in this thesis the bubble flowmeter is connected by a rubber pipe to the top of the oven, where a three way valve has been placed. Switching the valve, the gas feed is directed to the instrument to quantify its flow.
The working principle is easy: there is some soap in the bottom part of the instruments; pinching the bulb a bubble forms and it behaves as a plug in the tube. The bubble is pulled and dragged by the gas flow and goes up to the top of the tube. By measuring the required time to reach a known volume the gas flow can roughly me measured. This kind of analysis is used in parallel with an H_2 detector to measure leakages that can affect the results with EIS.

Figure 4.7. Bubble flowmeter.

References

[1] Rostrup- Nielsen, Christiansen, Internal steam reforming in fuel cells and alkali poisoning, 1995.

[2] http://en.wikipedia.org/wiki/Scanning_electron_microscope.

[3] Anders Werner, Bredvei Skilbred, Harald Fjeld, Scanning Electron Microscopy (SEM).

[4] http://en.wikipedia.org/wiki/Bragg%27s_law.

[5] Sachin M. Jadhav, x-ray diffractions slides.

[6] http://www.polycrystallography.com/XRDanalysis.html.

[7] P.V. Aravind, Studies on High Efficiency Energy Systems based on Biomass Gasifiers and Solid Oxide Fuel Cells with Ni/GDC Anodes, PhD thesis, November 2007.

[8]http://en.wikipedia.org/wiki/Inductively_coupled_plasma_mass_spectrometry

[9] http://www.cee.vt.edu/ewr/environmental/teach/smprimer/icpms/icpms.htm.

[10] http://en.wikipedia.org/wiki/Mass_spectrometry.

Chapter 5

Physical and chemical design of the setup

It was shown in the experimental section how sensitive impedance measurements are, not only to conditions of the cell, but also to every external condition. It may happen that a result is in line with references, but due to different causes. If no detailed information is available about the employed setup results from different laboratories are hardly comparable and to pursue the same objective it may be needed to restart the research every time. This is why we think it is useful to describe the results also as functions of the particular employed setup and hence try to get a physical model for it. The system can show the mixed effect of many processes: condensation may take place in the piping, carbon containing fuels could give rise to carbon deposition in the sample holder or on the sample itself, a gas feed with contaminants could degrade so much the cell as to make it impossible to measure any impedance spectra.

This part of the study stems from the considerations made after the experiments. For each of them the working conditions and the procedure for analysis were gradually refined, as to finally obtain a solid procedure for fitting and reliable results. In order to make them also reproducible a theoretical approach must go along with experience, so that tools are created for interpreting what was not expected in the results. It is intended to model all the gas line step-by-step and to highlight the physical governing processes of every section and its criticalities. This part of the study is believed to be the most delicate and important. At the same time, a modified setup for experiments with KCl addition in the flow to simulate contaminated biosyngas must be validated. Some parts in this case are designed and built ad hoc, so they must be modeled before. The only reference is partly Aravind's setup [1], but it has to be anyway modified to suit the new conditions and the different laboratory equipment available. It is then clear why setting the reference point and having reproducible results is so important: no effect of KCl over the anodes will be discovered if more variations of the spectra occur for unknown reasons. In the following sections a brief theoretical introduction about the governing principles of equilibrium thermodynamics and chemistry will be given, followed by a step-by-step description of the processes occurring along the gas line, assuming steady state conditions.

First of all, it is the thermodynamics that states which reactions take place at given conditions and in which direction. Kinetics tells if the same reactions are likely to be observed and at which rate. One way of having a first indication of what could be expected is thus performing calculations of the equilibrium state for all the reactions and materials involved. In some cases the assumption of equilibrium perfectly suits the physics, since the surface for the reaction to take place is huge or one of the reactants is much more abundant than the other, or the products are suddenly removed, or the flows are small enough to be the rate limiting condition in the system; in other cases the equilibrium will not be reached and the result must only be considered as a time-limit for the process, that is, the situation towards which the system tends to evolve. Equilibrium computations are performed with the software Factsage. It should be taken into account that equilibrium is an approximation for the actual conditions and, in addition, the software further approximates solutions, so that what is given as an output isn't indeed the real equilibrium result as coming from theory.

5.1 Theoretical background

First of all a theoretical review of how equilibrium in a reacting system is influenced by thermodynamic parameters can be helpful.

Considering a system, closed to the exchange of matter, from the first and the second Principles of Thermodynamics it can be inferred that [5]:

$$dU_{P,T} + d(PV)_{P,T} - d(TS)_{P,T} \leq 0 \tag{5.1}$$

$$d(U + PV - TS)_{P,T} \leq 0 \tag{5.2}$$

and being

$$H = U + PV \tag{5.3}$$

$$G = H - TS = U + PV - TS \tag{5.4}$$

where H is the enthalpy, U the internal energy, P the pressure, V the volume, T the temperature, S the entropy, G the Gibbs free energy, for a system where some spontaneous transformation is taking place, the following relation is valid:

$$(dG)_{T,P} < 0 \tag{5.5}$$

which in the case of a reacting system can also be written as a function of the reaction coordinate ε when T and P are constant:

$$(dG)_{T,P} = \left.\frac{\partial G}{\partial \varepsilon}\right|_{T,P} d\varepsilon < 0 \tag{5.6}$$

At equilibrium the differential of Gibbs free energy is zero, because G reaches a minimum.

It is of particular interest considering reactions at constant temperature and pressure, since with such reactions a fuel cell can be modelled. In the present study the pressure and temperature profile in the cell won't be taken into account and a single constant value for both will be assumed. This is not a strong simplification, as far as the system consists in a single cell, not a stack.

Being G = G (T,P,n_i), where n_i is the number of moles of each component "i", the differential of G at constant T and P can be written as:

$$(dG)_{T,P} = \sum_i \left.\frac{\partial G}{\partial n_i}\right|_{T,P,n_{j\neq i}} dn_i \tag{5.7}$$

and by definition of the chemical potential

$$\left.\frac{\partial G}{\partial n_i}\right|_{T,P,n_{j\neq i}} = \mu_i \tag{5.8}$$

the Gibbs free energy can be written either in one or the other of the two following forms.

$$(dG)_{T,P} = \sum_i \mu_i dn_i \tag{5.9}$$

$$(dG)_{T,P} = \sum_i \nu_i \mu_i d\varepsilon \tag{5.10}$$

Consequently the equilibrium condition is $\sum_i \nu_i \mu_i = 0$

In the case of ideal gas the chemical potential can be related to the thermodynamic properties of the system, through the following equation

$$d\mu_i^{i.g.} = RTlnP_i \tag{5.11}$$

which Lewis generalized for all gas, condensed, ideal, real species and integrated, introducing the fugacity:

$$\mu_i = \mu_i^0 + RT\frac{f_i}{f_i^0} \tag{5.12}$$

Finally, if the activity is defined as $a_i = \frac{f_i}{f_i^0}$ and $\Delta G = \frac{\partial G}{\partial \varepsilon}\Big|_{T,P}$ the general form of Lewis equation is reached:

$$\Delta G = \sum_i \nu_i \mu_i^0 + \sum_i \nu_i RTlna_i \tag{5.13}$$

$$\Delta G = \Delta G_R^0 + RT\prod_i a_i^{\nu_i} \tag{5.14}$$

From which also Nernst equation can be derived from a thermodynamic point of view. The superscript "0" means that the state variable is given for standard conditions, which can be different for different phases and cases, according to what is most comfortable. In fact, it is important to have a reference state, but which one is irrelevant, because the difference between two states is always calculated, not an absolute value. The subscript "R" indicates that ΔG is calculated for a reaction, as follows:

$$\Delta G_R^0 = \sum_{i=1}^{NC} \nu_i G_i^0 \tag{5.15}$$

As mentioned above, at equilibrium, ΔG = 0, so that

$$\Delta G_R^0 = -RTln\prod_i a_{i,eq}^{\nu_i} \tag{5.16}$$

and if the reaction's equilibrium constant is introduced

$$K_{eq} = \prod_i a_{i,eq}^{\nu_i} \tag{5.17}$$

the equation results

$$\Delta G_R^0 = -RTlnK_{eq} \tag{5.18}$$

This all was shown in order to give an indication of the theory equilibrium calculations are based on. K_{eq} is eventually only temperature dependent and it states to which extent the backward and forward reaction balance each other, that is, to which extent the products form (knowing its value permits calculating the reaction coordinate ε). When the equilibrium temperature is not known, a system of the two equations above determines the equilibrium state, including the concentrations of reactants and products.

Some considerations may be done now, which turn useful when validating the results of the computations on the software.

From the first and second principle of thermodynamics the Van't Hoff equation can be inferred, which gives the relation between K and T:

$$\left.\frac{\partial lnK_{eq}}{\partial T}\right|_P = \frac{\Delta H^0(T)}{RT^2} \tag{5.19}$$

From the equation it can be seen that for an exothermic reaction ($\Delta H<0$) at constant pressure when T increases K_{eq} decreases, so the conditions become less favorable to the reaction and the equilibrium shifts towards the reactants; on the contrary, when the reaction is endothermic an increase in temperature causes a shift of the equilibrium towards the products, because the forward reaction is enhanced.

As for the effect of the pressure, it doesn't affect K, since it is only temperature dependent. So the following relation is valid:

$$K_{eq} = cost = \prod_i (x_i)^{\nu_i} P^{\sum_{i=1}^{NC} \nu_i} \tag{5.20}$$

This means that, to maintain K_{eq} constant, when the reaction sees an increase in the total number of moles ($\nu_i>0$), an increase in the pressure implies a decrease in the concentration of the products (term Π (x_i)), that is, an equilibrium which

is closer to the reactants; consequently, a decrease in the pressure has the opposite effect.

The considerations about the temperature dependency of the equilibrium result useful for the computations of the present study, since different temperatures will be used for the experiments, ranging from 750 C to 900 °C. Some calculations will involve reactions, like formation of K species in the presence of H_2 and water or at the anode surface or reactions of the anode material with the gas feed. Some others just involve phase equilibrium and no reactions occur (humidification of the gas feed and saturation of the gas flow with KCl). It is then intended to give a little overview on how the equilibrium calculations change when this is the case.

In a multi-component system equilibrium at a certain T and P requires that the free Gibbs energies of each component in the different phases equal each other. This means that the chemical potentials must be the same and, more generically, the fugacities:

$$f_i^1 = f_i^2 = .. = f_i^n \tag{5.21}$$

where i is the component and 1,2,...,n are the phases. This law is thus valid for a component in different states, like gas-liquid, gas-solid. For instance, in a gas-liquid non ideal multi-component system at equilibrium (the most general relation):

$$f_i^g = y_i P \Phi_i^v = x_i \gamma_i P_i^{vap}(T) \Phi_i^v\left(T, P^{vap}(T)\right) \exp\left(\frac{V^l (P - P^{vap})}{RT}\right) = f_i^l \tag{5.22}$$

where y_i and x_i are the molar fractions of component i in the gas and liquid phase respectively, γ_i is the activity, Φ are the fugacity coefficients for the vapour at T and P of the system and for the vapour at T and $P^{vap}(T)$. Eventually, the exponential function in the right hand term is the Poyinting factor, which suits the fugacity of the liquid to the actual pressure conditions. The fugacity coefficients can be calculated based on different state equations for real gases and liquids.

The formula presented above states that in a multi-component system the gas and liquid phase are at equilibrium at the total pressure of the system itself, so

that a single component in the gas phase is at its vapour pressure for the employed temperature. These considerations are the theoretical background for calculation with the software of the water vapour pressure in the humidifier and the KCl vapour pressure at equilibrium with its solid state.

5.2 Step by step steady state design of the gas line

Here the sketch of the setup (modifications included) is presented again, to give a picture of the path of the gas.

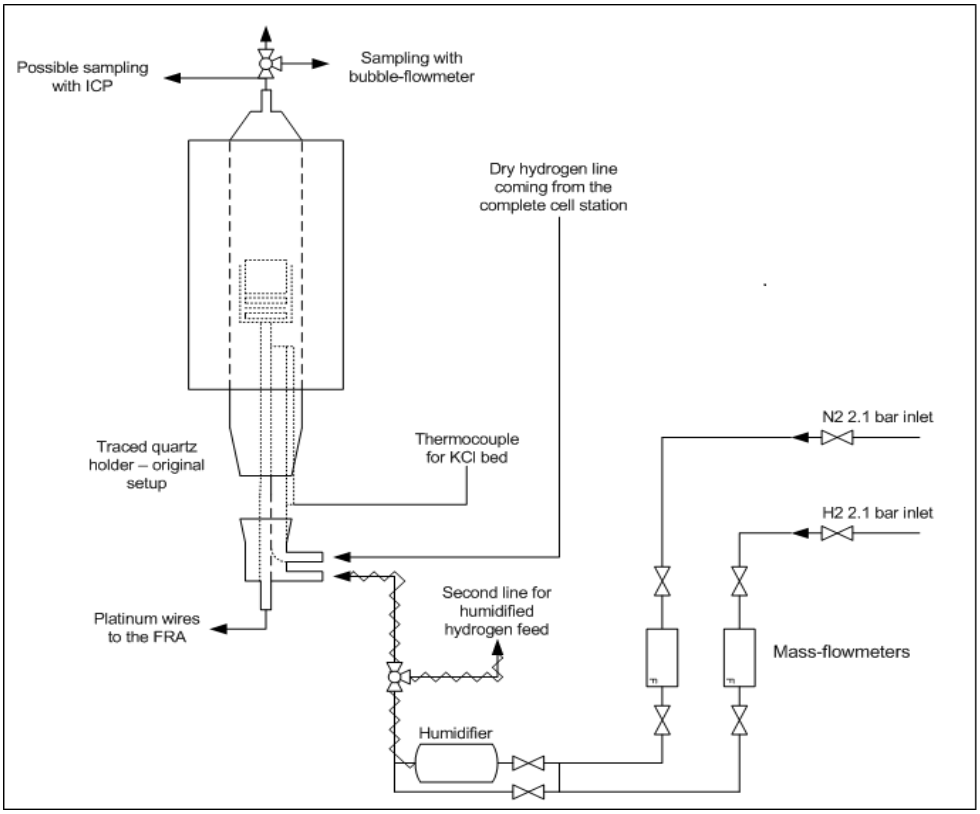

Figure 5.1. Sketch of the experimental asset for impedance measurements on symmetric cells at TU, with planned modifications included.

The real system is an open system, in which for many reactions the equilibrium won't be reached. Anyway, since the mass flow is low and most times the quantity of at least one of the reactants can be considered infinite compared to the others, equilibrium is often a good approximation. In Factsage, the equilibrium module is used and the systems are modelled as closed, because the

equilibrium concentration of reactants and products is the same for flowing or still gas as long as the ratios and the external conditions are the same. The pressure is low, around 1 bar with differences only due to drops along the piping (the maximum feed pressure, before the setup, is around 1.05 bar), so all the gases can be treated as ideal with good approximation. The temperature is varied.

This approach follows the one Aravind used when performing the experiments to show the short term behaviour of the anodes with H_2 or biosyngas feed, but it is extended. Every computation represents the simplified physical model of one element of the setup, so that the frame of the overall system is designed step by step in this chapter.

5.2.1 Humidification of the H_2 through control of the humidifier temperature

First of all the gas feed coming from the tanks (the results don't change either with H_2 or simulated biosyngas composition, since at the employed conditions ideal gases can be considered with good approximation) must be humidified, in order not to have too much a reducing environment and damage the cell. The flow is thus bubbled through a humidifier consisting in a pot with water at a controlled temperature. Another temperature controller is placed on the top of the humidifier (from where the humidified gas comes out) and set to 5 °C more than the pot to have a better control of the outlet temperature. Equilibrium at the exit is a good approximation, since the gas bubbles and the concentration of water at the outlet can be considered the saturation one, for the given temperature. The level of moisture is controlled by the temperature of the pot.

A humidification T of 303.15 K is chosen to have the same starting conditions as one could have in summer, when the temperature of the environment is close to that value.

Inlet: 1 mol H_2O liquid, 1 mol H_2 gas. The saturation concentration is independent from the flow, it is just a function of temperature.

Outlet: gas phase with 1 mol H_2 and 0.043825 mol H_2O; that is, 4.198% molar fraction of steam.

A check with real gases is done, with negligible differences.

The following graph represents the moisture fraction in the feed gas as a function of temperature.

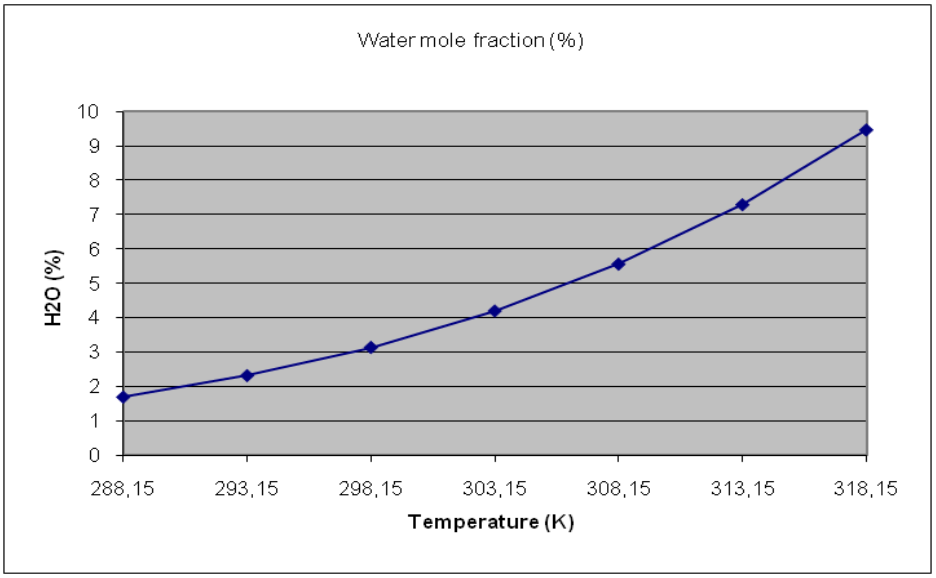

Figure 5.2. Equilibrium moisture content in the gas feed.

5.2.2 Possible spots for condensation

In the experiments condensation in some point of the gas line was suggested to be a possible cause for the low frequency arc being small with low volume flows. If condensation occurs at a cold spot, when the flow is switched to a lower value it could get more saturated by condensed water, as it is slower and at high temperature.

Since this behaviour appeared only for experiments during the coldest days of the year, when the room temperature was around 10 °C lower than for the last experiment, it is speculated that the critical points for condensation may be the most exposed: the humidifier pot, the top of the humidifier, the traced gas feed pipe, the connection between this pipe and the quartz holder. However if these parts are modelled some conclusions can be done: the top of the humidifier is hardly affected by the external temperature and cannot be cause for a temperature gradient. It is a metallic part and it is heated to 5 °C more than the bulk of the humidifier by an electric resistance, so it is heated almost uniformly to the very displayed temperature; as for the humidifier, it is heated to 30 °C for obtaining 4.2% humidification. It was shown how the width of the low

frequency arc at 850 °C, 80 Nml/min, nominal 4% of water corresponded to an actual water content of 12.2% (from the diffusion model, considering the diffusion length to be constantly 2 cm). The temperature which gives this vapour pressure is higher than 40 °C, so such saturation cannot occur in the pot. Humidity measurements at the outlet of the traced pipe can give the most significant conclusions, since its temperature is much higher.

5.2.3 Thermocouples

Thermocouple are placed in different spots to record the temperature and have it displayed: bulk of the humidifier, metallic head of the humidifier, beginning of the traced gas feed pipe, quartz holder below the reactor, hot spot of the reactor. Some of these points are at very high temperature and they are not sensitive to changes in room temperature. For some others, like the traced pipe and the humidifier, a change of 10 °C like the one which occurred between the third and the fourth experiment could affect the operation. In fact, thermocouples measure the voltage between two wires made of different metals (Seebek effect) connected to a hot and a cold end. The cold end is a reference and if its temperature is not controlled, the difference calculated by the software could give a wrong high temperature. This may happen with sharp drops of the ambient temperature. One way to avoid the issue is to use an ice/water bath as cold end; otherwise in industrial applications a “cold junction compensator” is employed. It must be verified whether it is used in the present laboratory equipment, because no ice/water bath is present.

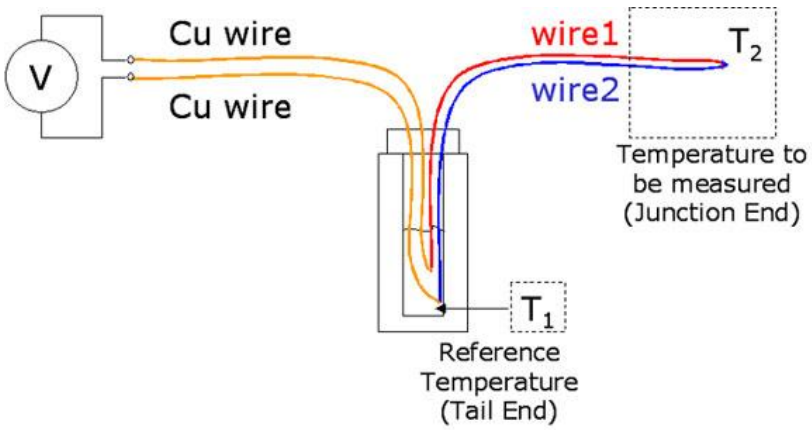

Figure 5.3. Schematic of a thermocouple circuit.

5.2.4 Flow of hydrogen through the KCl bed in the evaporator tube

As explained in the section describing the experimental setup in detail, the H_2 is fed through an evaporator tube with a bed of KCl crystals to get at the outlet the desired contaminant concentration in the gas. A gas sampling is then performed, to see if the equilibrium calculated ppm level corresponds to the actual one. As Aravind showed in his former study [1], the concentrations are not the same and an explanation of this is given elsewhere. Two gas inlets are available on the quartz evaporator, so that the same experience as Aravind's can be performed. Dry Hydrogen is fed through the bed and humidified Hydrogen bypasses the evaporator tube and mixes with the other flow at the top of the quartz element, just before the ceramic gas diffuser. With such a setup Aravind finds that a non perfect mixing of the two flows can occur and cause a widening of the diffusion arcs in the spectra in case the ratio between dry flow and humidified flow increases. This is ascribed to water not reaching the anode surface homogeneously. It is suggested in this study that a solution to the problem is to flow humidified hydrogen through the bed itself. The fastest and cheapest way to realize this configuration was connecting another pipe to the one exiting the humidifier and putting an on-off valve between them. Such a setup allowed to by-pass the evaporator during heating up and reduction. However this way during the experiment humidified flow has to go completely through the bed and the desired outlet concentration cannot be obtained by mixing to flows. Only one level will be employed each experiment.

Since in this case humidified Hydrogen is led through the evaporator, unlike in Aravind's experience, a check is necessary of which species form by reaction with H_2O and in which quantity (it is suggested that special care be taken for KOH and HCl). Practically, a way to get the desired KCl concentration must be found. Here a brief explanation of what was done in this study follows, referring to Aravind's experience. As most part of the evaporator pipe goes into the oven, its upper part is supposed to heat very much and a gradient of temperature is supposed to be present along it. According to equilibrium considerations (which are a good assumption as the flow is really small) the outlet gas contains KCl in the quantity which is given by the equilibrium conditions at the exit of the bed. It is released by simple sublimation (equilibrium solid-vapor), as explained above, to the extent which is decided by the vapor pressure. So the height of the KCl bed is set up to the point where the temperature is the equilibrium one for getting the desired gas phase KCl concentration in the H_2.

In the present computation the equilibrium of a closed system with humidified hydrogen and solid KCl salt is calculated in a temperature range from 656 to 668 °C, in order to see what the equilibrium composition is (and what species originate) and at what temperature the desired contaminant levels are found. The inlet data of the calculation and the results are presented.

Humidified hydrogen flowing through the KCl bed:

Inlet: 0.04198 mol H_2O, 0.95802 mol H_2, as found in the former computation for humidification at 303.15 K; 1 mol solid KCl.

Table 5.1. Concentrations at the KCl bed outlet.

T(°C)	656	658	660	662	664	666	668
Mole fr.							
H(g)	2,88E-10	3,065E-10	3,26E-10	3,46E-10	3,68E-10	3,91E-10	4,16E-10
H2(g)	0,957995	0,9579936	0,957992	0,95799	0,957988	0,957987	0,957985
H2O(g)	0,041979	0,0419787	0,041979	0,041979	0,041978	0,041978	0,041978
HCl(g)	1,83E-07	1,923E-07	2,02E-07	2,12E-07	2,23E-07	2,34E-07	2,45E-07
K(g)	2,13E-08	2,279E-08	2,44E-08	2,61E-08	2,78E-08	2,98E-08	3,18E-08
KOH(g)	1,62E-07	1,695E-07	1,78E-07	1,86E-07	1,95E-07	2,04E-07	2,14E-07
KCl(g)	1,94E-05	2,054E-05	2,18E-05	2,31E-05	2,44E-05	2,59E-05	2,74E-05
(KCl)2(g)	6,36E-06	6,794E-06	7,25E-06	7,74E-06	8,26E-06	8,8E-06	9,39E-06
TOT	3,21E-05	3,413E-05	3,63E-05	3,85E-05	4,09E-05	4,35E-05	4,62E-05

Desired contaminant level: the bed outlet concentration is in this case also the overall one. So the highest desired concentration is chosen as a reference, because it represents the harshest conditions. It is decided to be 40 ppm (as will be shown later), close to the highest concentration Aravind used in his experiments. In facts it is suggested that first experiments with KCl contamination are carried out in the short term with medium-high concentrations of contaminants. If effects are recorded and causes explained, then longer term experiments with less contaminant can be made, to simulate the real composition of a syngas after hot gas cleaning.

The closest concentrations to the desired one are marked in red. They are obtained for 664 °C as outlet temperature. HCl and KOH form in the presence of water, as it was expected, but their concentration stays as low as sub ppm levels for the whole temperature range. It is then concluded that theoretically the presence of water in the feed gas should not affect the performance of the cell, compared to the dry H_2 flow which was considered safer. The red boxes represent the temperatures which allow the closest composition to the desired one at the outlet. As can be seen, also $(KCl)_2$ forms, which is the same molecule as KCl, but in the form of small ensembles. Its formation is investigated since it could affect the performance of the cell in a different way than simple KCl. Though kinetic effects will be the same, as the type of molecule and bonding is the same, a bigger molecule could show different diffusion effects on the anodes. However a simple mass balance shows that at higher temperatures most molecules of this compound split into two molecules of the salt with a negligible part of them forming new KOH. In the table the equilibrium temperature is approximately chosen by summing the KCl concentration with double the $(KCl)_2$ concentration as if it all split into KCl by thermal dissociation. However, further computations at the cell temperature show that not all the $(KCl)_2$ splits, so that between 750 and 900 °C the KCl concentration at the anode will be from 35.6 to 38.6 ppm (it increases with temperature). These values are acceptable, because it was shown that the actual concentration is expected to be higher. So the employed temperature for the KCl bed outlet is 664 °C.

How much the concentration of KCl carried in the feed gas varies with temperature is shown below. The behaviour has the same shape for KOH, HCl, $(KCl)_2$, just with different slopes, being this a thermally activated process. The same result is obtained with dry H_2 flowing through the bed.

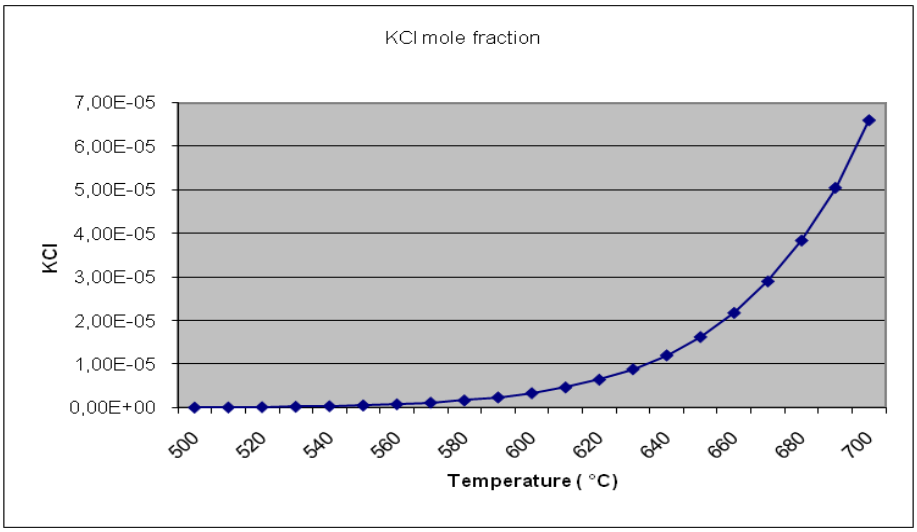

Figure 5.4. Equilibrium KCl concentration at the outlet of the bed with T.

A sensitivity analysis of the outlet KCl concentration over the moisture level of the carrier gas is made. The concentration of KCl ideally depends only on temperature. A check with real gases at a chosen temperature (in this case 664 °C) over a wider range of water mole fraction in the feed gas is performed.

Table 5.2. Concentration at the outlet of the bed with varying water content in the feed.

X-H_2O	0,02	0,04	0,06	0,07	0,09	0,11
Mole fr.						
H	3,72E-10	3,69E-10	3,65E-10	3,62E-10	3,59E-10	3,55E-10
H_2	0,98036	0,961507	0,943365	0,925895	0,909061	0,892828
HCl	1,63E-07	2,14E-07	2,54E-07	2,88E-07	3,16E-07	3,42E-07
K	3,85E-08	2,90E-08	2,42E-08	2,12E-08	1,91E-08	1,75E-08
KOH	1,24E-07	1,85E-07	2,30E-07	2,66E-07	2,97E-07	3,24E-07
KCl	2,44E-05	2,44E-05	2,44E-05	2,44E-05	2,44E-05	2,44E-05
$(KCl)_2$	8,25E-06	8,25E-06	8,25E-06	8,25E-06	8,25E-06	8,25E-06

With increasing water mole fraction KCl and $(KCl)_2$ mole fraction keeps constant, as expected. Fluctuations or small errors in the actual moisture level of the feed gas during the experiments will not affect the expected results. In fact, if an experiment with humidified flow is carried out, the moisture level will be kept as constant as possible, since a variation in it would affect the anode impedance much more than its effect on KCl deposition or diffusion.

One problem in humidifying the flow through the KCl bed is the chance of packing of the bed, since water could be adsorbed by the salt. This is going to be verified during the experiments.

Dry hydrogen flowing through the bed (most general case):

Inlet: 1 mol H_2; 1 mol KCl.

Before showing the results it must be underlined that in this case the desired contaminant concentration results from a mass flow balance between the humidified flow bypassing the evaporator and the flow which goes through. During the experiments the concentration will be then varied by only changing the mixing ratio: both the flows are derived from piping controlled by massflowmeters. In the experimental section it is explained how the setup was modified and organized to take the measurements. It is suggested to change as few conditions as possible, keeping the other ones constant, to better see their effect on the anode. The total flow is then kept constant, at 300 Nml/min (which is considered to be within a safe range for getting a stable behavior of the system, from results of the preliminary experiments), while the ratio between the dry and the humidified flow is varied. Also the concentration of KCl at the outlet of the bed is kept constant, since it is determined by the temperature of the cell and the height of the bed itself (which of course will not be changed during one experiment). It is as a first try decided to be 90 ppm, with subsequent mix with the pure flow. By determining the mixing between the two flows and the total humidification after the mixing (which is also kept constant at 4.2%), the needed moisture concentration of the humidified flow results decided. The necessity of not having too much a humidification (for it needs higher temperatures of the humidifier and with higher water content occasional condensation may be easier) is taken into account when deciding the flows. The overall calculation is then an optimization between mass flow rates, humidification and desired contaminant concentration in the total flow.

In all the three cases concentrations are kept around the maximum value which was used by Aravind (36.3 ppm). This way it is expected to see some effects in the short term. Once the contamination mechanism is understood, it is possible to lower concentrations and operate in the long term.

Desired contaminant level: total 24, 30, 40 ppm; for all three cases concentration in the dry flow at the outlet of the bed is constant, 90 ppm.

Table 5.3. Employed conditions for the mass flow balance.

CASE	Dry flow (Nml/min)	Hum flow. (Nml/min)	KCl conc. Dry flow (ppm)	Water hum.flow (%)	KCl conc. Total flow (ppm)
1	80	220	90	5,7	24
2	100	200	90	6,3	30
3	133	167	90	7,5	40

Table 5.4. Resulting KCl concentrations with the conditions presented above.

T(°C)	640	650	660	670	680	690	700
Moles							
H_2	1	1	1	1	1	1	1
HCl	3,92E-08	5,29E-08	7,09E-08	9,45E-08	1,25E-07	1,65E-07	2,15E-07
K	3,92E-08	5,29E-08	7,09E-08	9,45E-08	1,25E-07	1,65E-07	2,15E-07
KCl	1,2E-05	1,62E-05	2,18E-05	2,9E-05	3,83E-05	5,04E-05	6,59E-05
$(KCl)_2$	3,72E-06	5,22E-06	7,25E-06	1E-05	1,37E-05	1,86E-05	2,52E-05
TOT						8,77E-05	0,000116

The concentrations of KCl and $(KCl)_2$ into the bed don't vary compared to the case of humidified flow going through the bed. They are not supposed to, as they depend on the vapor pressure of the compound and the employed temperature. On the contrary, HCl concentration is one order of magnitude lower than for the former case and KOH isn't present at significant concentrations. To sum up, as far as the desired contaminant fraction is concerned the two options give the same result, while as for the undesired species formation, it is avoided by flowing dry hydrogen through the bed. The temperature for having 90 ppm at the bed outlet is found to be 691 °C, with linear interpolation between the results at 690 and 700 °C.

5.2.5 Pressure drop along the KCl bed

The last check on this asset aims at verifying that the pressure drop along the bed is not too much for the gas to flow. The pressure of the gases coming from the tanks is reduced to 2.1 bar before the mass flowmeters. However, after the mass flowmeters, it is around 1.05 bar (nearly atmospheric) and in case of counter pressure the flow is shut down because the mass flowmeters are not able to control the pressure. Big pressure drops can completely stop the flow. For

calculating the pressure drop along the bed Ergun's equation can be used. Protopapas [2] used it for fixed beds of comparable dimensions (r = 0.024 m and l = 0.3 m).

$$\frac{\Delta P}{l} = \frac{150(1-\varepsilon)^2 \mu v_s}{\varepsilon^3 d_p^2} + \frac{1{,}75(1-\varepsilon)\rho v_s^2}{\varepsilon^3 d_p} \tag{5.23}$$

where l is the height of the particle bed, ε is the void fraction, μ and ρ are the viscosity and density of the gas flow, v_s is the velocity of the gas flow and d_p is the particle diameter. The void fraction is calculated as $\varepsilon = 1 - \rho_b/\rho_p$, where ρ_b is the density of the bed, ρ_p is the density of the material. For the solid KCl of laboratory purity which was ordered a mean particle size of 363.5 and 364.8 μm was found through analysis of two samples. Once the height of the KCl bed is known from a blank experiment with the modified setup the void fraction can be calculated and consequently the total pressure drop. If it is too high for the setup to guarantee the flow, KCl with bigger particle size must be employed.

It must be taken into account that also big leakages could prevent the gas from flowing, as happened during one of the experiments.

5.2.6 Redox reactions of Ceria

Some stabilization time is required when ramping up the system, not only for reduction of NiO to take place, but also for reduction of Ceria. Its O^{2-} conductivity is activated when, under a reducing environment, it passes from the stoichiometric form to a non-stoichiometric one:

$$CeO_2 \leftrightarrow CeO_{2-x} + \frac{x}{2} O_2 \tag{5.24}$$

This reaction formally represents the ability of Ceria to form Ce^{3+} ions from Ce^{4+}. If some oxidant is fed, the inverse reaction could occur, some ions oxidize and the global conductivity decreases. This reversibility is less important at higher temperatures.

It is worth highlighting that the temperature range for change of one of the reduction states in Ceria is exactly the one of the present experiments, 973 to

1273 K [4]. In this region reduction of bulk Ceria takes place, while at 573-873 K surface reduction takes place. Both the mechanisms are water producing and the first one is slower. This helps identify the proper temperature for reduction of the samples and the required times.

5.2.7 Interaction of the flow feed with the anode materials for a fixed ppm level of contaminant and different temperatures

Since the effects of the presence of alkali compounds in the feed gas are still unknown, it is important to predict if and how they can affect the performance of the cell. Equilibrium computations on the interaction of the salt with the anode materials are suggested. The anodes which will be used are fairly the same structure as the ones Aravind used. As a starting point, the same composition as the one after the mixing of 133 Nml/min contaminated dry H_2 with 167 Nml/min humidified H_2 is used. This corresponds to the highest employed concentration in the experiments (40 ppm), so it is believed to be safe with respect to the effects KCl could possibly show. Results at 1023, 1073, 1123, 1173 K are presented, with following discussion of the results.

Inlet: 1 mol H_2, 0.043825 mol H_2O, 2.44E-5 mol KCl, 8.26E-6 $(KCl)_2$.

Anode material (as declared by the company): CeO_2 + Gd_2O_3 with molar fractions respectively 0.9 and 0.1 for the functional layer and 0.6 and 0.4 for the adherence layer. Being both Ceria and Gadolinia abundant for the reaction, their ratio is simplified and the quantities are set to 10 moles each for CeO_2, Gd_2O_3, Ni (assuming it at reduced state). The limiting reactant will then be the gas feed.

Table 5.5. Resulting concentrations at the anode with contaminated feed.

T(°C)	750	800	850	900
Moles				
H(g)	3,77E-09	1,19E-08	3,31E-08	8,27E-08
H_2(g)	0,796484	0,691855	0,58095	0,474449
H_2O(g)	0,24734	0,351968	0,462871	0,56937
HCl(g)	1,3E-06	2,31E-06	3,73E-06	5,56E-06
KOH(g)	1,24E-06	2,21E-06	3,55E-06	5,3E-06
$(KOH)_2$(g)	1E-10	1,1E-10	1,09E-10	9,98E-11
KCl(g)	3,51E-05	3,68E-05	3,65E-05	3,51E-05
$(KCl)_2$(g)	2,26E-06	9,14E-07	3,62E-07	1,46E-07
Ni(g)	7,16E-15	7,38E-14	6,16E-13	4,28E-12

NiH(g)	3,45E-15	2,62E-14	1,61E-13	8,32E-13
NiO(g)	2,69E-21	9,05E-20	2,22E-18	4,14E-17
$Ni(OH)_2$(g)	1,15E-12	9,52E-12	6,24E-11	3,34E-10
NiCl(g)	1,71E-15	1,42E-14	9,53E-14	5,34E-13
$NiCl_2$(g)	7,19E-17	4,84E-16	2,62E-15	1,19E-14
Ni(s)	10	10	10	10
CeO_2(s)	8,778903	8,151127	7,485702	6,846696
Ce_2O_3(s)	0	0	0	0
Ce_6O_{11}(s)	0,203516	0,308145	0,41905	0,525551
$Ce_{18}O_{31}$(s)	0	0	0	0
Gd_2O_3(s)	10	10	10	10

The reducing environment leads to reduction of CeO_2 into Ce_6O_{11}, with an ideally large production of water. Of course there's no indication of the rate of the process, since kinetics is not investigated. Gadolinia is completely inert, as expected, while Ni may have some catalytic effect, which is of course not shown, since these are equilibrium results. There's an increase of KCl and a decrease of $(KCl)_2$ concentration compared to the inlet, which means that most probably large part of the $(KCl)_2$ splits into KCl molecules (as already suggested above), while KCl and $(KCl)_2$ partly react with water to form a small amount of KOH and HCl in addition to the outlet amount from the KCl bed. At high temperatures these concentrations go as high as ppm levels, so they might become a problem. A sensitivity analysis with variation of moisture will give more information. If further steps are calculated, in which the produced water is assumed to be removed, we see that Ceria further reduces by the same amount, until when it is completely transformed into Ce_6O_{11}. Then, for the highest temperature level only, reduction to $Ce_{18}O_{31}$ begins and goes on. The Ce_2O_3 phase will be present at equilibrium only several hundreds of °C higher.

Table 5.6. Resulting concentrations at the anode considering Ceria at a reduced state.

T(°C)	750	800	850	900
Moles				
H(g)	4,22E-09	1,43E-08	4,34E-08	1,19E-07
H_2(g)	1	1	1	0,983345
H_2O(g)	0,043825	0,043824	0,043824	0,060479
HCl(g)	6,18E-07	9,82E-07	1,49E-06	2,39E-06
KOH(g)	4,7E-07	6,69E-07	8,91E-07	1,43E-06
$(KOH)_2$(g)	1,44E-11	1,01E-11	6,83E-12	7,24E-12
KCl(g)	3,56E-05	3,8E-05	3,86E-05	3,82E-05

$(KCl)_2$(g)	2,33E-06	9,75E-07	4,06E-07	1,73E-07
Ni(g)	7,16E-15	7,38E-14	6,16E-13	4,28E-12
NiH(g)	3,87E-15	3,15E-14	2,12E-13	1,2E-12
NiO(g)	3,8E-22	7,8E-21	1,22E-19	2,12E-18
$Ni(OH)_2$(g)	2,87E-14	1,02E-13	3,25E-13	1,82E-12
NiCl(g)	7,24E-16	5,02E-15	2,91E-14	1,59E-13
$NiCl_2$(g)	1,29E-17	6,03E-17	2,43E-16	1,06E-15
Ni(s)	10	10	10	10
CeO_2(s)	0	0	0	0
Ce_2O_3(s)	0	0	0	0
Ce_6O_{11}(s)	1,6667	1,6667	1,6667	1,641718
$Ce_{18}O_{31}$(s)	0	0	0	0,008327
Gd_2O_3(s)	10	10	10	10

KCl concentration reaches a maximum within this temperature range (at 850 °C), while $(KCl)_2$ decreases with temperature, to allow more KOH and HCl form.

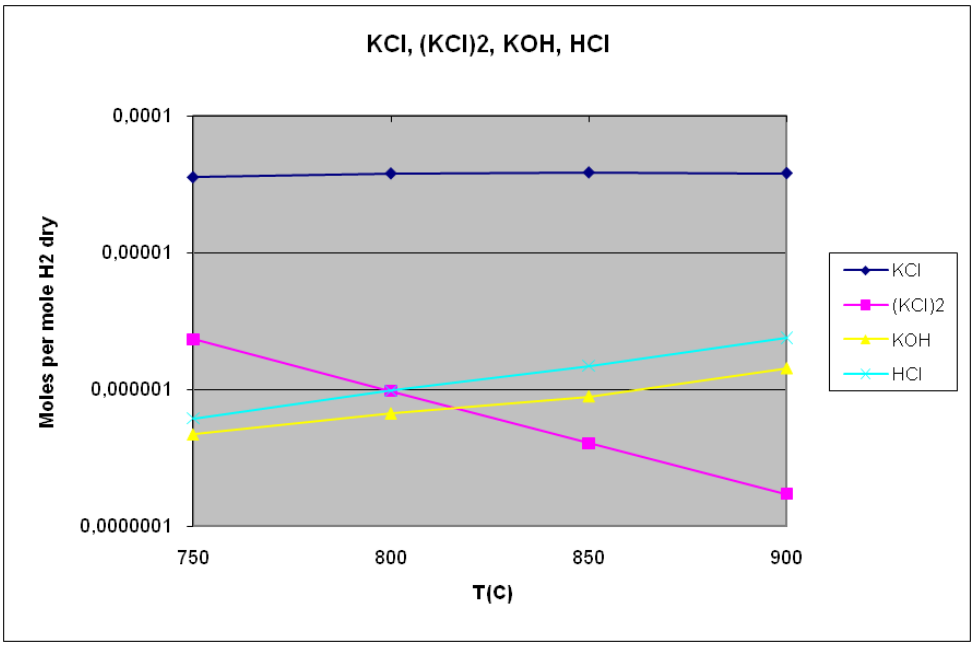

Figure 5.5. Concentrations of K species with temperature.

Formation of NiCl and $NiCl_2$ is detected, up to a negligible amount in the considered temperature range. Despite this, it must be recorded that NiCl

formation seems to have an exponential dependence on temperature. The same be said for Ni(g), NiH and above all $Ni(OH)_2$. Formation of NiO is totally negligible.

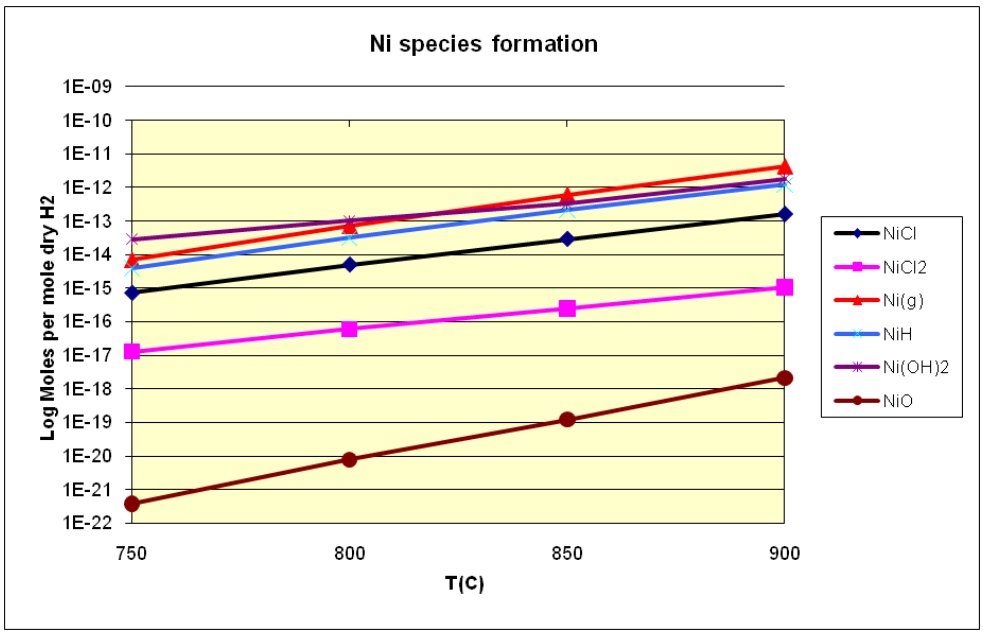

Figure 5.6. Concentrations of Ni species with temperature.

5.2.8 Interaction of the flow feed with the anode materials for a fixed temperature (1123 K) and different concentration of contaminants / water.

Performing the former computations with the highest level of contaminant is safe with respect to the possible effects on the anode. Anyway results with a wider range of contaminant are presented, as calculated at 1123 K. At this temperature Aravind carried out the experiments with contaminated gas feed over anodic symmetrical cells. Additionally, calculations with different humidification are carried out, to investigate the chance of Ni oxidation with higher water content.

The employed conditions don't correspond to any in the experiments, but they just represent a sensitivity analysis over the most important parameters.

Anode materials: 10 mol of Ce_6O_{11}, Gd_2O_3, Ni.

Table 5.7. Concentrations at the anode with varying KCl content in the feed at 850 °C.

Nominal ppm	20	30	40	50
Mol-KCl(g)	1,88E-05	2,83E-05	3,78E-05	4,71E-05
(KCl)2(g)	9,58E-08	2,18E-07	3,88E-07	6,04E-07
H(g)	4,34E-08	4,34E-08	4,34E-08	4,34E-08
H_2(g)	1	1	1	1
H_2O(g)	0,043824	0,043824	0,043824	0,043824
HCl(g)	1,04E-06	1,28E-06	1,47E-06	1,65E-06
KOH(g)	6,21E-07	7,63E-07	8,81E-07	9,84E-07
$(KOH)_2$(g)	3,32E-12	5,00E-12	6,67E-12	8,33E-12
Ni(g)	6,16E-13	6,16E-13	6,16E-13	6,16E-13
NiH(g)	2,12E-13	2,12E-13	2,12E-13	2,12E-13
NiO(g)	1,22E-19	1,22E-19	1,22E-19	1,22E-19
$Ni(OH)_2$(g)	3,25E-13	3,25E-13	3,25E-13	3,25E-13
NiCl(g)	2,03E-14	2,49E-14	2,87E-14	3,21E-14
$NiCl_2$(g)	1,18E-16	1,78E-16	2,38E-16	2,97E-16
Ni(s)	10	10	10	10
CeO_2(s)	0	0	0	0
Ce_2O_3(s)	0	0	0	0
Ce_6O_{11}(s)	1,6667	1,6667	1,6667	1,6667
$Ce_{18}O_{31}$(s)	0	0	0	0
Gd_2O_3(s)	10	10	10	10

The calculation is performed at 850 °C, at which temperature Ce_6O_{11} is stabile. No harmful compound shows big variation in concentration within this range. Ni Hydroxide, which is the highest Ni compound in concentration, has no dependence on KCl content, while Ni Chlorines are not worrying. HCl and KOH are present by the same order of magnitude, which of course must be taken care of, because it is around ppm level.

The results with variation of humidification follow.

Inlet conditions:

- Temperature: 1123 K
- Flow: 1 mol H_2, 2.44E-5 mol KCl, 8.26E-6 mol $(KCl)_2$, variable water content.

Table 5.8. Ni species formation with varying water content in the feed.

Mol-H2O	0,05	0,15	0,25	0,35	0,45	0,55	0,65
KCl(g)	3,86E-05	3,79E-05	3,74E-05	3,7E-05	3,67E-05	3,63E-05	3,61E-05
$(KCl)_2$(g)	4,02E-07	3,54E-07	3,18E-07	2,88E-07	2,63E-07	2,42E-07	2,24E-07
Ni(g)	6,2E-13	6,79E-13	7,38E-13	7,97E-13	8,56E-13	9,15E-13	9,74E-13
NiH(g)	2,13E-13	2,22E-13	2,32E-13	2,41E-13	2,5E-13	2,58E-13	2,66E-13
NiO(g)	1,4E-19	4,61E-19	8,35E-19	1,26E-18	1,74E-18	2,28E-18	2,86E-18
$Ni(OH)_2$(g)	4,23E-13	3,81E-12	1,06E-11	2,07E-11	3,43E-11	5,12E-11	7,15E-11
NiCl(g)	3,03E-14	4,74E-14	6,14E-14	7,4E-14	8,58E-14	9,71E-14	1,08E-13
$NiCl_2$(g)	2,64E-16	5,89E-16	9,06E-16	1,22E-15	1,53E-15	1,83E-15	2,13E-15
Ni(s)	10	10	10	10	10	10	10

No significant NiO formation is found at equilibrium with variation of water content, neither valuable increase in any other Ni species. Humidification variations employed in the experiments (from 3% to 7.5%) are absolutely safe with respect to Ni degradation. However, since degradation of Ni may invalidate the measurements, validation of these results from experience is needed (as a starting point with SEM and XRD analysis).

Appendix 5 A

Interaction of the flow feed with the anode, when CO is present, with and without KCl

Equilibrium computations for fixed chosen compositions are performed along with ternary diagrams calculations in order to verify the possibility of carbon deposition when CO is present in the feed. The chance of formation of other carbon species is considered too. The results will serve as a reference for calculations with KCl in the feed, which are the next step in the research which was presently started. The presence of CO makes the composition more similar to that of a biosyngas because it introduces the effects of carbon. No experiment was carried out with CO in the present study, but this first theoretical approach will be of use for further experimental investigation.

Three feed compositions are employed, which were already used by Aravind in his study. As an anode material, only Ceria at the reduced state is taken into account, assuming that complete reduction has already occurred and the deposited carbon cannot be oxidized by free oxygen atoms.

Inlet composition:

1. 0.55 moles H_2; 0.45 moles CO; 0.043825 moles H_2O.
2. 0.70 moles H_2; 0.30 moles CO; 0.043825 moles H_2O.
3. 0.85 moles H_2; 0.15 moles CO; 0.043825 moles H_2O.

Anode material:

10 moles Ni, 10 moles Gd_2O_3, 1.6667 moles Ce_6O_{11}.

Here the results with 45% CO on dry basis are displayed, for they represent the most critical condition.

Table 5A.1. Main concentrations at the anode with humidified H_2 and CO feed.

T(K)	1023	1073	1123	1173
Moles				
H_2(g)	0,503424	0,538342	0,555868	0,556812
CH_4(g)	0,019907	0,012453	0,004768	0,001403

H_2O(g)	0,050586	0,030576	0,028421	0,034206
CO(g)	0,349984	0,411844	0,425059	0,427652
CO_2(g)	0,046628	0,025702	0,020172	0,020944
H_2CO(g)	2,45E-07	2,73E-07	2,69E-07	2,54E-07
C(s)	0,033481	0	0	0
CeO_2(s)	0	0	0	0
Ce_6O_{11}(s)	1,66667	1,66667	1,66667	1,651788

Carbon formation occurs at equilibrium only at the minimum operation temperature and at the maximum CO concentration. In the actual system however, as Aravind showed [1], carbon deposition doesn't occur, because the gas composition is too close to the phase transition line and because probably there's not enough time for equilibrium to be reached. It is suggested that in practice a lower quantity of steam is required for avoiding carbon deposition than what thermodynamically calculated. The results with varying KCl concentration into the feed (nominally from 20 to 50 ppm) show no dependence of carbon formation on KCl content, though K is believed to inhibit carbon deposition [3], so they are not presented here.

Other carbon containing species form starting from CO, due to gas shift, dry and steam reforming, methane formation reactions. CH_4 and CO_2 are the only ones at a considerable concentration. A higher water mole fraction is also obtained, as a product of the methane formation reaction. Here the possible reactions follow:

$$CO + H_2O \leftrightarrow CO_2 + H_2 \qquad -41 \text{ kJ/mol} \qquad (5.25)$$

$$CO + 3H_2 \leftrightarrow CH_4 + H_2O \qquad -206 \text{ kJ/mol} \qquad (5.26)$$

In the presence of water and solid carbon also an uptake of the deposited carbon could occur:

$$C + H_2O \leftrightarrow CO + H_2 \qquad (5.27)$$

A graph representing the evolution of the main species in the temperature range and one comparing the different equilibrium amounts coming from the three gas feeds are useful to understand the global scenario of the possible reactions.

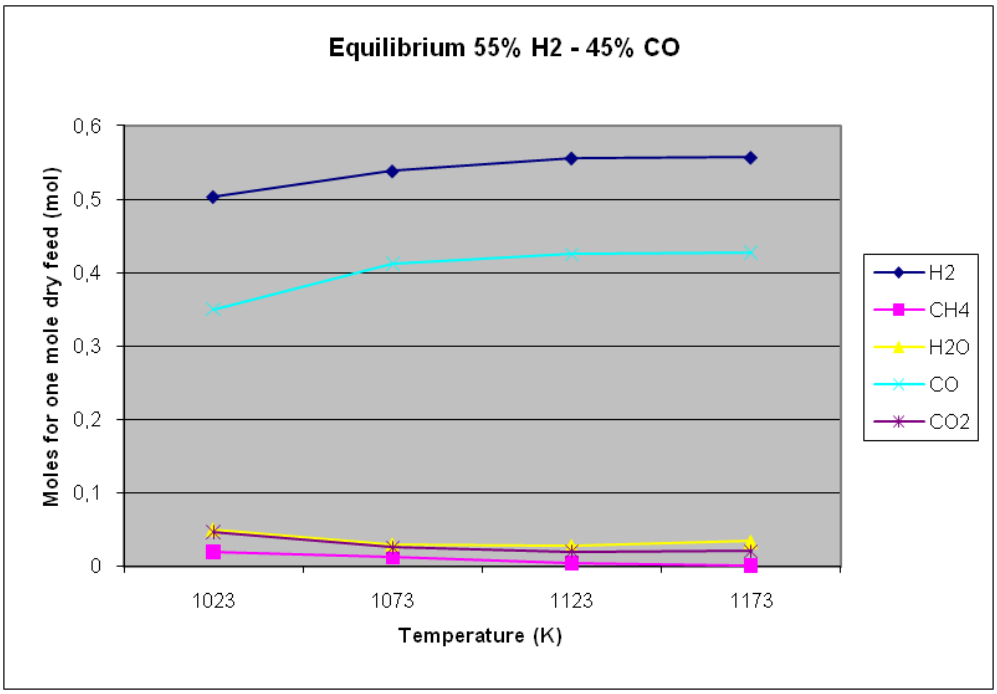

Figure 5A.1 Equilibrium species at the anode with different temperatures.

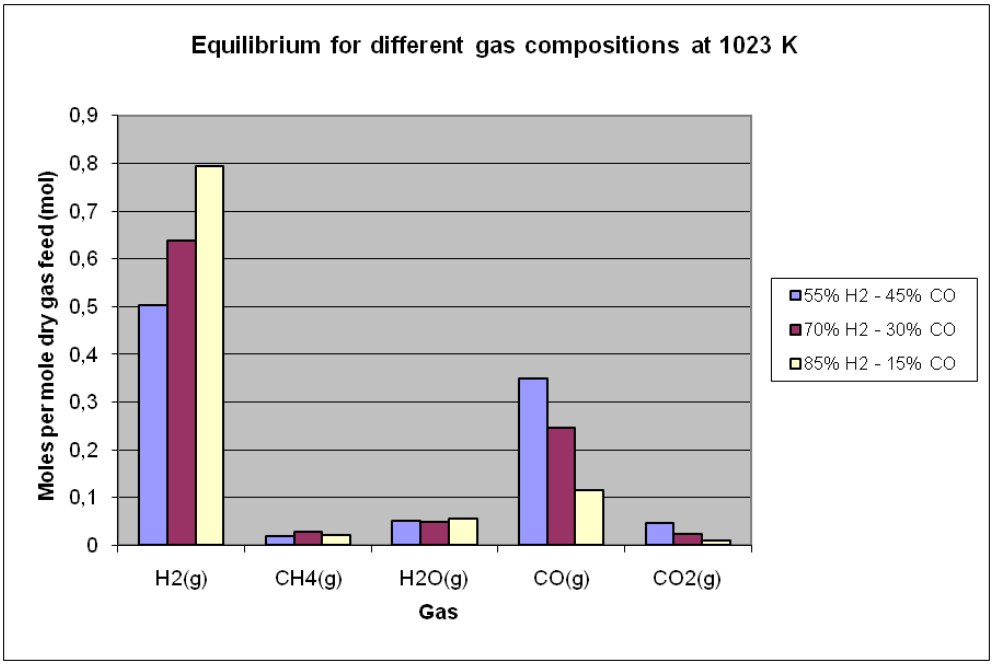

Figure 5A.2. Equilibrium species for three different 4% humidified feeds.

Computations are also performed with KCl contaminating the flow at different concentrations (20, 30, 40, 50 ppm). As a temperature, 1023 K is chosen, since it is the only one at which carbon deposition can occur. The equilibrium doesn't result influenced by the presence of ppm values of KCl, though it is known as a catalyst promoter to avoid solid carbon formation in steam reforming [3].

Appendix 5 B

C_H_O ternary diagrams

C_H_O ternary diagrams are phase diagrams which represent the equilibrium phases forming when the gas feed contains C, H, O as elements (like a mix of H_2, H_2O and CO). Into the already present gas phase also solid carbon deposits may form, depending on the ratio of the elements and the temperature. A line with different possible slopes divides the region in which only gas is present from the one where gas and graphite are present. These diagrams may be of help in verifying how far from or how into the double phase region is the gas flow considered. The anode materials are not taken into account in the computations, as they can only influence kinetics. Maybe because of kinetics deposition doesn't have enough time to occur, but this is to be verified by experiments.

Inlet:

The inlet compositions are the same as the previous computation with CO.

1. 0.55 moles H_2; 0.45 moles CO; 0.043825 moles H_2O.
2. 0.70 moles H_2; 0.30 moles CO; 0.043825 moles H_2O.
3. 0.85 moles H_2; 0.15 moles CO; 0.043825 moles H_2O.

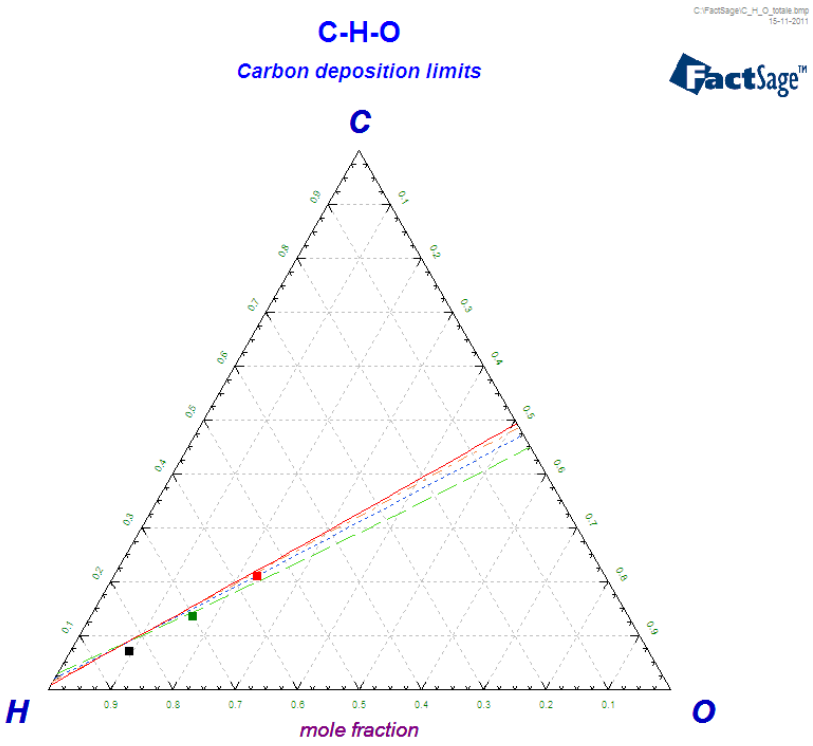

Figure 5B.1. CHO ternary diagram for the employed temperatures and feeds.

The four lines correspond to the four temperature levels. The higher is the temperature, the higher is the slope, because the upper region (with carbon deposition) reduces. As stated before, the red dot, which represents the composition when 45% CO is added to the gas on molar dry basis, lies within this region. The molar concentrations of the single elements which were used for setting the dots are the following (taken at the inlet from the gas feed composition, not considering the following carbon deposition):

1. C: 21.11 %
   H: 55.72 %
   O: 23.17 %
2. C: 14.97 %
   H: 69.79 %
   O: 16.13 %
3. C: 7.04 %
   H: 83.87 %
   O: 9.09 %

References

[1] P.V. Aravind, Studies on High Efficiency Energy Systems based on Biomass Gasifiers and Solid Oxide Fuel Cells with Ni/GDC Anodes, PhD thesis, November 2007.

[2] G. Protopapas, Integrated Biomass Gasification – SOFC Systems, MSc Thesis, Delft, March 2006.

[3] J.R. Rostrup-Nielsen, L.J. Christiansen, Internal steam reforming in fuel cells and alkali poisoning, Applied Catalysis A, 1995, pp. 381-390.

[4] G. Ranga Rao, Braja Gopal Mishra, Structural redox and catalytic chemistry of ceria based materials, Bulletin of the Catalysis Society of India 2, 2003, pp.122-134.

[5] G. Groppi, Dispense del corso di Processi chimici per l'energia e l'ambiente, Politecnico di Milano, 2009.

Chapter 6

Conclusions

Many recent studies demonstrate how high temperature fuel cells are suitable to operate with syngas and biosyngas as fuels. This makes it possible to conceive Gasifier-SOFC-GT systems, which theoretically have very high energetic and exergetic efficiency and represent a solution for combined heat and power generation either on big scale or small scale systems. This is possible as long as contaminants present up to some extents in the syngas are tolerated by the fuel cells or stacks. EIS is found to be a good tool for investigation of the influences of each contaminant on the processes occurring in the cell, because it breaks down activation and concentration losses into specific contributions. However it is verified by experience that EIS is very sensitive on geometry of the setup and experimental conditions: this makes research in the field slow, because many groups use their own setups and results of the experiments are hardly comparable. Moreover, even with the same geometry, many casualties may show up on one setup and don't show up on another.

In the present research tests were carried out through an iterative refining of the procedure. This allowed to obtain reproducible and reliable results with humidified H_2 to make a reference point for future experiments with alkali contamination in the gas feed on Ni/GDC anodes at typical gasification temperatures. This was found to be the most important step for being able to explain results when the contaminant is added: since no literature background is available in this field and possible effects aren't known yet, every externality in experimentation must be avoided. First impedance measurements with humidified H_2 on 35 μm thick anodes (with symmetric cells) resulted not reliable, neither reproducible: high noise in the high frequency region of the spectra was recorded, partly due to the wiring, partly to higher stabilization times than expected being required. Tests were carried out every time improving the setup and the procedures, until consistent results were found. Temperature and humidification were changed, to have a sensitivity analysis over parameters which could also be varied when performing experiments with KCl; flows were also changed, between 50 Nml/min and 400 Nml/min, since no information was available for the employed geometry about possible influences on the results and conclusions could turn useful when modifying the setup for KCl testing.

With flows above 200 Nml/min spectra were found to be reproducible with different experiments and consistent with variations of experimental conditions (temperature and humidity). High flows are therefore suggested for measurements with KCl contamination. Variations of R_s resistance (electrolyte and contacting) were ascribed either to degradation or to progressive sintering of the mesh on the surface of the anode, according to the trend and to considerations about the employed temperature.

On the other hand, unexpected results were recorded when switching to low flows. Wide variations of the low frequency arc showed up, which had to be deeper investigated because in preliminary experiments with KCl it was the low frequency to make interpretation of the spectra difficult. Much smaller arcs appeared as oscillating with 100 Nml/min and as stabilized with 80 Nml/min, when low humidification was used (3 and 4%). On the contrary at 7% humidification spectra were consistent and reproducible. This behaviour did not appear in one further experiment. The only difference was the room temperature, much higher in the latter case. Understanding the causes for this problem will provide wider flow ranges for investigation of KCl effects and better knowledge of influences of the setup on the measurements.

For this reason it is suggested that condensation may have occurred in some low temperature part of the gas line and this is proposed as a future topic for investigation. The diffusion model for the low frequency, which is a mono-dimensional linear model accounting for a diffusion limitation in a stagnant gas layer over the anode, proved to be reliable. However, it is based on a preliminary CFD model of the geometry and a more detailed CFD analysis is suggested for study of the low frequency part.

Results were also found to be highly dependent on the fitting procedure and on the initial parameters chosen for fitting. This is also influenced by arbitrariness of the operator. An iterative and statistical approach was then found to validate results from the fittings. Furthermore, three different methods for fitting were used, with help of functions in ZView software for EIS analysis, and results were compared: fittings were found to be reliable and within an acceptable error interval. Such analysis is suggested as a tool for validating results, to be employed together with already known ones (KK transform, instant fit function, check of capacitances and frequencies). Not a single check but a cross control is believed to give the best results.

When a set of reliable spectra was obtained and a set of problems identified, a step-by-step modelling of the setup was made. This allows integrate experience and theory and gives more tools for understanding influences on the measurements and for investigating what results were unexpected from the experiments. From such analysis also a physical modelling of the modification of the setup for experiments with KCl stemmed. This led to design and build the parts of the setup which are now available to be used in further analysis. Eventually, on basis of all the considerations from the experiments with pure H_2 and from modelling of the modified setup, the parameters for analysis with KCl are calculated (flows, contaminant concentration, humidification) and it is suggested to start from them for the prosecution of the research.